

國 立 交 通 大 學
機 械 工 程 學 系

博士論文

應用非結構性網格之平行化三維 PIC-FEM 程式

的研究與發展



Development of a Parallelized PIC-FEM Code Using a
Three-Dimensional Unstructured Mesh and Its Applications

研 究 生：許國賢

指 導 教 授：吳宗信博士

2006 年 07 月 14 日

應用非結構性網格之平行化三維 PIC-FEM 程式的研究與發展

**Development of a Parallelized PIC-FEM Code Using a
Three-Dimensional Unstructured Mesh and Its Applications**

研究生：許國賢

Student : Kuo-Hsien Hsu

指導教授：吳宗信 博士

Advisor : Dr. Jong-Shinn Wu



Submitted to Institute of Mechanical Engineering Collage of Engineering
National Chiao Tung University
In Partial Fulfillment of the Requirements
for the Degree of
Doctor of Philosophy
in
Mechanical Engineering
July 2006

Hsinchu, Taiwan, Republic of China

中華民國九十五年七月

誌謝

首先由衷感謝論文指導老師 吳宗信教授在學術研究上的細心及辛苦的指導。在兩年碩士班和五年博士班的學習期間，學生深切地感受到老師對學術研究的熱情與願景，淺移默化間也成為激勵學生本身不斷追求進步的動力；在待人處事的生活哲學上，老師更是樹立了我們學習的好榜樣，時時刻刻提醒我們身為國家社會一份子所應擔當的責任與義務。

感謝口試委員傅武雄主任、蔡惠峰副主任、陳彥升研究員、洪哲文教授以及江仲驊教授給與本論文撰寫及研究成果的建議。在此特別感謝大學專題指導老師江仲驊教授，多年來的關心與鼓勵。江老師總是在電話筒的那端耐心傾聽學生那不善表達的心情告白，能親自邀請老師擔任口試委員，是學生心目中對您最大的敬意。感謝劉晉良教授、黃楓南教授與鄭宗杰博士分別在數值方法及實驗研究上的指導與討論。

感謝曾經是 GDKL 實驗室和現在 MuST 實驗室一同打拼的夥伴們：許佑霖學長、邵雲龍學長，曾坤樟學長、連又永同學、李允民學弟、周欣芸學妹、洪捷祭學弟、李富利學弟、許哲維學弟、鄭凱文學弟以及所有碩士班的學弟妹們。感謝主內弟兄陳百彥學弟在論文發表上的協助和主前的代禱，讓我能安心和專心在程式上的發展。特別感謝邵雲龍學長、洪捷祭學弟和李富利學弟在我博士論文最後階段，全力的協助與幫忙。謝謝你們大家豐富了我的研究生生活，更讓我享受到 team work 的甘甜。

深深感謝父親 許忠裕先生和母親 陳幸雪女士在我求學生涯的過程，在經濟上和生活上的不間斷的支持和鼓勵。感謝我的岳父 吳義行先生和岳母 鄭秀月女士，願意讓他們的寶貝女兒嫁給一個還在求學的學生；謝謝您們對我們的信任以及信仰上的相互扶持；感謝您們無怨無悔的愛，希望這份畢業的榮耀，是我這兩位父親今年父親節最特別的禮物。感謝小妹淑貞、妹婿碩賢和小弟志豪，在我外出求學的期間，對父母的孝順與付出。感謝文博、敏慈、大勇和美嬋對我們的鼓勵，也謝謝你們總是開心地跟我們分享姪子和姪女可愛的成長照片。特別感謝我最親愛的老婆 美蔓，總是陪伴在我身邊，給予我最直接的幫助；謝謝妳每天在上帝面前為我所作的禱告，因著妳的愛，所有的逆境遭遇，我都能甘之如飴。

感謝光復教會的牧者、傳道與所有弟兄姐妹在日常生活中彼此的幫忙與代禱，引領著我一次又一次經歷上帝那奇妙的恩典。最後，深願將這所有的榮耀歸於上帝祢自己的名。

許國賢 謹誌

2006年7月于風城交大

Development of a Parallelized PIC-FEM Code Using a Three-Dimensional Unstructured Mesh and Its Applications

Student: Kuo-Hsien Hsu

Advisor: Prof. Jong-Shinn Wu

Department of Mechanical Engineering
National Chiao-Tung University

Abstract

A general parallel three-dimensional electrostatic particle-in-cell scheme with finite element method (PIC-FEM) using an unstructured mesh is proposed and verified in this dissertation. A multi-level graph-partitioning technique is used to dynamically decompose the computational domain to improve the parallel performance during runtime. Completed parallelized PIC-FEM code is used to simulate several important physical problems, including field emission, DC/RF gas discharge and DC/RF magnetron plasmas. In this thesis, research is divided into three different phases.

In the first phase, a parallelized three-dimensional electrostatic Poisson's equation solver using Galerkin finite element method using an unstructured mesh is developed and validated. In addition, a parallelized three-dimensional vector potential magnetostatic Poisson's equation solver is developed and validated. Furthermore, these two solvers are coupled, respectively, with a parallel adaptive mesh refinement (PAMR) module, to automatically improve the resolution of solution near where the property gradient is large. In both solvers, resulting algebraic equations are solved using either the parallel conjugate gradient method with a subdomain-by-subdomain scheme for more processors (>10) or the direct sparse matrix solver for fewer processors (<10). Parallel speedup test for solvers using parallel conjugate gradient

method is performed on a HP-IA64 cluster system up to 32 processors at NCHC of Taiwan. Results show that parallel efficiency can reach 84% and 75% at 32 processors for the electrostatic Poisson's equation solver and magnetostatic vector Poisson's equation solver, respectively.

In the second phase, a general parallel three-dimensional PIC-FEM code is developed and validated. This PIC-FEM code integrates the parallelized Poisson's equation solver, developed in the first phase, with the PIC and Monte Carlo collision (MCC) schemes on an unstructured tetrahedral mesh. Charged particles are traced either cell-by-cell on an unstructured mesh. This is achieved using leap-frog time-integration method and Boris rotational scheme when magnetic field is involved. Charge assignment and force (field) interpolation between charged particles and grid points is implemented using the same interpolation function originated from the FEM. In addition, dynamic domain decomposition (DDD) with weighting based on number of particles is used to balance the workload among processors during runtime. Study of parallel performance of the parallelized PIC-FEM code is performed on the HP-IA64 clusters. Results using DDD show that parallel efficiency can reach 83% at 32 processors.

In the third phase, the parallelized PIC-FEM code is used to simulate several important problems to demonstrate its superior capability in handling practical problems. These problems include field emission from a CNT /silicon based emitter under external electric field and magnetic field, two typical three-dimensional DC and RF gas discharge plasmas, and two typical three-dimensional DC and RF magnetron plasmas with permanent magnets.

Keyword: Particle-In-Cell with Monte-Carlo collision, finite element method, unstructured mesh, parallel, graph-partitioning, field emission, DC and RF gas discharge plasmas, DC and RF magnetron plasmas



應用非結構性網格之平行化三維 PIC-FEM 程式的研究與發展


學生：許國賢

指導教授：吳宗信

國立交通大學機械工程學系

摘要

本論文研究目的主要是發展與驗證一平行化三維粒子式 Particle-In-Cell (PIC-FEM)和蒙地卡羅法程式，並使用 multi-level 圖形切割技術於三維非結構性網格的動態區域切割法。此程式可應用於許多重要物理問題上的模擬，包括場發射元件、直流氬氣放電電漿、射頻氬氣放電電漿、直流氬氣磁控式電漿和射頻氬氣磁控式電漿。



本研究主要可分為三部分。第一部份：使用 Galerkin 有限元素法來分別離散靜電 Poisson 方程式來求解三維靜電場問題以及靜磁向量 Poisson 方程式來求解三維靜磁場問題。當平行電腦叢集數目大於 10 時，程式使用的平行化 conjugate gradient method 來求解矩陣問題；反之，當平行電腦叢集數目小於 10 時，則使用直接矩陣法 MUMPS 來求解矩陣問題。再者，將以上所發展的平行化靜電和靜磁程式結合平行可調適網格再切割模組(parallel adaptive mesh refinement module, PAMR)；因此，當計算區域出現位勢場變化較大處，計算網格將會自動被切割以獲得更正確的數值解。兩者程式平行效率測試於國家高速電腦提供的 32 台 HP-IA64 平行電腦叢集上進行，結果顯示靜電和靜磁程式的平行化效率於 32 台電腦叢集下分別可達到 84%和 75%。

論文的第二部份：主要是結合第一部份發展的三維平行化靜電和靜磁程式及三維平行 PIC-FEM 程式於三維非結構性四面體網格上。PIC-FEM 程式使用蛙跳法與 Boris 法來計算粒子運動方程式。因計算網格的不同，粒子追蹤法可利用非結構性網格關係來追蹤運動粒子軌跡。帶電粒子和計算網格點之間的權重函數為有限元素法中的形狀函數。再者，使用動態區域切割法來平均分散平行電腦間的工作量以改善平行化效率。最後模擬一近似一維的直流氬氣放電電漿和射頻氬氣放電電漿來驗證程式的正確性，並模擬三維射頻氬氣放電電漿來測試程式平行效率，測試結果顯示，如使用粒子數目為動態區域切割法的權重，於 32 台 HP-IA64 電腦叢集下還可達到 83% 平行效率。

論文最後部份，為展現三維平行 PIC-FEM 程式在許多重要物理問題上優秀的模擬能力，其應用問題包括三維奈米碳管式場發射元件與矽式場發射元件、三維直流氬氣放電電漿、三維射頻氬氣放電電漿、三維直流氬氣磁控式電漿和射頻氬氣磁控式電漿。

關鍵字：粒子式和蒙地卡羅法、有限元素法、非結構性網格、平行化、圖形切割法、場發射元件、直流氬氣放電電漿、射頻氬氣放電電漿、直流氬氣磁控式電漿和射頻氬氣磁控式電漿

Table of Contents

Abstract	III
摘要	VI
Table of Contents	VIII
List of Tables	XI
List of Figures	XII
Chapter 1. Introduction	1
1.1 Motivation and Background.....	1
1.2 Literature Surveys.....	2
1.2.1 Modeling of Field Emission.....	3
1.2.2 Modeling of Low-temperature Plasma.....	6
1.3 Objectives of the thesis.....	13
1.4 Organization of the thesis.....	14
Chapter 2. The Parallel Computing of Finite Element Method for Three-dimensional Electrostatic Field Problems	16
2.1 Background of Computational Electromagnetic.....	17
2.2 Finite Element Method (FEM).....	20
2.2.1 Background.....	20
2.2.2 The Galerkin Weighted Residual Method.....	21
2.3 Calculation of Electrostatic Field.....	21
2.4 Sparse Matrix Storage Schemes.....	28
2.5 Preconditioned Conjugate Gradient Method (PCG).....	29
2.6 Multi-frontal Massively Parallel Solver (MUMPS).....	30
2.7 Parallel Computing of FEM.....	33
2.7.1 Domain Decomposition Method.....	37
2.8 Parallel Adaptive Mesh Refinement Using a Tetrahedral Mesh (PAMR).....	38
2.9 Coupling of PAMR with Parallel Electrostatic Field Solver.....	42
2.10 Validation and Parallel Performance of the Electrostatic Field Solver with PAMR.....	43
2.11 Some Remarks.....	48
Chapter 3. The Parallel Computing of Finite Element Method for Three- dimensional Magnetostatic Field Problems	49
3.1 Calculation of Magnetostatic Field.....	49
3.2 Coupling of PAMR with Parallel Magnetostatic Field Solver.....	53
3.3 Validation and Parallel Performance of the Magnetostatic Field Solver with PAMR.....	55
3.4 Some Remarks.....	57

Chapter 4. An Overview of the PIC-FEM Method Using an Unstructured Mesh and Its Parallel Implementation.....	58
4.1 General Description of Conventional PIC-MCC Method.....	59
4.2 The PIC-MCC Procedures.....	60
4.2.1 Initialization.....	60
4.2.2 Force Interpolation and Charge Extrapolation.....	61
4.2.3 Equations of Motion.....	61
4.2.3.1 Particle Ray Tracking.....	63
4.2.4 Monte-Carlo Collision Algorithm (MCC).....	63
4.2.4.1 Electro-Molecule Collision.....	65
4.2.4.2 Ion-Molecule Collision.....	67
4.2.5 Indexing.....	68
4.2.6 Particle Reduction.....	68
4.2.7 Data Sampling.....	69
4.3 Parallel Computing of PIC-FEM Method.....	69
4.3.1 The Parallel PIC-FEM Method.....	70
4.3.2 Dynamic Domain Decomposition (DDD).....	71
4.4 Validation of the Parallel PIC-FEM Method.....	73
4.4.1 Quasi One-dimensional DC Gas Discharge Plasma Simulation.....	73
4.4.2 Quasi One-dimensional RF Gas Discharge Plasma Simulation.....	75
4.5 Parallel Performance of the Parallel PIC-FEM Method Using DDD.....	78
4.6 Some Remarks.....	82
Chapter 5. Applications to Realistic Problems.....	83
5.1 Simulation on Field Emission Display (FED).....	84
5.1.1 FED Simulation Without Considering Space-Charge effect.....	85
5.1.2 FED Simulation With Considering Space-Charge effect.....	91
5.2 Simulation on Gas Discharge Plasma.....	92
5.2.1 Three-Dimensional DC Gas Discharge Plasma.....	92
5.2.2 Three-Dimensional RF Gas Discharge Plasma.....	94
5.3 Simulation on Magnetron Plasma.....	95
5.3.1 Three-Dimensional DC Magnetron Plasma.....	95
5.3.2 Three-Dimensional RF Magnetron Plasma.....	97
5.4 Some Remarks.....	98
Chapter 6. Concluding Remarks.....	100
6.1 Summary.....	100
6.2 Recommendation for Future Work.....	102
Reference.....	104
Tables.....	120

Figures.....126
Autobiography.....214
Publications.....215



List of Tables

Table 1. Main excellent features of a field emission display.....	120
Table 2. Table 2. Time breakdown and speedup of Poisson’s equation solver at the different number of processors.....	121
Table 3. Evolution of simulation parameters at different levels of mesh refinement. (E_{MAX} is the local maximum electric field strength at the surface of CNT field emitter)	122
Table 4. Evolution of simulation parameters at different levels of mesh refinement. (B_{MAX} is the local maximum magnetic field strength at the center of magnet arrays).....	123
Table 5. The important geometrical parameters of CNT triode- and tetrode-type field emitters.....	124
Table 6. Characteristics of device performance for different focus types.....	125



List of Figures

Figure 1.1 Representation of the parameter space in plasma etching. The key internal plasma properties (middle) are the bridge between externally controlled variables (top) and the figures of merit (bottom).....	126
Figure 2.1 Element equation from a typical element (e) are used for each element in the mesh.....	127
Figure 2.2 A three-Dimensional C^0 -linear standard tetrahedral element.....	128
Figure 2.3 A three-Dimensional C^0 -linear standard hexahedral element.....	129
Figure 2.4 (a) Vertex-based. (b) edge-based (c) element-based partition of 4×3 mesh into two sub-regions.....	130
Figure 2.5 An L-shape domain subdivided into three sub-domains.....	131
Figure 2.6 Sketch of graph and mesh.....	132
Figure 2.7. Flowchart of the parallel mesh refinement module.....	133
Figure 2.8 Flowchart of the coupled PPES-PAMR method.....	134
Figure 2.9 The flowchart of parallel FEM.....	135
Figure 2.10 Contours of the potential distribution of (a) a grounded conducting sphere ($\Phi = 0$ Volts) immersed in a uniform electric field ($\vec{E} = 10 \text{Volts} / m$) and (b) uniform positive charges distribution between two infinite grounded conducting plates ($\Phi = 0$ Volts).....	136
Figure 2.11 Schematic diagram of the simulation domain for a typical CNT triode-type field emitter within a periodic cell. The important geometrical parameters are: $R=500$ nm, $r=10$ nm, $h_e=600$ nm, $h=500$ nm, $L=49.3 \mu$ m, $d=200$ nm and $W=25 \mu$ m.....	137
Figure 2.12 Surface mesh distribution of a typical single CNT triode-type field emitter within a periodic cell. Only $\frac{1}{4}$ of a periodic cell is simulated for the study of parallel performance of the Poisson's equation solver.....	138
Figure 2.13 Parallel speedup as a function of the number of processors on the PC-cluster system (maximum 32 processors) for CNT triode-type field emitter with gate voltage 150 volts, anode voltage 400 volts and the grounded cathode.....	139
Figure 2.14 Close-up of the unstructured adaptive surface mesh at different levels for a single CNT triode-type field emitter with gate voltage 150 volts, anode voltage 400 volts and the grounded cathode ($\epsilon_{ref} = 0.08$). (a) Level-0 (7006 nodes). (b) Level-1 (22750 nodes). (c) Level-2 (34927 nodes). (d) Level-5 (61241 nodes).....	140

Figure 3.1	Flowchart of the coupled PVPES-PAMR method.....	141
Figure 3.2	Arrangement of magnetization vectors of each permanent magnet segment for producing uniform flux density in the center of the permanent magnet array consisting of eight segments.....	142
Figure 3.3	Surface mesh distribution of the permanent magnet array consisting of eight segments.....	143
Figure 3.4	Figure 3.4 (a) Contour of magnetic flux density and (b) magnetic flux lines of permanent magnetic arrays (see Fig. 3.2).....	144
Figure 3.5	Unstructured adaptive mesh distribution at different levels the permanent magnet array consisting of eight segments. ($\epsilon_{ref} = 0.08$). (a) Level-0 (7845 nodes). (b) Level-1 (38364 nodes). (c) Level-2 (54355 nodes). (d) Level-4 (98743 nodes). (e) Level-5 (108415 nodes). (f) Level-6 (108840 nodes).....	145
Figure 3.6	Parallel speedup as a function of the number of processors on the PC-cluster system (maximum 32 processors) for of the permanent magnet array consisting of eight segments.....	146
Figure 4.1	The flowchart of conventional PIC-MCC method.....	147
Figure 4.2	Schematic of leap-frog integration method.....	148
Figure 4.3	Collisions in argon plasma.....	149
Figure 4.4	Nambu's method to sample a collisional event.....	150
Figure 4.5	The electron-molecule cross sections in argon.....	151
Figure 4.6	Vector diagram for scattering collision.....	152
Figure 4.7	The ion-molecule cross sections in argon.....	153
Figure 4.8	Flowchart of parallel PIC-FEM.....	154
Figure 4.9	PIC-MCC module of parallel PIC-FEM.....	155
Figure 4.10	Flowchart of parallel PIC-FEM with dynamic domain decomposition..	156
Figure 4.11	Sketch of the decomposed domain and the local data structure.....	157
Figure 4.12	Schematic overview of the basic plasma processes in a magnetron plasma.....	158
Figure 4.13	Schematic diagram of the spatial regions present in D.C. glow discharges, (a) at short cathode–anode distance and/or low pressure; (b) at longer inter electrode distance and/or higher pressure.....	159
Figure 4.14	(a) Potential and (b) electric profiles of quasi-1D DC glow discharge...	160
Figure 4.15	Ion and electron number densities of quasi-1D DC glow discharge.....	161
Figure 4.16	The net charge density of quasi-1D DC glow discharge.....	162
Figure 4.17	Ion and electron kinetic energies of quasi-1D DC glow discharge.....	163

Figure 4.18 Energy distribution functions of a impinging on the cathode of quasi-1D DC glow discharge.....	164
Figure 4.19 The potential profile of quasi-1D RF glow discharge.....	165
Figure 4.20 Ion and electron number densities of quasi-1D RF glow discharge...	166
Figure 4.21 Ion and electron kinetic energies of quasi-1D DC glow discharge...	167
Figure 4.22 Electron energy probability functions of (a) 50mtorr and (b) 20mtorr in the bulk region of quasi-1D DC glow discharge.....	168
Figure 4.23 Sketch of the 3D RF gas discharge plasma.....	169
Figure 4.24 Parallel speedup as a function of number of processors for 3D RF plasma at different numbers of particle on HP IA-64 clusters machine (maximum 32 processors).....	170
Figure 4.25 Evolution of domain decomposition using 20 processors, during the simulation for a RF gas discharge plasma (a) initial (b) intermediate (c) final.....	171
Figure 4.26 Time breakdown of various steps in PIC-FEM on 32 processors with (a) 10 particles per cell (b) 40 particles per cell.....	172
Figure 5.1 Schematic diagram of the simulation domain for a typical CNT triode-type field emitter within a periodic cell. The important geometrical parameters are: $R=500$ nm, $r=10$ nm, $h_e=600$ nm, $h=500$ nm, $L=49.3$ μ m, $d=200$ nm and $W=25$ μ m.....	173
Figure 5.2 Contours of the (a) electric potential and the (b) electric field distribution near the tip of the CNT triode-type field emitter with gate voltage 150 volts, anode voltage 400 volts and the grounded cathode.....	174
Figure 5.3 FN plot of the field emission characteristics of CNT triode-type field emitter (height is 600 nm) with gate voltage 110-160 volts, anode voltage 400 volts and the grounded cathode. ($S \equiv slope = -3244.25 \phi^{3/2} / \beta$, $\phi = 4.52$ eV).....	175
Figure 5.4 Trajectories of the emitted electrons inside the periodic cell of CNT triode-type field emitter with the grounded cathode, anode voltage 400 volts and two different gate voltages: (a) 110 volts (b) 160 volts.....	176
Figure 5.5 Effect of the gate voltage on the emission current for two different CNT triode-type field emitter heights with anode voltage 400 volts and the grounded cathode.....	177

Figure 5.6 Schematic diagram of the simulation domain for a typical CNT tetrode-type field emitter within a periodic cell. The important parameters are: $R=500$ nm, $R_f=1500$ nm, $r=10$ nm, $h_e=600$ nm, $h_1=500$ nm, $h_2=500$ nm, $L=48.6 \mu\text{m}$, $d_1=200$ nm, $d_2=200$ nm and $W=25 \mu\text{m}$	178
Figure 5.7 Comparisons of the trajectories of the emitted electrons between (a) CNT triode-type field emitter with the grounded cathode, anode voltage 400 volts and the gate voltage 150 volts and tetrode-type field emitter with the additional three different focusing voltages: (b) 5 volts (c) 0 volts (d) -5 volts.....	179
Figure 5.8 Perspective view of the structure of the magnetic focusing carbon nanotube field emission arrays.....	180
Figure 5.9 Schematic diagram of the 1/4 simulation domain for a typical CNT-based triode-type field emitter within a periodic cell. The important geometrical parameters are: $R=500$ nm, $r=10$ nm, $h_e=600$ nm, $h=500$ nm, $d=200$ nm, $L=0.9$ mm and $W=0.3$ mm.....	181
Figure 5.10 LHS shows surface mesh distribution of a single CNT triode-type field emitter within a periodic cell. RHS shows surface mesh distribution of the CNT field emitter and equipotential lines near the tip for $V_g=120$ V. Unstructured tetrahedral adaptive mesh is ideal for the simulation structure, which consists of a smaller emitter within a larger periodic cell.....	182
Figure 5.11. Field emission I-V characteristic of a single gated CNT field emitter without the externally applied downward magnetic field.....	183
Figure 5.12 Snapshots and trajectories of electrons for (a) $B_z = 0$ T, (b) $B_z = -0.2$ T, (c) $B_z = -0.5$ T, and (d) $B_z = -1.0$ T. The gate voltage and the anode voltage are fixed to 120V and 1 kV, respectively.....	184
Figure 5.13 Dependence of electron beam diameter at the anode on the flux density of magnetic focusing field.....	185
Figure 5.14 (a) SEM image and (b) surface mesh distribution of a single silicon based field emitter within a periodic cell.....	186
Figure 5.15 Contours of the (a) electric potential and the (b) electric field distribution near the tip of the single silicon based field emitter with anode voltage 200 volts.....	187
Figure 5.16 Field emission I-V characteristic and F-N plot of single silicon based field emitter with work function 4.5eV and 4.9eV.....	188
Figure 5.17 (a) The surface mesh plot and (b) domain decomposition profile of 3D DC gas discharge plasma.....	189

Figure 5.18 Contours of the (a) electric potential and the (b) electric field distribution of 3D DC glow discharge.....	190
Figure 5.19 Contours of (a) electron and (b) ion number densities of 3D DC glow discharge.....	191
Figure 5.20 Contours of (a) electron and (b) ion kinetic energies of 3D DC glow discharge.....	192
Figure 5.21 (a) The surface mesh plot and (b) domain decomposition profile of 3D RF gas discharge plasma.....	193
Figure 5.22 Sketch and boundary condition of the 3D RF discharge plasma enclosed by a dielectric chamber wall.....	194
Figure 5.23 Potential contour of 3D RF discharge plasma enclosed by a dielectric chamber wall.....	195
Figure 5.24 Contours of (a) electron and (b) ion number densities of 3D RF discharge plasma enclosed by a dielectric chamber wall.....	196
Figure 5.25 Contours of (a) electron and (b) ion kinetic energies of 3D RF discharge plasma enclosed by a dielectric chamber wall.....	197
Figure 5.26 Sketch and surface mesh distribution of the 3D DC magnetron plasma.....	198
Figure 5.27 Contours of magnetic flux density with magnetization (a) 0.25 T (b) 0.5 T (c) 0.75 T (d) 1.0 T of permanent magnet systems	199
Figure 5.28 Potential contours of 3D RF magnetron plasma with (a) $\mathbf{M}=0.125\text{T}$, $\gamma =0.06$, (b) $\mathbf{M}=0.125\text{T}$, $\gamma =0.1$, and (c) $\mathbf{M}=0.1875\text{T}$, $\gamma =0.0$	200
Figure 5.29 Contours of (a) electron and (b) ion number densities of 3D DC magnetron plasma with $\mathbf{M}=0.125\text{T}$ and $\gamma =0.06$	201
Figure 5.30 Contours of (a) electron and (b) ion number densities of 3D DC magnetron plasma with $\mathbf{M}=0.125\text{T}$ and $\gamma =0.1$	202
Figure 5.31 Contours of (a) electron and (b) ion number densities of 3D DC magnetron plasma with $\mathbf{M}=0.1875\text{T}$ and $\gamma =0.06$	203
Figure 5.32 Contours of (a) electron and (b) ion kinetic energies of 3D DC magnetron plasma with $\mathbf{M}=0.125\text{T}$ and $\gamma =0.06$	204
Figure 5.33 Contours of (a) electron and (b) ion kinetic energies of 3D DC magnetron plasma with $\mathbf{M}=0.125\text{T}$ and $\gamma =0.1$	205
Figure 5.34 Contours of (a) electron and (b) ion kinetic energies of 3D DC magnetron plasma with $\mathbf{M}=0.1875\text{T}$ and $\gamma =0.06$	206
Figure 5.35 Potential contours of 3D RF magnetron plasma with (a) $\mathbf{M}=0.125\text{T}$, $\gamma =0$ (b) $\mathbf{M}=0.125\text{T}$, $\gamma =0.06$ (c) $\mathbf{M}=0.25\text{T}$, $\gamma =0.06$	207
Figure 5.36 Contours of (a) electron and (b) ion number densities of 3D RF magnetron plasma with $\mathbf{M}=0.125\text{T}$ and $\gamma =0$	205

Figure 5.37 Contours of (a) electron and (b) ion number densities of 3D RF magnetron plasma with $M=0.125T$ and $\gamma=0.06$209

Figure 5.38 Contours of (a) electron and (b) ion number densities of 3D RF magnetron plasma with $M=0.25T$ and $\gamma=0.06$210

Figure 5.39 Contours of (a) electron and (b) ion kinetic energies of 3D RF magnetron plasma with $M=0.125T$ and $\gamma=0.0$211

Figure 5.40 Contours of (a) electron and (b) ion kinetic energies of 3D RF magnetron plasma with $M=0.125T$ and $\gamma=0.06$212

Figure 5.41 Contours of (a) electron and (b) ion kinetic energies of 3D RF magnetron plasma with $M=0.25T$ and $\gamma=0.06$213



Chapter 1

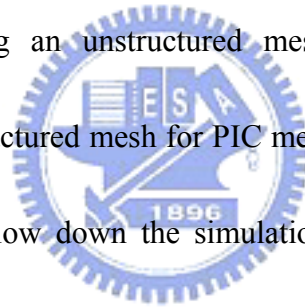
Introduction

1.1 Motivation and Background

Understanding of several important physical and engineering problems, for example, field emission [Itoh *et. al.*, 2004] and low-temperature rarefied (low-pressure) plasma [Lieberman and Lichtenberg, 1994], requires the consideration of space-charged effects self-consistently due to the motion of charged particles. Some common characteristics of these problems may include three-dimensional, geometrically complicated, thermally non-equilibrium and low-pressure. In addition to studying these problems experimentally, modeling through computer simulation may become one of the most efficient ways to understand the underlying physics due to the rapid advancement of the modern computer technology. Modeling technique that assumes thermally equilibrium, such as fluid modeling [Kushner, 2005], fails in correctly capturing the important physical features of the-above mentioned problems.

Until 1960s, the plasma physicists had devised an important simulation technique, Particle-In-Cell (PIC) [Birdsall and Langdon, 1991], which equivalently solves the collisionless Boltzmann equation for charged particles self-consistently. However, a self-consistent PIC simulation is often computationally intensive even at low pressure. In general, the conventional PIC solves the fields with finite difference method using

a structured mesh. This is not flexible enough or becomes awkward to simulate the device with complicated geometries. In addition, the structured mesh is often difficult to manage efficiently when dynamic domain decomposition is required in a typical parallel particle simulation, such as the PIC method. In contrast, not only does the finite element method (FEM), which often uses an unstructured mesh, offer much greater flexibility in handling the complicated geometry, but also it provides excellent flexibility in dynamic domain decomposition for parallel computing. In addition, mesh refinement that is important in several simulations can be easily coupled to the finite element method using an unstructured mesh. However, there are some disadvantages by using unstructured mesh for PIC method. Firstly, particle tracing on an unstructured mesh may slow down the simulation. Secondly, the programming may become complicated. Nevertheless, there were very few studies directed along this line. Taking all these intertwining factors together, it is still very valuable to develop a PIC simulation code using an unstructured mesh. Therefore, in this thesis our goal is to develop a parallelized three-dimensional PIC-FEM code considering Monte-Carlo collision, which can be run on memory-distributed parallel machines, such as PC clusters.



1.2 Literature Surveys

Since we are mainly interested in simulating field emission and low-temperature

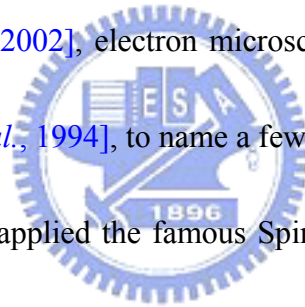
low-pressure plasma, past studies of modeling and simulation in these two disciplines are reviewed in detail in the following in turn.

1.2.1 Modeling of Field Emission

Field emission display (FED) is the new type of flat-panel display and its working principle is similar with traditional CRTs. The colored light is generated from the phosphor, which is excited by electrons. The electrons are emitted from cathode. Instead of thermo-ionic emission in CRT, the electrons in FED are emitted by a cold pixel electron source that typically consists of a large array of low-work-function emitter micro-tips. Moreover, FED needs the lower power input than CRT since there is a power-inefficient deflection system in CRT to steer the emitted electrons. Furthermore, when FED is compared with TFT LCD, the FED also exhibits some better performances than TFT LCD. For example, FED offer a superior viewing angle and are several microseconds quicker in response time. In addition, FED also has the potential for high brightness and contrast. The advantages of applying FED in display technology include lower driving voltage, higher lighting frequency, and possibly, better display resolution. In general, three types of FED can be classified depend on their structures, which are diode, triode, and tetrode types. **Table 1** also shows the main features of these different type of FED [Itoh *et. al.*, 2004].

Using carbon nanotubes (CNTs) as field emission cathodes has attracted

tremendous interest in the past few years for their remarkable field emission (FE) properties such as high aspect ratios, whisker-like in shape for optimum geometrical field enhancement, high electrical conductivity, and extraordinary environment stability, e.g., [de Heer *et. al.*, 1995], [Rao *et. al.*, 2000], [Nishimura *et. al.*, 2004], and [Nilsson *et. al.*, 2000]. Therefore, CNTs have great potential to be used as field emission cathodes for various applications of vacuum microelectronic devices, including field-emission displays (FED), e.g., [Wang *et. al.*,1997], [Fowler and Nordheim, 1928], and [Spindt,1968], high-frequency microwave amplifier, e.g., [Choi *et. al.*,1999], and [Pirio *et. al.*,2002], electron microscopy and parallel electron beam lithography (EBL) [Hong *et. al.*, 1994], to name a few.



Most of the FE devices applied the famous Spindt-type structure [Wang *et. al.*, 1997], which has a metallic or silicon etched field emitter with an integrated gate electrode aperture surrounding the emitter tip to control the extraction of emission current. The multiple carbon nanotubes based field emission cathodes within the integrated gate electrode aperture have been reported in many papers over the past six years, e.g., [Fowler and Nordheim,1928], [Spindt, 1968], [Lei *et. al.*,1998], and [Hu and Huang, 2003]. For some applications, such as electron beam lithography and microscopy, individual gated carbon nanotube field emitter was specifically fabricated to eliminate the-screening effects and to optimize the emitted current and electron

beam diameter [Lan *et. al.*, 2004]. The electrons emitted from a very small area on the top of CNT inherently spread with a large dispersion angle. Thus, an appropriate electron-beam focusing system is necessary for developing a well-focused electron beam source.

From the Fowler-Nordheim law [Fowler and Nordheim, 1928], the magnitude of the electron flux emitted from the surface depends upon the local electric field at the surface and the work function of the solid. In addition to finding materials with lower work functions, enhancing the local electric field near the surface is one of the most critical tasks in improving field emission properties. As a trial-and-error method is often expensive in terms of time and cost, a computer simulation may speed up the design process by revealing the detailed physics with the FED. In practice, the geometry of the field emitter and the gates involved in the FED design is three-dimensional and often very complicated, e.g., [Spindt, 1968], [Choi *et. al.*, 1999], and [Pirio *et. al.*, 2002].

In the past, several numerical studies have been conducted for the prediction of field emission properties, e.g., [Hong *et. al.*, 1994], [Wang *et. al.*, 1997], [Lei *et. al.*, 1998], [Hu and Huang, 2003], [Lan *et. al.*, 2000], and [Lan *et. al.*, 2004]. Most of these studies use either the 2-D or 3-D finite difference method, e.g., [Wang *et. al.*, 1997], [Lei *et. al.*, 1998], [Hu and Huang, 2003], [Lan *et. al.*, 2000], and [Lan *et. al.*, 2004], or

the 2-D finite element approach [Hong *et. al.*, 1994] for discretizing the electrostatic Poisson's equation. As mentioned earlier, a practical FED design often involves three-dimensional objects with a complicated geometry, rendering the use of the finite-difference method as very difficult or unsuitable. The finite-element or finite-volume method using unstructured grids should represent the best choice for the numerical method in this regard. In addition, parallel processing can be necessary in simulating the practical three-dimensional design of field emitters or when including space-charged effect with high emission currents in the Particle-In-Cell (PIC) method ,e.g., [Hu and Huang, 2003], [Lan *et. al.*,2000], and [Lan *et. al.*, 2004]. Otherwise, in Ref.,e.g., [Hu and Huang, 2003], [Lan *et. al.*,2000], and [Lan *et. al.*,2004], the computational time for a typical run to emit only a few electrons can take up to one week. Also, the accuracy of the electron-flux prediction from the emitters strongly depends on the accuracy of the local electrical field at the surface, which makes the grid resolution at the surface a critical issue in the simulation. In the following, the very similar concerns are also arising from the low-temperature plasma simulation



1.2.2 Modeling of Low-temperature Plasma

Plasma is ionized gas. Hence, it consists of ions and electrons, as well as neutral species. The ionization degree of plasma varies from 100% (fully ionized plasma) to

very low values (e.g. 10^{-4} – 10^{-6} ; weakly ionized plasma). Besides the space plasma, the laboratory plasma is divided into two main groups, which are the high-temperature plasma (fusion plasma), and the low-temperature plasma (gas discharges plasma). Moreover, two sub-groups of gas discharge plasma are classified depended on its working gas pressure, which are thermal equilibrium plasma and non-thermal equilibrium plasma [Lieberman and Lichtenberg, 1994]. The efficient energy exchange between the plasma species due to many collisions occur for high-pressure plasma. Thermal equilibrium discharge is typically used for applications where heat is required, such as for cutting, spraying, welding. On the other hand, for low gas pressure plasma, different temperatures of the plasma species due to its inefficient energy transfer. Non-thermal equilibrium plasma is typically used for applications where heat is not desirable. In recent years, this field of non-thermal equilibrium plasma applications has rapidly expanded due to its non-equilibrium aspect of the plasma. The latter sub-group of gas discharge plasmas is also the second subject of this dissertation.

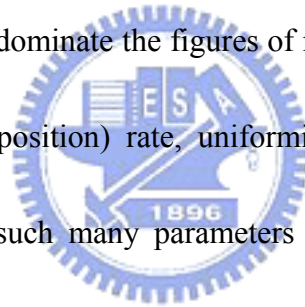
Some important operating parameters for obtaining different non-equilibrium conditions are briefly summarized as follows [Economou, 2000]:

- The chemical input of working gas and its corresponding gas pressure
- The imposed external electromagnetic field structure

- The configurations of plasma chamber and electrodes
- The temporal behavior (e.g. pulsing the plasma)

One can realize that the non-equilibrium plasma conditions are strongly influenced by any one or many of these summarized parameters. For example, the representation of the parameter space in plasma etching is shown in **Fig. 1.1**. It clearly illustrates that the above-mentioned operating parameters (in the top block) determine the following key plasma properties (listed in the middle block) including the electron velocity distribution function (EVDF), the space and time variation of electron, etc.

Finally, these properties may dominate the figures of merit (listed in the bottom block) including the etching (or deposition) rate, uniformity, etc. Therefore, a computer simulation code should use such many parameters as inputs to help optimize the expected non-equilibrium plasma conditions easily and understand the underlying physics.



Dimensionality of plasma reactor simulations ranges from zero-dimensional to three-dimensional. Low dimensional simulations, such as zero-dimensional, e.g., [Font *et. al.*, 1998], [Meeks and Shon, 1995], and [Deshmukh. and Economou, 1992], and one-dimensional models, e.g., [Midha and Economou, 2000], [Kline *et. al.* 1989], and [Nedelea and Urbassek, 2004], are best choice in handling very complicated chemistry [Meeks *et. al.*, 1997]. However, two-dimensional simulations can address

the important aspect of reaction uniformity across the wafer radius, e.g., [Shon and Lee, 2002], [Shon *et. al.*,1999], and [Shon *et. al.*,1998]. Three-dimensional simulations are useful for studying azimuthal asymmetries in the reactor due to non-axisymmetric power deposition, or non-axisymmetric gas inlets and pumping ports, e.g., [Kushner *et. al.*,1996], and [Kushner, 1997].

In general, there are three kinds of plasma simulation approaches; the first is the fluid model, the second is the kinetic model and the third is the hybrid model. In addition, Maxwell's equations for electromagnetic fields also need to be solved self-consistently coupled with the plasma densities and currents from plasma simulations. For the fluid model, one need to solve the equations, which are derived after taking the moments of the Boltzmann equation with some assumptions regarding, e.g., [Meyyappan, 1994], and [Gogolides and Sawin, 1992]. They are species continuity equation, species momentum equation and species energy equation. Related publications of fluid model could be found in numerous articles, e.g., [Ventzek *et. al.*,1993], [Lymeropoulos *et. al.*,1995], [Bukowski and Graves, 1996], and [Ventzek *et. al.*,1994], and are not repeated here. Unlike fluid model, kinetic approach yields the particle distribution functions as an output of the simulation. Especially, it is more accurate than fluid model at low pressures when the species mean free path is comparable to or longer than a characteristic length scale or for

highly non-equilibrium situations. However, Kinetic approach is computationally intensive as compared to fluid model. One of the well-established kinetic approaches is the Particle-In-Cell with Monte-Carlo Collisions (PIC-MCC) method, e.g., [Birdsall, 1991], and [Vahedi *et. al.*,1993]. In the past two decades, PIC-MCC method has long been used to study the nonlinear kinetic problems in space and laboratory plasma physics. For self-consistent treatment of the plasma and the background gas, Nanbu combined the Direct Simulation Monte Carlo method (DSMC) with PIC-MCC, e.g., [Nanbu, 2000], and [Serikov *et. al.*,1997].

Each time step in the PIC-MCC consists of four major steps: charge extrapolation, force interpolation from the solution of the Maxwell's equations, particle movement, and Monte-Carlo collisions. Briefly speaking, based on the particle positions, charges are assigned to each mesh point and current densities are assigned to the faces between the mesh points. Maxwell's equations are then solved to compute the electric and magnetic fields on the grid. The force on the particles is obtained from the fields at these grid points by interpolation based on the particle position. Particles are then moved according to Newton's law. Particle collisions are handled stochastically in a Monte Carlo module in-between field adjusting time steps. The details of the PIC-MCC method will be given in chapter 4.

As mentioned earlier, most conventional PIC-MCC, e.g., [Birdsall and Langdon,

1991], and [Birdsall, 1991], a structured mesh is usually construed for the computational domain. However, until very recently, there have been few developments of electrostatic PIC method using a three-dimensional unstructured mesh, mostly designed for thruster plume simulations due to their complicated computational geometry. A hybrid PIC-DSMC code using unstructured mesh, called AQUILA, which has been developed by [Santi *et al.*, 2003] on hall thruster plume simulation. They obtained the improved current density results from better the unstructured mesh resolution. AQUILA uses finite element method to discretize Poisson's equation with electrons from Boltzmann relation, and then uses Newton-Raphson method to solve the non-linear resulting matrix. [Spirkin *et al.*, 2004] has also developed a three-dimensional Particle-In-Cell code on a unstructured tetrahedral mesh with finite volume method. This PIC code was applied to the simulation of the flow inside the segmented micro-channel of a directional-retarding potential analyzer. Results show the flow characteristics of the ions and electrons and provide estimates of the collected current by the micro-plate.

Parallel PIC-MCC method has been previously studied by various researchers using different schemes, e.g., [Seidel *et al.*, 2002], [Kawamura *et al.*, 2000], [Decyk, 2002], [Walker, 1991], [Walker, 1990], [Lee and Azari, 1992], [Akarsu *et al.*, 1996], [Decyk and Norton, 2004], and [Liewer and Decyk, 1989], since it is the most

computationally demanding compared with other models. Most parallel PIC-MCC schemes, e.g., [Kawamura *et al.*,2000], [Seidel *et al.*,2002], and [Lee and Azari, 1992] employ a *Eulerian* decomposition scheme in which just paralleling the particle processing without paralleling the field solver since the field solver can be a small percentage of the work load especially when FFT methods are used. In this report, for a fixed number of grid points, the speedup just for this parallel particle processing became more linear with increasing particle number on 2 and 4 CPU symmetric multiprocessor (SMP) machines and on a distributed network of workstations (NOW).

In the past, there have been very few studies concerning on developing dynamic load-balancing technique for particle-based PIC-MCC code, e.g., [Seidel *et al.*,2002] , [Decyk and Norton, 2004], and [Liewer and Decyk, 1989]. In Seidel's work [Seidel *et al.*,2002], he has proposed a method in which the code will dynamically repartition the computational domain and intends to balance the workload among processors under the framework of structured mesh. Decyk *et al.* have developed a new algorithm just for PIC method on concurrent processors with distributed memory, which named the general concurrent PIC algorithm (*GCPIC*). In this algorithm, the physical domain of particle simulation was divided into sub-domains, which are equal to the number of processors. The sub-domain can be re-created to keep the processor loads of particle computations balance (dynamic load balancing) during the transient

period of the simulation, which was called *primary decomposition*. Again, each sub-domain may have equal numbers of particles, however, unequal numbers of grid numbers. Thus, GCPIC used *secondary decomposition* to divide the physical domain into number of processors equal sub-domains with equally number of grid points under MIMD paradigm for computing field solver efficiently. However, these reviews showed that parallel PIC methods are not suitable using the SIMD paradigm.

1.3 Objectives of the Thesis

Specific objectives of the present thesis are briefly summarized as follows:

1. To develop and verify a parallelized three-dimensional Poisson's equation solver using FEM for predicting electrostatic distribution;
2. To develop and verify a parallelized three-dimensional vector potential Poisson's equation solver using FEM for predicting magnetostatic distribution;
3. To develop and verify a parallelized three-dimensional PIC-FEM code using an unstructured mesh by combining the Poisson's equation solvers mentioned in the above;
4. To apply the completed PIC-FEM code to simulate field emission, DC/RF gas discharge plasma and DC/RF magnetron plasma and compare with

experimental data wherever available.

1.4 Organization of the Thesis

The chapters of this thesis are organized as follows.

Chapter 2 details a parallel three-dimensional electrostatic field solver formulated via Galerkin finite element method based on the subdomain-by-subdomain non-overlapping domain decomposition method. After finite element assembling procedure, the resulting matrix is stored in compressed sparse row format and is solved using either the parallel conjugate gradient method or a direct matrix solver, MUMPS. A parallel adaptive mesh refinement module (PAMR) is also coupled into the developed electrostatic field solver for obtaining better solution, especially, when there is a large variation of potential in the computational domain. Some benchmark problems are presented for demonstrating the accuracy and applicability of the electrostatic field solver. In the end of this chapter, the parallel performances of the Poisson's equation solver are studied and their time breakdown is analyzed in detail.

Chapter 3 details a parallel three-dimensional magnetostatic field solver. This solver is developed and parallelized follows the techniques presented in chapter 2. Also, PAMR is coupled into the developed magnetostatic field solver. Some

benchmark problems are presented for demonstrating the accuracy and applicability of the parallel magnetostatic field solver. In the end of this chapter, the parallel performances of these solvers are studied and their time breakdown is analyzed.

Chapter 4 presents the proposed parallel three-dimensional PIC-FEM method using an unstructured mesh. The PIC-FEM is developed follows the main principles of the conventional PIC-MCC method. In addition, the parallel implementation of PIC-FEM is done via domain decomposition method. Dynamic domain decomposition is developed for alleviating the load between the processors. Two benchmark problems are presented for demonstrating the accuracy and applicability of the parallel PIC-FEM code. In the end of this chapter, the parallel performance of the PIC-FEM code using DDD is studied and its time breakdown is analyzed in detail.

In chapter 5, the proposed parallel three-dimensional PIC-FEM code is used to simulate three different realistic problems. They are: three-dimensional field emission display (FED), three-dimensional DC/RF gas discharge plasma, and three-dimensional DC/RF magnetron plasma. Most of the simulated results are then compared with the previous studied available in the literature. Finally, the conclusions of this work and some possible directions for the future research work are presented in the chapter 6 in turn.

Chapter 2

The Parallel Computing of Finite Element Method for Three-Dimensional Electrostatic Field Problems

This chapter begins with the introduction to background of computational electromagnetic. In solving electrostatic problems, only the finite element Galerkin weighted residual method (GWRM) is chosen and introduced for using either a tetrahedral or a hexahedral mesh. Globe coordinate and local coordinate shape functions are used for tetrahedral and hexahedral meshes, respectively. Before the parallel computing of FEM, the computational domain is firsts decomposed into a number of non-overlapping sub-domains using multi-level graph-partitioning library, METIS. Then, some preprocessing procedure is used in converting the output data from graph-partitioning tool into the input data for field solvers. The second step is that the Poisson's equation is formulated via GWRM using subdomain-by-subdomain method (SBS). After applying the assembling procedure of FEM, only the non-zero entries of the system of equation are stored in compressed sparse row format and solve the matrix using either parallel conjugate gradient method or direct matrix solver, MUMPS. The parallel adaptive mesh refinement module is then coupled with the parallel Poisson's equation solver in order to improve the resolution of solution

near where the property gradient is large. Some benchmark problems are presented for demonstrating the accuracy and applicability of the Poisson's equation solver. In the end of this chapter, the parallel performance of the Poisson's equation solver is studied and its time breakdown is analyzed in detail.

2.1 Background of Computational Electromagnetic

For the whole electromagnetic theory, it could be regarded as the logical deduction from the Maxwell's equations, which were first formulated by James Clerk Maxwell in 1873 [Cheng, 1995]. They are:

$$\nabla \times \vec{E} = -\frac{\partial \vec{B}}{\partial t} \quad (2-1)$$

$$\nabla \times \vec{B} = \frac{1}{c^2} \frac{\partial \vec{E}}{\partial t} + \mu \vec{J} \quad (2-2)$$

$$\nabla \cdot \vec{E} = \frac{\rho}{\varepsilon} \quad (2-3)$$

$$\nabla \cdot \vec{B} = 0 \quad (2-4)$$



where \vec{E} is the electric field intensity, \vec{B} is the magnetic flux density, \vec{J} is the current density, ε is the dielectric permittivity of the medium, μ is the dielectric permeability of the medium, c is the speed of light and ρ is the volume charge density.

In this thesis, we only consider the *electrostatic* (ES) and *magnetostatic* (MS) field problems, hence, the Maxwell's equations can be simplified to the scalar and vector Poisson's equations for ES and MS fields, respectively. They are:

$$\nabla^2 \phi = -\frac{\rho}{\varepsilon} \quad (2-5)$$

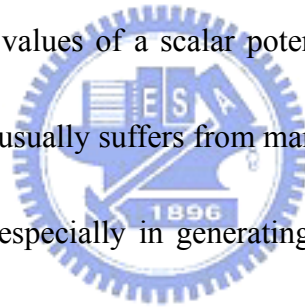
$$\frac{1}{\mu} \nabla^2 \vec{A} = -\vec{J} \quad (2-6)$$

where ϕ is electric potential and \vec{A} is the magnetic vector potential. From these two equations, it is clear that the electrostatic fields are contributed from the static electric charges and the magnetostatic fields are due to motion of electric charges with uniform velocity (direct current) or external magnets. The details in solving the magnetostatic field problems are presented in the next chapter.

In the past years, Maxwell's equations have long been studied in dealing with electromagnetic problems. Two different approaches for solving Maxwell's equations are analytic and numerical approached. For the simple structured device, there are many analytic solutions available which could easily derived from the series expansions, separation of variables, Bessel and Legendre polynomials, Laplace transformations, and the like [Umashankar, 1993]. However, there is almost no solution available when one consider a device with a complicated structure that involve a number of conductors, dielectric, permanent magnets, and semiconductors of arbitrary shapes, etc. Thus, an extremely accurate numerical method for solving Poisson's equation is required to model these complicated structures.

Fortunately, with the developments in numerical techniques in the past two decades, nowadays it is possible to solve large-scale electromagnetic problems

numerically within reasonable time limits. The numerical methods can be generally divided into three separate groups, which are integral method, differential method, and variational method. For the integral method, it is based on the basis of the superposition principle and one can integrate such effects at any point obtaining the potential at that point. The well-known integral method is the boundary element method [Kythe, 1995], which is particularly suitable for problems with material homogeneity. Finite difference method [Sullivan, 2000] is the most popular among the differential methods. For this method, the computational domain is usually divided into structured mesh and the values of a scalar potential field are sought at all grid points. However, this method usually suffers from many problems when considering a complicated structured case, especially in generating the structured mesh on object with arbitrary geometrical shape, imposing the boundary conditions, interface approximation of multi-material region. For the variational method, it is based on the differential or integral form of the field equations to be solved [Zeidler, 1985]. The well-known variational method is the finite element method, which is widely used in many fields, e.g., [Beltzer, 1990], [Winslow, 1967], [Silvester and Pelosi, 1994], and [Jin, 2002], which also include the electromagnetic problems [Winslow, 1967].



2.2 Finite Element Method (FEM)

2.2.1 Background

The FEM is the numerical technique for obtaining approximate numerical solution of the *partial differential equations* (PDEs) arising from any physical system subjected to its boundary conditions. For FEM, the computational domain is first divided into smaller non-overlapping regions called *elements (cells)*, and a trial function is postulated over each of the elements. For example, the trial solution with global coordinates for a three-dimensional tetrahedral mesh is:

$$\tilde{U}(x, y, z; a) = a_0 + a_1 N_1(x, y, z) + a_2 N_2(x, y, z) + \dots + a_n N_n(x, y, z) \quad (2-7)$$

Where x, y, z are the independent variables in the problems. The functions $N(x, y, z)$ are known functions called trial functions. The coefficients, a_i , are undetermined parameters and n is called *degree of freedom* (DOF). After formulating the PDEs using Galerkin weighted residual method with the trial solution, the element equations are obtained for a typical element. These element equations can then be used for other the elements over the domain as shown in **Fig. 2.1**. Then, larger sets of algebraic equations, which are called system equations, are formed after assembling these element equations. Moreover, the matrix structure of such huge system equations is sparse in essence; the matrix may be solved efficiently only storing the non-zero entries.

2.2.2 The Galerkin Weighted Residual Method (GWRM)

In FEM, we employ *Galerkin weighted residual method* (GWRM) with the three-dimensional C^0 -linear shape-function for a tetrahedral mesh and for a hexahedral mesh. In GWRM, a weighted average of residual over the entire domain should be zero and the trial function is the element shape function associated with each a_i . The representations of GWRM with three-dimensional C^0 -linear global coordinate shape function and local coordinate shape function are given in **Eqs. (2-8a)** and **Eqs. (2-8b)**, respectively.

$$\iiint R(x, y, z; a) N_i(x, y, z) dx dy dz = 0 \quad (2-8a)$$

$$\iiint R(\xi, \eta, \rho; a) N_i(\xi, \eta, \rho) dx dy dz = 0 \quad (2-8b)$$

where $R(x, y, z; a)$ or $R(\xi, \eta, \rho; a)$ is the residual of the governing equation.

2.3 Calculation of Electrostatic (ES) Field

Since the concept of GWRM is introduced, this section begins with derivation of the element equation of Poisson's equation for typical ES fields (as shown in **Eqs. (2-5)**). A trial solution is first constructed to approximate the exact electric potential, $\phi(r) \approx \tilde{U}(r; \alpha)$, which can be written with shape function using global coordinate for a tetrahedral mesh,

$$\tilde{U}(x, y, z; a) = \sum_{j=1}^4 a_j N_j(x, y, z) \quad (2-9)$$

The local coordinate shape for a hexahedral mesh will be presented later. The major

steps for formulating **Eqs.(2-5)** using GWRM with a three-dimensional tetrahedral mesh in global coordinates are described in detail as follows.

Step 1: Derive the typical element equation of Eqs. (2-5) using GWRM.

$$\iiint \left(\frac{\partial^2 \tilde{U}^{(e)}}{\partial x^2} + \frac{\partial^2 \tilde{U}^{(e)}}{\partial y^2} + \frac{\partial^2 \tilde{U}^{(e)}}{\partial z^2} \right) N_i^e dx dy dz = - \iiint \left(\frac{\rho}{\varepsilon_0} \right) N_i^e dx dy dz \quad (2-10)$$

$i = 1 - 4$

Step 2: Integrate by parts.

$$N_i^{(e)} \frac{\partial^2 \tilde{U}^{(e)}}{\partial x^2} = \frac{\partial}{\partial x} \left(N_i^{(e)} \frac{\partial \tilde{U}^{(e)}}{\partial x} \right) - \frac{\partial N_i^{(e)}}{\partial x} \frac{\partial \tilde{U}^{(e)}}{\partial x} \quad (2-11a)$$

$$N_i^{(e)} \frac{\partial^2 \tilde{U}^{(e)}}{\partial y^2} = \frac{\partial}{\partial y} \left(N_i^{(e)} \frac{\partial \tilde{U}^{(e)}}{\partial y} \right) - \frac{\partial N_i^{(e)}}{\partial y} \frac{\partial \tilde{U}^{(e)}}{\partial y} \quad (2-11b)$$

$$N_i^{(e)} \frac{\partial^2 \tilde{U}^{(e)}}{\partial z^2} = \frac{\partial}{\partial z} \left(N_i^{(e)} \frac{\partial \tilde{U}^{(e)}}{\partial z} \right) - \frac{\partial N_i^{(e)}}{\partial z} \frac{\partial \tilde{U}^{(e)}}{\partial z} \quad (2-11c)$$

Substituting **Eqs.(2-11)** into the RHS of **Eqs. (2-10)**, and **Eqs. (2-10)** becomes

$$\begin{aligned} & \iiint \left[\frac{\partial}{\partial x} \left(\frac{\partial \tilde{U}^{(e)}}{\partial x} N_i^{(e)} \right) + \frac{\partial}{\partial y} \left(\frac{\partial \tilde{U}^{(e)}}{\partial y} N_i^{(e)} \right) + \frac{\partial}{\partial z} \left(\frac{\partial \tilde{U}^{(e)}}{\partial z} N_i^{(e)} \right) \right] dx dy dz \\ & - \iiint \left[\left(\frac{\partial \tilde{U}^{(e)}}{\partial x} \frac{\partial N_i^{(e)}}{\partial x} \right) + \left(\frac{\partial \tilde{U}^{(e)}}{\partial y} \frac{\partial N_i^{(e)}}{\partial y} \right) + \left(\frac{\partial \tilde{U}^{(e)}}{\partial z} \frac{\partial N_i^{(e)}}{\partial z} \right) \right] dx dy dz \quad (2-12) \\ & = - \iiint \left(\frac{\rho}{\varepsilon_0} \right) N_i^{(e)} dx dy dz \quad i = 1 - 4 \end{aligned}$$

Eqs. (2-12) can be reformulated using divergence theorem, it may be written,

$$\begin{aligned} & \iiint \left[\left(\frac{\partial \tilde{U}^{(e)}}{\partial x} \frac{\partial N_i^{(e)}}{\partial x} \right) + \left(\frac{\partial \tilde{U}^{(e)}}{\partial y} \frac{\partial N_i^{(e)}}{\partial y} \right) + \left(\frac{\partial \tilde{U}^{(e)}}{\partial z} \frac{\partial N_i^{(e)}}{\partial z} \right) \right] dx dy dz \\ & = \iiint \left(\frac{\rho}{\varepsilon_0} \right) N_i^{(e)} dx dy dz + \iint_A N_i^{(e)} \left(\frac{\partial \tilde{U}^{(e)}}{\partial x} \bar{i} + \frac{\partial \tilde{U}^{(e)}}{\partial y} \bar{j} + \frac{\partial \tilde{U}^{(e)}}{\partial z} \bar{k} \right) \cdot \bar{n} dA \\ & = \iiint \left(\frac{\rho}{\varepsilon_0} \right) N_i^{(e)} dx dy dz - \iint_A N_i^{(e)} \bar{\tau}^{(e)} \cdot \bar{n} dA \quad (2-13) \\ & = \iiint \left(\frac{\rho}{\varepsilon_0} \right) N_i^{(e)} dx dy dz - \iint_A N_i^{(e)} \bar{\tau}_n^{(e)} dA \quad i = 1 - 4 \end{aligned}$$

where $\vec{\tau}_n^{(e)}$ is the outward-normal component of the flux. All load terms are placed on the

RHS; this includes the interior load and the boundary fluxes.

Step 3: Substitute the trial solution into element equations.

Inserting **Eqs. (2-9)** into **Eqs. (2-13)** yields,

$$\begin{aligned} \iiint [(\frac{\partial N_i^{(e)}}{\partial x} \frac{\partial N_j^{(e)}}{\partial x}) + (\frac{\partial N_i^{(e)}}{\partial y} \frac{\partial N_j^{(e)}}{\partial y}) + (\frac{\partial N_i^{(e)}}{\partial z} \frac{\partial N_j^{(e)}}{\partial z})] dx dy dz a_j \\ = \iiint (\frac{\rho}{\epsilon_0}) N_i^{(e)} dx dy dz - \iint_A N_i^{(e)} \vec{\tau}_n^{(e)} dA \quad i = 1-4, j = 1-4 \end{aligned} \quad (2-14)$$

Writing it also in matrix form,

$$\begin{bmatrix} K_{11}^{(e)} & K_{12}^{(e)} & \dots & K_{1n}^{(e)} \\ K_{21}^{(e)} & K_{22}^{(e)} & \dots & K_{2n}^{(e)} \\ \vdots & \vdots & \dots & \vdots \\ K_{n1}^{(e)} & K_{n2}^{(e)} & \dots & K_{nn}^{(e)} \end{bmatrix} \begin{bmatrix} a_1 \\ a_2 \\ \vdots \\ a_n \end{bmatrix} = \begin{bmatrix} F_1^{(e)} \\ F_2^{(e)} \\ \vdots \\ F_n^{(e)} \end{bmatrix} \quad (2-15)$$

Where the coefficient matrix and load matrix are defined as:

$$\begin{aligned} K_{ij}^{(e)} &= \iiint [(\frac{\partial N_i^{(e)}}{\partial x} \frac{\partial N_j^{(e)}}{\partial x}) + (\frac{\partial N_i^{(e)}}{\partial y} \frac{\partial N_j^{(e)}}{\partial y}) + (\frac{\partial N_i^{(e)}}{\partial z} \frac{\partial N_j^{(e)}}{\partial z})] dx dy dz \\ F_i^{(e)} &= \iiint (\frac{\rho}{\epsilon_0}) N_i^{(e)} dx dy dz - \iint_A N_i^{(e)} \vec{\tau}_n^{(e)} dA \end{aligned}$$

Step 4: Substitute the 3-D C^0 -linear shape function for a tetrahedral mesh into element equation.

The LHS of **Eqs. (2-14)** may be reformulated,

$$K_{i,j}^{(e)} = \iiint (\mathbf{b}_i^{(e)} \mathbf{b}_j^{(e)} + \mathbf{c}_i^{(e)} \mathbf{c}_j^{(e)} + \mathbf{d}_i^{(e)} \mathbf{d}_j^{(e)}) dx dy dz \quad (2-16)$$

Where

$$N_i^{(e)}(x, y, z) = \frac{1}{6V} (\mathbf{a}_i^{(e)} + \mathbf{b}_i^{(e)} x + \mathbf{c}_i^{(e)} y + \mathbf{d}_i^{(e)} z) \quad i = 1-4 \quad (2-17a)$$

$$\mathbf{a}_i^{(e)} = \begin{vmatrix} x_k & y_k & z_k \\ x_l & y_l & z_l \\ x_m & y_m & z_m \end{vmatrix} \quad (2-17b)$$

$$\mathbf{b}_i^{(e)} = - \begin{vmatrix} 1 & y_k & z_k \\ 1 & y_l & z_l \\ 1 & y_m & z_m \end{vmatrix} \quad (2-17c)$$

$$\mathbf{c}_i^{(e)} = - \begin{vmatrix} x_k & 1 & z_k \\ x_l & 1 & z_l \\ x_m & 1 & z_m \end{vmatrix} \quad (2-17d)$$

$$\mathbf{d}_i^{(e)} = - \begin{vmatrix} x_k & y_k & 1 \\ x_l & y_l & 1 \\ x_m & y_m & 1 \end{vmatrix} \quad (2-17e)$$

Where V is the volume of cell and the subscripts i, k, l, m have the values 1, 2, 3, 4 (see [Fig. 2.2](#)) for $N_1^{(e)}(x, y, z)$ and are permuted cyclically for $N_2^{(e)}(x, y, z)$, $N_3^{(e)}(x, y, z)$ and $N_4^{(e)}(x, y, z)$.

Step 5: Evaluate the interior load term and boundary flux term of Eqs.(2-14).

For coupling with Particle-In-Cell method in later chapter, here we interpolate charges from the particles to the nodes [Santi *et. al.*, 2003], that is:

$$\rho_i^{(e)} = \sum_k q_k N_i^{(e)}(x_k, y_k, z_k) \quad i = 1-4 \quad (2-18)$$

Where the subscript k represents charged particle properties. Substituting [Eqs. \(2-18\)](#) into the interior load term, it becomes

$$\begin{aligned}
& \iiint \left(\frac{\rho}{\epsilon_0}\right) N_i^{(e)} dx dy dz \\
&= \frac{1}{\epsilon_0} \sum_{i=1}^4 \rho_i^{(e)} \iiint N_i^{(e)} dx dy dz \\
&= \frac{V}{4\epsilon_0} \sum_{i=1}^4 \rho_i^{(e)}
\end{aligned} \tag{2-19}$$

Where V is the volume of cell. Now consider the boundary flux integral, we

assume the flux is constant and move $\bar{\tau}_n^{(e)}$ outside the integrals:

$$\begin{aligned}
& \iint_A N_i^{(e)} \bar{\tau}_n^{(e)} dA \\
&= \bar{\tau}_n^{(e)} \iint_A N_i^{(e)} dA \\
&= \bar{\tau}_n^{(e)} \frac{\Delta^{(e)}}{3}
\end{aligned} \tag{2-20}$$

Where $\Delta^{(e)}$ is the face area of the element.

Step 6: Assemble the element equations into a system equation

Using an assembly procedure,

$$W^T (K_{i,j}^{(e)} a_j) = W^T (F_i^{(e)}) \tag{2-21}$$

The system equation is formed,

$$K_{i,j}^{(s)} a_j = F_i^{(s)} \tag{2-22}$$

After these theoretical developments, we may apply the boundary conditions to **Eqs. (2-22)**.

For a three-dimensional hexahedral mesh with local coordinate shape function, the same steps 1-3 and 6 are repeated for **Eqs.(2-5)**, and the step 4-5 are be modified as follows.

Step 4: Substitute the 3-D C^0 -linear shape function for a hexahedral mesh into element equation.

The **Eqs. (2-15)** is transformed into a form appropriate for numerical evaluation.

$$\begin{aligned}
 K_{ij}^{(e)} = & \int_{-1}^1 \int_{-1}^1 \int_{-1}^1 \frac{\partial N_i^{(e)}}{\partial x} \frac{\partial N_j^{(e)}}{\partial x} \frac{\partial N_k^{(e)}}{\partial x} |J^{(e)}| d\xi d\eta d\rho \\
 & + \int_{-1}^1 \int_{-1}^1 \int_{-1}^1 \frac{\partial N_i^{(e)}}{\partial y} \frac{\partial N_j^{(e)}}{\partial y} \frac{\partial N_k^{(e)}}{\partial y} |J^{(e)}| d\xi d\eta d\rho \\
 & + \int_{-1}^1 \int_{-1}^1 \int_{-1}^1 \frac{\partial N_i^{(e)}}{\partial z} \frac{\partial N_j^{(e)}}{\partial z} \frac{\partial N_k^{(e)}}{\partial z} |J^{(e)}| d\xi d\eta d\rho
 \end{aligned} \tag{2-23}$$

$$F_i^{(e)} = \int_{-1}^1 \int_{-1}^1 \int_{-1}^1 \left(\frac{\rho}{\epsilon_0} \right) N_i^{(e)} |J^{(e)}| d\xi d\eta d\rho - \iint_A N_i^{(e)} \bar{\tau}_n^{(e)} dA \tag{2-24}$$

Where $N_i(\xi, \eta, \rho)$ is the shape function with local coordinate,

$$N_i(\xi, \eta, \rho) = \frac{1}{8} (1 + \xi \xi_i) (1 + \eta \eta_i) (1 + \rho \rho_i) \tag{2-25}$$

And ξ_i , η_i and ρ_i are the local coordinate of grid node for a standard

hexahedral element (as shown in **Fig.2-3**). And, $|J^{(e)}|$ is the Jacobian [Shao,

2006]:

$$[J] = \begin{bmatrix} \frac{\partial N_1}{\partial \xi} & \frac{\partial N_2}{\partial \xi} & \frac{\partial N_3}{\partial \xi} & \frac{\partial N_4}{\partial \xi} & \frac{\partial N_5}{\partial \xi} & \frac{\partial N_6}{\partial \xi} & \frac{\partial N_7}{\partial \xi} & \frac{\partial N_8}{\partial \xi} \\ \frac{\partial N_1}{\partial \eta} & \frac{\partial N_2}{\partial \eta} & \frac{\partial N_3}{\partial \eta} & \frac{\partial N_4}{\partial \eta} & \frac{\partial N_5}{\partial \eta} & \frac{\partial N_6}{\partial \eta} & \frac{\partial N_7}{\partial \eta} & \frac{\partial N_8}{\partial \eta} \\ \frac{\partial N_1}{\partial \rho} & \frac{\partial N_2}{\partial \rho} & \frac{\partial N_3}{\partial \rho} & \frac{\partial N_4}{\partial \rho} & \frac{\partial N_5}{\partial \rho} & \frac{\partial N_6}{\partial \rho} & \frac{\partial N_7}{\partial \rho} & \frac{\partial N_8}{\partial \rho} \end{bmatrix} \begin{bmatrix} X_1 & Y_1 & Z_1 \\ X_2 & Y_2 & Z_2 \\ X_3 & Y_3 & Z_3 \\ X_4 & Y_4 & Z_4 \\ X_5 & Y_5 & Z_5 \\ X_6 & Y_6 & Z_6 \\ X_7 & Y_7 & Z_7 \\ X_8 & Y_8 & Z_8 \end{bmatrix} \tag{2-26}$$

$$= \frac{1}{8} \begin{bmatrix} -(1-\eta)(1-\rho) & +(1-\eta)(1-\rho) & +(1+\eta)(1-\rho) & -(1+\eta)(1-\rho) \\ -(1-\xi)(1-\rho) & -(1+\xi)(1-\rho) & +(1+\xi)(1-\rho) & +(1-\xi)(1-\rho) \\ -(1-\xi)(1-\eta) & -(1+\xi)(1-\eta) & -(1+\xi)(1+\eta) & -(1-\xi)(1+\eta) \\ -(1-\eta)(1+\rho) & +(1-\eta)(1+\rho) & +(1+\eta)(1+\rho) & -(1+\eta)(1+\rho) \\ -(1-\xi)(1+\rho) & -(1+\xi)(1+\rho) & +(1+\xi)(1+\rho) & +(1-\xi)(1+\rho) \\ +(1-\xi)(1-\eta) & +(1+\xi)(1-\eta) & +(1+\xi)(1+\eta) & +(1-\xi)(1+\eta) \end{bmatrix} \begin{pmatrix} X_1 & Y_1 & Z_1 \\ X_2 & Y_2 & Z_2 \\ X_3 & Y_3 & Z_3 \\ X_4 & Y_4 & Z_4 \\ X_5 & Y_5 & Z_5 \\ X_6 & Y_6 & Z_6 \\ X_7 & Y_7 & Z_7 \\ X_8 & Y_8 & Z_8 \end{pmatrix}$$

The stiffness integral may now be written as the following quadrature expressions:

$$K_{ij}^{(e)} = \sum_{k=1}^n \sum_{l=1}^n \sum_{m=1}^n w_{nk} w_{nl} w_{nm} \left[\left(\frac{\partial N_i^{(e)}}{\partial x} \frac{\partial N_j^{(e)}}{\partial x} \frac{\partial N_k^{(e)}}{\partial x} + \frac{\partial N_i^{(e)}}{\partial y} \frac{\partial N_j^{(e)}}{\partial y} \frac{\partial N_k^{(e)}}{\partial y} + \frac{\partial N_i^{(e)}}{\partial z} \frac{\partial N_j^{(e)}}{\partial z} \frac{\partial N_k^{(e)}}{\partial z} \right) |J^{(e)}|_{(\xi_{nk}, \eta_{nl}, \rho_{nm})} \right] \quad (2-27)$$

Where w_{nk} , w_{nl} , and w_{nm} are weight factors. ξ_{nk} , η_{nl} , and ρ_{nm} are so called Gauss points at which the integral is evaluated. n is the number of Gauss points.

Here, the derivative of shape function with respect to x , y , z is handled using the chain rule of differentiation, and it yields:

$$\begin{bmatrix} \frac{\partial N_k(\xi, \eta, \rho)}{\partial X} \\ \frac{\partial N_k(\xi, \eta, \rho)}{\partial Y} \\ \frac{\partial N_k(\xi, \eta, \rho)}{\partial Z} \end{bmatrix} = [J^{-1}] \begin{bmatrix} \frac{\partial N_k(\xi, \eta, \rho)}{\partial \xi} \\ \frac{\partial N_k(\xi, \eta, \rho)}{\partial \eta} \\ \frac{\partial N_k(\xi, \eta, \rho)}{\partial \rho} \end{bmatrix} = \frac{1}{8} \frac{adj([J])}{|\det([J])|} \begin{bmatrix} \xi_k (1 + \eta \eta_k) (1 + \rho \rho_k) \\ \eta_k (1 + \xi \xi_k) (1 + \rho \rho_k) \\ \rho_k (1 + \xi \xi_k) (1 + \eta \eta_k) \end{bmatrix} \quad (2-28)$$

Step 5: Evaluate the interior load term and boundary flux term of Eqs .(2-24).

Again, for coupling with Particle-In-Cell method in later chapter, we

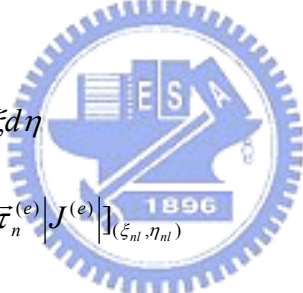
interpolate charges from the particles to the nodes, that is:

$$\rho_i^{(e)} = \sum_k q_k N_i^{(e)}(\xi_k, \eta_k, \rho_k) \quad i = 1-8 \quad (2-29)$$

Where the subscript k represents charged particle properties. Then, $\rho_i^{(e)}$ is weighted to the Gauss point becomes $\rho_{(\xi_{nk}, \eta_{nl}, \rho_{nm})}^{(e)}$, and substitute this into the interior load integral term in quadrature expressions:

$$\begin{aligned} & \int_{-1}^1 \int_{-1}^1 \int_{-1}^1 \left(\frac{\rho}{\epsilon_0} \right)^{(e)} N_i^{(e)} |J^{(e)}| d\xi d\eta d\rho \\ &= \sum_{k=1}^n \sum_{l=1}^n \sum_{m=1}^n w_{nk} w_{nl} w_{nm} \left[\left(\frac{\rho}{\epsilon_0} \right)^{(e)} N_i^{(e)} |J^{(e)}| \right]_{(\xi_{nk}, \eta_{nl}, \rho_{nm})} \end{aligned} \quad (2-30)$$

Now considering the boundary flux integral term in quadrature expressions,

$$\begin{aligned} & \iint_A N_i^{(e)} \bar{\tau}_n^{(e)} dA \\ &= \int_{-1}^1 \int_{-1}^1 N_i^{(e)} \bar{\tau}_n^{(e)} |J^{(e)}| d\xi d\eta \\ &= \sum_{k=1}^n \sum_{l=1}^n w_{nk} w_{nl} [N_i^{(e)} \bar{\tau}_n^{(e)} |J^{(e)}|]_{(\xi_{nk}, \eta_{nl})} \end{aligned} \quad (2-31)$$


2.4 Sparse Matrix Storage Schemes

The FEM formulations and assembly techniques typically lead to large and sparse matrices. Thus, it becomes essential to store sparse matrix in some kind of storage schemes, especially for an efficient matrix-by-vector product of the iterative method. Nearly all schemes have these two following storage components, e.g., [Golub and Van Loan, 1996], and [Saad, 2003]:

1. A one-dimensional array, which is called the *primary array* with the size of the number of non-zero entries, for storing the non-zero entries.

2. Two one-dimensional arrays of integer identifiers, which are called *secondary arrays* with the size of the number of non-zero entries, for recognizing which entries of the matrix are stored in the primary array.

The *Compressed Sparse Row (CSR)* scheme is used for storing the current FEM sparse matrix, in which scheme the each entry of primary array is stored row-by-row.

2.5 Preconditioned Conjugate Gradient Method (PCG)

Among the iterative methods, the *Preconditioned Conjugate Gradient method* (PCG) is extremely effective for solving the symmetric positive definite systems. The PCG method was developed in 1952 by Hestenes and Stiefel, which is an improvement to the steepest descent method [Saad, 2003]. The steepest descent approaches the solution asymptotically, however, the disadvantage of this method is that the speed of convergence may be very slow if the condition number of the matrix A is large. PCG is an efficient implementation of the conjugate directions method in which the search directions are constructed by conjugation of the residuals. In this section, the theory of PCG will not be described in detail, which can be found elsewhere, e.g., [Golub and Van Loan, 1996], [Saad, 2003], and [Barrett and Berry, 1994]. The algorithm is given in the following,

Algorithm 1. Preconditioned Conjugate Gradient Method

Choose x^0
 $r^0 = b - Ax^0$
solve $Mz^0 = r^0$
 $p^0 = z^0$
 $r^0 = \text{inner product } (z^0, r^0)$
DO $k = 0, 1, 2, \dots, k_{\max}$
 $q^k = \text{matrix multiply } (A, p^k)$
 $\tau^k = \text{inner product } (p^k, q^k)$
 $\alpha^k = \gamma^k / \tau^k$
 $x^{k+1} = x^k + \alpha^k p^k$
 $r^{k+1} = r^k - \alpha^k q^k$
 $r^{k+1} = \text{inner product } (r^{k+1}, r^{k+1})$
solve $Mz^{k+1} = r^{k+1}$
 $r^{k+1} = \text{inner product } (z^{k+1}, r^{k+1})$
If ($\sqrt{\gamma^{k+1}} \leq \text{tolerance}$) exit
 $\beta^k = \gamma^{k+1} / \gamma^k$
 $p^{k+1} = \gamma^k + \beta^k p^k$
ENDDO



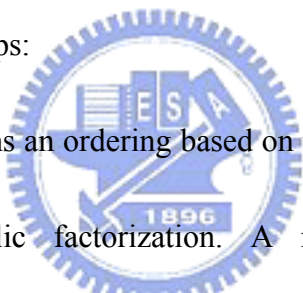
Where k is the iterative number, r is the residual, x is the solution vector, p is the step direction, α is the step length, and β is the correction factor. Preconditioner M is defined as the diagonal of stiffness A , known as *Jacobi preconditioning*, is equivalent to scaling the quadratic form along the coordinate axes.

2.6 Multi-frontal Massively Parallel Solver (MUMPS)

MUMPS [Amestoy *et. al.*, 2000] is a package for solving systems of linear equations of the form $Ax = b$. Unlike PCG, the stiffness matrix, A , is a square sparse matrix that can be either un-symmetric, symmetric positive definite, or general

symmetric. MUMPS uses a multi-frontal technique, which is a direct method based on either the LU or the LDLT factorization of the matrix. In the following, the main features and steps of MUMPS from its userguide are given in turn.

The main features of the MUMPS package include the solution of the transposed system, input of the matrix in assembled format (distributed or centralized) or elemental format, error analysis, iterative refinement, scaling of the original matrix, return of a Schur complement matrix, and several built-in ordering algorithms. The details of this technique can be found in the reference of its user-guide. The system $Ax = b$ is solved in three main steps:

- 
1. *Analysis*. The host performs an ordering based on the symmetrized pattern $A+A^T$, and carries out symbolic factorization. A mapping of the multifrontal computational graph is then computed, and symbolic information is transferred from the host to the other processors. Using this information, the processors estimate the memory necessary for factorization and solution.
 2. *Factorization*. The original matrix is first distributed to processors that will participate in the numerical factorization. The numerical factorization on each frontal matrix is conducted by a *master* processor (determined by the analysis phase) and one or more *slave* processors (determined dynamically). Each processor allocates an array for contribution blocks and factors; the factors must

be kept for the solution phase.

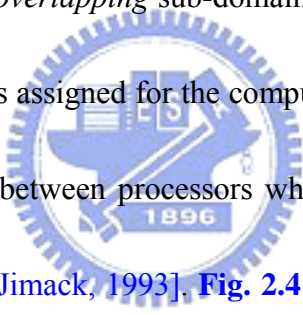
3. *Solution.* The right-hand side b is broadcast from the host to the other processors.

These processors compute the solution x using the (distributed) factors computed during Step 2, and the solution is either assembled on the host or kept distributed on the processors. Each of these phases can be called separately and several instances of MUMPS can be handled simultaneously. MUMPS allows the host processor to participate in computations during the factorization and solve phases, just like any other processor. For both the symmetric and the unsymmetric algorithms used in the code, MUMPS has chosen a fully asynchronous approach with dynamic scheduling of the computational tasks. Asynchronous communication is used to enable overlapping between communication and computation. Dynamic scheduling was initially chosen to accommodate numerical pivoting in the factorization. The other important reason for this choice was that, with dynamic scheduling, the algorithm can adapt itself at execution time to remap work and data to more appropriate processors. In fact, we combine the main features of static and dynamic approaches; MUMPS uses the estimation obtained during the analysis to map some of the main computational tasks; the other tasks are dynamically scheduled at execution time. The main data structures (the original matrix and the factors) are similarly partially mapped according to

the analysis phase.

MUMPS distributes the work tasks among the processors, but an identified processor (the host) is required to perform most of the analysis phase, to distribute the incoming matrix to the other processors (slaves) in the case where the matrix is centralized, and to collect the solution.

2.7 Parallel computing of FEM

In parallel computing of FEM, the computational domain is first partitioned divided into a number of *non-overlapping* sub-domains, which is equal to the number of processors. One processor is assigned for the computation of each sub-domain, and communications are required between processors whenever needed, e.g., [Farhat et al., 1995], and [Hodgson and Jimack, 1993].  Fig. 2.4 shows the three different kinds of partitioning methods, which are common used in *graph-partitioning* techniques [Saad, 2003]. We use the *element-based* partitioning to partition the domain, in which partitioning method, there is no element should be split between two sub-domains, e.g., [Gullerud and Dodds, 2001], and [Thiagarajan and Aravamuthan, 2002].

The different type of approach is used for the different type of domain decomposition [Saad, 2003]. When the domain is partitioned into a set of overlapping sub-domains in which case *overlapping Schwartz methods* are used for the solution of the system. On the other hand, *iterative sub-structuring methods* are used for domain

is partitioned into a set of non-overlapping sub-domains. There are two typical non-overlapping domain decomposition methods used in parallel computing of FEM, which are the *subdomain-by-subdomain* (SBS) and the *Schur complement* method. We use the SBS approach for paralleling FEM, in which the global stiffness matrix is divided a numbers of partitioned matrices and be stored on each corresponding processor. Then the PCG method should be performed on the SBS basis. The details of SBS method are described in the following.

Before introducing SBS method, the graph-partitioning library, METIS [Karypis, and Kumar, 1995], is first used to decompose the computational domain Ω into p non-overlapping sub-domains (see Fig. 2.5).

$$\Omega = \bigcup_{i=1}^p \Omega_i \quad (2-32)$$

and

$$\Omega_i \cap \Omega_j = \{\} \quad \text{when } i \neq j \quad (2-33)$$

The following Eqs. (2-34) is the standard *block-arrowhead structure* of the stiffness matrix usually formed from SBS method.

$$\begin{bmatrix} A_1 & & & & B_1 \\ & A_2 & & & B_2 \\ & & \ddots & & \vdots \\ & & & A_p & B_p \\ B_1^T & B_2^T & \cdots & B_p^T & A_s \end{bmatrix} \begin{bmatrix} x_1 \\ x_2 \\ \vdots \\ x_p \\ x_s \end{bmatrix} = \begin{bmatrix} b_1 \\ b_2 \\ \vdots \\ b_p \\ b_s \end{bmatrix} \quad (2-34)$$

This kind of matrix structure stems from the special nodes re-ordering on each

sub-domain using SBS method. For each sub-domain, the rule of nodes re-ordering is that the internal nodes is numbered first and last the interfacial nodes. The matrices of internal nodes ($A_i, B_i, B_i^T, x_i,$ and b_i) are contributed entirely from its corresponding sub-domain, and the matrices of interfacial matrices ($A_s, B_s, B_s^T, x_s,$ and b_s) have the contributions from all sub-domains. Since all these matrices are concurrently assembled on each processor, the PCG algorithm using SBS method is given as follows, e.g., [Saad, 2003], [Gullerud and Dodds, 2001], [Khan and Topping, 1996], and [Jimack, and Touheed, 1997],

Algorithm 2. Parallel Preconditioned Conjugate Gradient Method

$$x_i^0 = 0.; x_{s_i}^0 = 0.$$

$$b_{s_i} = \text{Updated}(b_{s_i})$$

$$r_i^0 = b_i.; r_{s_i}^0 = b_{s_i}^0$$

$$\text{solve } M(z_i^0, z_{s_i}^0) = (r_i^0, r_{s_i}^0)$$

$$p_i^0 = z_i^0, p_{s_i}^0 = z_{s_i}^0$$

$$r^0 = \text{inner product } (z_i^0, z_{s_i}^0; r_i^0, r_{s_i}^0)$$

DO $k = 0, 1, 2, \dots, k_{\max}$

$$q_i^{k+1} = A_i p_i^k + B_{s_i} p_{s_i}^k$$

$$q_{s_i}^{k+1} = \text{update}(B_i^T p_i^k + A_{s_i} p_{s_i}^k)$$

$$\tau^k = \text{inner product } (p_i^0, p_{s_i}^0; q_i^k, q_{s_i}^k)$$

$$\alpha^k = \gamma^k / \tau^k$$



$$x_i^{k+1} = x_i^k + \alpha^k p_i^k ; x_{s_i}^{k+1} = x_{s_i}^k + \alpha^k p_{s_i}^k$$

$$r_i^{k+1} = r_i^k - \alpha^k q_i^k ; r_{s_i}^{k+1} = r_{s_i}^k - \alpha^k q_{s_i}^k$$

$$\text{solve } M(z_i^{k+1}, z_{s_i}^{k+1}) = (r_i^{k+1}, r_{s_i}^{k+1})$$

$$r^{k+1} = \text{inner product } (z_i^{k+1}, z_{s_i}^{k+1}; r_i^{k+1}, r_{s_i}^{k+1})$$

If ($\sqrt{\gamma^{k+1}} \leq \text{tolerance}$) exit

$$\beta^k = \gamma^{k+1} / \gamma^k$$

$$p_i^{k+1} = \gamma_i^k + \beta^k p_i^k ; p_{s_i}^{k+1} = \gamma_{s_i}^k + \beta^k p_{s_i}^k$$

ENDDO

This algorithm shows that the PCG with SBS method should be performed concurrently on each processor, whereas the communication is performed in two matrix operators: inner product and update [Jimack, and Touheed, 1997]. The subroutine inner product is used to calculate the inner product of two distributed vector between processors and then it requires a single globe communication for providing each processor with a copy of this sum. Since this sum is calculated repeatedly, it should be scaled by the reciprocal of the number of processor. The subroutine update is used to sum the distributed contribution of interfacial nodes via local communication.

The technique of non-overlapping domain decomposition we utilized in parallel computing of FEM is briefly described in the next section.

2.7.1 Domain Decomposition Method

There are two typical domain decomposition methods, which are *geometry-based* and *graph-based* domain decomposition. Since Geometry-based method provided poor edge cut (E_c) and poor load balance, e.g., [Tseng, 2005], [Wehage and Haug, 1982], and [Simon, 1991], we use the graph-based method for our domain decomposition method. For the graph theory, a sketch of two-dimensional triangle mesh (graph) is shown in Fig. 2.6. This figure shows that a graph is the collection of the vertices of each cell and edge cuts between the cells. Most of this method was developed by the scientists who major in computer science, and the main idea of this method is to subdivide the n vertices between the NP sub-domains while minimizing the number of edge cuts, and balancing the weight in each sub-domain. Tseng [Tseng, 2005] had reviewed the partition method using graph-based method, e.g. [Simon, 1991], [Vanderstraeten *et. al.*, 1996], and [Barnard and Simon, 1994] including Greedy partitioning, recursive spectral bisection, multi-level scheme, two-step method. And he recommended that the graph-partitioning library, named METIS, developed by University of Minnesota using multi-level scheme, especially has impressive performance in terms of CPU time and very easy for implementation. After obtaining the partitioned data, a converter should be designed for preprocessing the mesh (grid) data. The main function of this converter is to reorder the fully unstructured mesh data into the *globally sequential but locally unstructured* mesh data

for obtaining the relationship between global and local cell data by a simple arithmetic operation due to this special cell-numbering design [Tseng, 2005]. In addition, the nodes numbers of each sub-domain must be re-ordered follow the requirement for FEM using SBS method. This converter is a improvement of Tseng's method.

2.8 Parallel Adaptive Mesh Refinement using a Tetrahedral Mesh (PAMR)

Fig. 2.7 shows the proposed overall procedures of parallel adaptive mesh refinement for an unstructured tetrahedral mesh. Only the general procedures are described in this thesis, while the details and results of the parallel implementation can be found elsewhere [Lian *et. al.*, 2006]. Basically, the parallel mesh refinement procedures in **Fig. 2.7** are similar to those presented earlier for serial mesh refinement elsewhere [Wu *et. al.*, 2004]. In the serial mesh refinement, the cells are first examined to identify if cell refinement is necessary. If so, then they are refined “isotropically” into eight child cells. The generated hanging nodes are then removed following the procedures proposed in Wu *et al.* [Wu *et. al.*, 2004] in which the cells are further refined into two, four, or eight child cells.

However, the detailed procedures and related data structure become more complicated than those in serial mesh refinement because of the parallel processing.

Domain decomposition is also used in line with parallel implementation of the current Poisson's equation solver. Each spatial sub-domain belongs to a specific processor in practice. The overall procedure shown in [Fig. 2.7](#) can be summarized as follows:

1. Preprocess the input data at the host processor, and distribute them to all other processors.

2. Index the cells which require refinement based on the refinement criteria.

In the current study, we use the variation of potentials among elements as the criterion for cell refinement which, in practice, is equivalent to a generally accepted error estimator as will be shown in the next section.

3. Check if further mesh refinement is necessary. If it is, then proceed to the next step. If not, proceed to Step 9.

4. Add new nodes into those cells that require refinement.

4a. Add new nodes onto all edges of isotropic cells.

4b. Add new nodes into the anisotropic cells which require further refinement as decided upon in the following steps.

4c. Communicate the hanging-node data to corresponding neighboring processor if the hanging nodes are located at IPB.

4d. Remove the hanging nodes following the procedures as shown in Wu, et al. [[Wu et. al., 2004](#)]. The basic idea is to remove the hanging nodes for

all kinds of conditions, and then refine the cell into two, four, or eight child cells.

5. Unify the global node and cell numberings caused by the newly added nodes in all processors.
 - 5a. Add up the number of the newly added nodes in each processor, excluding those located at interprocessor boundaries (IPBs).
 - 5b. Gather this number from all other processors, and add them up to obtain the updated total number of nodes, including old and new nodes, but excluding the newly added nodes at IPBs.
 - 5c. Build up the updated node-mapping and corresponding cell-mapping arrays for those newly added nodes in the interior part of each sub-domain based on the results in Step 5b.
 - 5d. Communicate the data of newly added nodes at the IPBs among all processors.
 - 5e. Build up the node-mapping array for the new nodes received at IPBs in each processor.
6. Build up new connectivity data for all cells to include the newly added nodes.
7. Build up the new neighbor-identifying array based on the new connectivity

data obtained in Step 6.

- 7a. Reset the neighbor-identifying array.
- 7b. Build up the neighbor-identifying arrays for all cells based on the new connectivity data, excluding the data associated with the faces lying on the IPBs that require the updated information of the global cell number which is not yet known at this stage.
- 7c. Record all the neighbor-identifying arrays that have not been rebuilt in Step 7b.
- 7d. Broadcast all the recorded data in all processors.
- 7e. Build up the neighbor-identifying arrays on the IPBs, considering the overall connectivity data structure.
8. Decide if it reaches the preset maximum number of refinement. If it does, then proceed to the next step. Otherwise, return to Step 3.
9. Synchronize all processors.
10. The host processor gathers and outputs the data.

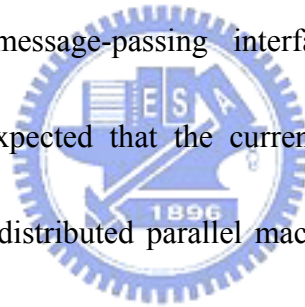
In the current study, by coupling the PAMR with the parallel Poisson's equation solver as stated in Step 3, the maximum number of refinement is set to be "one", since the option whether further refinement is necessary is decided outside the PAMR, as can be seen in the next section.

2.9 Coupling of PAMR with Parallel Electrostatic Field Solver

The PAMR presented in the previous section can be easily coupled to the current parallel electrostatic field solver since both utilize 3-D unstructured tetrahedral mesh and MPI for data communication. One can readily wrap up the PAMR as a library and insert it into the source code of any parallel numerical solver to be used. However, some problems may occur due to memory conflicts between the inserted library and the numerical solver itself that could reduce the problem size one can handle in practice. As such, a simple coupling procedure, written in shell script ([Fig. 2.8](#)) that is standard on all Unix-like systems, can be prepared to link the PAMR and the current parallel electrostatic field solver. In doing so, we can keep the source codes intact and without alterations. Indeed, it is especially justified if only a steady state of the physical problem is sought, in which normally only several times of mesh refinement is enough to have a fairly satisfactory solution. Thus, the total I/O time, which is in proportion to the number of couplings in switching between two codes, can be reduced to a minimum in practical applications. In addition, as shown in [Fig. 2.8](#), after identifying those cells that require refinement before PAMR, the domain is repartitioned based on the new mesh refinement requirements. For example, the weight factors of the cells (vertex in graph theory) are set as eight for those cells which are flagged to be refined; otherwise, they are set as unity. With this distribution

of weight factors as the input to ParMETIS [Karypis, 1998], an approximate (but rather good) load balancing can be achieved in the PAMR module. Then the electrostatic field solvers read in the output refined mesh from the PAMR module and partition the new mesh with equal weight factors for all cells, in which the workload is balanced in the electrostatic field solvers.

The current parallel electrostatic field solvers along with PAMR are implemented and tested on a PC-cluster system with the Linux OS at the National Center for High-Performance Computing in Taiwan (64-node, dual processor and 8 GB RAM per node). The standard message-passing interface (MPI) is used for data communication. It is thus expected that the current parallel code will be highly portable among the memory-distributed parallel machines that are running with the Linux (or its equivalent) operating system.



2.10 Validation and Parallel Performance of the Electrostatic Field Solver

Fig. 2.9 shows a simplified flowchart of the parallel computing of FEM proposed in the current chapter, which incorporates the multi-level graph-partitioning library. **Fig. 2.9** shows that after reading the preprocessed cell and node data on a master processor (CPU 0), the data are then distributed to all other processors according to the designated initial domain decomposition. With these data, every

processor will concurrently construct shape function, coefficient matrix and then impose the boundary conditions. Once every processor has the above information the system will ready be solved using parallel PCG. The final results are then output when L2 error norm is less then the specified convergence criteria.

Validation of the parallel electrostatic field solver

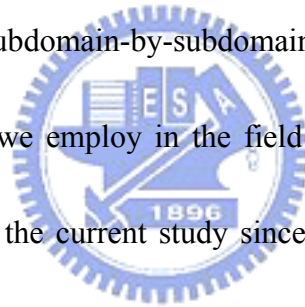
Many analytical solutions of Poisson's equation are available for comparison either with or without the source term. In the current study, we have selected one problem without a source term and another with a constant source term. The former is a grounded conducting sphere with diameter (D_{sphere}) 2 meters immersed in a uniform electric field ($\vec{E} = 10$ volts/m, ~40,000 elements, 20 processors), while the latter is a uniformly charged distribution between two infinite, grounded conducting plates at $L=0m$ and $L=0.02m$ (quasi 1-D, number density of singly-charged ions= $10^{16} m^{-3}$, ~8,500 elements, 20 processors). About ~56,000 particles are used. The charge weighting used in this is based on the volume coordinates that originated from the finite element method. The simulation and analytic solutions of these two problems are both in excellent agreement with the analytical solution as shown in **Fig. 2.10(a)** and **Fig. 2.10(b)**, respectively. These results validate the accuracy of the current parallel Poisson's equation solver.

Parallel performance of the electrostatic field solver

The simulation of a typical single CNT field emitter within a periodic cell using 0.47 million elements (~97,000 nodes), as shown in **Fig. 2.11**, is employed to test the parallel performance of the current Poisson's equation solver. This size of the mesh is typical for further production run as will be presented in chapter 5. Only $\frac{1}{4}$ of the volume is used for the simulation by taking advantage of the symmetry in this problem. The gate voltage is applied with 150 volts, while the cathode and anode electrodes are grounded and applied with 400 volts, respectively. At the planes of symmetry, Neumann boundary conditions are used. A very refined grid (**Fig. 2.12**) is used near the silicon tip to improve the accuracy of the predicted electrical field. No parallel adaptive mesh refinement is used in the simulation since at this stage; we are only interested in obtaining the parallel performance of the Poisson's equation solver.

Fig. 2.13 illustrates the parallel speedup as a function of the number of processors up to 32. The corresponding time breakdown of various components of the solver along with speedup is summarized in **Table 2**. The runtime using a single processor is about 138.17 seconds, while it is reduced to 5.13 seconds using 32 processors, which results in ~26.93 of parallel speedup. Most of the time is consumed in the parallel CG matrix solver, in which the percentage of communication time generally increases with the number of processors used. Note that the communication time, including the

send/receive and allreduce commands required in a parallel CG solver, is relatively short (~3.53 seconds or 4.5% of the total time) at 2 processors which is attributed to the fast access to the same memory by the dual-processor per node architecture of this cluster system. An appreciable portion of the runtime is spent in the communication for a large number of processors, e.g., 35.4% at 16 processors. A further improvement of the solver efficiency by adding a robust parallel preconditioner before the parallel CG solver is highly expected and will be reported elsewhere in the future. Nevertheless, the present results clearly show that the parallel implementation of the Poisson's equation using a subdomain-by-subdomain procedure performs very well for the typical problem size we employ in the field emission prediction. A smaller problem size is not tested in the current study since it is irrelevant for this kind of application. It is expected that the parallel speedup can be even better if a larger problem size is simulated, e.g., for an array of field emitters. Thus, the current parallel implementation can greatly help to reduce the runtime required for the parametric study of optimizing the field emitter design.



Performance of parallel adaptive mesh refinement

A case with the same boundary conditions as the above test case for parallel performance is used to demonstrate the improvement of prediction using parallel adaptive mesh refinement. **Fig. 2-14** shows a close-up view of the mesh distribution

near the single CNT tip using PAMR where the initial mesh is rather coarse (7,006 nodes), while the level-5 mesh is very fine (61,241 nodes) near the tip. In this case, an element is refined into eight child elements if the standard deviation of the potentials among the nodes of this element is larger than the value of a preset criterion, ε_{ref} . In this case, ε_{ref} is set to 0.08. **Table 3** lists the number of nodes/elements and the corresponding maximal electric field in the simulation domain at different levels of mesh refinement. In addition, the data in the parentheses are obtained by using an *a posteriori* error estimator as proposed by Zienkiewicz and zhu [Zienkiewicz and Zhu, 1987]. We have employed a very simple gradient recovery scheme by averaging the cell values of the FE solution to extract the “exact” solution of the electric field in each cell. A prescribed global relative error ε_{pre} of 0.0003 is used to control the level of accuracy. The absolute error in each element is then compared with a current mean absolute error at each level, based on ε_{pre} , to decide if refinement is required. From **Table 3**, it is clear that the results are nearly the same by using either the variation of potential or the error estimator in the current study, although the implementation of variation of potential is more cost effective. For all the data presented in the present study, mesh refinement based on variation of potential is used throughout the study, unless otherwise specified.

After level-5 refinement, the maximum value of the electric field near the tip

reaches an approximately constant value of 11.323 V/nm. Note that the parallel performance of the PAMR module is not discussed here for brevity purposes but it appears in detail elsewhere [Lain *et. al.*, 2006]. All the cases shown in succeeding sections apply this mesh refinement module for a better resolution near the emitter tip.

2.11 Some Remarks

From the benchmark validations, the developed 3D parallel Poisson's equation solver is verified successfully with and without the source term considering an Neumann boundary condition and Dirichlet boundary condition. The 3D parallel Poisson's solver coupled with PAMR is used in simulating a typical CNT emitter and the results show a good resolution of potential distribution around a very narrow emitter tip. Such an accurate potential distribution usually plays an important role in correctly predicting the emission current from the CNT emitter tip. Parallel speedup performance shows 84% at 32 processors, and a more robust precondition should be implemented in the near future.

Chapter 3

The Parallel Computing of Finite Element Method for Three-Dimensional Magnetostatic Field Problems

As will be shown in later chapter, for simulating the typical DC and RF magnetron plasma, there is usually a permanent magnet system behind the cathode electrode, which has to be simulated before plasma modeling. In general, this magnetic field plays an important role in sustaining magnetron plasma at very low temperature. Thus, the main purpose of developing a parallel magnetostatic field solver is to obtain the magnetic field induced by permanent magnet system. Since both the finite element Galerkin weighted residual method (GWRM) and subdomain-by-subdomain (SBS) method are introduced in previous chapter in detail, in this chapter, we only interest in developing the parallel magnetostatic field solver using the GWRM and SBS coupled with PAMR directly. Some benchmark problems are presented for demonstrating the accuracy and applicability of the parallel magnetostatic field solver. In the end of this chapter, the parallel performances of these solvers are studied and their time breakdown is analyzed.

3.1 Calculation of magnetostatic (MS) Field

For the magnetostatic field problem, the Maxwell's equation is reduced to a vector Poisson's equation as shown as Eqs. (2-6) in the previous chapter. The magnetic vector potential in Eqs. (2-6) is expressed in terms of current density \vec{J} with the following definition,

$$\vec{J} = \nabla \times \vec{M} \quad (3-1)$$

Where \vec{M} is the magnetization vector of permanent magnet. Substituting Eqs. (3-1) into Eqs. (2-6), Eqs. (2-6) yields

$$\frac{1}{\mu} \nabla^2 \vec{A} = -(\nabla \times \vec{M}) \quad (3-2)$$

In Cartesian coordinates, Eqs. (3-2) is equivalent to three scalar Poisson equations:

$$\frac{1}{\mu} \nabla^2 A_x = -(\nabla \times \vec{M})_x \quad (3-3a)$$

$$\frac{1}{\mu} \nabla^2 A_y = -(\nabla \times \vec{M})_y \quad (3-3b)$$

$$\frac{1}{\mu} \nabla^2 A_z = -(\nabla \times \vec{M})_z \quad (3-3c)$$

In general, both \vec{M} and μ can be functions of position. In the following, the same developing steps of GWMR are used for Eqs. (3-3). After employing GWRM, we can obtain the element equation similar to previous Poisson's equation. For the *x-component* element equation,

$$\begin{aligned} & \iiint \left[\left(\frac{\partial N_i^{(e)}}{\partial x} \frac{\partial N_j^{(e)}}{\partial x} \right) + \left(\frac{\partial N_i^{(e)}}{\partial y} \frac{\partial N_j^{(e)}}{\partial y} \right) + \left(\frac{\partial N_i^{(e)}}{\partial z} \frac{\partial N_j^{(e)}}{\partial z} \right) \right] dx dy dz] a_{xj} \\ & = \iiint \left(\frac{\partial M_y}{\partial z} - \frac{\partial M_z}{\partial y} \right) N_i^{(e)} dx dy dz - \iint_A N_i^{(e)} \vec{\tau}_n^{(e)} dA \quad i = 1-4, j = 1-4 \end{aligned} \quad (3-4a)$$

or in matrix form,

$$\begin{bmatrix} K_{11}^{(e)} & K_{12}^{(e)} & \cdots & K_{1n}^{(e)} \\ K_{21}^{(e)} & K_{22}^{(e)} & \cdots & K_{2n}^{(e)} \\ \vdots & \vdots & \cdots & \vdots \\ K_{n1}^{(e)} & K_{n2}^{(e)} & \cdots & K_{nn}^{(e)} \end{bmatrix} \begin{bmatrix} a_{x1} \\ a_{x2} \\ \vdots \\ a_{xn} \end{bmatrix} = \begin{bmatrix} F_1^{(e)} \\ F_2^{(e)} \\ \vdots \\ F_n^{(e)} \end{bmatrix}$$

Where

$$K_{ij}^{(e)} = \frac{1}{\mu} \iiint \left[\left(\frac{\partial N_i^{(e)}}{\partial x} \frac{\partial N_j^{(e)}}{\partial x} \right) + \left(\frac{\partial N_i^{(e)}}{\partial y} \frac{\partial N_j^{(e)}}{\partial y} \right) + \left(\frac{\partial N_i^{(e)}}{\partial z} \frac{\partial N_j^{(e)}}{\partial z} \right) \right] dx dy dz \quad (3-4b)$$

$$F_i^{(e)} = - \iiint \left(\frac{\partial M_y}{\partial z} - \frac{\partial M_z}{\partial y} \right) N_i^{(e)} dx dy dz - \frac{1}{\mu} \iint_A N_i^{(e)} \bar{\tau}_n^{(e)} dA$$

Steps 1-4 and 6 of GWRM are not repeated here, and we only describe the detail in step 5 for **Eqs. (3-3)**.

Step 5: Evaluate the interior load term and boundary flux term of Eqs.(3-4).

The divergence theorem could be written as follows,

$$\iiint (u \nabla \cdot \vec{F}) dv = \iint u \vec{F} \cdot \vec{n} d\Omega - \iiint \nabla u \cdot \vec{F} dv \quad (3-5)$$

with the identity

$$\nabla \cdot (u \vec{F}) = \nabla u \cdot \vec{F} + u \nabla \cdot \vec{F} \quad (3-6)$$

where u is an arbitrary scalar and \vec{F} is an arbitrary vector. After employing

Eqs. (3-5), the interior load integral becomes,

$$\begin{aligned} & \iiint \left(\frac{\partial M_y}{\partial z} - \frac{\partial M_z}{\partial y} \right) N_i^{(e)} dx dy dz \\ & = \iint N_i^{(e)} (\vec{M} \times \vec{n})_x d\Omega - \iiint (\vec{M} \times \nabla N_i^{(e)})_x dx dy dz \end{aligned} \quad (3-7)$$

and the boundary flux term is

$$\frac{1}{\mu} \iint_A N_i^{(e)} \bar{\tau}_n^{(e)} dA = \bar{\tau}_n^{(e)} \frac{\Delta^{(e)}}{3\mu} \quad (3-8)$$

The **Eqs. (3-4b)** can be rewritten with **Eqs. (3-7)** and **Eqs. (3-8)**, and the same manners are handled in y- and z- components. The final forms of element equations of

Eqs. (3-3) are:

x-component:

$$\begin{aligned} & \frac{1}{\mu} \left[\iiint \left(\frac{\partial N_i^{(e)}}{\partial x} \frac{\partial N_j^{(e)}}{\partial x} + \frac{\partial N_i^{(e)}}{\partial y} \frac{\partial N_j^{(e)}}{\partial y} + \frac{\partial N_i^{(e)}}{\partial z} \frac{\partial N_j^{(e)}}{\partial z} \right) dx dy dz \right] a_{x_j} \\ & = - \iint N_i^{(e)} (\vec{M} \times \vec{n})_x d\Omega + \iiint (\vec{M} \times \nabla N_i^{(e)})_x dx dy dz - \vec{\tau}_n^{(e)} \frac{\Delta^{(e)}}{3\mu} \end{aligned} \quad (3-9a)$$


$i = 1-4, j = 1-4$

y-component:

$$\begin{aligned} & \frac{1}{\mu} \left[\iiint \left(\frac{\partial N_i^{(e)}}{\partial x} \frac{\partial N_j^{(e)}}{\partial x} + \frac{\partial N_i^{(e)}}{\partial y} \frac{\partial N_j^{(e)}}{\partial y} + \frac{\partial N_i^{(e)}}{\partial z} \frac{\partial N_j^{(e)}}{\partial z} \right) dx dy dz \right] a_{y_j} \\ & = - \iint N_i^{(e)} (\vec{M} \times \vec{n})_y d\Omega + \iiint (\vec{M} \times \nabla N_i^{(e)})_y dx dy dz - \vec{\tau}_n^{(e)} \frac{\Delta^{(e)}}{3\mu} \end{aligned} \quad (3-9b)$$

$i = 1-4, j = 1-4$

z-component:



$$\begin{aligned} & \frac{1}{\mu} \left[\iiint \left(\frac{\partial N_i^{(e)}}{\partial x} \frac{\partial N_j^{(e)}}{\partial x} + \frac{\partial N_i^{(e)}}{\partial y} \frac{\partial N_j^{(e)}}{\partial y} + \frac{\partial N_i^{(e)}}{\partial z} \frac{\partial N_j^{(e)}}{\partial z} \right) dx dy dz \right] a_{z_j} \\ & = - \iint N_i^{(e)} (\vec{M} \times \vec{n})_z d\Omega + \iiint (\vec{M} \times \nabla N_i^{(e)})_z dx dy dz - \vec{\tau}_n^{(e)} \frac{\Delta^{(e)}}{3\mu} \end{aligned} \quad (3-9c)$$

$i = 1-4, j = 1-4$

After the theoretical development, the boundary conditions are imposed to **Eqs. (3-9)**

and ready be solved using either the precondition conjugated gradient method (PCG)

or the direct matrix package MUMPS. In parallel computing **Eqs. (3-9)**, PCG is used

based on the SBS method, the same description is given in the previous chapter and it

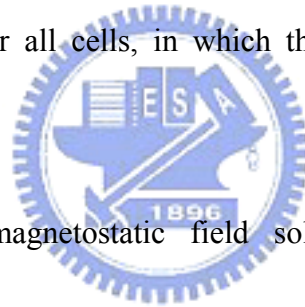
will not be repeated for brevity.

3.2 Coupling of PAMR with Parallel Magnetostatic Field Solver

In the previous chapter, PAMR is described and successfully coupled with the parallel Poisson's equation solver for electrostatic field problems. In the subsection, the same idea is followed for coupling PAMR and current parallel vector Poisson's equation for magnetostatic field problems. Therefore, almost the same developing procedures are given as those for electrostatic field solvers as follows.

The PAMR presented in the previous section can be easily coupled to the current parallel magnetostatic field solvers since both utilize 3-D unstructured tetrahedral mesh and MPI for data communication. One can readily wrap up the PAMR as a library and insert it into the source code of any parallel numerical solver to be used. However, some problems may occur due to memory conflicts between the inserted library and the numerical solver itself that could reduce the problem size one can handle in practice. As such, a simple coupling procedure, written in shell script ([Fig. 3.1](#)) that is standard on all Unix-like systems, can be prepared to link the PAMR and the current parallel magnetostatic field solvers. In doing so, we can keep the source codes intact and without alterations. Indeed, it is especially justified if only a steady state of the physical problem is sought, in which normally only several times of mesh refinement is enough to have a fairly satisfactory solution. Thus, the total I/O time, which is in proportion to the number of couplings in switching between two codes,

can be reduced to a minimum in practical applications. In addition, as shown in [Fig. 3.1](#), after identifying those cells that require refinement before PAMR, the domain is repartitioned based on the new mesh refinement requirements. For example, the weight factors of the cells (vertex in graph theory) are set as eight for those cells which are flagged to be refined; otherwise, they are set as unity. With this distribution of weight factors as the input to ParMetis, an approximate (but rather good) load balancing can be achieved in the PAMR module. Then the magnetostatic field solvers read in the output refined mesh from the PAMR module and partition the new mesh with equal weight factors for all cells, in which the workload is balanced in the magnetostatic field solvers.



The current parallel magnetostatic field solvers along with PAMR are implemented and tested on a PC-cluster system with the Linux OS at the National Center for High-Performance Computing in Taiwan (64-node, dual processor and 8 GB RAM per node). The standard message-passing interface (MPI) is used for data communication. It is thus expected that the current parallel code will be highly portable among the memory-distributed parallel machines that are running with the Linux (or its equivalent) operating system.

3.3 Validation and Parallel Performance of the Magnetostatic Field

Solver

Since the parallel computing of the vector Poisson's equation solver is the same with those techniques for Poisson's equation solver presented in the previous chapter, the only difference of computing procedures is that Poisson's equation has to be solved three times in order to obtain three different component of vector potential. Therefore, we also use the [Fig. 2.9](#) for representing the procedures of parallel vector Poisson's equation solver, and the details of [Fig. 2.9](#) can be found in previous chapter.

Validation of the parallel magnetostatic field solver

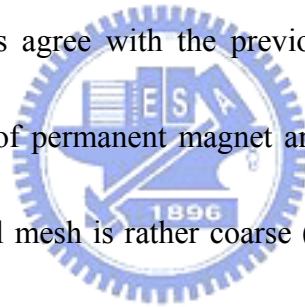
A permanent magnet array made up of eight segments is used to be the benchmark problem for validating the parallel magnetostatic field solver. [Fig. 3.2](#) shows a cross section of the permanent magnet array. There are the experimental data and analytical solution available to this problem, e.g., [\[Leupold et. al., 1993\]](#), [\[Leupold et. al., 2000\]](#), and [\[Halbach, 1980\]](#). The experimental data shows that the magnetic flux density in the center air gap of the permanent magnet array is about 80-90% of the ideal value of analytic prediction. The analytic solution for this system is also given as follows:

$$B = B_R \ln(r_o/r_i) \tag{3-10}$$

Where B_R is the remanence of the permanent magnet, and r_o and r_i are the outer and

inner radii of the permanent magnet array, respectively.

Fig. 3.3 shows the mesh distribution of the permanent magnet array made up of eight segments using 0.63 million elements (~108,840 nodes). And in this simulation, the remanence B_R of the permanent magnet material is 1 Tesla, the relative permeability is 1, the inner radius is 1 inch, and the outer radius is 2.74 inch. After substituting these parameters to **Eqs. (3-10)**, the calculated magnetic flux density in the air gap is expected to be 1 Tesla. The **Fig. 3.4** shows that the simulated magnitude of the magnetic flux density of the permanent magnet array at the center of the air gap is about 0.87 Tesla, which is agree with the previous experimental data. **Fig. 3.5**



shows the mesh distribution of permanent magnet array made up of eight segments using PAMR where the initial mesh is rather coarse (7,845 nodes), while the level-6 mesh is very fine (108,840 nodes) around the permanent magnets array. **Table 4** lists the number of nodes/elements and the corresponding maximal magnitudes of the magnetic flux density of the permanent magnet array at the center of the air gap in the simulation domain at different levels of mesh refinement with the ε_{ref} is set to 0.08 based on the variation of vector potential is used. It also shows that better solution obtained after using PAMR.

Parallel performance of the magnetostatic field solver

The previous validation simulation case is also employed to test the parallel

performance of the current parallel magnetostatic field solver. **Fig. 3.6** illustrates the parallel speedup as a function of the number of processors up to 32. The corresponding time breakdown of various components of the solver along with speedup is similar with the time breakdown of parallel electrostatic solver since they used the same parallel CG matrix solver. And, detailing the analysis on this time breakdown structure is not repeated here. The runtime using a single processor is about 259.86 seconds, while it is reduced to 10.82 seconds using 32 processors, which results in ~ 24.01 of parallel speedup.

3.4 Some Remarks



Following the development steps in previous chapter, the parallel vector Poisson's equation solver is developed and verified successfully using a typical permanent magnet system. When our simulation results compare with the simulation results from commercial software, it especially shows a better resolution in magnetic field distribution since the parallel PAMR module is coupled into the parallel vector Poisson's equation solver. Parallel speedup performance shows 75% at 32 processors, and a more robust precondition should also be implemented in the near future.

Chapter 4

An Overview of the PIC-FEM Method Using an Unstructured Mesh and Its Parallel Implementation

This chapter begins with the introduction to the overview of the conventional Particle-In-Cell and Monte-Carlo method (PIC-MCC), which is a well-known kinetic approach for plasma simulation. Since the conventional PIC-MCC is less flexible in simulating the device with complicated geometric shape when using a structured mesh. Therefore, the first main contribution of this chapter is to develop a PIC-MCC code for especially using an unstructured tetrahedral mesh, named PIC-FEM code. However, the PIC-FEM code with a large number of particles does make the computation become very expensive. For sure, the second main contribution of this chapter is to accelerate the code using the parallel computing technique. In parallel computing of PIC-FEM method, the computational domain is first decomposed in a number of sub-domains, which is equal to the number of processors via the multi-level graph-partitioning library, METIS. Dynamic domain decomposition (DDD) technique is employed for alleviating the load unbalance among sub-domains. Two benchmark problems are presented for demonstrating the accuracy and applicability of the parallel PIC-FEM code. In the end of this chapter, the parallel performance of the PIC-FEM code using DDD is studied and its time breakdown is analyzed in detail.

4.1 General Description of PIC-MCC Method

The PIC-MCC method is the particle method coupling with the Maxwell's equations. The original PIC method without MCC method was developed by plasma physicists, and it mainly be used in simulating the charged particles motion under electromagnetic field. This important theory greatly reduces the computational load in considering that N^2 Coulomb interactions among N particles based on the charge extrapolation and force interpolation. Since PIC does not consider particle collisions, it could be represent as the collisionless Boltzmann equation, i.e., Vlasov's equation [Nanbu, 2000]. The more details of PIC method can be found in Birdsall and Landon's book [Birdsall and Langdon, 1991], Hockey and Eastwood's book [Hockney and Eastwood, 1988], and Birdsall's review [Birdsall, 1991]. Until 1980s, Monte-Carlo collisions method was included in PIC method for modeling the self-sustained plasma discharge [Birdsall, 1991]. In simulating the plasma discharge using PIC-MCC, the cell size should be a fraction of the Debye length in order to resolve the plasma sheath. Moreover, in order to resolve the plasma oscillation, the electron time-step must be one order smaller than $1/(\text{plasma frequency})$.

4.2 The PIC-MCC Procedures

The conventional flowchart of the PIC-MCC scheme is shown as Fig. 4.1. It

shows that after initialization, one time step consists of eight stages as follows:

1. Charge extrapolation to each grid points
2. Calculation of electromagnetic fields
3. Force interpolation to each particle
4. Calculation of motion of each particle
5. Calculation of Monte-Carlo collision of each particle
6. Indexing (or sorting) all the particles
7. Calculation particle reduction
8. Sampling the particles within cells to determine the macroscopic quantities

In order to significantly speedup the simulation, sub-cycling scheme [Brackbill and Cohen, 1985] is used since ion move very slowly in one time step due to it is heavier than electron. In such scheme, after repeating the calculation of stages 1-8, 10 times for Δt_e , we calculate the stages once for Δt_i , thus advancing the system time by Δt_i .

Since step 2 was introduced in chapter 2, the other steps will be given in detail as follows:

4.2.1 Initialization

Before beginning stage 1-8, the data of geometry and simulation conditions should be read in the code. The number of simulated particles of each cell is calculated according to the particle number density and current cell volume. Since plasma is electrically neutral, we have the same initial number of simulated electrons

and ions. The particle velocities are assigned to each particle based on Maxwell-Boltzmann distribution according to the particle velocities and temperature. The positions for each simulated electron are randomly allocated within the cells and the same positions are assigned to the simulated ions.

4.2.2 Force Interpolation and Charge Extrapolation

The same weighting function should be used for force interpolation and charge extrapolation in order to eliminate the self-force and conserves momentum [Birdsall and Langdon, 1991]. For an unstructured mesh, the derived finite element volume coordinate in previous chapter [Santi *et. al.*, 2003] is used to as the interpolation and extrapolation weighting function. The force interpolation and charge extrapolation using volume coordinate are written in Eqs. (4-1) and (4-2), respectively.

$$\rho_i = \sum_k q_k N_i(\vec{r}_k) \quad (4-1)$$

$$\vec{F}_k = q_k \sum_i [\vec{E}_i N_i(\vec{r}_k)] + q_k \vec{v}_k \times \sum_i [\vec{B}_i N_i(\vec{r}_k)] \quad (4-2)$$

where the subscript i represents mesh node properties and subscript k represents particle properties.

4.2.3 Equations of Motion

The leap-frog scheme [Birdsall and Langdon, 1991] is used for solving the equation of motion (see Fig. 4.2), in which scheme is second-order accuracy in time through use of a velocity that is staggered at half time steps relative to the particle position. In addition, this scheme requires minimal storage information of particle

velocity and position since only the updated particle velocity and position are stored.

Eqs.(4-3) and **Eqs. (4-4)** are the particle position and velocity derivatives in finite

difference form with leap-frog scheme, respectively:

$$m \frac{\bar{v}^{n+1/2} - \bar{v}^{n-1/2}}{\Delta t} = \bar{F}^n \quad (4-3)$$

$$\frac{\bar{x}^{n+1} - \bar{x}^n}{\Delta t} = \bar{v}^{n+1/2} \quad (4-4)$$

Where n is the time step counter. The force term in the RHS of **Eqs. (4-3)** can also be

formulated using leap-frog scheme, it yields

$$\frac{\bar{v}^{n+1/2} - \bar{v}^{n-1/2}}{\Delta t} = \frac{q}{m} (\bar{E}^n + \frac{\bar{v}^{n+1/2} + \bar{v}^{n-1/2}}{2} \times \bar{B}) \quad (4-5)$$

Then **Eqs. (4-5)** is ready to be solved using Boris's method [Birdsall and Langdon,

1991]. In this method, the magnetic and electric fields are separated completely after

introducing two new variables into **Eqn. (4-5)**. They are:

$$\bar{v}^- = \bar{v}^{n-1/2} + \frac{q\bar{E}}{m} \frac{\Delta t}{2} \quad (4-6)$$

$$\bar{v}^{n+1/2} = \bar{v}^+ + \frac{q\bar{E}}{m} \frac{\Delta t}{2} \quad (4-7)$$

After substituting **Eqs. (4-6)** and **Eqs. (4-7)** into **Eqs. (4-5)**, **Eqs. (4-5)** becomes

$$\frac{\bar{v}^+ - \bar{v}^-}{\Delta t} = \frac{q}{m} (\bar{v}^+ + \bar{v}^-) \times \bar{B}^n \quad (4-8)$$

Therefore, from **Eqs. (4-6)** to **(4-8)**, the main ideas of Boris's method can be

explained that \bar{v}^- is obtained after adding the half of the electric impulse to the

initial velocity via **Eqs. (4-6)**. Then \bar{v}^+ is obtained after rotating \bar{v}^- with magnetic

field via **Eqs. (4-7)**. Finally, the updated velocity $\bar{v}^{n+1/2}$ can be obtained after adding

the half of the electric impulse to \bar{v}^+ via **Eqs. (4-8)**. The detail of this method is also can be found in Birdsall's book [[Birdsall and Langdon, 1991](#)].

4.2.3.1 Particle Ray Tracing

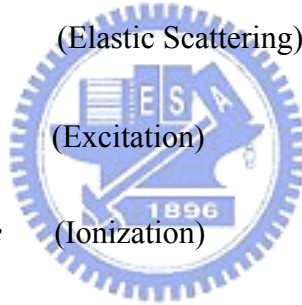
There are two different methods for particle ray tracing, which are *cell-by-cell* and *coordinate* particle tracking for an unstructured mesh, respectively. For an unstructured mesh, the cell-by-cell particle tracking takes the advantage of cell connectivity provided by the unstructured mesh data [[Tseng, 2005](#)]. The first step of the particle tracing is to determine whether the particle will across if the particle will stay in or leave the current cell. If the particle leaves, then the second step is to determine the intersection point on the intersecting face. Further journey of the particle depends on the face condition. If it is the normal face between cells, then it will continue its movement until the time step ends. If the intersection face is an I/O or specified boundary, the particle will be removed. If not, then process the interaction according to the wall boundary conditions. The more details of this particle tracking can be found elsewhere [[Tseng, 2005](#)].

4.2.4 Monte Carlo Collision Algorithm (MCC)

In order to simulate a self-sustained and self-consistent plasma discharge, the dominant reactions between species should be considered properly. Since we use argon gas for plasma discharge, the simulation species are electron (e), ion (Ar^+), and

ground state atom (Ar). In general, there are three different collision algorithms for these plasma species (see [Fig. 4.3](#)) [Nanbu, 2000], which are short-range collision between unlike particles, short-range collision between like particles, and Coulomb collisions. For the low-temperature plasma, the plasma density is usually less than $10^{17} m^{-3}$, the Coulomb collisions are all negligible. Moreover, argon gas is assumed in equilibrium and at rest, the short-range collision between like particles are also negligible in current work. Therefore, totally five reactions in the argon Monte Carlo collision which are listed as follows,

- (1) $e + Ar \rightarrow e + Ar$ (Elastic Scattering)
- (2) $e + Ar \rightarrow e + Ar^*$ (Excitation)
- (3) $e + Ar \rightarrow e + Ar^+ + e$ (Ionization)
- (4) $Ar^+ + Ar \rightarrow Ar + Ar^+$ (Charge Exchange)
- (5) $Ar^+ + Ar \rightarrow Ar^+ + Ar$ (Elastic Scattering)



In general, there are two methods for treating $e-Ar$ and Ar^+-Ar collisions, which are null-collision method and Nanbu's method. Since only one random number used in Nanbu's method [Vahedi and Surendra, 1995], it makes collision computation becomes more efficient than using the typical null-collision method, and Nanbu's method is very simple and straightforward in treating such collisions. For treating the $e-Ar$ collision using this method, the total collisional probability (P_T) is written as

$$1 = P_T + (1 - P_T) = \sum_{k=1}^K [P_k + (\frac{1}{K} - P_k)] \quad (4-9)$$

Where P_k is probability of the k th collisional event,

$$P_k = N_g v \sigma_k(\varepsilon) \Delta t_e \quad (4-10)$$

Then one can sample a collisional event k randomly

$$k = 1 + UK \quad (4-11)$$

and evaluate P_k at the energy ε of the electron. The k th collisional event occurs when $U > (k/K) - P_k$, otherwise the collisional event not occurs (as shown in [Fig. 4.4](#)).

This method is also used for treating the $Ar^+ - Ar$ collisions. In the following,

each collisional event in the electron-molecule and ion-molecule collision is described

briefly. The more detailed theory can be found in Ref. [\[Vahedi and Surendra, 1995\]](#).

4.2.4.1 Electron-Molecule Collision

The electron-molecule collision cross sections are the same as the ones used by Nanbu [\[Nanbu, 2000\]](#) as shown in [Fig. 4.5](#). The only difference is we averaged 26 elastic collisions into one for fitting cross section data easily. When a elastic collision occurs, the incident electron scatters through an angle χ which is computed follows the formulation in Ref. [\[Vahedi and Surendra, 1995\]](#). It is

$$\cos \chi = \frac{2 + \varepsilon - 2(1 + \varepsilon)^R}{\varepsilon} \quad (4-12)$$

where R is the random number and ε is the energy of the incident electron. The [Eqs. \(4-16\)](#) also holds for determining electron scattering angle for all types of

electron-neutral collisions. Since the azimuthal scattering angle ϕ , is uniformly distributed on the interval $[0, 2\pi]$, and is determined by

$$\phi = 2\pi R \quad (4-13)$$

where R is the random number. Once χ and ϕ are obtained, the direction of the scattered velocity (as shown in **Fig. 4.6**) is determined by [Vahedi and Surendra, 1995]

$$\vec{v}_{scat} = \vec{v}_{inc} \cos \chi + \vec{v}_{inc} \times \vec{i} \frac{\sin \chi \sin \phi}{\sin \theta} + \vec{v}_{inc} \times (\vec{i} \times \vec{v}_{inc}) \frac{\sin \chi \cos \phi}{\sin \theta} \quad (4-14)$$

Where θ is given by $\cos \theta = \vec{v}_{inc} \cdot \vec{i}$, \vec{v}_{inc} and \vec{v}_{scat} are unit vector parallel to the incident and scattered velocities, respectively. Then the scattered velocity components can be determined by taking the projection of \vec{v}_{scat} on the coordinates axes. In an excitation collision, the incident electron loses the excitation threshold energy of 11.55eV and is scattered through an angle χ determined by **Eqs. (4-12)**.

In an ionizing event, the incident electron strips an electron off the neutral, and the neutral becomes an ion, continuing on its trajectory virtually undisturbed. The energy balance equation with this assumption, it yields

$$\mathcal{E}_{scat} + \mathcal{E}_{ej} = \mathcal{E}_{inc} - \mathcal{E}_{ion} \quad (4-15)$$

$$\mathcal{E}_i = \mathcal{E}_N \quad (4-16)$$

Where \mathcal{E}_{scat} , \mathcal{E}_{ej} and \mathcal{E}_i are energies of the scattered, ejected and incident electrons, respectively. \mathcal{E}_{inc} and \mathcal{E}_N are the energies of the created ion and the target neutral

atom, and ε_{ion} is the ionization threshold energy. The energy of the incident electron is given by

$$\varepsilon_{ej} \approx R\left(\frac{\varepsilon_{inc} - \varepsilon_{ion}}{2}\right) \quad (4-17)$$

Then energy of the scattered electron is obtained from [Eqs. \(4-15\)](#). After the energy assignment, each of the scattered and ejected electrons scatters through angles χ and φ determined by [Eqs. \(4-12\)](#) and [\(4-13\)](#), respectively. From the [Eqs. \(4-16\)](#), the velocity of the created ion is calculated from 3V Maxwellian distribution at the molecule temperature.

4.2.4.2 Ion-Molecule Collision

[Fig. 4.7](#) shows the ion-neutral cross sections we used in the model. In a simple charge exchange collision, an electron is assumed to hop from the neutral onto the ion. Therefore, the velocity of the new ion is assigned with the velocity of the incident neutral and the new neutral takes the velocity of incident ion. The hard-sphere collisions assumption is used in treating the ion-neutral elastic scattering collision.

And the energy of the scattered ions are determined by [\[Vahedi and Surendra, 1995\]](#)

$$\varepsilon_{scat} = (1 - \alpha_L)\varepsilon_{inc} \quad (4-18)$$

Where ε_{inc} and ε_{scat} are the energies of the incident and scattered ions, respectively.

The energy loss factor, α_L , is given by

$$\alpha_L = \sin^2 \chi \quad (4-19)$$

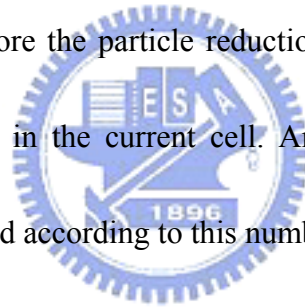
where χ is the scattering angle in the laboratory frame which is determined by

$$\cos \chi = \sqrt{1-R} \quad (4-20)$$

Where R is the random number. The azimuthal scattering angle φ is determined with [Eqs. \(4-13\)](#).

4.2.5 Indexing

The location of the particle after movement with respect to the cell is important information for particle reduction. The relations between particles and cells are reordered according to the order of the number of particles and cells using a simple algorithm [\[Tseng, 2005\]](#). Before the particle reduction, the removed particle will be chosen by a random method in the current cell. And the number of the removed particle can be easily determined according to this numbering system.



4.2.6 Particle Reduction

For simulating plasma discharge, the number of simulated particles usually increases rapidly due to ionization, which makes computational load become very heavy. In this case, speedup, particle reduction technique should be employed with switching the particle weighting factor in order to speed up the code, e.g., [\[Nanbu, 2000\]](#), [\[Shon et. al., 2001\]](#). The particle reduction technique we used is the improvement of Nanbu's particle reduction technique [\[Nanbu, 2000\]](#). The main idea of this technique is given as follows.

When the current number of ion ($N_i(t)$) is equal to 1.2 times the initial number of ion ($N_i(0)$), the particle weighting function is increased from initial weighting function (W_0) to $1.2W_0$ by removing excess sampled particles cell by cell. The numbers of sampled particles in a cell are chosen in proportion to their number density in each cell. This procedure is repeated whenever $N_i(t)$ exceeds $N_i(0)$. However, it is clear that this particle reduction has no effect on charge density distribution and the number of real electron is also unchanged before and after switching.

4.2.7 Data sampling

A steady state of the plasma system is reached by monitoring the total numbers of particle in the computational domain. Once a steady state is reached; we can obtain the data with small statistical fluctuations by time-averaging a set of temporal data sampled for equal time interval. The data for the electron density, ion density, charge density, electric potential, and electric field, are sampled at the grid points. And, the electron temperature, ion temperature, and electron energy distribution function are sampled in each cell.

4.3 Parallel computing of PIC-FEM method

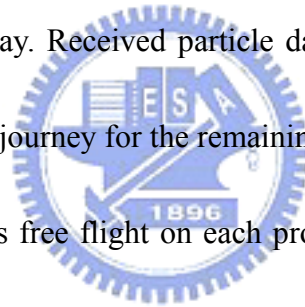
Since the computational domain has been partitioned using multi-level graph partitioning tool, the PIC-MCC is then ready for paralleling under single-instruction

multiple-data (SIMD) paradigm. Under SIMD paradigm, the PIC-MCCC code is executed in serial on its own sub-domain. Communications are required when particle meets the inter-processor boundary (*IPB*) and also in field solver. High parallel performance can only be achieved if communication is minimized and the computational load is evenly distributed among processors. Therefore, dynamic load balancing (DDD) technique should be used to re-partition the domain using the weights base on the number of particle in each domain when load becomes unbalance. The reason for selecting the number of particle as the weight for DDD is that the particle computation is the most expensive component of PIC-MCC.

4.3.1 The Parallel PIC-FEM Method

Fig. 4.8 and 4.9 shows a simplified flowchart of the parallel PIC-FEM method proposed in the current study. A converter should be designed for preprocessing the mesh (grid) data obtained from the domain decomposition and for proving a processor neighbor-identifying array. The main function of this converter is to reorder the fully unstructured mesh data into the *globally sequential but locally unstructured* mesh data for obtaining he relationship between global and local cell data by a simple arithmetic operation due to this special cell-numbering design [Tseng, 2005]. In addition, the node numbers of each sub-domain are must re-ordered follow the requirement for FEM SBS method. Except for parallel computing of FEM, most of the particle computation follows the experience from the previous parallel DSMC method [Tseng, 2005].

Again referring to [Fig. 4.8](#), the master processor first reads in the preprocessed mesh data and then distributes it to all other processors. Once all preprocessor has the information of mesh data, the PIC-MCC code is executed in serial on its own processor. After force interpolation, particle starts to move and be tracked using cell-by-cell. When particle meets the IPB during its journey within a simulation time step, the particle related data is then stored into a buffer array and are numbered sequentially for considering communication efficiency [[Tseng, 2005](#)]. After all the particles in a processor are moved, a local communication among processor is occurred for communicating the buffer array. Received particle data are then unpacked and each particle continues to finish its journey for the remaining time step.



After all particles finishing its free flight on each processor, the program carries out the Monte-Carlo collisions, indexing the particles, extrapolating the charges and solving the field equations in parallel. The particles in each cell are then sampled at the appropriate time.

4.3.2 Dynamic Domain Decomposition (DDD)

For reaching the high parallel performance during simulation, the computational load should be balanced properly when the load becomes unbalance since particle moves very frequency through sub-domains. This dynamic load balance is achieved by employed the dynamic domain decomposition technique (DDD). The DDD technique we used is an improvement of previous method in DSMC [[Tseng, 2005](#)].

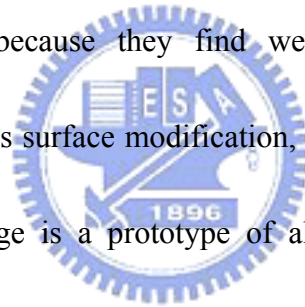
The flowchart of parallel PIC-FEM method with DDD technique is shown as [Fig. 4.10](#). It shows that there are three main processes in DDD, which are repartition the domain, cell/particle migration, and node re-ordering. In the following, these main processes of this technique will be given and the details also can be found elsewhere [\[Tseng, 2005\]](#).

The main idea of the dynamic domain decomposition technique is to repartition the computational domain using the multi-level graph-partitioning library ParMetis [\[Karypis et. al., 1998\]](#). The library ParMetis is the parallel version of library METIS which are also developed by University of Minnesota. In parallel PIC-FEM simulation, the workload of each processor is approximately proportional to the number of particles in the corresponding sub-domain. Thus, the weight of each vertex for graph-partitioning library is assigned using number of particle in the corresponding cell. After repartitioning the domain based on this weight, a fairly particle distribution among processors is obtained. Once the domain has been repartitioned, the relationship for cell and sub-domain will be updated via cell and particle migration technique [\[Tseng, 2005\]](#). The main idea of this technique is that the to-be-transferred particle related and cell related data on each processor are packed into the corresponding buffer array and migrate these arrays into a whole array. Then local communication is occurs for this to-be-transferred array between sub-domains.

For the sub-domain in this communication, the array is unpacked and then updates the particle and cell related relationship. Finally, node re-ordering on internal and interfacial nodes is carried out (as shown in [Fig. 4.11](#)) for the requirement of parallel FEM using SBS method.

4.4 Validation of the Parallel PIC-FEM Method

For validating the PIC-FEM code, two benchmark problems are presented, which are the quasi one-dimensional DC and RF gas discharge plasma. Gas discharge plasmas are benchmarked because they find well-established use in practical industrial applications, such as surface modification, lasers, lighting, etc. In addition, one-dimensional DC discharge is a prototype of all discharge simulation. Before simulating these plasma systems, the elementary gas discharge plasma physics is introduced. Then, the simulation conditions are described and the results are compared with experimental data and previous simulation wherever available.



4.4.1 Quasi One-dimensional DC Gas Discharge Plasma

A schematic picture of the elementary glow discharge processes is presented in [Fig. 4.12](#). When a constant potential difference is applied between the cathode and anode, the ions are accelerated by the electric field in front of the cathode sheath and collide with the cathode electrode. Then the secondary electrons are emitted from the

cathode electrode, which are accelerated toward bulk region by electric field in front of the cathode sheath and collide with neutral species. This leads to many important collisions for sustaining plasma, such as ionization, excitation, elastic scattering, etc. It is clear that the secondary electrons emission play an essential role for sustaining the DC gas discharge plasma. The main structure of the DC glow discharge plasma is shown in [Fig. 4.13](#). It shows that there are many regions in DC glow discharge plasma, which are cathode dark space (CDS), negative glow (NG), Faraday dark space (FDS), the positive column (PC), and anode zone (AZ). However, when the distance between cathode and anode is short, there are only CDS, NG, and AZ formed in DC glow discharge plasma [[Bogaerts et al., 2002](#)]. Here, the mechanism of each region is not described in detail for the brevity purposes.



Simulation Conditions

Consider the discharge sustained between two parallel electrodes by 40mm under an operation argon pressure of 42mtorr . The cathode and anode potentials are set to -1000Volts and 0Volts , respectively. The computational domain is divided with the cell size 0.2mm ($\approx \lambda_D$) using an unstructured mesh. Initially, the spatial distributions of the ion and electron number densities are assumed uniform to each other. The electron timestep is $0.5 \times 10^{-10}\text{s}$ and the number of sub-cycling is 10. The particle velocities are sampled from the Maxwellian distribution at a corresponding

temperature, e.g., $T_i = 232 K$ for ions and $KT_e = 0.5 eV$ for electrons, where K is the Boltzmann constant. The secondary electron emission coefficient is 0.3. The initial velocity of the emitted electrons is assumed to be zero. The ions and electrons incident on the solid surfaces are always neutralized.

Simulation Results

The potential and electric field are shown in [Fig. 4.14\(a\)](#) and [Fig. 4.14\(b\)](#), respectively. The plasma potential is nearly constant and slightly positive ($\approx 10V$) and hence, the electric field is very small in the bulk region. The ion and electron number densities are shown in [Fig. 4.15](#). The net charge density is shown in [Fig. 4.16](#).

One can easily recognize the cathode and anode sheaths. The ion and electron kinetic energies are shown in [Fig. 4.17](#). Ions are rapidly accelerated in the sheath, reaching a velocity of about $10^4 m/s$ before impinging on the cathode. The ion energy distribution function (IEDF) onto the cathode surface has been sampled in the course of simulation as shown in [Fig. 4.18](#). IEDF is falling off exponentially with energy, which demonstrates a good match with the theoretical predictions, e.g., [\[Serikov. and Nanbu, 1997\]](#), and [\[Abril et. al., 1983\]](#).

4.4.2 Quasi One-dimensional RF Gas Discharge Plasma

When one or both of the electrodes are non-conductive materials, the electrodes should be applied with an alternating voltage. The frequency of the alternating

voltages is typically in the radio-frequency (RF) range with a most common value of 13.56 MHz. With this applied alternating voltage, each electrode will act alternately as the cathode and anode in order to eliminate the charge accumulation on insulator electrodes. For RF gas discharge plasma, the electrons will follow the instantaneous electric fields, however, the ions can only follow time-averaged electric fields produced by the applied RF frequency. This totally different behavior can be easily explained by the different masses of ions and electrons.

Simulation Conditions

Consider the discharge sustained between two parallel electrodes by 20mm under an operation argon pressure of 50mtorr. The cathode potential is in the following,

$$\phi = -V_{rf} \cos 2\pi ft \quad (4.21)$$

Where f is the frequency, $V_{rf} = 500Volts$ is the amplitude. The conventional frequency is 13.56MHz. The computational domain is divided with the cell size 0.1mm ($\approx 0.5\lambda_D$) using an unstructured mesh. Initially, the spatial distributions of the ion and electron number densities are assumed uniform to each other. The electron timestep is $3.695 \times 10^{-11}s$ and the number of sub-cycling is 10. The particle velocities are sampled from the Maxwellian distribution at a corresponding temperature, e.g., $T_i = 232K$ for ions and $KT_e = 0.5eV$ for electrons, where K is the Boltzmann constant. The secondary electron emission coefficient is 0. The ions

and electrons incident on the solid surfaces are always neutralized.

Simulation Results

The potential are shown in **Fig. 4.19**. The plasma potential is nearly constant and positive ($\approx 0.5V_{rf}$) and hence, the electric field is very small in the bulk region. The ion and electron number densities are shown in **Fig. 4.20**. One can easily recognize the cathode and anode sheaths. The ion and electron kinetic energies are shown in **Fig. 4.21**. The electron energy probability function (EEPF) of two different pressures in the bulk region has been sampled in the course of simulation as shown in **Fig. 4.22**. In **Fig. 4.22(a)** (50 mtorr), EEPF shows a weakly bi-Maxwellian distribution ($T_L=1.58$ eV, $T_H=2.58$ eV), while **Fig. 4.22(b)** (20 mtorr) shows strong bi-Maxwellian distribution ($T_L=0.833$ eV, $T_H=3.264$ eV), which is comparable with previous studies under similar simulation conditions, e.g., [Godyak *et. al.*, 1992], [Mahony *et. al.*, 1999], [Raizer *et. al.*, 1995], [Turner *et. al.*, 1993], and [Vahedi *et. al.*, 1993]. At low pressures the bi-Maxwellian EEPF revealing the stochastic electron heating mechanism, leading to the formation of cold bulk and oscillating hot tail electrons, which demonstrates a good match with the experimental data.

4.5 Parallel Performance of the Parallel PIC-FEM Method Using Dynamic Domain Decomposition

In order to study the parallel performance of the current parallel PIC-FEM code using DDD, the three-dimensional RF gas discharge plasma with different numbers of particle is used as the test problem. This parallel performance is studied using 32 processors on the HP IA-64 clusters at National Center for High-performance Computing (NCHC), which is a memory-distributed machine. In the following, the simulation conditions, dynamic domain decomposition, parallel performance, and time breakdown analysis of the parallel PIC-FEM code with DDD is presented in turn.

Simulation Conditions

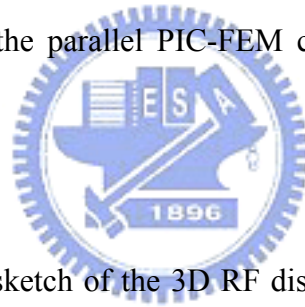


Fig. 4.23 illustrates the sketch of the 3D RF discharge plasma. Considering the discharge sustained between two parallel circular electrodes in a grounded cylindrical chamber by 20mm under an operation argon pressure of 50mtorr. **Eqs. (4.21)** is used for the cathode potential with $V_{rf} = 500V$ and $f = 13.56\text{MHz}$. The computational domain is divided using an unstructured mesh ($\sim 165,000$ cells). Initially, the spatial distributions of the ion and electron number densities are assumed uniform to each other. The electron timestep is $3.695 \times 10^{-11} s$ and the number of sub-cycling is 10. The particle velocities are sampled from the Maxwellian distribution at a corresponding temperature, e.g., $T_i = 232 K$ for ions and $KT_e = 0.5 eV$ for electrons,

where k is the Boltzmann constant. The secondary electron emission coefficient is 0. The ions and electrons incident on the solid surfaces are always neutralized. In addition, two different numbers of particles are considered for simulation, which are 10 particles per cell and 40 particles per cell.

Parallel Performance

Results of parallel speedup and efficiency of the 3D RF gas discharge plasma computation, with different numbers of particle, as a function of the number of processors are presented in **Fig. 4.24**. In **Fig. 4.24**, there are five curves with circle, square, diamond and triangle symbols with respect to static domain decomposition (SDD), dynamically domain decomposition (DDD) at intervals of $1500\Delta t$ with different numbers of particles. And the linear dash line with square symbol represents the ideal case. As expected, the parallel performance of those using dynamic domain decomposition is much better than those using static dynamic domain decomposition. Several trends for different numbers of particle are described in detail as follows.



10 Particles per Cell

Linear speedup occurs clearly for number of processors less than or equal to 10 is shown in **Fig. 4.24**. However, the efficiency decreases with increasing number of processors (up to 32) as expected, due to heavy FEM solver communication among processors and particle load unbalance, if only the static domain decomposition is

applied. As the number of processors increases over 10, FEM begin to play a more important role than the particle load unbalance. Thus, the parallel efficiency decreases monotonously with increasing number of processors (up to 32) even if dynamic domain decomposition is used. However, for the this problem the parallel efficiency using dynamic domain decomposition improves appreciably in the range of 5-10%, as compared with static domain decomposition.

40 Particles per Cell

Similarly, linear speedup exists for this problem up to 10 processors, if static domain decomposition is activated (see [Fig. 4.24](#)). However, the quasi-linear speedup (up to 28 processors) is seen if the dynamic domain decomposition is deactivated, which demonstrates the effectiveness of implementing dynamic domain decomposition in particle load unbalance. However, as the number of processors is over 28, this quasi-linear speedup decreases due to increasing FEM solver communication among processors. For this problem, parallel performance using dynamic domain decomposition is generally improve 10-30% parallel efficiency than that using static domain decomposition as the number of processors is less than or equal to 32. Note that approximately 85% of parallel efficiency can be reached at processor numbers of 64 for this problem.

Typical evolutions of dynamic domain decomposition using graph-partitioning

technique are shown in [Fig. 4.25](#). METIS used to form the initial partition by assigning the unitary weight on each vertex, and ParMetis is used to repartition at constant time interval. It is clear that region covered by each sub-domain (processor) changes as the simulation proceeds due to repartitioning among processors when the initial size of each domain is approximately the same. There exists a smallest sub-domain in the middle of the camber due to the presence of highest density in this region (see [Fig. 4.25](#)). In addition, the size of the sub-domains near the electrodes is generally larger as compared with others due to the rarefied conditions caused by the sheath potential. It clearly demonstrates that the current implementation of dynamic domain decomposition is very effective in dealing with such plasma system.



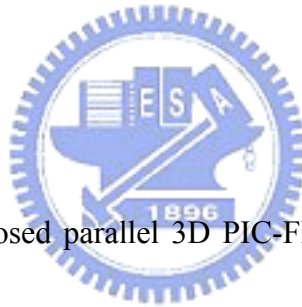
Time Breakdown Analysis

[Fig. 4.26](#) illustrates the typical fraction of time spending in PIC-FEM computation and dynamic domain decomposition of 32 processors. It can be seen that, for the both problem the cost of repartition is very small and can be neglected by comparing with “useful” PIC-FEM. For problem of 10 particles per cell, the average fraction of time spending in FEM solver is larger than the fraction time for the particle movement. This explains the rapid decrease of parallel efficiency at this condition even if using dynamic domain decomposition for load balance (See [Fig. 4.24](#)). Fraction time for parallel communication (is almost proportional to FEM solver)

among processors is large in PIC-FEM, which causes the parallel efficiency increase dramatically with the number of processors.

On the contrast, for the problem of 40 particles per cell, the fraction of time for particle movement is larger than the fraction of time for FEM solver. For this problem, parallel efficiency using dynamic domain decomposition could be generally improved 10-30% than that using static domain decomposition as the number of processors is less than or equal to 32. This shows the current parallel PIC-FEM method may be scalable at least for the large numbers of particles.

4.6 Some Remarks



In this chapter, the proposed parallel 3D PIC-FEM code using an unstructured mesh with DDD mainly follows the major steps of conventional PIC-MCC code in order to keep first principal and self-consistent approach. This code has successfully been verified in simulating quasi-1D DC and RF gas discharge plasma since the results agree with the previous studies very well. Parallel speedup of PIC-FEM shows that better speedup is performed with larger number of particles in both SDD and DDD cases. And, when the number of particles is fixed, DDD performed better speedup than SDD. The reasons were clearly explained from the detailed time breakdown analysis.

Chapter 5

Applications to Realistic Problems

In this chapter, the proposed parallel 3D PIC-FEM code is used to simulate three different realistic problems. They are: 3D field emission display (FED), 3D DC/RF gas discharge plasma, and 3D DC/RF magnetron plasma. The backgrounds of these studying cases can be found in the chapter 1 of this thesis, here, we only interest in the simulation work using PIC-FEM code. In simulating FED, Monte-Carlo collision module does not take into account since the gas pressure is very low. When the space-charge effect is ignored, only parallel Poisson's equation solver is used to solve the electrostatic field once, the particles are then moved and collected when on the anode surface. Two studying cases of FED simulation without considering space-charge effect are presented. However, whenever there is a high charge density distribution in FED cell, space-charge effect has to be considered properly, and a studying case is simulated and compared with the experimental data. In simulating 3D DC and RF gas discharge, the simulation conditions is similar with those in previous 1D simulation work, the main different is the computational domain is pure 3D, which is close to the geometry of practical plasma chamber. From the results, one can clearly see the important 3D geometry effect on spatial distribution of plasma

macroparameter. In simulating 3D DC and RF magnetron plasma, two concentric cylindrical magnets behind the cathode, which is used to confine electrons for providing higher ionization rate. Therefore, before plasma simulation, this magnetic field induced by the permanent magnets has to be solved in advance using vector Poisson's equation solver. Once the magnetic field is obtained, and then the following simulation work is similar with those in 3D DC/RF gas discharge. Different cases with different magnetization (\mathbf{M}) and different secondary electron emission coefficient (γ) on the spatial distribution of plasma macroparameter are studied.

5.1 Simulation on Field Emission Display (FED)

In this section, FED is simulated using the PIC method without considering space charge-effect and with considering space-charge effect in turn. Thus a completed parallel Poisson's equation solver with parallel adaptive mesh refinement is used to compute the electric field distribution of a CNT-based field emitter without considering space-charge effect as the first simulation case.

The generally accepted Fowler-Nordheim theory [Fowler and Nordheim, 1928] for a clean metal surface relates the field emission's current density, J , to the electric field at the tip surface of the emitter, E , in volts/nm and the work function of the emitter, ϕ , in electron volts (eV) by the equation,

$$J = \frac{AE^2}{\phi t^2(y)} \exp\left(-B \frac{\phi^{3/2}}{E} v(y)\right) \text{ Ampere/cm}^2, \quad (5-1)$$

where

$$A = 1.5414 \times 10^{-6}, \quad (5-2)$$

$$B = 6.8309 \times 10^7, \quad (5-3)$$

$$y = 3.79 \times 10^{-4} E^{1/2} / \phi. \quad (5-4)$$

and y is the image charge lowering the contribution to the work function. The functions $t(y)$ and $v(y)$ are approximated by $t^2(y) = 1.1$, $v(y) = 0.95 - y^2$.

5.1.1. FED Simulation Without Space-Charge Effect

The Electron trajectory from the emitter surface to the anode surface is traced on the unstructured mesh based on the computed electric field distribution from the Poisson's equation solver, by using the cell-by-cell particle tracking technique. The current density is then computed as the time average of the accumulated charges due to electron flow reaching the anode surface. In the following, two different cases are studied. The first studying case is to predict the FED emission current and investigate the spatial distribution of electron trajectory under different applied voltages. The second studying case is to add the external uniform magnetic field into FED to demonstrate the focus-ability and FED emission current are also strongly influenced by the magnetic field.

Case I

Fig. 5.1 depicts the simulation domain for a typical CNT triode-type field emitter within a periodic cell. Only $\frac{1}{4}$ of the full emitter is used due to the intrinsic symmetry with Neumann boundary conditions applied at all symmetric planes. Important geometrical conditions (also summarized in part in **table 5**) include a tip radius of 10 nm, an emitter height of 600 and 400 nm, a distance of 0.5 μm between the gate and the cathode, a gate radius of 0.5 μm above the emitter, a distance of 50 μm between the anode and the cathode, a thickness of the gate of 0.2 μm , and the half width of each cell measuring 25 μm . The applied voltage of the gate ranges from 110 to 190 volts, while the cathode and anode are grounded and applied with 400 volts, respectively. The refined final number of nodes used for the simulation is approximately 90,000. The typical results of the predicted potential distribution along with electric field distribution (gate voltage=150 volts, height= 600 nm) are shown in **Fig. 5.2a** and **Fig. 5.2b**, respectively. The maximal value of the electric field can reach up to ~ 11.47 V/nm at the emitter tip when the gate voltage is 150 volts.

The predicted current and voltage data with an emitter height of 600 nm are presented in Fowler-Nordheim format in **Fig. 5.3**, with an anode voltage of 400 volts. It is clear that the computed I-V data follow the Fowler-Nordheim law very well as the gate voltage varies from 110 to 160 volts. The fitted field enhancement factor

$(\beta = E \frac{d}{V})$ is 26.1, where V is the applied cathode voltage, and d is the vacuum gap in the field emission diode configuration. The corresponding electron trajectories are illustrated in **Fig. 5.4** at two different gate voltages (110 and 160 volts) with a height of 600 nm. The results show that the spreading angle of electrons from the tip increases with the increasing gate voltage. This is attributed to the fact that the area of the tip surface which has a larger local electric field increases as the applied voltage increases, which results in the greater emission of electrons from the side of the emitter near the tip. As will be shown later, adding a focusing gate can help to effectively reduce the spreading angle.

The effects of CNT height and gate voltage to the emission current under an applied voltage of 400 volts are presented in **Fig. 5.5**, with the CNT measuring 400 and 600 nm, respectively. The results show that the turn-on voltage increases with the decreasing height of the CNT emitter. Also, the emission current increases dramatically with the given CNT height. This is reasonable since the larger the height of the CNT, the larger the local electric field which results at the tip surface (shorter anode-cathode distance with the same voltage difference), which in turn induces greater emission of electrons.

Fig. 5.6 shows schematically the same field emitter as shown in **Fig. 5.1** with an additional focusing gate in-between the gate electrode and anode. Most geometrical

conditions (also summarized in part in [table 6](#)) are the same as those in [Fig. 5.1](#), except for the distance between the focusing electrode and the gate electrode measuring $0.5\ \mu\text{m}$, the thickness of the focusing electrode measuring $0.2\ \mu\text{m}$, and the radius of the hole in the center of the focusing electrode which is $1.5\ \mu\text{m}$. Similar to that in the previous case without the focusing gate, only $\frac{1}{4}$ of a periodic cell is used for the simulation. [Fig. 5.7b](#) to [Fig.5.7d](#) present a comparison of the focusing effects of electron trajectories using different focusing electrode voltages (5, 0, -5 volts). Likewise, data involving the absence of focusing electrode are presented for the purpose of comparison ([Fig. 5.7a](#)). The results show that the addition of a focusing electrode above the gate electrode can effectively reduce the spreading angle of the electron trajectories, which can possibly increase the resolution and the intensity at the anode. Among the cases simulated, focusing the electrode with 5 volts represents the best choice in focusing the electron flows at the anode.

Case II

Another simulation case for parallel Poisson's equation solver is the magnetic focusing structure consists of a solenoid (or a permanent magnet) outside of the FE device, as shown in [Fig. 5.8](#), which is used to induce the tunable magnetic flux density (B_z), which is assumed uniformly in space. A $\frac{1}{4}$ simulation domain of a single gated cathode structure is shown in [Fig. 5.9](#), while a typical final adaptive

refined mesh (91930 nodes) is shown in **Fig. 5.10**. Important geometrical conditions include a tip radius of 10 nm, emitter height of 600 nm, distance of 0.5 μm between the gate and the cathode, gate radius of 0.5 μm above the emitter, distance of 900 μm between the anode and the cathode, thickness of the gate of 0.2 μm , and the half width of each cell measuring 300 μm . The applied voltage of the gate ranges from 50 to 120 volts, while the cathode and anode are grounded and applied with 1,000 volts, respectively.

Without the externally applied magnetic focusing field, the simulated anode current versus gate voltage (I-V) curve is shown in **Fig. 5.11**, which displays a turn-on voltage of approximate 95V. Note the turn-on voltage is defined as the gate voltage at which the current to anode is 1 μA . The anode current plotted in Fowler-Nordheim coordinate (FN plot) is also shown as an inset to **Fig. 5.11**. The linearity of FN plot clearly shows that the computed I-V data follow the Fowler-Nordheim model very well. The corresponding electron snapshots and trajectories with the gate voltage of 120 V are illustrated in **Fig. 12 (a)**, which will be explained shortly.

Furthermore, we simulate the electron trajectories considering the presence of the externally applied downward magnetic field in the range of 0-1 Tesla to study influence of magnetic field to the electron focusing. In **Fig. 12 (a)~(d)** several 3-D

electron snapshots and trajectories are presented at the gate voltage of 120V, the anode voltage of 1kV, and the different magnetic flux density of 0T, -0.2 T, -0.5T, -1T, respectively. Based on the simulated electron trajectories, the maximum diameter of beam spot on the anode plane can be estimated. The dependence of electron beam diameter on the magnetic flux density is shown in [Fig. 5.13](#), which demonstrates an Airy-function like structure. It is clear that the electron beam diameter rapidly decreases from 500 μm down to less than 100 μm as the magnetic flux density increases from zero to $\sim 0.3\text{T}$. At $B_z = -0.35\text{T}$ the beam spot size is estimated as 52 μm , which is a minimum in the present simulation conditions. The over focusing of electron beam, as shown in [Fig. 5.12\(c\)](#), is observed in some high magnetic flux density region and the oscillation amplitude in electron beam diameter diminishes as the magnetic field becomes very large. At very large value of magnetic field the electron beam size eventually converges to $\sim 70\mu\text{m}$. The total emission current and anode current with magnetic focusing field shown in [table 6](#) are the same as the results without magnetic field. From the simulation, we can find that this magnetic focusing design can optimally suppress the electron beam dispersion under a well-controlled magnetic field and the emission current to anode will not decrease by using this magnetic focusing method.

The above computational examples only serve to demonstrate the capability of

the current parallel Poisson's equation solver using FEM with parallel adaptive mesh refinement in predicting field emission properties with complicated geometries.

5.1.3. FED Simulation With Space-Charge Effect

In this subsection, PIC method is used for considering the space-charge effect in simulating the silicon field emission diode. **Fig. 5.14** shows the SEM image and surface mesh distribution for a typical silicon based field emitter within a periodic cell. Only 1/4 of the full emitter is used due to the intrinsic symmetry with Neumann boundary conditions applied on all symmetric planes. A conical etched single emitter has been used for our modeling. Important geometrical conditions include an emitter height of 400 nm, a distance of 20 nm between the anode and the cathode, and the half width of each cell measuring 25 μm . The applied voltage of the anode probe ranges from 140 to 320 volts, while the cathode are grounded The refined final number of nodes used for the simulation is approximately 96,326. **Fig. 5.15** shows the simulated potential and electric field profile with anode voltage 200 volts.

The simulated and experimental anode current versus gate voltage (I-V) curve is shown in **Fig. 5.16**. **Fig.5.16** shows simulations with work function is 4.5eV agree very well with measurement after turn-on. And before turn-on, simulations using work function is 4.9eV agree very well with measurements probably due to the contamination on the tip surface. It also displays a turn-on voltage of approximate 175

volts. Note the turn-on voltage is defined as the gate voltage at which the current to anode is $1 \mu\text{A}$. The anode current plotted in Fowler-Nordheim coordinate (FN plot) is also shown as an inset to [Fig. 5.16](#). The linearity of FN plot clearly shows that the computed and experimental I-V data follow the Fowler-Nordheim model very well. The above computational examples serve to demonstrate the capability of the current PIC-FEM code with parallel adaptive mesh refinement in predicting field emission properties with complicated geometries.

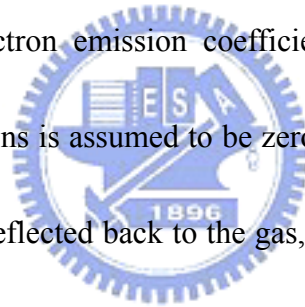
5.2 Simulation on Gas Discharge Plasma

In this section, PIC-FEM code is used to investigate the structure of typical 3D DC and RF gas discharge plasma. The argon discharge under a low pressure has been simulated as taking place between two cylindrical electrodes in a dielectric cylindrical chamber. In the following, the related simulation conditions and results are given in turn.

5.2.1 Three-dimensional DC gas discharge plasma

Consider the discharge sustained between two parallel cylindrical electrodes by 20mm enclosed in a dielectric cylindrical chamber under an operation argon pressure of 42 mtorr. And, the Neumann boundary condition can be imposed on the chamber wall. The background gas is assumed to be at rest and in local equilibrium. We ignore

all collisions among charged particles and consider only their collisions with background gas. The cathode potential is set to -300 Volts. A uniform mesh dividing the electrode gap into 164,865 cells in the computational domain (see [Fig. 5.17a](#)) and decomposed by 20 processors (see [Fig. 5.17b](#)). The electron timestep is 0.5×10^{-10} s and the number of sub-cycling is 10. Initially, the spatial distributions of the ion and electron number densities are assumed uniform to each other. The particle velocities are sampled from the Maxwellian distribution at a corresponding temperature, e.g., $T_i = 232$ K for ions and $KT_e = 0.5$ eV for electrons, where K is the Boltzmann constant. The secondary electron emission coefficient for ions is 0.3. The initial velocity of the emitted electrons is assumed to be zero. The ions incident on the solid surfaces are neutralized and reflected back to the gas, while the incident electrons are always absorbed.



The potential and electric field are shown in [Fig. 5.18](#). The plasma potential is nearly constant and slightly positive (≈ 10 V) and hence, the electric field is very small in the bulk region. The field strength increases with the cathode potential, as expected. In addition, a very high electric field existing around the edge of cathode is observed, and ion will be accelerated rapidly due to this strong electric field. The electron and ion number densities are shown in [Fig. 5.19](#). One can easily recognize the cathode and anode sheaths. The ion and electron kinetic energies are shown in [Fig.](#)

5.20. Ions are rapidly accelerated in the sheath, reaching a velocity of about $10^4 m/s$ before impinging on the cathode.

5.2.2 Three-dimensional RF Gas Discharge Plasma

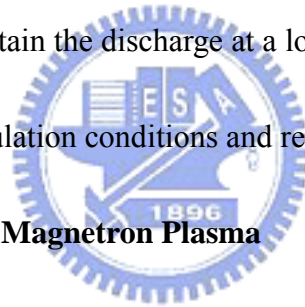
Consider the discharge sustained between two parallel cylindrical electrodes by 20mm under enclosed in a dielectric cylindrical chamber wall. The operation argon pressure is 20mtorr. By taking the advantage of symmetric, we only simulate 1/6 of the cylindrical chamber with a uniform mesh dividing the electrode gap into 164,865 cells (see **Fig. 5.21a**) and decomposed by 20 processors (see **Fig. 5.21b**). The boundary condition for dielectric wall is set to be the typically Neumann boundary condition (see **Fig. 5.22**). The radio-frequency is 13.56MHz, V_{rf} is 300 Volts. The electron timestep is $\Delta t_e = 3.695 \times 10^{-11} s = \frac{1}{2000f}$ and the number of sub-cycling is 10. Initially, the spatial distributions of the ion and electron number densities are assumed uniform to each other. Initial ion temperature is 232 K and initial electron temperature is 0.5 eV. The secondary electron emission coefficient for ions is 0. The ions incident on the solid surfaces are neutralized and reflected back to the gas, while the incident electrons are always absorbed.

The potential are shown in **Fig. 5.23**. The plasma potential is nearly constant and positive ($\approx 0.5V_{rf}$) and hence, the electric field is very small in the bulk region. A very high electric field existing around the edge of cathode and anode is observed, and ion will be accelerated rapidly due to this strong electric field. The electron and

ion number densities are shown in [Fig. 5.24](#). One can easily recognize the cathode and anode sheaths. The electron and ion kinetic energies are shown in [Fig. 5.25](#).

5.3 Simulation on magnetron Plasma

In this section, PIC-FEM code is used to investigate the structure of 3D DC and RF magnetron plasma. The magnetron has two concentric cylindrical magnets behind the cathode, which is used to confine electrons, enforcing $E \times B$ drift motion on electrons between N and S poles. This motion greatly enhances the ionization rate and hence makes it possible to sustain the discharge at a low pressure of 5 mtorr or less. In the following, the related simulation conditions and results are given in turn.



5.3.1 Three-dimensional DC Magnetron Plasma

The computational domain is a cube box with size 128mm×128mm×20mm as shown in [Fig. 5.26 \(a\)](#). The computation domain is divided into 82,000 unstructured meshes as shown in [Fig. 5.26 \(b\)](#). The anode is grounded and the cathode potential is fixed at –300 Volts. Except for the electrodes, the Neumann boundary condition is imposed. The permanent magnet behind the back of the cathode is also shown in [Fig. 5.26 \(a\)](#), which is formed by two concentric cylindrical magnets. The magnetic field \mathbf{B} is proportional to magnetization \mathbf{M} of the permanent magnet, which can clearly be seen from [Fig. 5.27](#). The gas pressure is 5 mtorr and the gas temperature is 323 K. The

electron timestep is $0.5 \times 10^{-10} s$ and the number of sub-cycling is 10. Initial ion temperature is 232 K and initial electron temperature is 0.5 eV. In this work, we examine the effects of magnetization \mathbf{M} and secondary electron emission coefficient γ on the discharge structure. Three cases are presented: (1.) $\mathbf{M}=0.125T$, $\gamma=0.06$, (2) $\mathbf{M}=0.125T$, $\gamma=0.1$, and (3) $\mathbf{M}=0.1875T$, $\gamma=0.06$.

Fig. 5.28 Shows the potential distributions of these three cases, which illustrates that the plasma potential is nearly constant and positive and there is a weak sheath in front of anode. As \mathbf{M} or γ increases, the thickness of cathode sheath between N and S poles

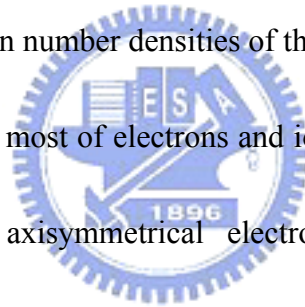
decreases. The electron and ion number densities of these three cases are shown in **Fig.**

5.29-5.31. Both show that the most of electrons and ions are confined between N and S poles, which show the axisymmetrical electron and ion number densities

distributions. As \mathbf{M} or γ increases, both the electron and ion number densities increase. The electron and ion energies of these three cases are shown in **Fig.**

5.32-5.34. They show that the mean electron energy in the bulk region is 2~5eV. The electron energy is larger at the region between bulk and cathode sheath, where is

located between N and S poles. This is because electrons are strongly magnetized and exhibit $E \times B$ drift motion. The mean ion energy can be accelerated to 60eV by the strong electric field in the cathode sheath and ions are hardly magnetized due to their heavy mass.



5.3.2 Three-dimensional RF Magnetron Plasma

In this studying case, we use the same computational domain and permanent magnet system as shown in the previous subsection. The radio-frequency is 13.56MHz, V_{rf} is 300 Volts. The electron timestep is $\Delta t_e = 3.695 \times 10^{-11} s = \frac{1}{2000f}$ and the number of sub-cycling is 10. Initial ion temperature is 232 K and initial electron temperature is 0.5 eV. In this work, we still examine the effects of magnetization \mathbf{M} and secondary electron emission coefficient γ on the discharge structure. Three cases are presented: (1.) $\mathbf{M}=0.125T$, $\gamma=0.$, (2) $\mathbf{M}=0.125T$, $\gamma=0.06$, and (3) $\mathbf{M}=0.25T$, $\gamma=0.06$.

Fig. 5.35 Shows the potential distributions of these three cases, which illustrates that the plasma potential is nearly constant and positive ($\approx 0.5V_{rf}$) and axisymmetric sheaths are formed near the powered and grounded electrodes. As \mathbf{M} or γ increases, the thickness of cathode sheath between N and S poles decreases. The electron and ion number densities of these three cases are shown in **Fig. 5.36-5.38**. Both show that the most of electrons and ions are confined between N and S poles, which also show the axisymmetrical electron and ion number densities distributions. As \mathbf{M} or γ increases, both the electron and ion number densities increase. The electron and ion energies of these three cases are shown in **Fig. 5.39-5.41**. They show that the mean electron energy in the bulk region is 5~9eV. The electron energy is larger at the region between bulk and cathode sheath, where is located between N and S poles. This is

because electrons are strongly magnetized and exhibit $E \times B$ drift motion. The mean ion energy can be accelerated to 50eV by the strong electric field in the two sheath regions and ions are hardly magnetized due to their heavy mass.

5.4 Some Remarks

In this chapter, our developed parallel 3D PIC-FEM code has performed its superior capability in dealing with the 3D field emission display and 3D low-temperature plasma sources since their corresponding results agree with the previous experimental or numerical studies. Some important simulation results are

summarized as follows:

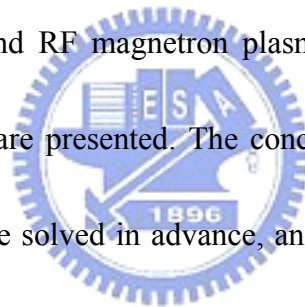
1. In simulating the 3D FED without considering the space-charge effect, we use a triode-type CNT-based emitter without a focusing electrode as the studying case.

The primarily results are: The first is the spreading angle of electrons from the tip increases with the increasing gate voltage. The second is the emission current increases dramatically with the given CNT height. The third is a magnetic focusing design can optimally suppress the electron beam dispersion under a well-controlled magnetic field and the emission current to anode will not decrease by using this magnetic focusing method. The second studying case for considering the space-charge effect is simulation on the silicon field emission diode. The

primarily result shows that simulated I-V curve agrees with the experimental work, especially when simulation work function is set to 4.5eV.

2. In simulating 3D DC and RF gas discharge plasmas, the spatial distributions of plasma macroparameters are presented. The results show that sheath does play an important role in sustaining plasma, which providing the field to accelerate the particles. Due to the 3D geometric shape of electrodes, there is a very strong electric field existing around the edges of electrodes. In other words, this field may lead to unexpected ion bombardment.

3. In simulating 3D DC and RF magnetron plasmas, the spatial distributions of plasma macroparameters are presented. The concentric cylindrical magnets with different magnetization are solved in advance, and the results that magnetic field is proportional to magnetization. With these magnetic fields, electrons are confined between N and S poles and exhibit the $E \times B$ drift motion, which leads to high ionization rate in plasma under very low gas pressure. The results also show that as M or γ increases, the plasma density increases.



Chapter 6

Concluding Remarks

6.1 Summary

In this dissertation, a general parallel three-dimensional electrostatic particle-in-cell scheme with finite element method (PIC-FEM) using unstructured mesh is proposed and verified. A multi-level graph-partitioning technique is used to dynamically decompose the computational domain to improve the parallel performance during runtime. Completed parallelized PIC-FEM code is used to simulate several important physical problems, including field emission, DC/RF gas discharge and DC/RF magnetron plasmas. In brief summary, the major achievements in the present dissertation can be listed as follows:

1. A parallelized three-dimensional electrostatic Poisson's equation solver using Galerkin finite element method with an unstructured mesh is developed and validated. Study of parallel performance of the parallelized PIC-FEM code is performed on the HP-IA64 clusters. With subdomain-by-subdomain scheme for parallel conjugate gradient method, parallel efficiency can reach 84% at 32 processors of HP PC clusters at NCHC. This code coupled with PAMR was used to accurately and efficiently simulate field emission from emitter with complicated geometry without considering space-charge effects, as demonstrated in Chapter 5.
2. A parallelized three-dimensional vector potential magnetostatic Poisson's equation solver using Galerkin finite element method with an unstructured mesh is developed and validated. Study of parallel performance of the parallelized

PIC-FEM code is performed on the HP-IA64 clusters. With subdomain-by-subdomain scheme for parallel conjugate gradient method, parallel efficiency can reach 75% at 32 processors of HP PC clusters at NCHC. This code was used to simulate the magnetic field around permanent magnets or coils for magnetron plasma simulation as demonstrated in Chapter 5.

3. A general parallelized three-dimensional PIC-FEM code is developed and validated. This PIC-FEM code integrates the parallelized Poisson's equation solver with the PIC and Monte Carlo collision (MCC) schemes on an unstructured tetrahedral mesh. Charged particles can be traced either cell-by-cell on an unstructured mesh. This is achieved using leap-frog time-integration method and Boris rotational scheme when magnetic field is involved. Charge assignment and force (field) interpolation between charged particles and grid points is implemented using the same interpolation function originated from the FEM. In addition, dynamic domain decomposition (DDD) with weighting based on number of particles is used to balance the workload among processors during runtime. Study of parallel performance of the parallelized PIC-FEM code is performed on the HP-IA64 clusters. Results using DDD for a typical RF gas discharge show that parallel efficiency can reach 83% at 32 processors.
4. Completed parallelized PIC-FEM code was used to simulate several important problems to demonstrate its superior capability in handling practical problems. These problems include field emission from a silicon tip under external electric field, two typical three-dimensional DC and RF gas-discharge plasmas, and two typical three-dimensional DC and RF magnetron plasmas with permanent magnets. Results are either compared well with experiments or demonstrate the correct physical pictures as expected.

6.2 Recommendation for Future Study

In the present dissertation, we have developed and tested a parallelized three-dimensional PIC-FEM code using an unstructured mesh on memory-distributed parallel machines. We have also applied this code to simulate several important physical problems. Based on the viewpoints of further improving this PIC-FEM code, several possible directions of research are recommended for the future study and are summarized as follows:

1. To implement a better preconditioner for parallel conjugate gradient method for solving the Poisson's equation more efficiently to shorten the runtime and improve the speedup at higher number of processors.
2. To incorporate a Maxwell's equation solver that uses edge-based finite element method into the present PIC-FEM code to further extend its applicability in plasma related simulation, such as ICP, ECR and microwave plasmas.
3. To incorporate a simulation module that can model realistic external circuits into the present PIC-FEM code, which are often coupled to a RF-type gas discharge.
4. To extend the database of collision data for other types of plasma, such as methane with hydrogen, which are very important in growing carbon nanotubes.
5. To incorporate a parallelized DSMC (direct simulation Monte Carlo) module into the PIC-FEM code to consider the neutral transport self-consistently that is

very important in some plasma flow, such as magnetron plasma.



Reference

- [1] Abril, I., Gras-Marti, A., and Valles-Abarca, J. A., "Energy distributions of particles striking the cathode in a glow discharge," *Physical Review A*, Vol. 28 pp. 3677-3678, 1983.
- [2] Akarsu, E., Dincer, K., Haupt, T., and Fox, G. C., "Particle-in-Cell Simulation Codes in High Performance Fortran," *Proceeding of Super Computing Conference*, Pittsburgh, PA, 1996.
- [3] Amestoy, P. R., Duff, I. S., and L'Excellent, J. Y., "Multifrontal parallel distributed symmetric and unsymmetric solvers," *Computer Methods in Applied Mechanical Engineering*, Vol. 184, pp. 501-520, 2000.
- [4] Barnard, S. T. and Simon, H. D., "A Fast Multilevel Implementation of Recursive Spectral Bisection for Partitioning Unstructured Problems," *Concurrence. Practice Experience*, Vol. 6, pp.101-117, 1994.
- [5] Barrett, R. and Berry, M., "Templates for the solution of linear systems: Building blocks for iterative methods," SIAM, Philadelphia, 1994.
- [6] Beltzer, A. I., "Variational and finite element methods: a symbolic computation approach," Springer-Verlag, Berlin, 1990.
- [7] Birdsall, C. K. and Langdon, A. B., "Plasma Physics via Computer Simulation," Institute of Physics Publishing, Bristol, 1991.

- [8] Birdsall, C. K., "Particle-in-cell charged-particle simulations, plus Monte Carlo collisions with neutral atoms, PIC-MCC," IEEE Transaction on Plasma Science, Vol. 19, pp. 65-85, 1991.
- [9] Bogaerts, A., Neyts, E., Gijbels, R., and Mullen J. V., "Gas discharge plasmas and their applications," Spectrochimica Acta Part B, Vol. 57, pp. 609-658, 2002.
- [10] Brackbill, J. U. and Cohen, B. I., "Multiple Time Scales," Academic Press, 1985.
- [11] Bukowski, J. D. and Graves, D. B., "Two-dimensional fluid model of an inductively coupled plasma with comparison to experimental spatial profiles," Journal of Applied Physics, Vol. 80, pp. 2614-2623, 1996.
- [12] Burnett, D. S., "Finite element analysis: from concepts to applications," Addison-Wesley, Reading Mass., 1987.
- [13] Cheng, D. K., "Field and wave electromagnetics," Addison Wesley, 2nd edition, 1989.
- [14] Choi, W. B., Chung, D. S., and Kang, J. H., "Fully sealed, high-brightness carbon-nanotube field-emission display" Applied Physics Letter, Vol. 75, pp. 3129-3131, 1999.
- [15] Decyk, V. K., "Skeleton PIC Codes for parallel computers", Computer Physics Communications, Vol.87, pp. 87-94, 1995.
- [16] Decyk, V. K. and Norton, C. D., "UCLA Parallel PIC Framework," Computer

Physics Communications, Vol. 164, pp. 80-85, 2004.

[17] de Heer, W. A., Chatelain, A., and Ugarte, D., “A Carbon Nanotube Field-Emission Electron Source,” Science Vol. 270, pp.1179-1180, 1995.

[18] Deshmukh, S. C. and Economou, D. J., “Factors affecting the Cl atom density in a chlorine discharge,” Journal of Applied Physics, Vol. 72, pp. 4597-4607, 1992.

[19] Economou, D. J., “Modeling and simulation of plasma etching reactors for microelectronics,” Thin solid film, Vol. 365, pp.348-367, 2000.

[20] Farhat, C., Maman, N., and Brown, G., “Mesh Partitioning for Implicit Computations via Domain Decomposition,” International Journal of Numerical Methods in Engineering, Vol. 38, pp.989-1000, 1995.

[21] Fenner, R. T., “Finite element methods for engineers,” Imperial College Press, London, 1996.

[22] Font, G. I., Boyd, I. D., and Bakakriahnan,J., “Effects of wall recombination on the etch rate and plasma composition of an etch reactor,” Journal of Vacuum Science and Technology B, Vol. 16, pp. 2057-2064, 1998.

[23] Fowler, R. H. and Nordheim, L., “Electron Emission in Intense Electric Fields,” Proc. Royal Society A, Vol. 119, pp.173-181, 1928.

[24] Godyak, V. A., Piejak, R. B., and Alexandrovich, B. M. “Measurements of electron energy distribution in low-pressure RF discharges,” Plasma Sources

Science and Technology, Vol.1, pp. 36-38, 1992.

[25] Gogolides, E. and Sawin, H. H., "Continuum Modeling of Radio-Frequency Glow Discharges I: Theory and Results for Electropositive and Electronegative Gases," Journal of Applied Physics, Vol. 72, pp. 3971-3987, 1992.

[26] Golub, G. H. and Van Loan, C. F., "Matrix computations," Johns Hopkins University Press, Baltimore, 1996.

[27] Gullerud, A. and Dodds, R. J., "MPI-based implementation of a PCG solver using an EBE architecture and preconditioner for implicit, 3-D finite element analysis," Computers and Structures, Vol. 79, pp. 553-575, 2001.

[28] Halbach, K., "Design of Permanent Multipole Magnets with oriented Rare Earth Cobalt Material," Nuclear Instruments and Methods, Vol. 169, pp.1-10, 1980.

[29] Hockney, R. W. and Eastwood, J. W., "Computer simulation using particles," Adam Hilger, Bristol & New York, 1988.

[30] Hodgson, D. and Jimack, P., "Efficient Mesh Partitoning for Parallel P.D.D. Solvers on Distributed Memory Machines," Proceedings of the sixth SIAM conference on Parallel Processing for Scientific Computing, 1993.

[31] Hong, D., Aslam, M., Feldmann, M., and Olinger, M. "Simulations of fabricated field emitter structures," Journal of Vacuum Science and Technology B, Vol. 12, pp.764-769, 1994.

- [32] Hu, Y. and Huang. C. H., “Computer simulation of the field emission properties of multiwalled carbon nanotubes for flat panel displays,” Journal of Vacuum Science and Technology B, Vol. 21, pp. 1648-1654 , 2003.
- [33] Itoh, S., Tanaka, M., and Tonegawa, T., “Development of field emission displays,” Journal of Vacuum Science and Technology B, Vol., 22, pp.1362-1366, 2004.
- [34] Jimack, P. and Touheed, N., “Developing Parallel Finite Element software Using MPI,” Department of Scientific computing, University of Leeds, UK, 1997.
- [35] Jin, J., “The finite element method in electromagnetics,” John Wiley & Sons, New York, 2002.
- [36] Karypis, G. and Kumar, V., “Metis: Unstructured Graph Partitioning and Sparse Matrix Ordering, Version 2.0 User Manual,” Minneapolis MN55455, Department of Computer Science, University of Minnesota, U.S.A, 1995.
- [37] Karypis, G., Schloegel, K., and Kumar, V., “ParMetis: Parallel version of METIS,” Department of Computer Science, University of Minnesota, September 1998.
- [38] Khan, A. and Topping, B., “Parallel finite element analysis using Jacobi-conditioned conjugate gradient algorithm,” Advance in Engineering Software, Vol. 25, pp. 309-319, 1996.

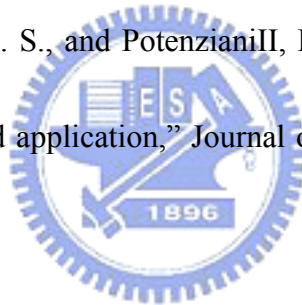
- [39] Kawamura, E., Birdsall, C. K., and Vahedi, V., "Methods in speeding up PIC-MCC codes applied to RF plasma discharges," ERL report, University of California at Berkeley, 2000.
- [40] Kline, L. E., Partlow, W. D., and Bies, W. E., "Electron and chemical kinetics in methane rf glow-discharge deposition plasmas," *Journal of Applied Physics*, Vol. 65, pp. 70-78, 1989.
- [41] Kushner, M. J., "Modeling of Microdischarge Devices: Plasma and Gas Dynamics", *Journal of Physics D*, Vol. 38, pp. 1633-1643, 2005.
- [42] Kushner, M. J., Collison, W. Z., Grapperhaus, M. J., Holl, J. P., and Barnes, M. S., "A 3-dimensional Model for Inductively Coupled Plasma Etching Reactors: Azimuthal Symmetry and Coil Properties", *Journal Applied Physics*, Vol. 80, pp. 1337-1344, 1996.
- [43] Kushner, M. J., "Consequences of Asymmetric Pumping in Low Pressure Plasma Processing Reactors: A 3-dimensional Modeling Study", *Journal Applied Physics*, Vol. 82, pp. 5312-5320, 1997.
- [44] Kythe, P. K., "An introduction to boundary element methods," CRC Press, Boca Raton, 1995
- [45] Lan, Y. C., Lai, J. T., Chen, S. H., Wang, W. C., Tsai, C. H., Tsai, K. L., and Sheu, C. Y., "Simulation of focusing field emission devices," *Journal of Vacuum*

Science and Technology B, Vol. 18, pp. 911-913, 2000.

[46] Lan, Y. C., Lee, C. T., Hu, Y., Chen, S. H., Lee, C. C., Tsui, B. Y., and Lin, T. L.,
“Simulation study of carbon nanotube field emission display with under-gate and
planar-gate structures,” Journal of Vacuum Science and Technology B, Vol. 22,
pp. 1244-1249, 2004.

[47] Leupold, H. A., Tilak, A. S., and PotenzianiII, E., “Adjustable multi-tesla perma-
nent magnet field sources,” IEEE Transaction on Magnetics., Vol. 29, pp.
2902-2904, 1993.

[48] Leupold, H. A., Tilak, A. S., and PotenzianiII, E., “Permanent magnet spheres:
Design, construction, and application,” Journal of Applied Physics, Vol. 87, pp.
4730-4734, 2000.



[49] Lee, S. Y. and Azari, N. G., “Hybrid task decomposition for Particle-In-Cell
methods on message passing systems,” Proceedings of International Conference
on Parallel Processing, St. Charles, IL, Vol. 3, pp. 141-144, 1992.

[50] Lei, W., Wang, B., and Yin, H., “Simulation study on performance of field
emitter array,” Journal of Vacuum Science and Technology B, Vol. 16, pp.
2881-2886, 1998.

[51] Lian, Y. Y., Hsu, K. H., Shao, Y. L., Lee, Y. M., Jeng, Y. W., and Wu, J. S.,
“Parallel Adaptive Mesh-Refining Scheme on Three-dimensional Unstructured

Tetrahedral Mesh and Its Applications," Computer Physics Communications, 2006 (accepted).

[52] Lieberman, M. A. and Lichtenberg, A. J. "Principles of Plasma Discharges and Materials Processing," Wiley, New York, 1994.

[53] Liewer, P. C. and Decyk, V. K., "A general Concurrent Algorithm for Plasma Particle-In-Cell Simulation Codes," Journal of Computational Physics, Vol. 85, pp. 302-322, 1989.

[54] Lymberopoulos, D. P. and Economou, D. J., "Two-dimensional simulation of polysilicon etching with chlorine in a high density plasma reactor," IEEE Transaction on Plasma Science, Vol.23, pp. 573-580, 1995.

[55] Mahony, C. M. O., McFarland, J., Steen, P. G., and Graham, W. G., "Structure observed in measured electron energy distribution functions in capacitively coupled radio frequency hydrogen plasmas," Applied Physics Letters, Vol. 75 , pp. 331-333, 1999.

[56] Meeks, E., Larson, R. S., Vosen, S. R., and Shon, J. W., "Modeling Chemical Downstream Etch Systems for NF₃/O₂ Mixtures," Journal of the Electrochemical Society, Vol.144, pp. 357-366, 1997.

[57] Meeks, E. and Shon, J. W., "Modeling of plasma-etch processes using well stirred reactor approximations and including complex gas-phase and surface

reactions,” IEEE Transaction on Plasma Science, Vol. 23, pp. 539-549, 1995.

[58] Meyyappan, M., “Computational Modeling in Semiconductor Processing”
Artech House, Boston, 1994.

[59] Midha, V. and Economou, D. J., “Spatio-temporal evolution of a pulsed chlorine
discharge,” Plasma Sources Science and Technology, Vol. 9, pp. 256-269, 2000.

[60] Nanbu, K., “Probability theory of electron-molecule, ion-molecule,
molecule-molecule, and Coulomb collisions for particle modeling of materials
processing plasmas and Gases,” IEEE Transaction on Plasma Science, Vol. 28 ,
pp. 971- 990, 2000.

[61] Nanbu, K., “Simple method to determine collisional event in Monte Carlo
simulation of electron-molecule collision,” Japanese Journal of Applied Physics,
Vol. 33, pp. 4752-4753, 1994.



[62] Nedelea, T. and Urbassek, H. M., “Parametric study of ion acceleration in a
one-dimensional plasma expansion using the particle-in-cell simulation,”
Physical Review E, Vol. 69, pp. 056408-1~6, 2004.

[63] Nilsson, L., Groening, O., Emmenegger, C., Kuettel, O., Schaller, E., Schlapbach
L., Kind, H., Bonard, J.M. ,and Kern, K., “Scanning field emission from
patterned carbon nanotube films,” Applied Physics Letter, Vol. 76, pp.
2071-2073, 2000.

- [64] Nishimura, K., Shen, Z., Fujikawa, M., Hosono, A., Hashimoto, N., Kawamoto, S., Watanabe, S., and Nakata, S., *Journal of Vacuum Science and Technology B*, Vol. 22, pp. 1377-1381, 2004.
- [65] Onate, E., Periauxand, J., and Samuelsson, A., “The finite element method in the 1990's,” Springer-Verlag, Berlin, 1991.
- [66] Pirio, G., Legagneux, P., Pribat, D., Teo, K. B. K., Chhowalla, M., Amaratunga, G. A. J., and Milne, W. I., “Fabrication and electrical characteristics of carbon nanotube field emission microcathodes with an integrated gate electrode,” *Nanotechnology*, Vol. 13, pp.1-4, 2002.
- [67] Raizer, Y. P., Shneider, M. N., and Yatsenko, N. A., “Radio-Frequency Capacitive Discharges,” CRC Press, Boca Raton, London, Tokyo, 1995.
- [68] Rao, A.M., Jacques, D., Haddon, R.C., Zhu, W., Bower, C., and Jin, S., “In situ-grown carbon nanotube array with excellent field emission characteristics,” *Applied Physics Letter*, Vol. 76, pp. 3813-3815, 2000.
- [69] Saad, Y., “Iterative methods for sparse linear systems,” Society for Industrial and Applied Mathematics, Philadelphia, 2003.
- [70] Santi, M., Cheng S., Celik, M., Martinez-Sanchez, M., and Peraire J., “further development and preliminary results of the aquila hall thruster plume model,” 39th AIAA/ASME/SAE/ASEE Joint Propulsion Conference and Exhibit

Huntsville, AL, pp.20-23, July 2003.

[71] Seidel, D. B., Plimpton, S. J., Pasik, M. F., Coats, R. S., and Montry, G. R.,
“Dynamic load-balancing for a parallel electromagnetic particle-in-cell code,”
Pulsed Power Plasma Science, Vol. 2 pp. 1000-1003, 2002.

[72] Serikov, V. V. and Nanbu, K., “The analysis of background gas heating in direct
current sputtering discharge via particle simulation,” Journal of Applied Physics,
Vol. 82, pp. 5948-5957, 1997.

[73] Shao, Y. L., “Development and Verification of a 3-D Parallelized
Poisson-Boltzmann Equation Solver Using Finite Element Method with
Adaptive Mesh Refinement,” PhD dissertation, Department of Mechanical
Engineering, National Chiao-Tung University, Taiwan, 2006.



[74] Shon, C. H. and Lee, J. K., “Modeling of Magnetron Sputter Plasmas,” Applied
Surface Science, Vol.192, pp. 258-270, 2002

[75] Shon, C. H., Park, J. S., and Lee, J. K., “Kinetic and Steady-State Properties of
Magnetron Sputter with Three-Dimensional Field,” Japanese Journal Applied
Physics Part I, Vol. 38, pp. 4440-4446, 1999.

[76] Shon, C. H., Lee, J. K., Lee, H. J., Shin, Y. K., Yang, Y., and Chung, T. H., IEEE
Transaction on Plasma Science, Vol. 26, pp.1635-1644, 1998.

[77] Shon, C. H., Lee, H. J., and Lee, J. K., “Method to increase the simulation speed

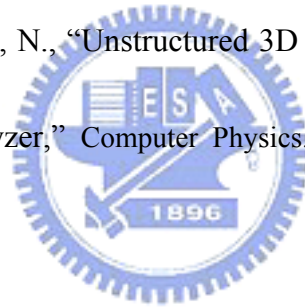
of particle-in-cell (PIC) code”, Computer Physics Communications, Vol. 141, pp.323-329, 2001.

[78] Silvester, P. P. and Pelosi, G., “Finite elements methods and techniques for wave electromagnetics,” IEEE, New York, 1994.

[79] Simon, H., “Partitioning of Unstructured Problems for Parallel Processing,” Computing Systems in Engineering, Vol. 2, pp. 135-148, 1991.

[80] Spindt, C. A., “A Thin-Film Field-Emission Cathode,” Journal of Applied Physics Vol. 39, pp.3504-3505, 1968.

[81] Spirkin, A. and Gatsonis, N., “Unstructured 3D PIC simulation of the flow in a retarding potential analyzer,” Computer Physics: Communication, Vol. 164, pp. 383-389, 2004.



[82] Sullivan, D. M., “Electromagnetic Simulation Using FDTD Method,” IEEE Press, New York, 2000.

[83] Surendra, M., Graves, D. B., and Morey, I. J., “Electron heating in low-pressure rf glow discharges,” Applied Physics Letters, Vol. 56, pp.1022-1024, 1990.

[84] Thiagarajan, G. and Aravamuthan, V., “Parallelization Strategies for Element-by-Element Preconditioned Conjugate Gradient Solver Using High-Performance Fortran for Unstructured Finite-Element Application On Linux Clusters,” Journal of Computing in Civil Engineering, Vol. 16, pp.1-4,

2002.

[85] Tseng, K. C., “Development of a General-Purpose Parallel Three-Dimensional DSMC code (PDSC) Using Unstructured Tetrahedral Mesh,” PhD dissertation, Department of Mechanical Engineering, National Chiao-Tung University, Taiwan, 2005.

[86] Turner, M. M., Doyle, R. A., and Hopkins, M. B., “Measured and simulated electron energy distribution functions in a low-pressure radio frequency discharge in argon,” Applied Physics Letters, Vol. 62, pp. 3247-3249, 1993.

[87] Vahedi, V., DiPeso, G., Birdsall, C. K., Lieberman, M. A., and Ronglien, T. D. “Capacitive RF discharges modeled by particle-in-cell Monte Carlo simulation. 1. Analysis of numerical techniques,” Plasma Sources Science and Technology, Vol. 2, pp. 261-268, 1993.

[88] Umashankar, K., “Computational electromagnetics,” Artech House, Boston 1993.

[89] Ventzek, P. L. G., Sommerer, T. J., Hoekstra, R. J., and Kushner, M. J., “A 2-dimensional Hybrid Model of Inductively Coupled Plasma Sources for Etching”, Applied Physics Letter, Vol. 62, pp.605-607, 1993.

[90] Ventzek, P. L. G., Hoekstra, R. J., and Kushner, M. J., “2-Dimensional Modeling of High Plasma Density Inductively Coupled Sources for Materials Processing,”

Journal of Vacuum Science and Technology B, Vol. 12, pp. 461-477, 1994.

[91] Vahedi, V. and Surendra, M., “A monte carlo collision model for the particle-in-cell method: applications to argon and oxygen discharges,” Computer Physics Communications, Vol. 87, pp. 179-198, 1995.

[92] Vahedi, V., DiPeso, G., Birdsall, C.K., Lieberman, M.A., and Roglien, T.D., “Capacitive RF discharges modeled by particle-in-cell Monte Carlo simulation. II comparisons with laboratory measurements of electron energy distribution functions,” Plasma Sources Science and Technology, Vol. 2, pp. 273-278, 1993.

[93] Vanderstraeten, D., Farhat, C., Chen P. S., Keunings, R., and Zone O., “A retrofit Based Methodology for the Fast Generation and Optimization of Large-Scale Mesh Partitions :Beyond the Minimum Interface Size Criterion,” Computer Methods in Applied Mechanics and Engineering, Vol. 133, pp. 25-45,1996.

[94] Wang, C., Wang, B. and Zhao, Z., “Numerical modeling of the disk-edge field emitter triode,” Journal of Vacuum Science and Technology B, Vol. 15, pp. 394-397, 1997.

[95] Wang, Q. H., Corrigan, T. D., Dai, J. Y., and Chang, R. P. H., “Numerical modeling of the disk-edge field emitter triode,” Journal of Vacuum Science and Technology B, Vol. 15, pp. 394-397, 1997.

[96] Walshaw, C., Cross, M., Everett, M. G., Johnson, S., and McManus, K.,

“Partitioning and Mapping of Unstructured Meshes to Parallel Machine Topologies,” Proceeding of Irregular Parallel Algorithms for Irregularly Structured Problems, Vol. 980 of LNCS (Springer), pp.121-126, 1995.

[97] Walker, D. W., “Particle-In-Cell Plasma Simulation Codes on the Connection Machine,” Computer Systems in Engineering, Vol. 2, pp. 307-319, 1991.

[98] Walker, D. W., “Characterizing the Parallel Performance of a Large-Scale, Particle-In-Cell Plasma Simulation Code,” Concurrency: Practice and Experience, Vol. 2, pp. 257-288, 1990.

[99] Wehage, R. A. and Haug, E. J., “Generalized Coordinate Partitioning for Dimension Reduction in Analysis of Constrained Dynamic Systems,” ASME Journal of Mechanical Design, Vol. 104, pp. 247-255, 1982.

[100] Winslow, A. M., “Numerical Solution of the quasi-linear Poisson equation in a non-uniform triangle mesh,” Journal of Computational Physics, Vol. 2, pp. 149-172, 1967.

[101] Wu, J. S., Tseng, K. C., and Wu, F. Y., "Parallel Three Dimensional Direct Simulation Monte Carlo Method Using Unstructured Adaptive Mesh and Variable Time Step," Computer Physics Communications, Vol. 162, pp. 166-187, 2004.

[102] Zeidler, E., “Variational methods and optimization,” Springer-Verlag, New York, 1985.

[103] Zienkiewicz, O. C. and Zhu, J. Z., “A simple error estimator and adaptive procedure for practical engineering analysis,” *International Journal for Numerical Methods in Engineering*, Vol. 24, pp. 337-357, 1987.



Table 1. Main excellent features of a field emission display

1.	Thin panel thickness (~2mm)
2.	Self-emissive
3.	Distortion free image
4.	Wide viewing angle (~170°)
5.	Quick response in the order of μs by controlling with analog or digital without active elements
6.	Tolerance to environment as high as that of receiving tubes
7.	Free from the terrestrial magnetic effect
8.	Free from the changes in the ambient magnetism
9.	Quick start of operation
10.	Less dead space of images
11.	Low power consumption display device
12.	Good stable characteristics in severe environmental conditions

Table 2. Time breakdown and speedup of Poisson's equation solver at the different number of processors

Processor No.	1	2	4	8	16	32
Total time (seconds)	138.17	79.17	42.53	14.78	8.21	5.13
CG solver time (%)	98.8	99.1	94.33	76.79	85.14	94.54
Matrix assembling time (%)	0.44	0.36	0.32	0.47	0.42	0.31
Communication time (%)	N/A	4.45	28.1	34.5	35.32	37
Speedup	1	1.74	3.25	9.35	16.83	26.93

Table 3. Evolution of simulation parameters at different levels of mesh refinement. (E_{MAX} is the local maximum electric field strength at the surface of CNT field emitter).

Refinement Level	Number of nodes	Number of elements	E_{MAX} (V/nm)
0	7006 (7006)	27814 (27814)	8.218482 (8.21848)
1	22750 (24892)	110218 (121064)	10.20636 (10.20257)
2	34927 (38896)	175254 (196378)	11.50804 (11.50135)
3	44080 (47984)	225156 (245975)	11.54894 (11.51166)
4	51638 (55488)	264259 (284766)	11.32366 (11.32647)
5	61241 (59279)	313092 (306368)	11.32303 (11.32665)
6	67173	345307	11.32324

* Numbers in the parentheses represent numerical data obtained using *a posteriori* error estimator with prescribed global relative error $\varepsilon_{pre}=0.0003$.

Table 4. Evolution of simulation parameters at different levels of mesh refinement. (B_{MAX} is the local maximum magnetic field strength at the center of magnet arrays).

Refinement Level	Number of nodes	Number of elements	B_{MAX} (T)
0	7845	46953	0.869774
1	38364	228201	0.870979
2	54355	319482	0.870808
3	70773	414616	0.871388
4	98743	574237	0.871401
5	108415	629268	0.871556
6	108840	631711	0.871553

Table 5. The important geometrical parameters of CNT triode- and tetrode-type field emitters.

	Triode-type (Fig. 7)	Tetrode-type (Fig. 12)
he	600 nm	600 nm
r	10 nm	10 nm
R	500 nm	500 nm
R _f	N/A	1500nm
d	200 nm	N/A
h	500 nm	N/A
d1	N/A	200 nm
d2	N/A	200 nm
h1	N/A	500 nm
h2	N/A	500 nm
L	49.3μm	48.6μm
W	25 μm	25 μm

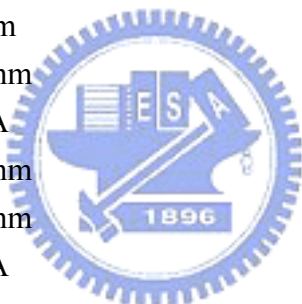


Table 6. Characteristics of device performance for different focus types.

Focus type	Emission current from tip (A)	Gate current (A)	Anode current (A)	Spot diameter at anode (μ m)
Without focus	2.48E-05	~0	2.48E-05	528.68
Magnetic focus (Bz= 0.2 T)	2.48E-05	~0	2.48E-05	296.99
Magnetic focus (Bz= 0.35 T)	2.48E-05	~0	2.48E-05	52.01
Electrostatic focus (Vf= -5 V)	5.47E-06	2.39E-06	3.08E-06	154.76
Electrostatic focus (Vf= 0 V)	5.69E-06	1.35E-06	4.35E-06	226.26
Electrostatic focus (Vf= 5 V)	6.50E-06	1.56E-06	4.93E-06	210.20

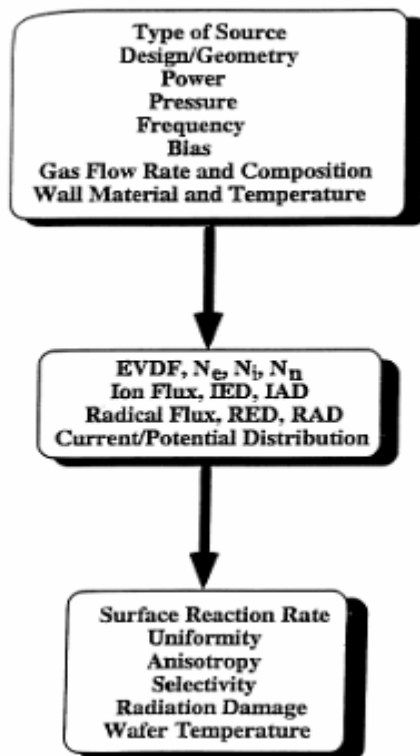


Figure 1.1 Representation of the parameter space in plasma etching. The key internal plasma properties (middle) are the bridge between externally controlled variables (top) and the figures of merit (bottom).

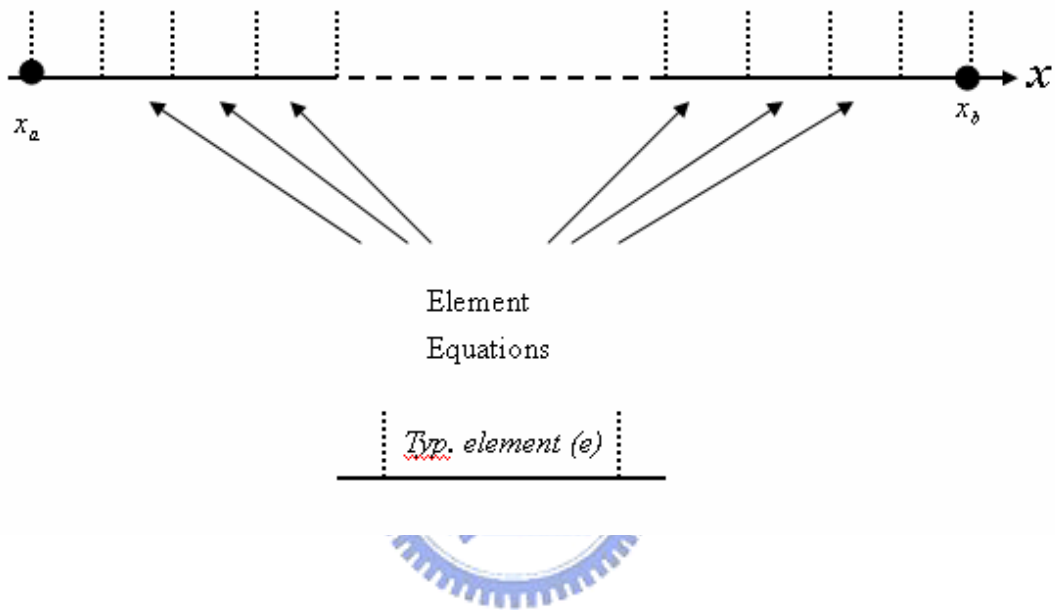


Figure 2.1 Element equation from a typical element (e) are used for each element in the mesh.

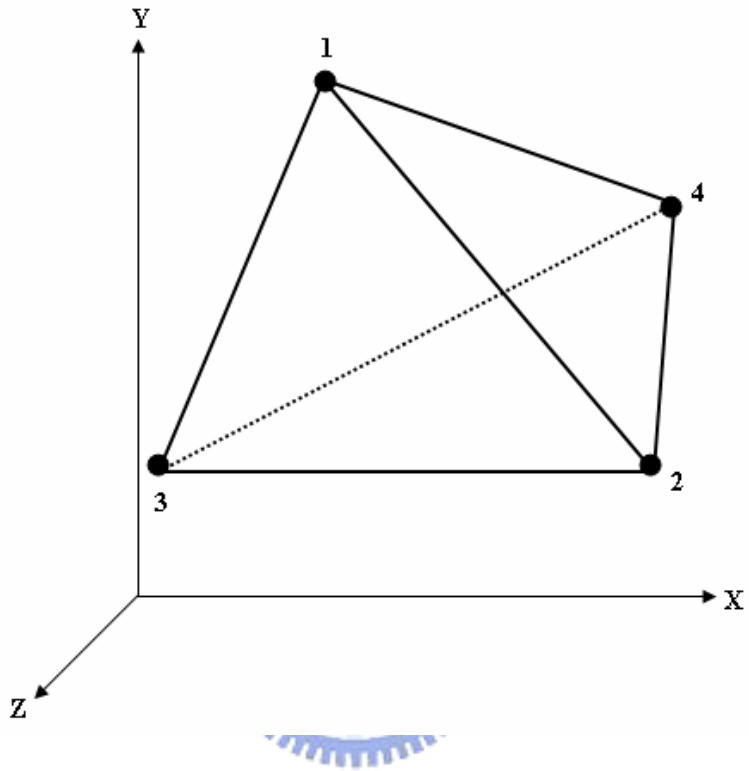


Figure 2.2 A three-Dimensional C^0 -linear standard tetrahedral element.

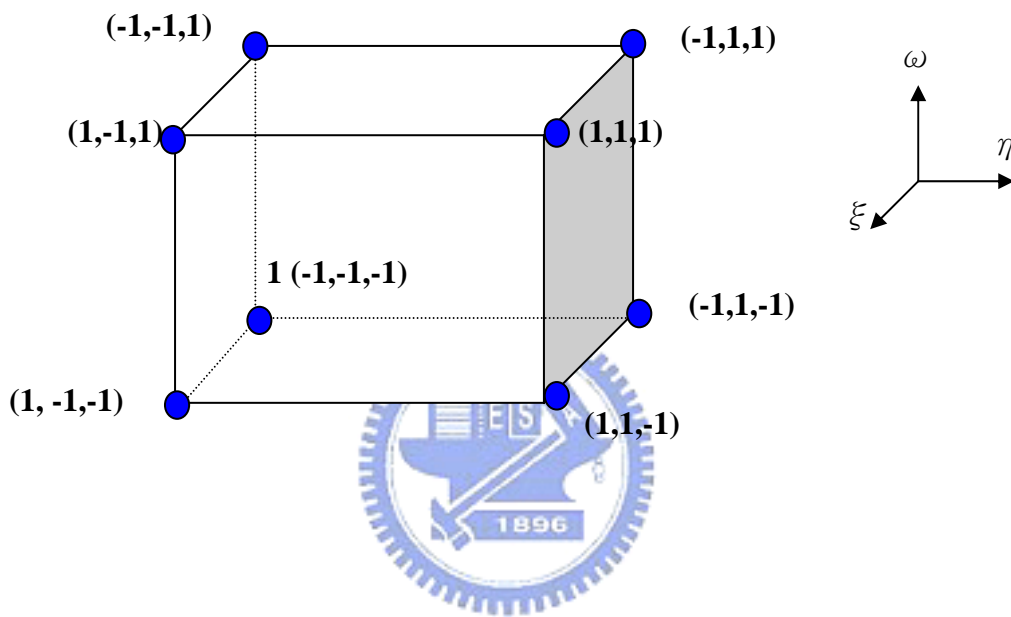
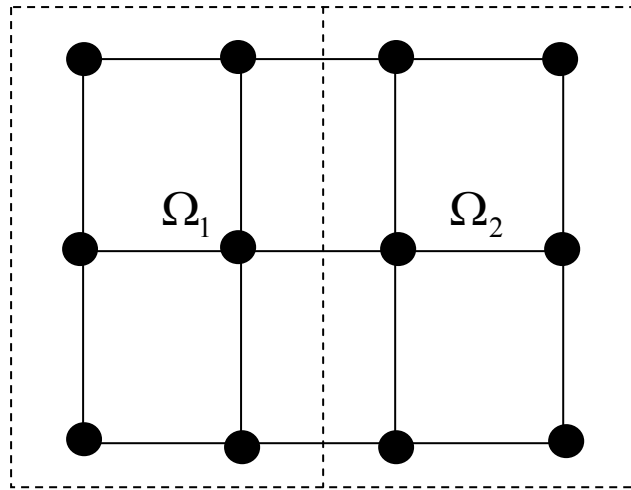
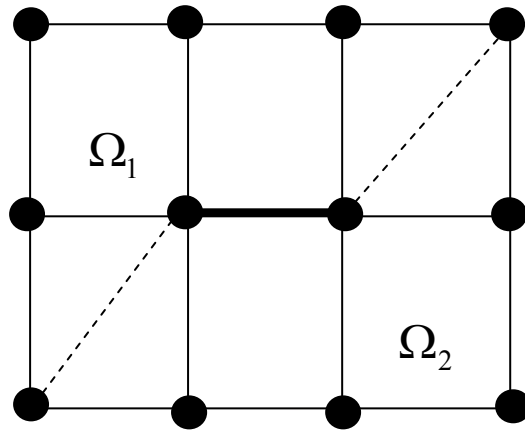


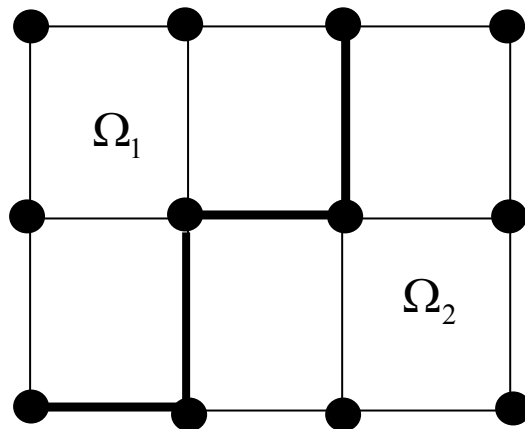
Figure 2.3 A three-Dimensional C^0 -linear standard hexahedral element.



(a)



(b)



(c)

Figure 2.4 (a) Vertex-based. (b) edge-based (c) element-based partition of 4×3 mesh into two sub-regions.

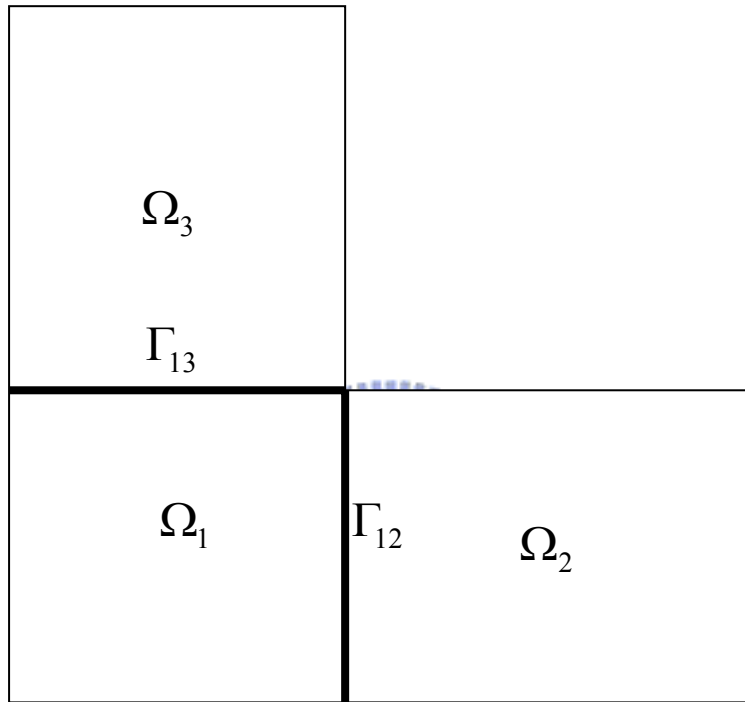


Figure 2.5 An L-shape domain subdivided into three sub-domains.

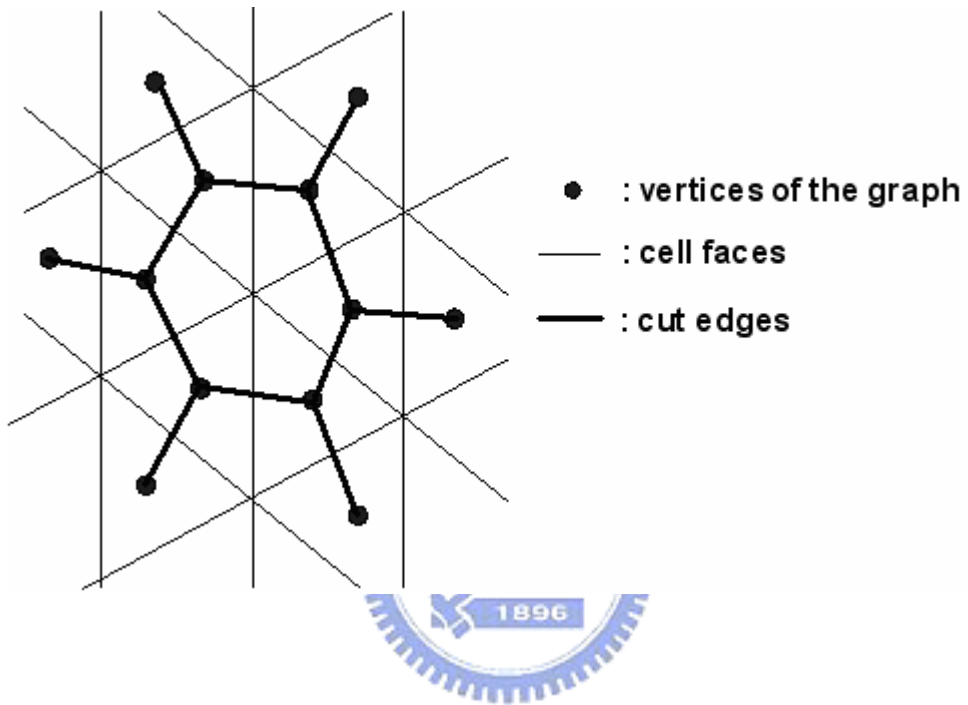


Figure 2.6 Sketch of graph and mesh.

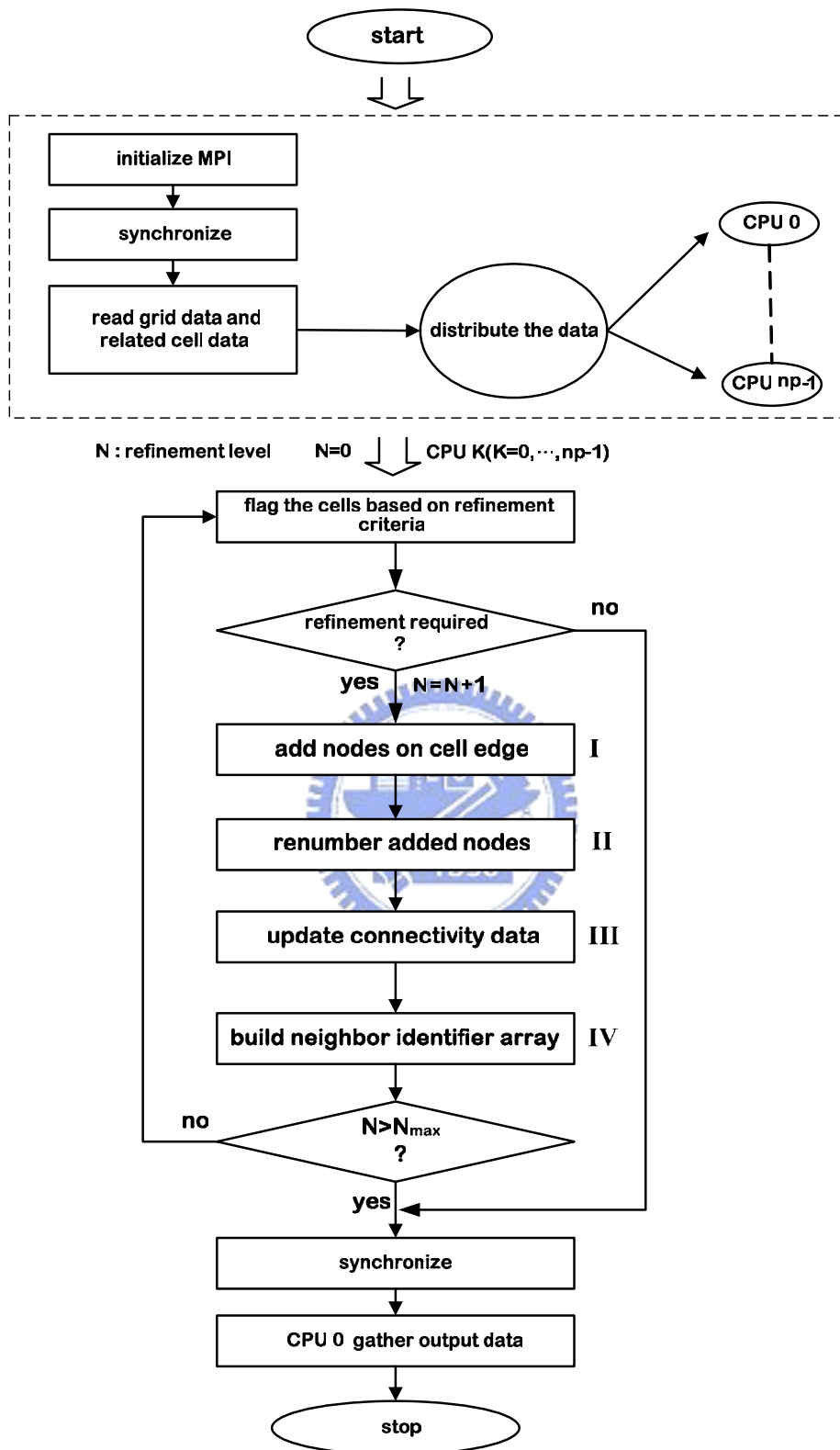


Figure 2.7. Flowchart of the parallel mesh refinement module.

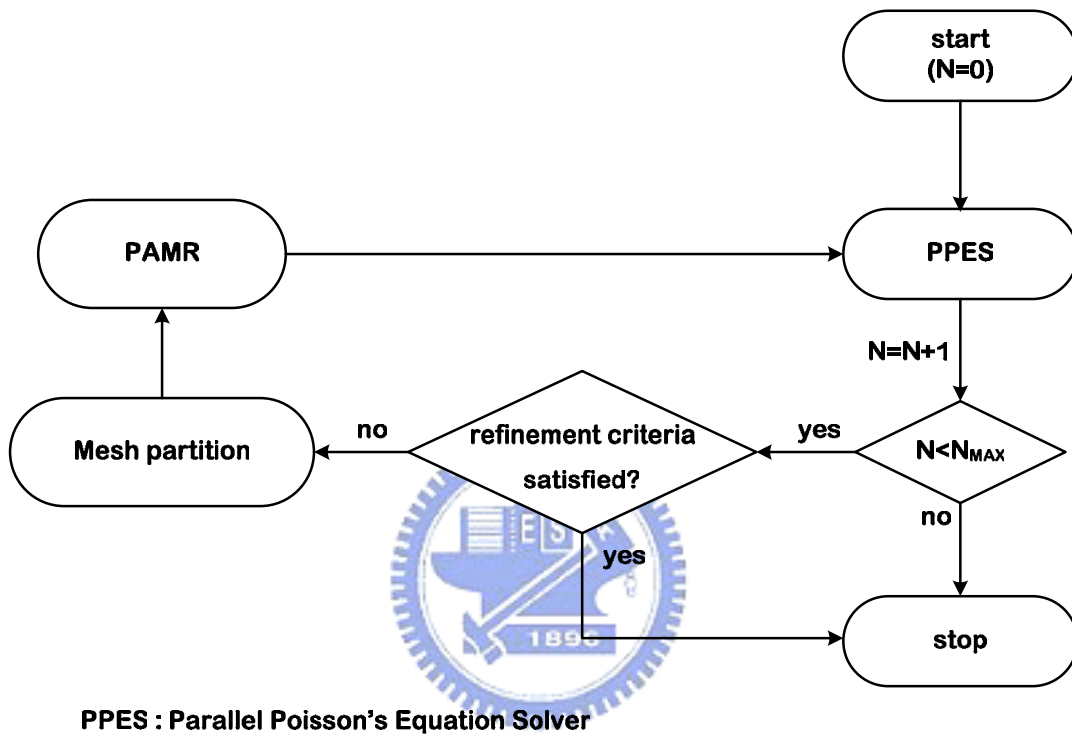


Figure 2.8 Flowchart of the coupled PPES-PAMR method.

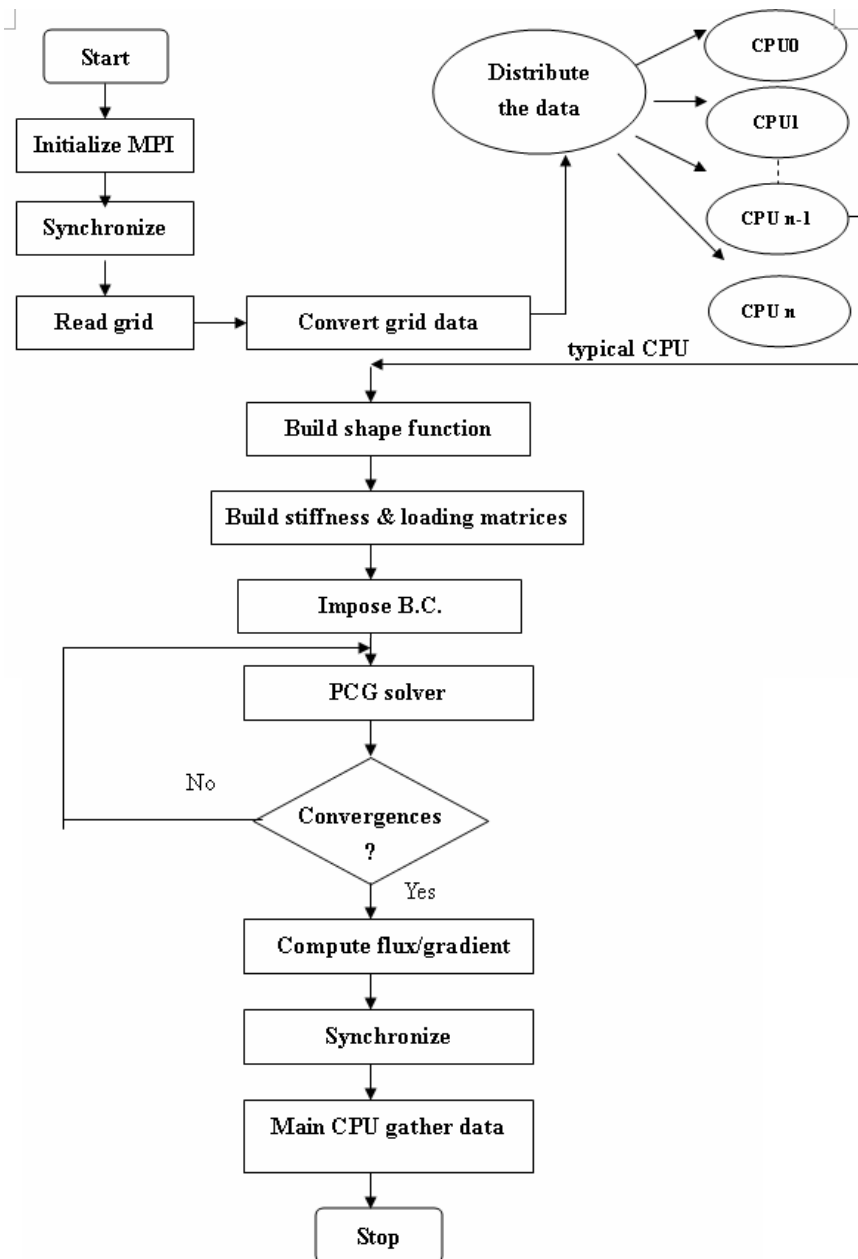
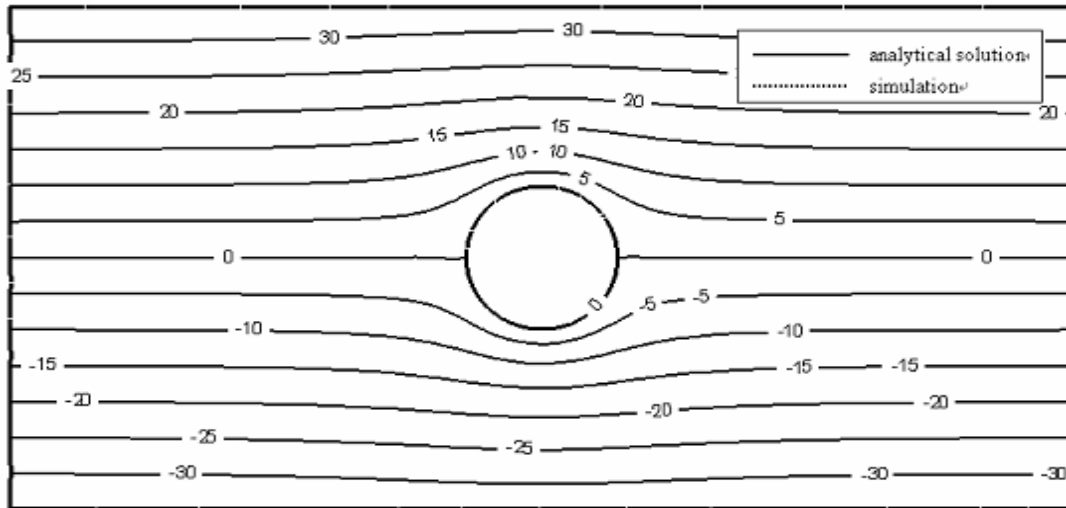
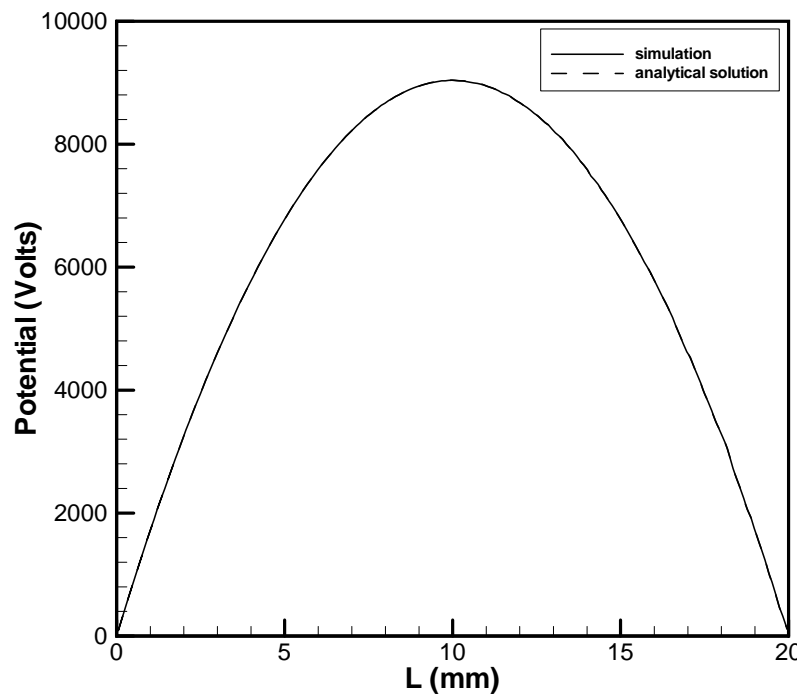


Figure 2.9 The flowchart of parallel FEM.



(a)



(b)

Figure 2.10 Contours of the potential distribution of (a) a grounded conducting sphere ($\Phi = 0$ Volts) immersed in a uniform electric field ($\vec{E} = 10 \text{ Volts/m}$) and (b) uniform positive charges distribution between two infinite grounded conducting plates ($\Phi = 0$ Volts)

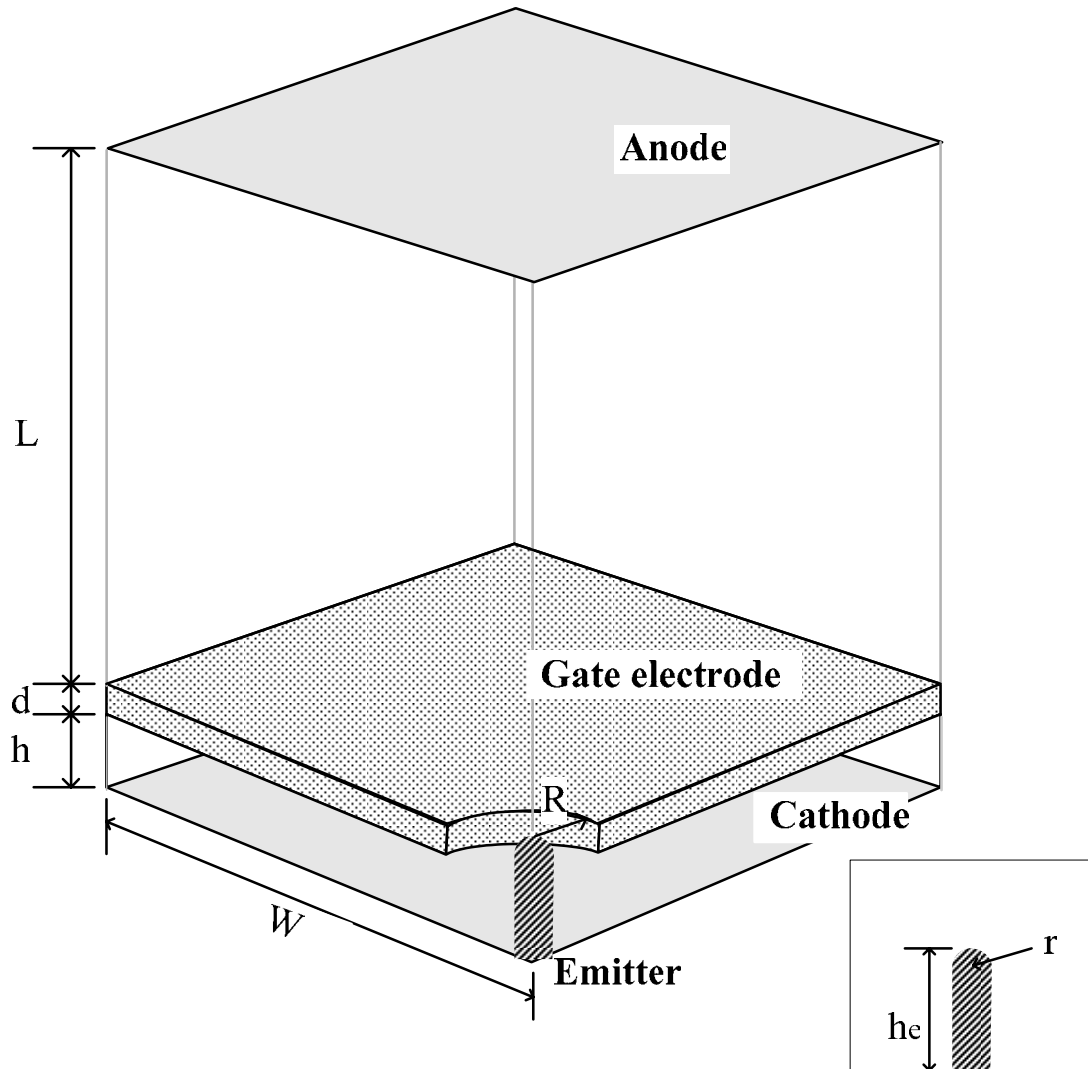


Figure 2.11 Schematic diagram of the simulation domain for a typical CNT triode-type field emitter within a periodic cell. The important geometrical parameters are: $R=500$ nm, $r=10$ nm, $he=600$ nm, $h=500$ nm, $L=49.3$ μ m, $d=200$ nm and $W=25$ μ m

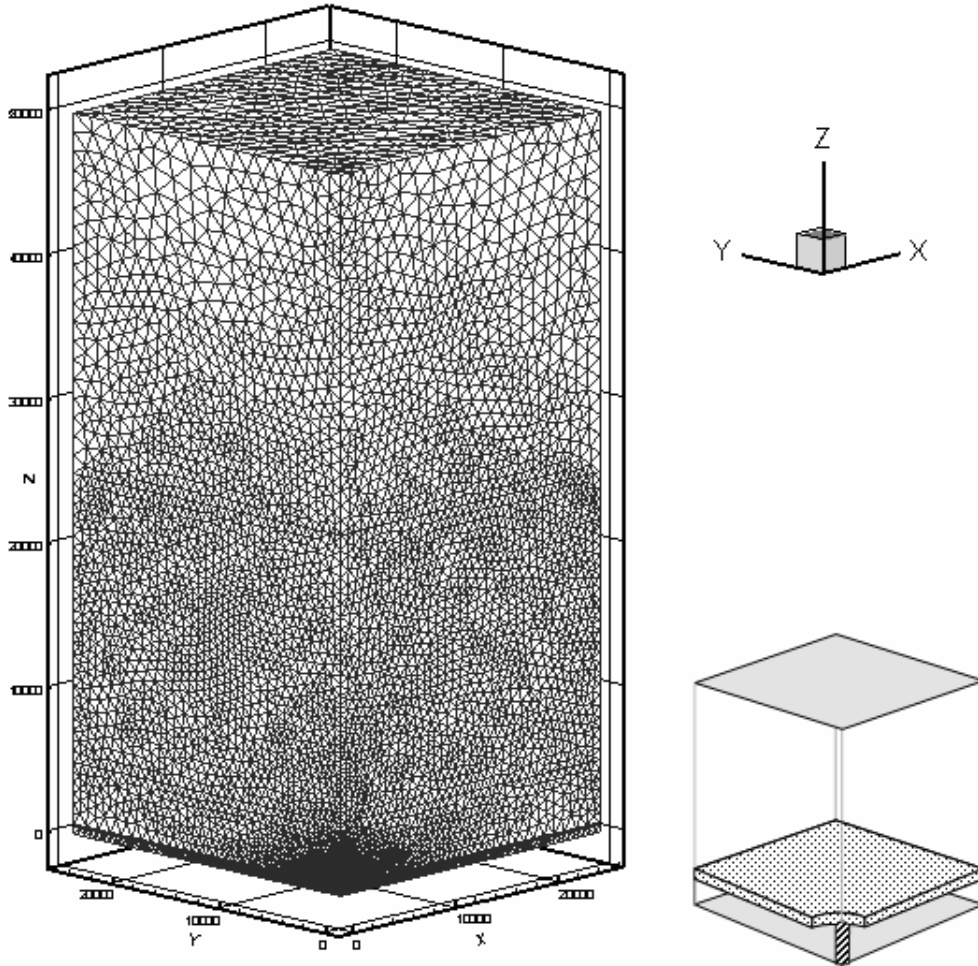


Figure 2.12 Surface mesh distribution of a typical single CNT triode-type field emitter within a periodic cell. Only $\frac{1}{4}$ of a periodic cell is simulated for the study of parallel performance of the Poisson's equation solver

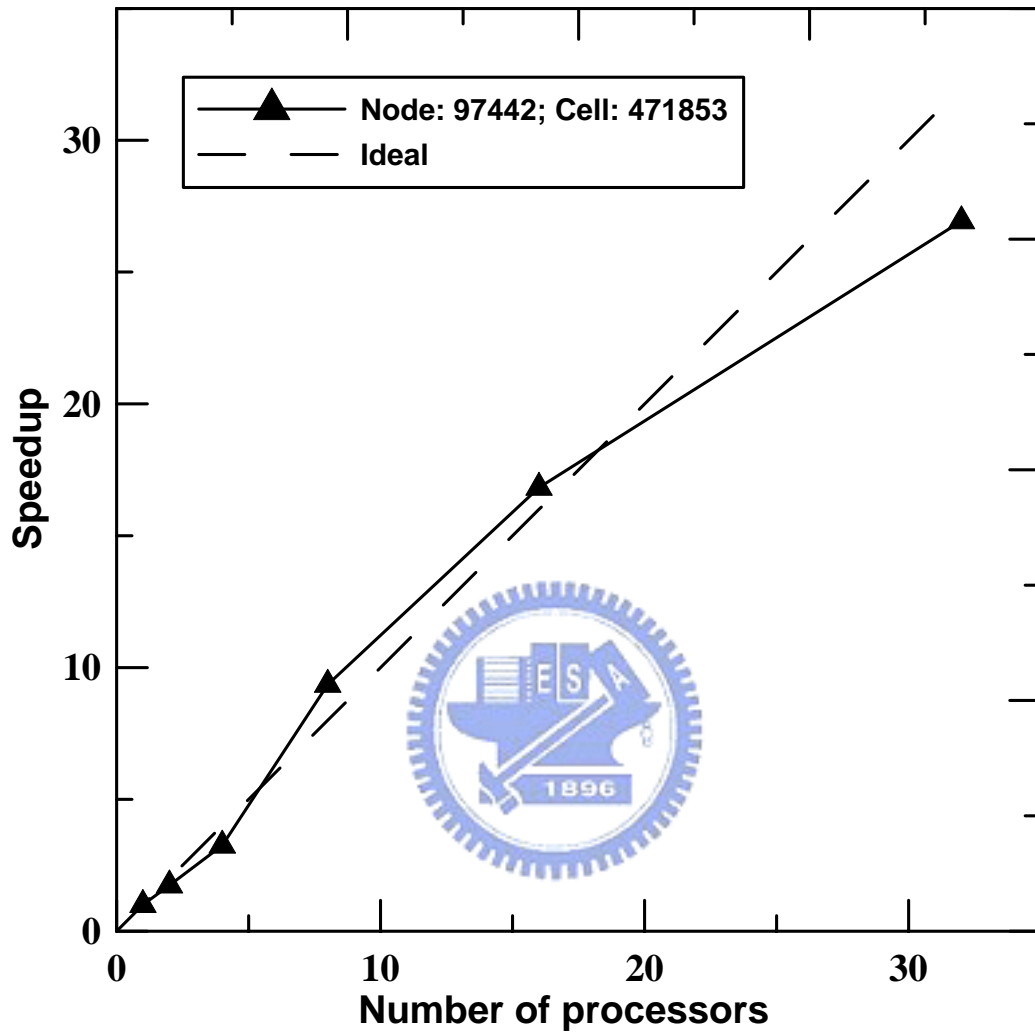


Figure 2.13 Parallel speedup as a function of the number of processors on the PC-cluster system (maximum 32 processors) for CNT triode-type field emitter with gate voltage 150 volts, anode voltage 400 volts and the grounded cathode

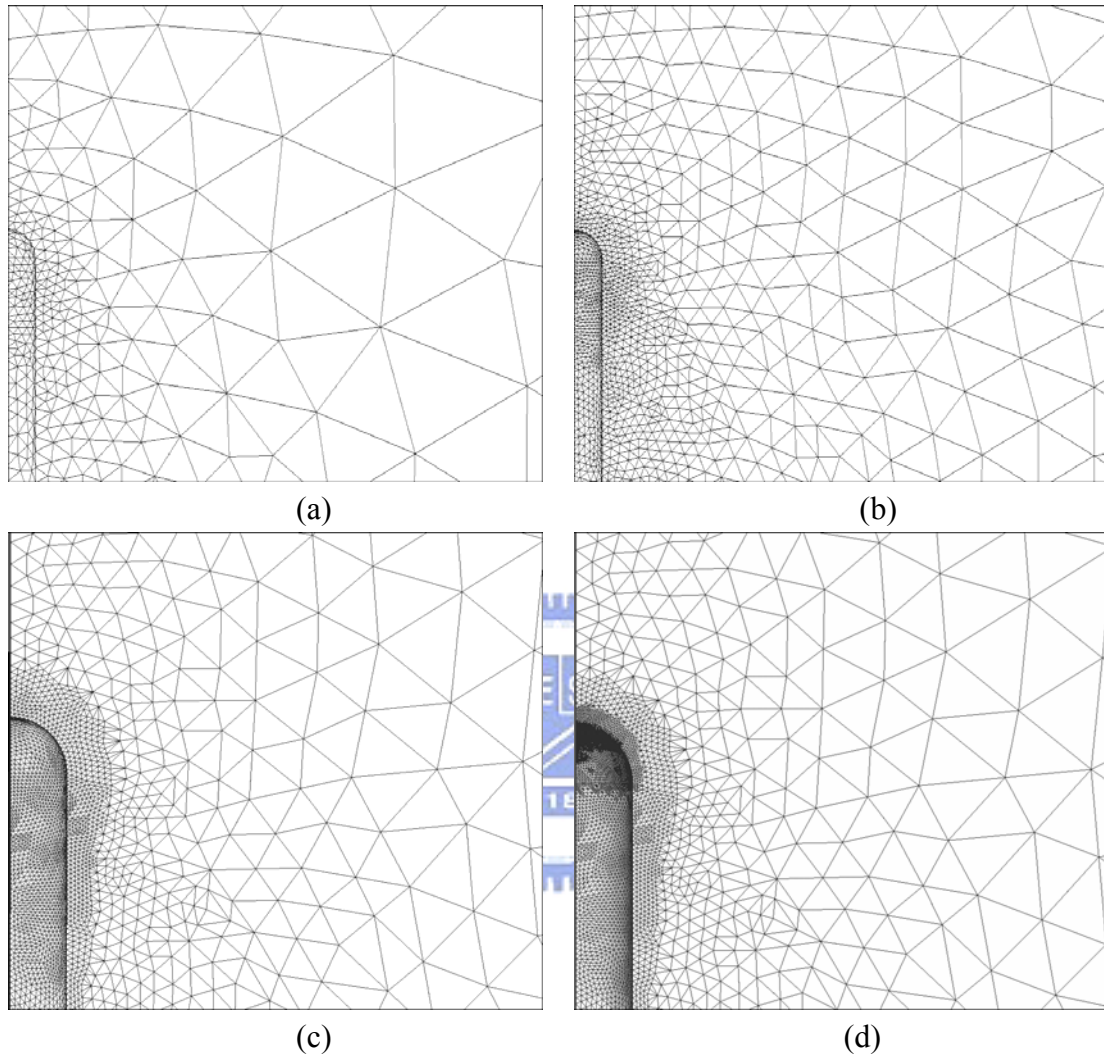


Figure 2.14 Close-up of the unstructured adaptive surface mesh at different levels for a single CNT triode-type field emitter with gate voltage 150 volts, anode voltage 400 volts and the grounded cathode ($\varepsilon_{ref} = 0.08$). (a) Level-0 (7006 nodes). (b) Level-1 (22750 nodes). (c) Level-2 (34927 nodes). (d) Level-5 (61241 nodes).

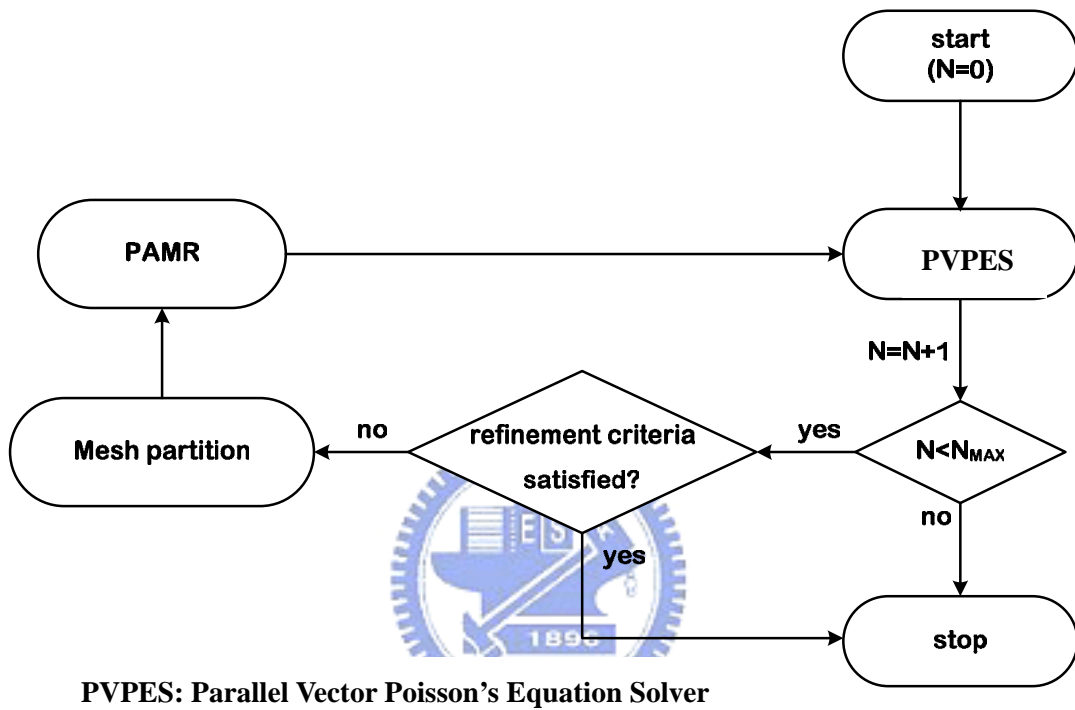


Figure 3.1 Flowchart of the coupled PVPES-PAMR method

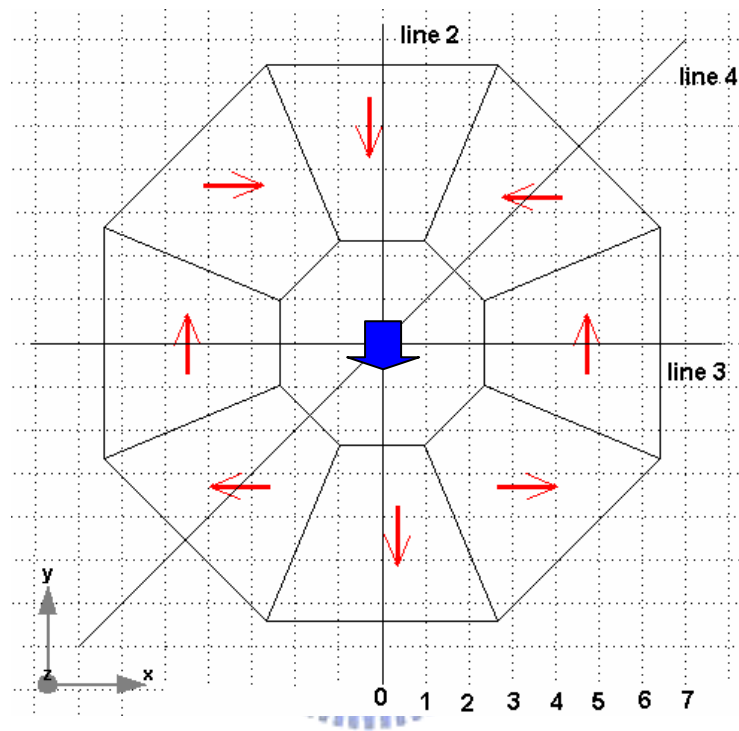


Figure 3.2 Arrangement of magnetization vectors of each permanent magnet segment for producing uniform flux density in the center of the permanent magnet array consisting of eight segments.

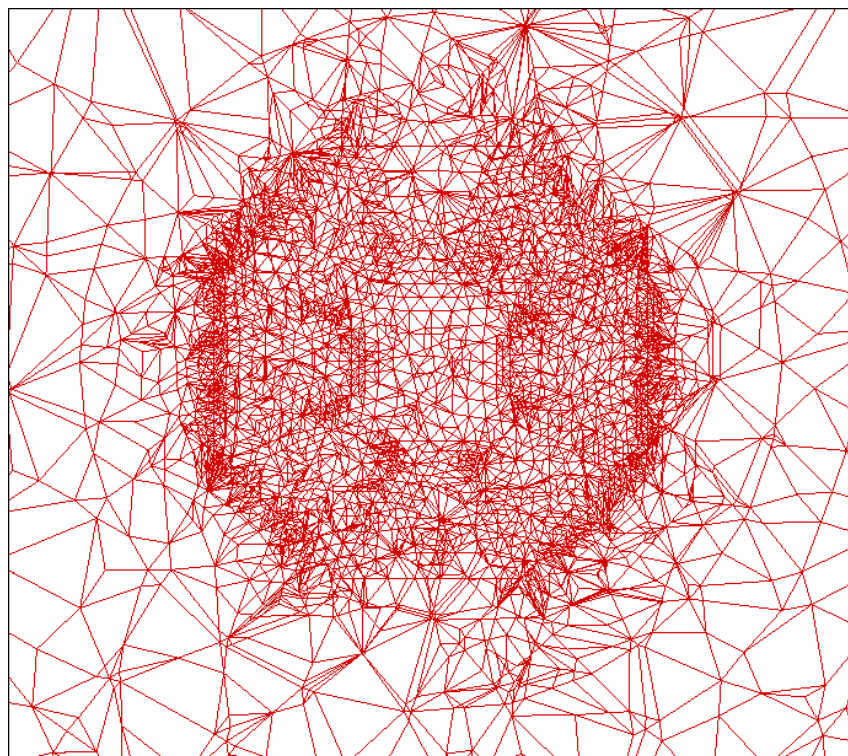


Figure 3.3 Surface mesh distribution of the permanent magnet array consisting of eight segments.

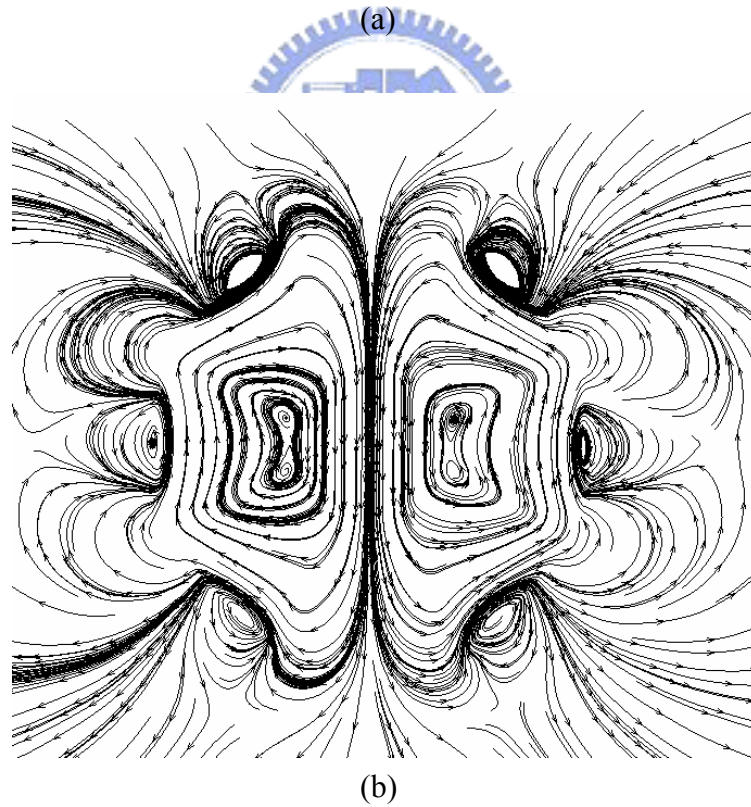
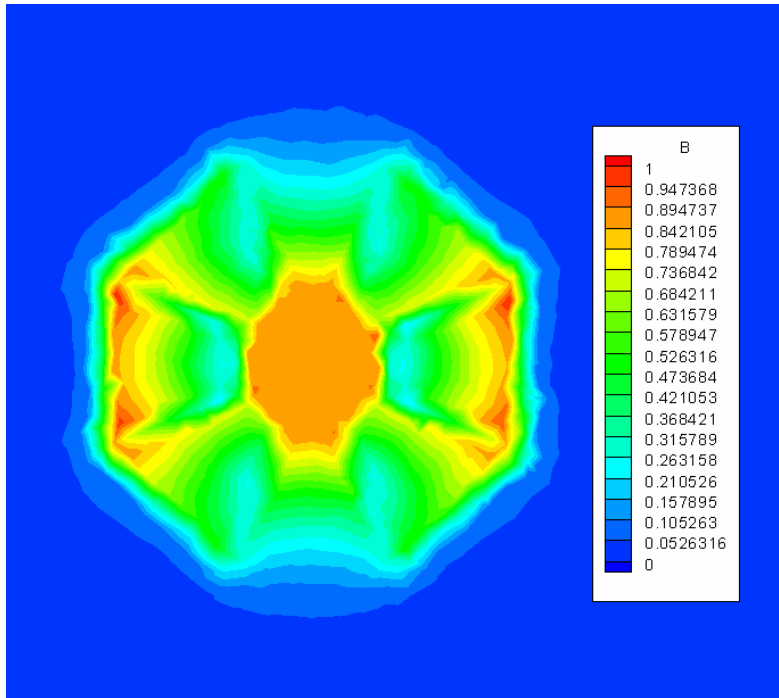


Figure 3.4 (a) Contour of magnetic flux density and (b) magnetic flux lines of permanent magnetic arrays (see Fig. 3.2).

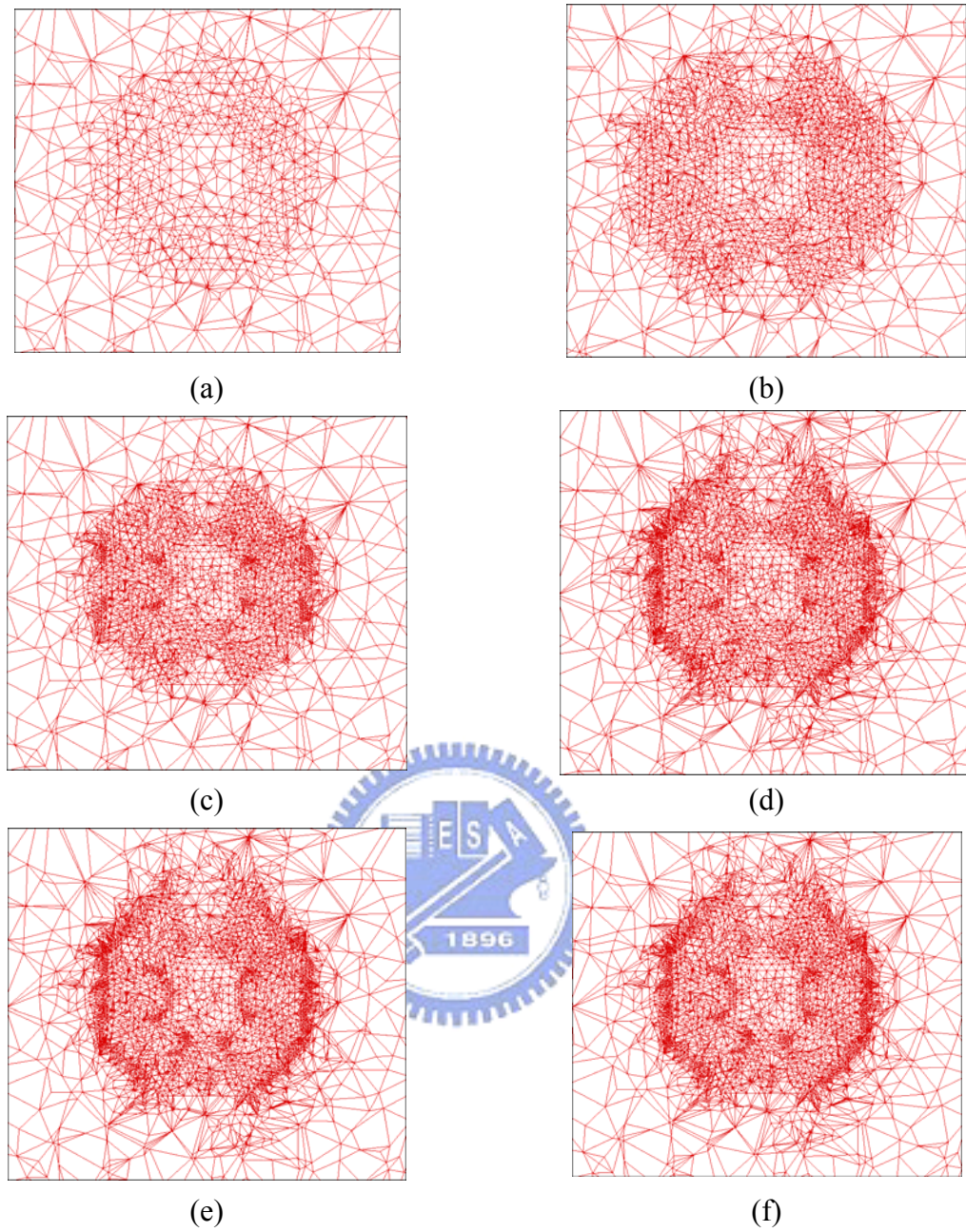


Figure 3.5 Unstructured adaptive mesh distribution at different levels the permanent magnet array consisting of eight segments. ($\varepsilon_{ref} = 0.08$). (a) Level-0 (7845 nodes). (b) Level-1 (38364 nodes). (c) Level-2 (54355 nodes). (d) Level-4 (98743 nodes). (e) Level-5 (108415 nodes). (f) Level-6 (108840 nodes).

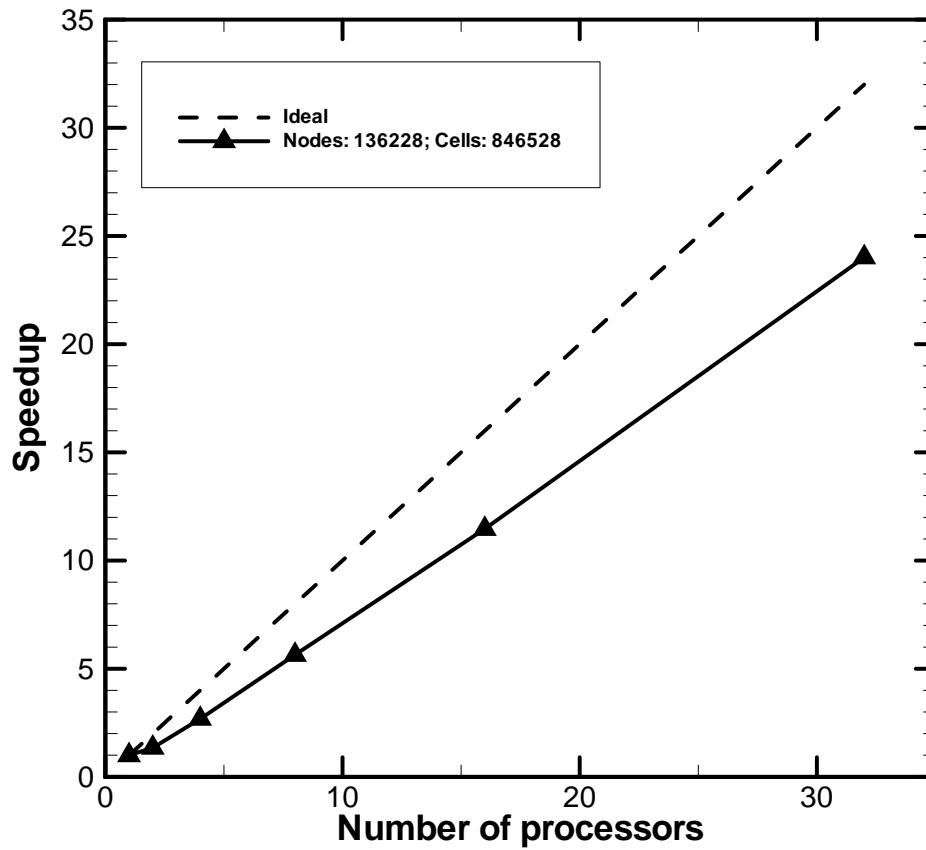


Figure 3.6 Parallel speedup as a function of the number of processors on the PC-cluster system (maximum 32 processors) for of the permanent magnet array consisting of eight segments

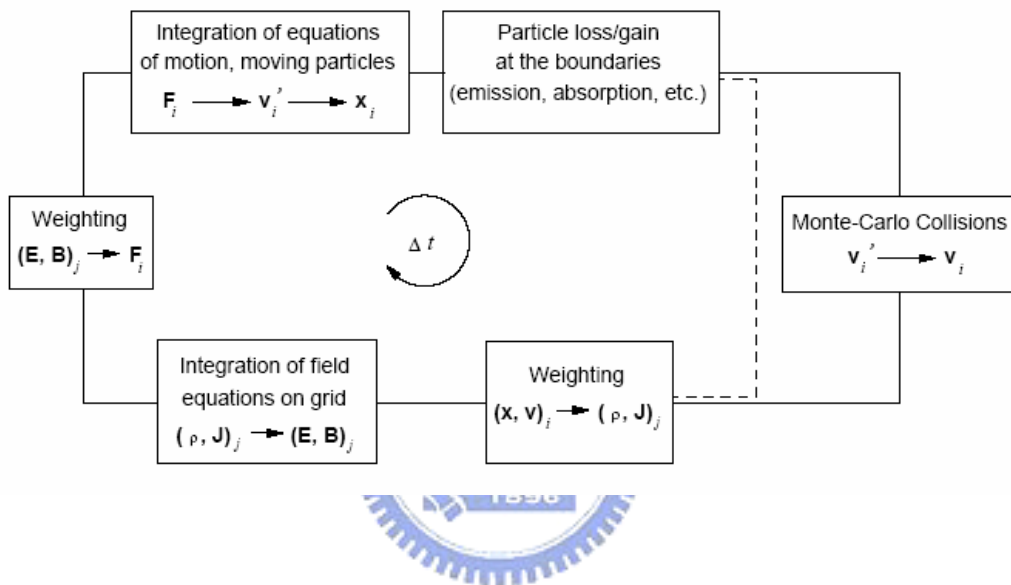


Figure 4.1 The flowchart of conventional PIC-MCC method

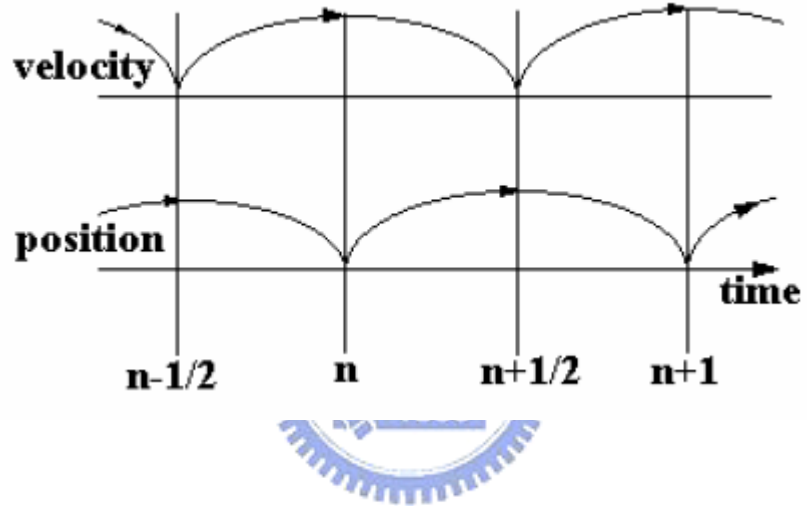


Figure 4.2 Schematic of leap-frog integration method.

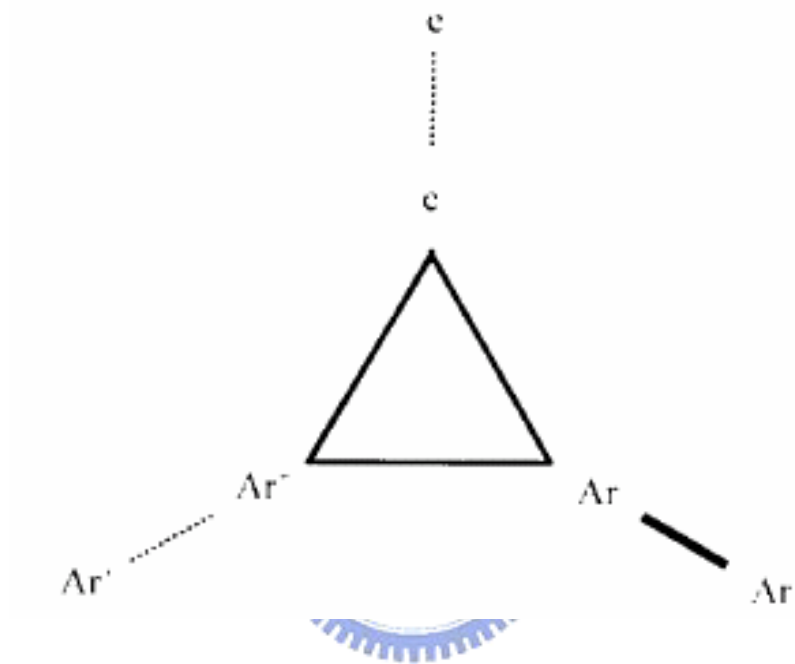


Figure 4.3. Collisions in argon plasma.

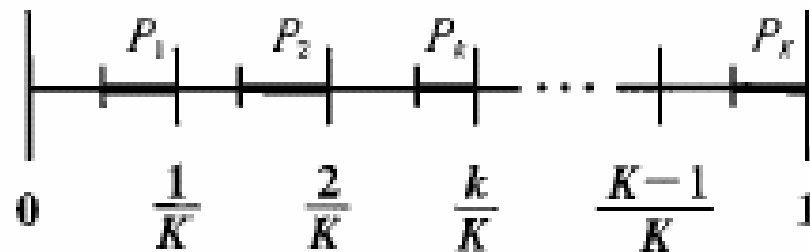


Figure 4.4. Nanbu's method to sample a collisional event.

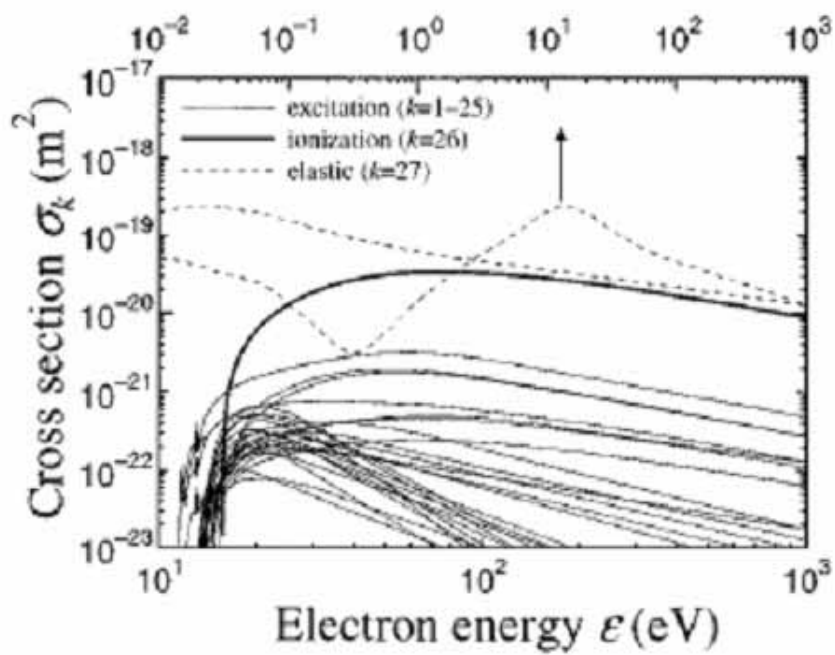


Figure 4.5 The electron-molecule cross sections in argon.

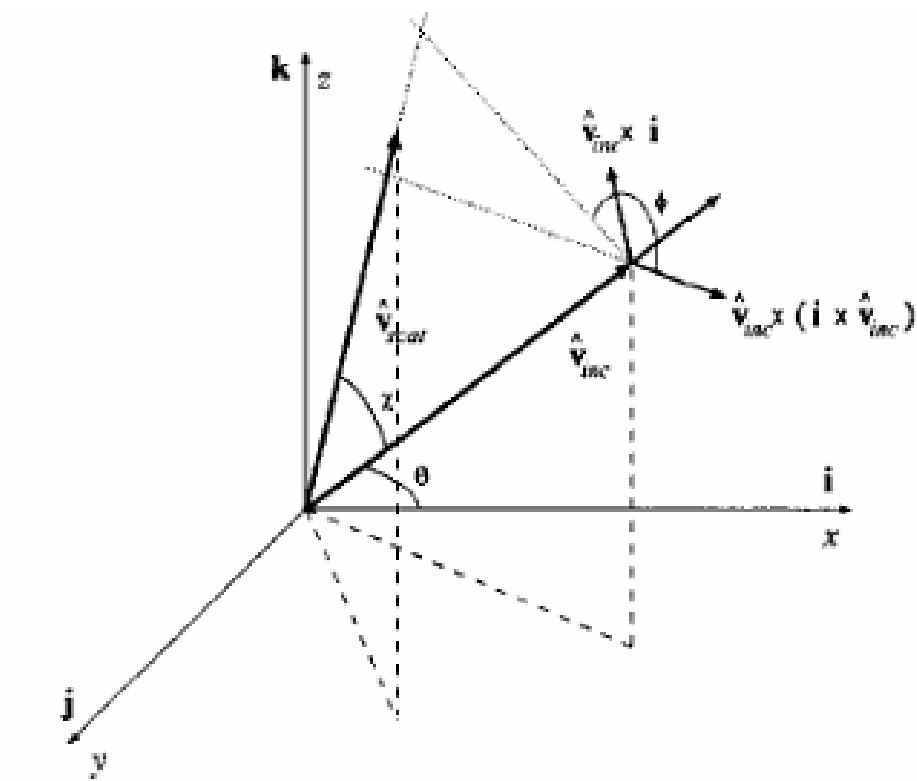


Figure 4.6 Vector diagram for scattering collision.

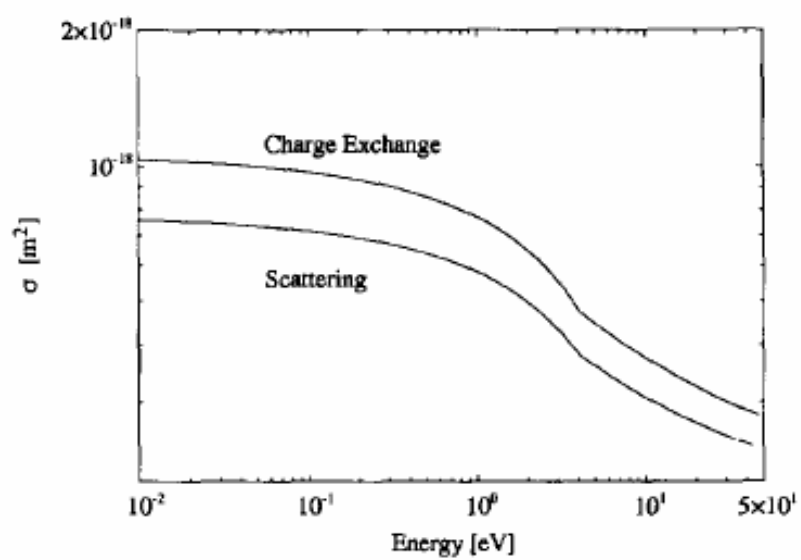


Figure 4.7 The ion-molecule cross sections in argon.

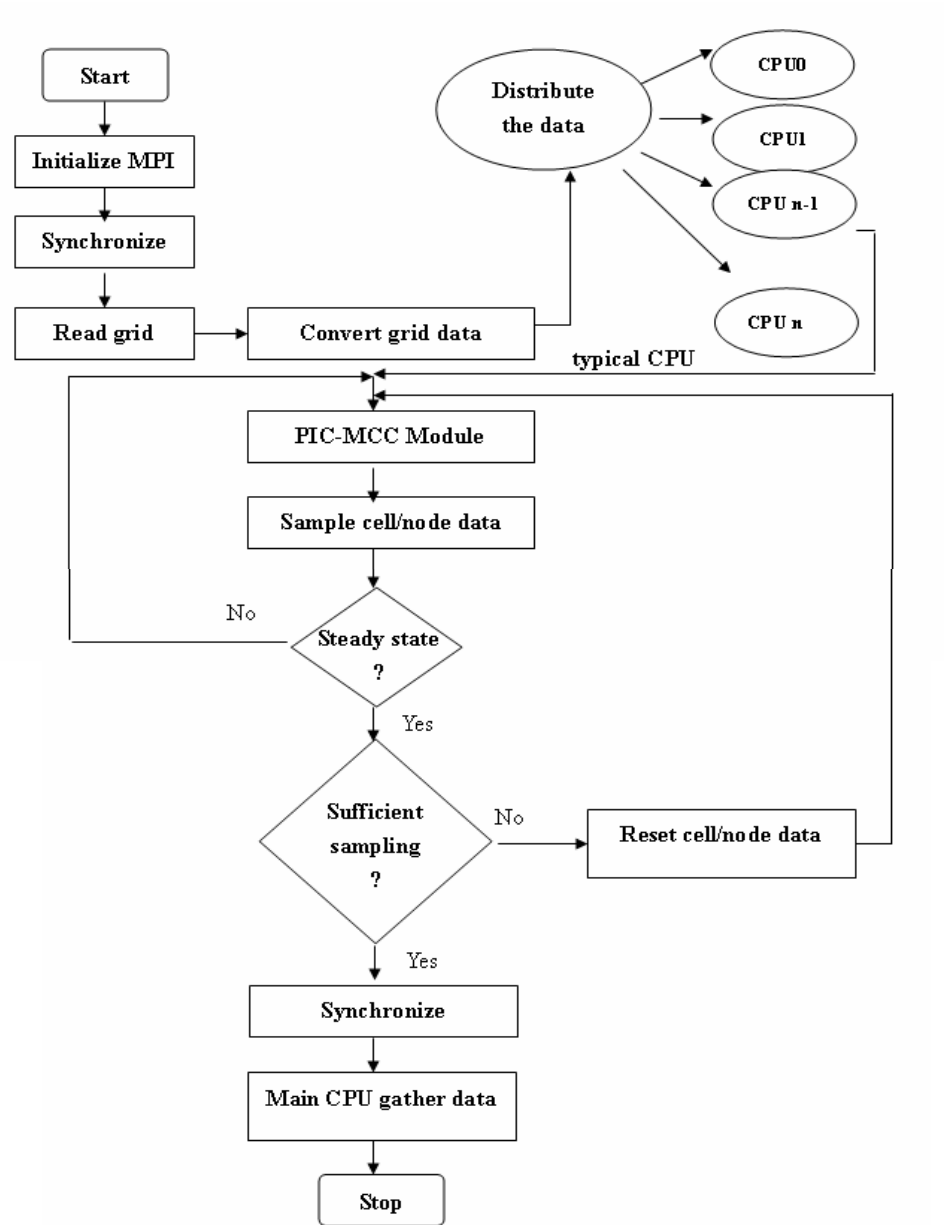


Figure 4.8 Flowchart of parallel PIC-FEM.

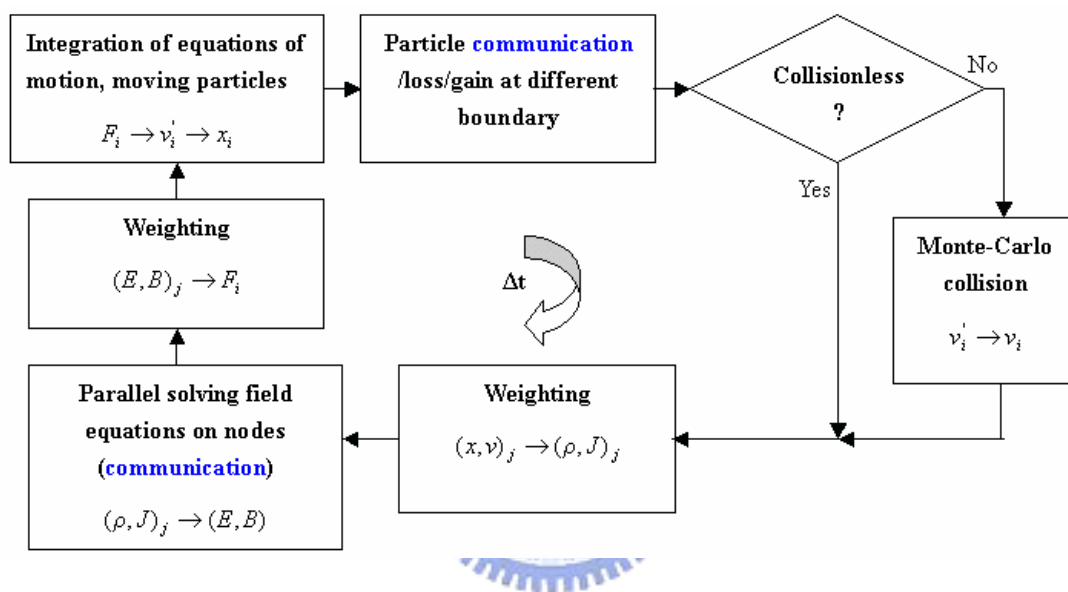


Figure 4.9 PIC-MCC module of parallel PIC-FEM.

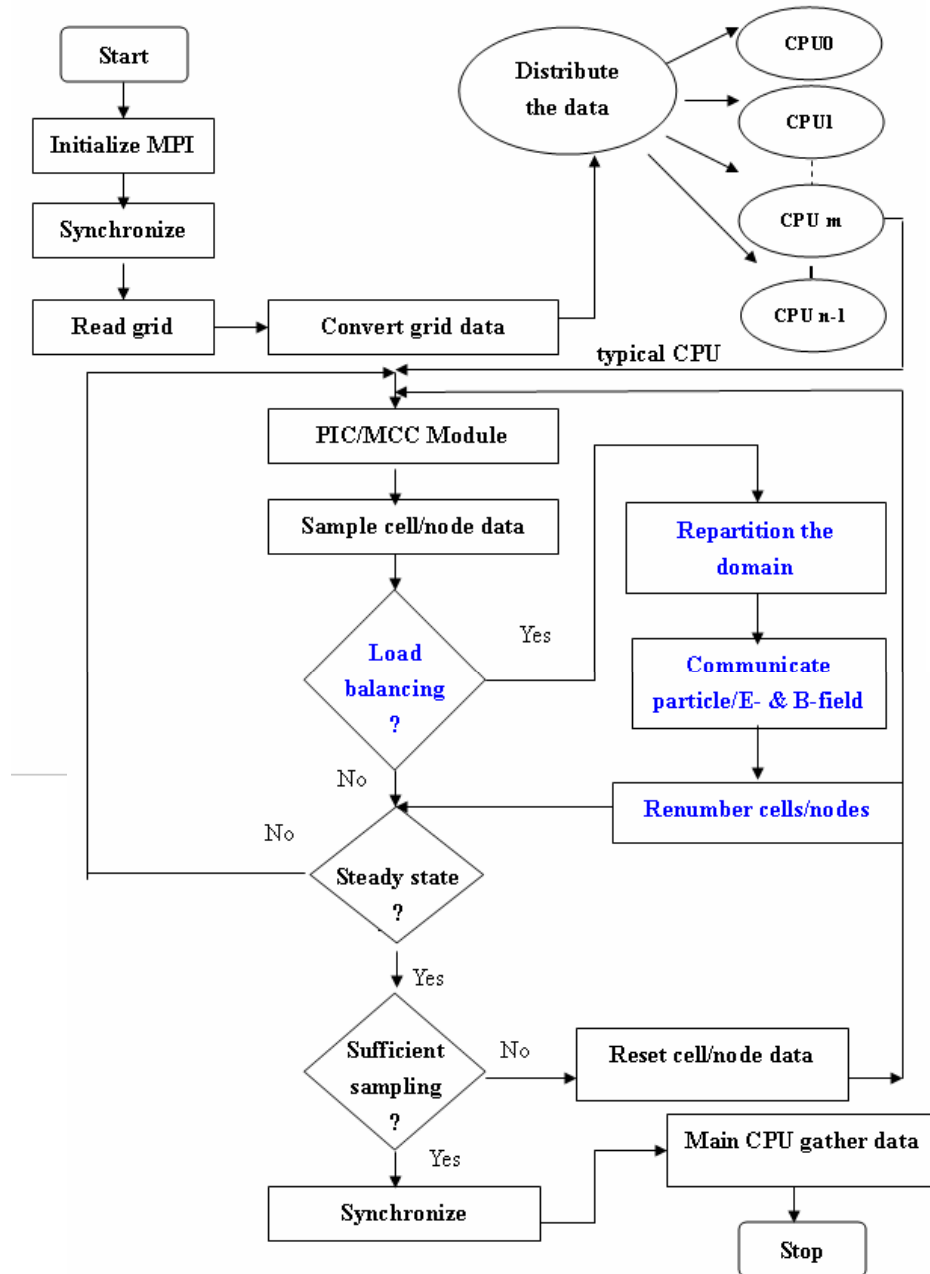


Figure 4.10 Flowchart of parallel PIC-FEM with dynamic domain decomposition

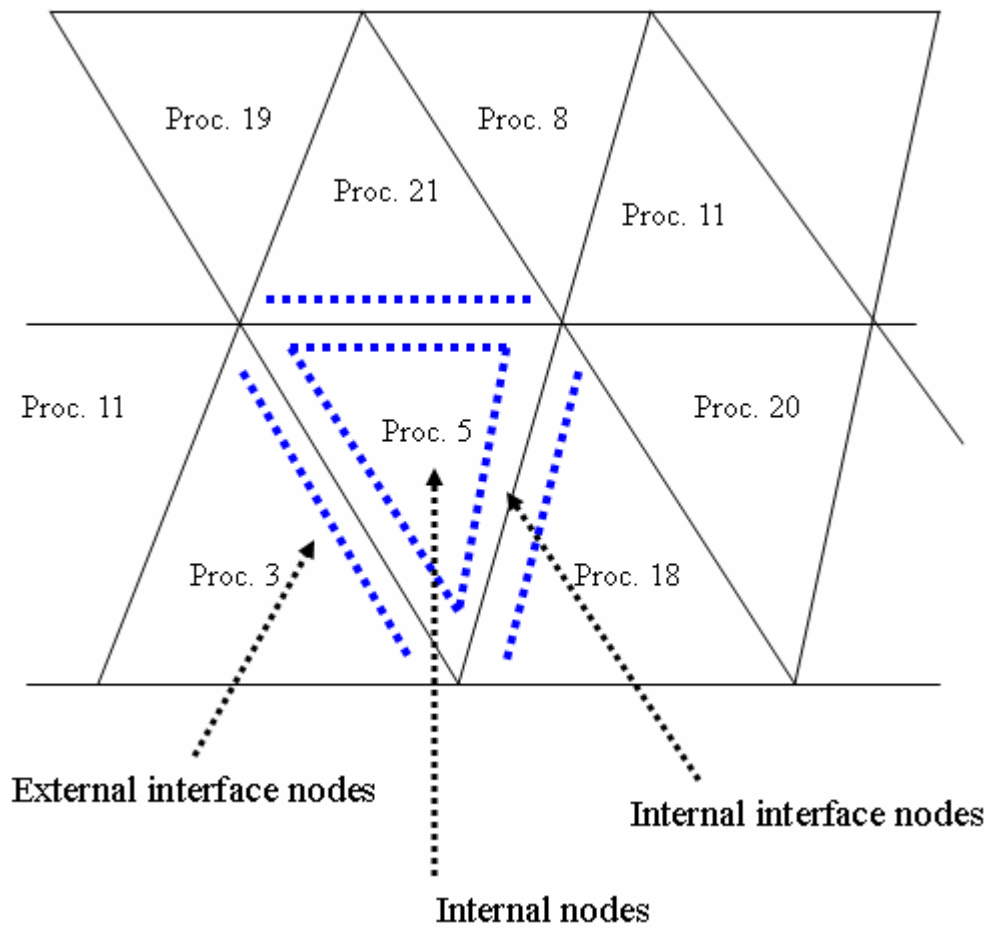


Figure 4.11 Sketch of the decomposed domain and the local data structure.

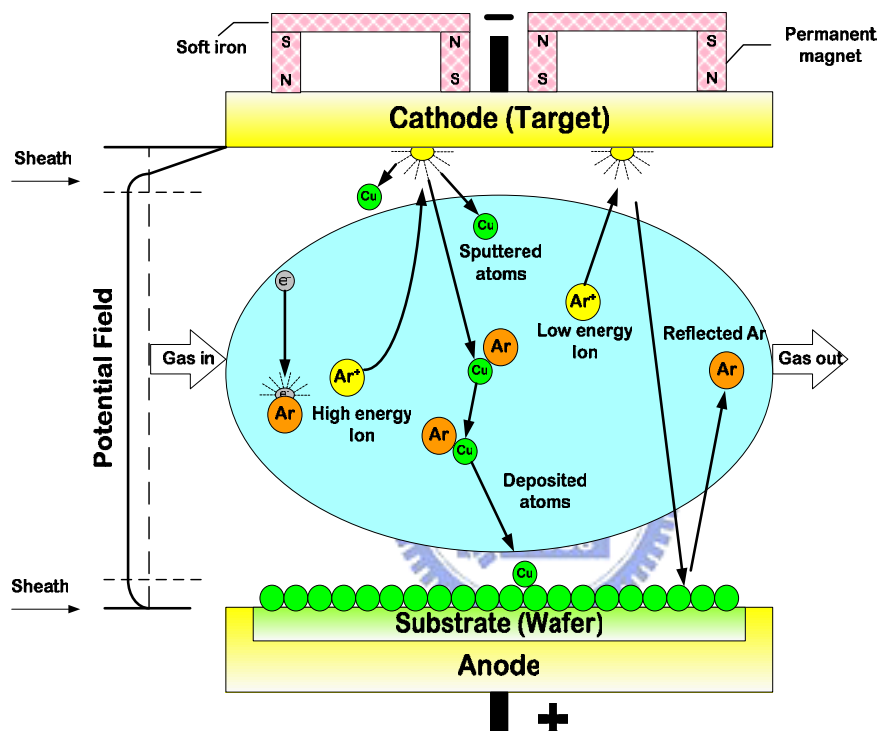
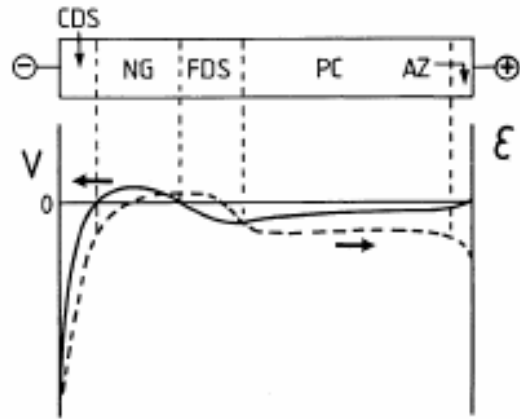
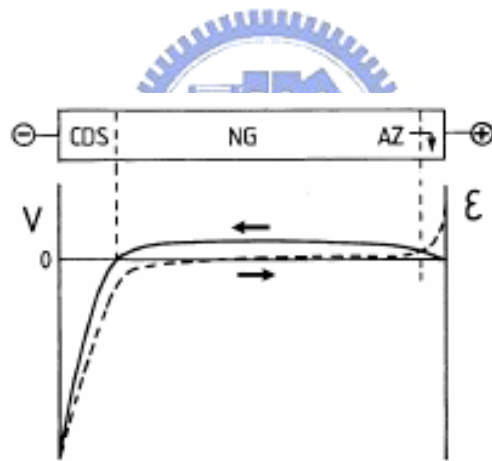


Figure 4.12 Schematic overview of the basic plasma processes in a magnetron glow discharge

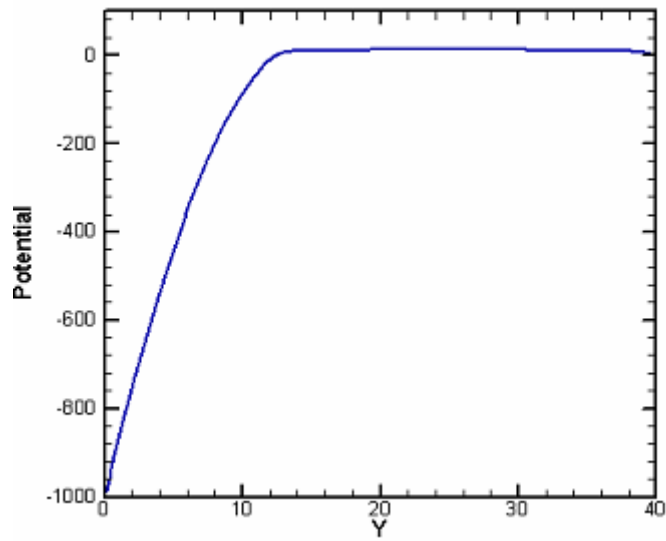


(a)

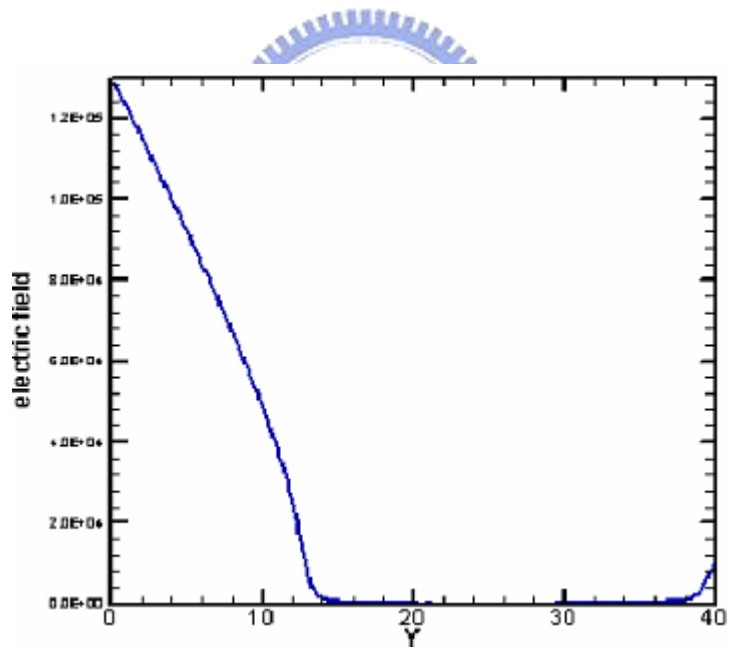


(b)

Figure 4.13 Schematic diagram of the spatial regions present in DC glow discharges, (a) at short cathode–anode distance and/or low pressure; (b) at longer interelectrode distance and/or higher pressure.



(a)



(b)

Figure 4.14 (a) Potential and (b) electric profiles of quasi-1D DC glow discharge.

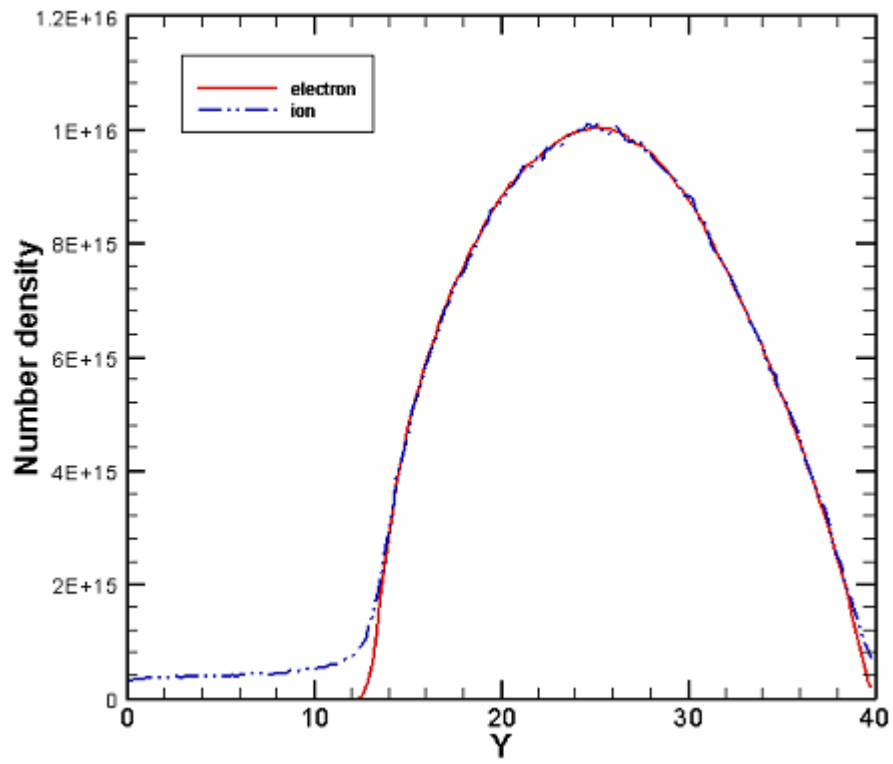


Figure 4.15 Ion and electron number densities of quasi-1D DC glow discharge

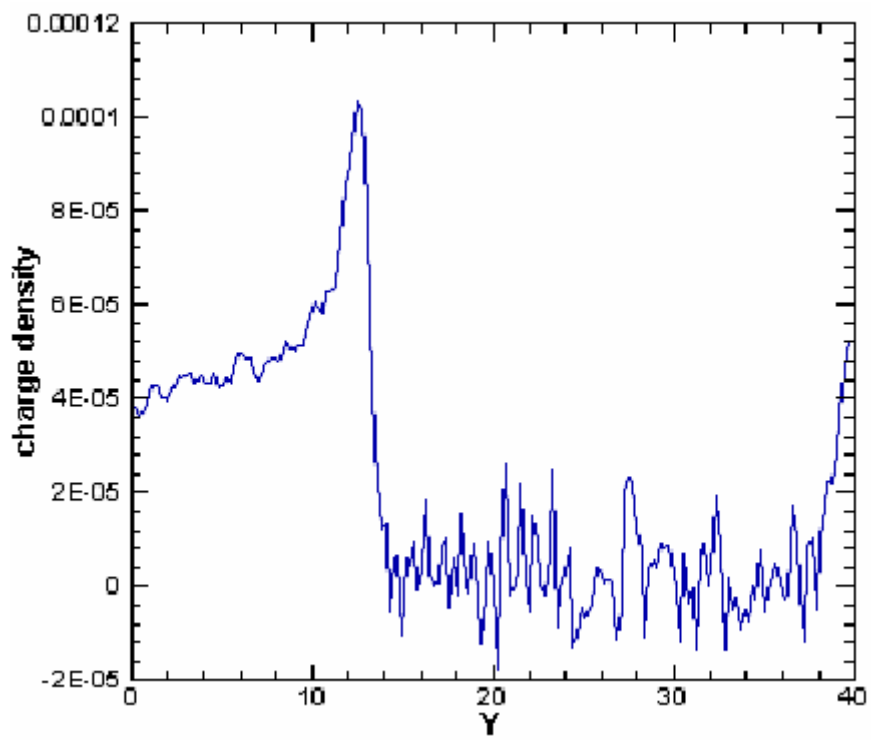


Figure 4.16 The net charge density of quasi-1D DC glow discharge.

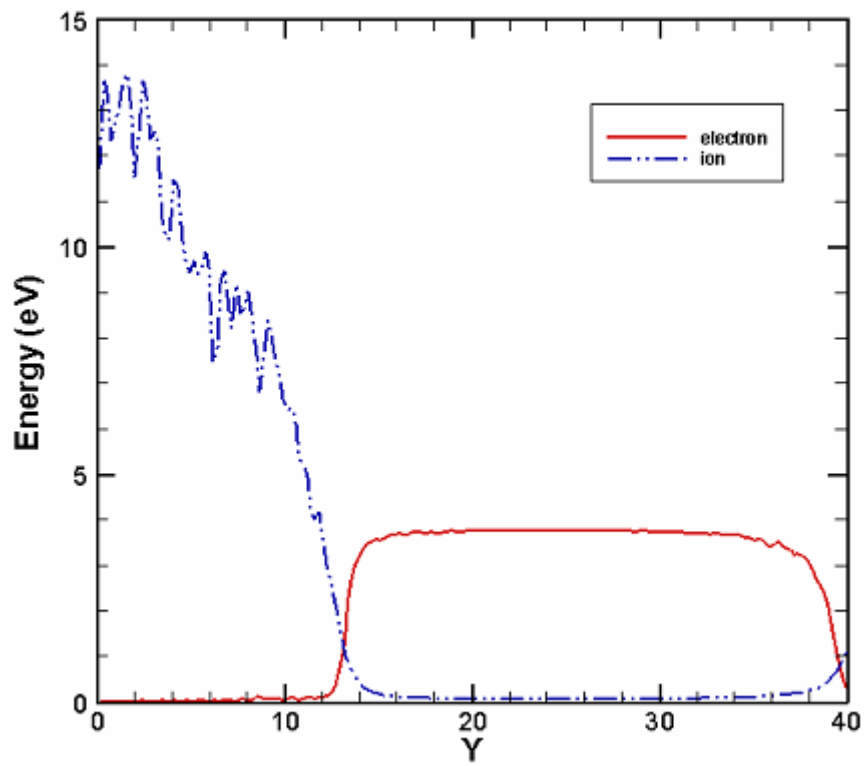


Figure 4.17 Ion and electron kinetic energies of quasi-1D DC glow discharge

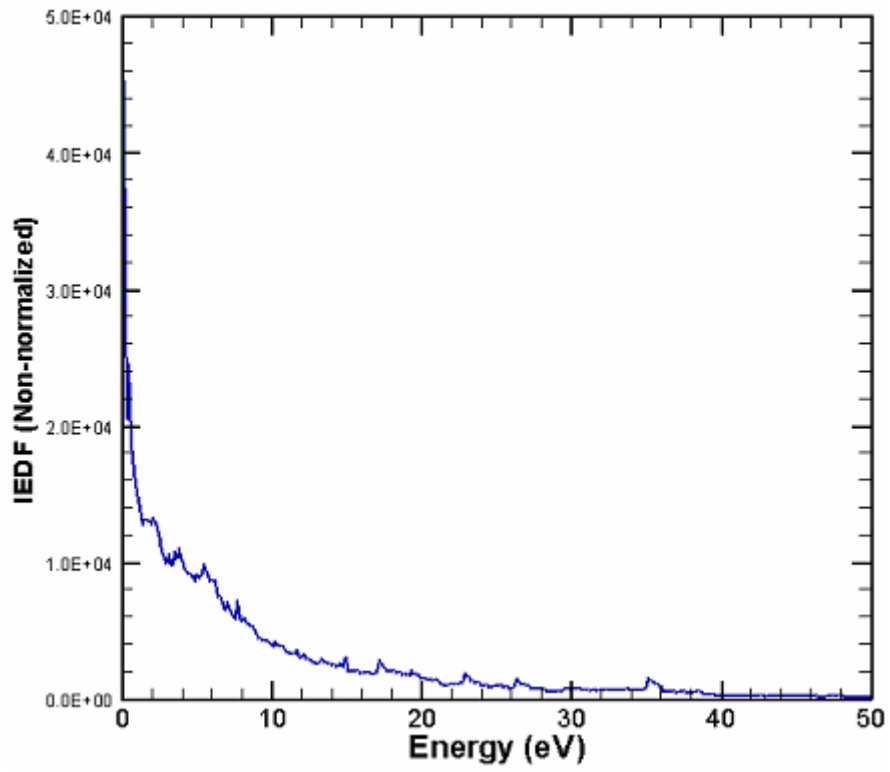


Figure 4.18 Energy distribution functions of a impinging on the cathode of quasi-1D DC glow discharge.

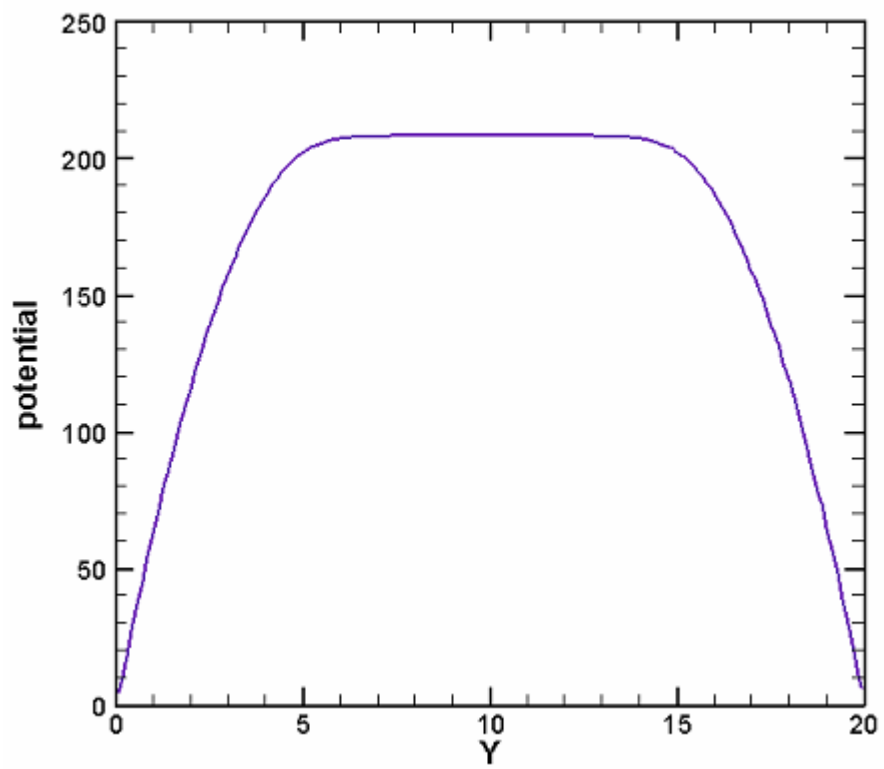


Figure 4.19 The potential profile of quasi-1D RF glow discharge

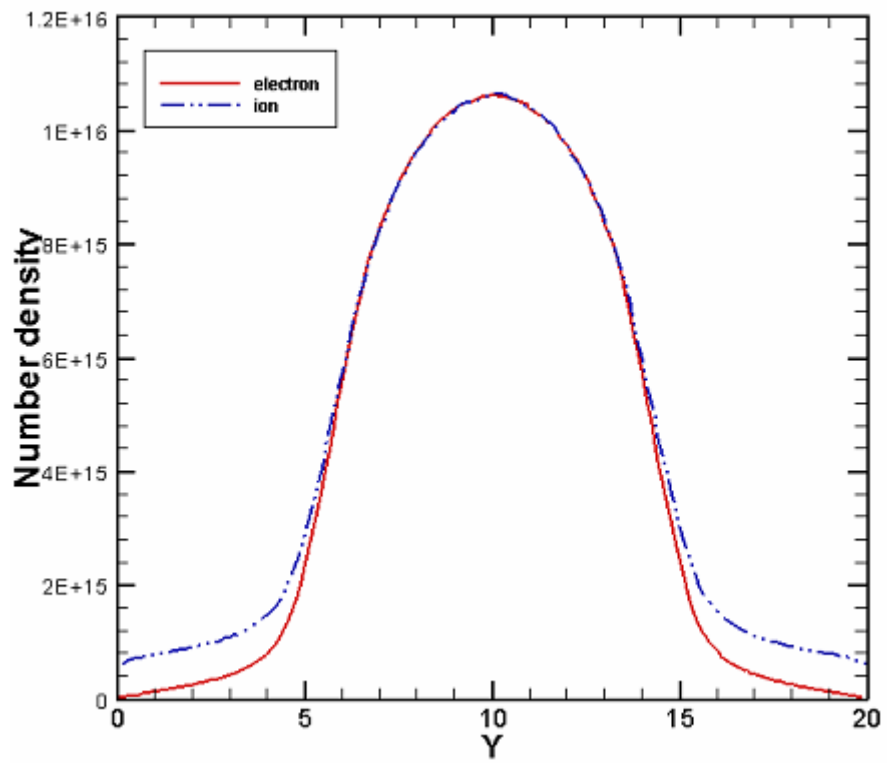


Figure 4.20 Ion and electron number densities of quasi-1D RF glow discharge.

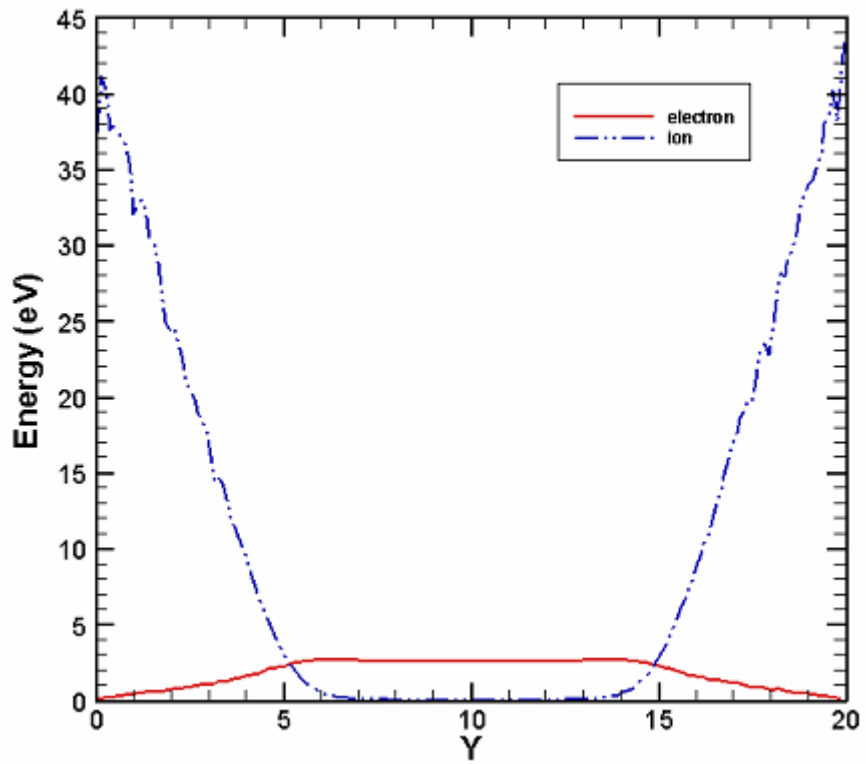
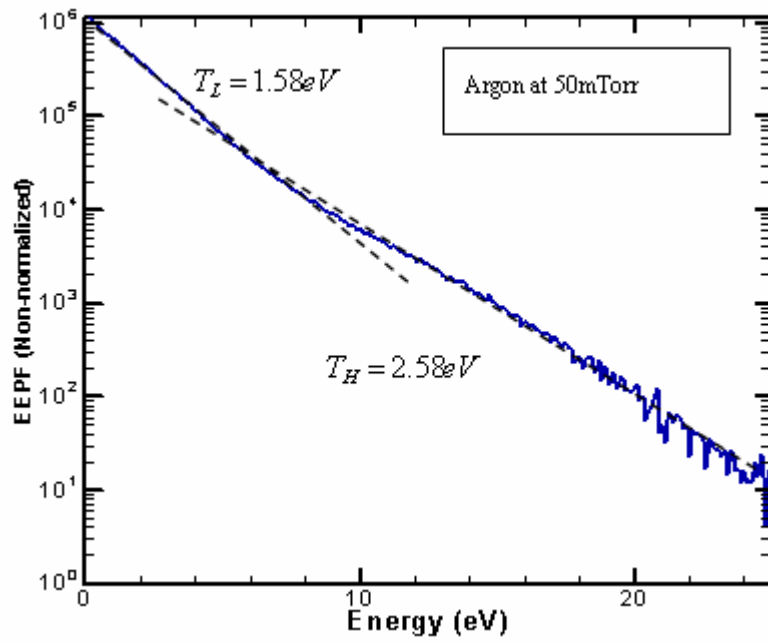
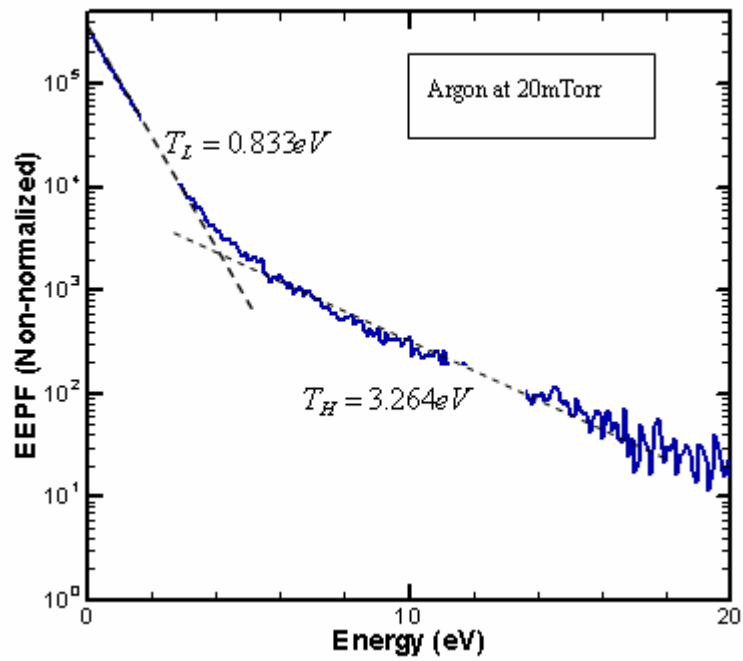


Figure 4.21 Ion and electron kinetic energies of quasi-1D DC glow discharge



(a)



(b)

Figure 4.22 Electron energy probability functions of (a) 50mtorr and (b) 20mtorr in the bulk region of quasi-1D DC glow discharge.

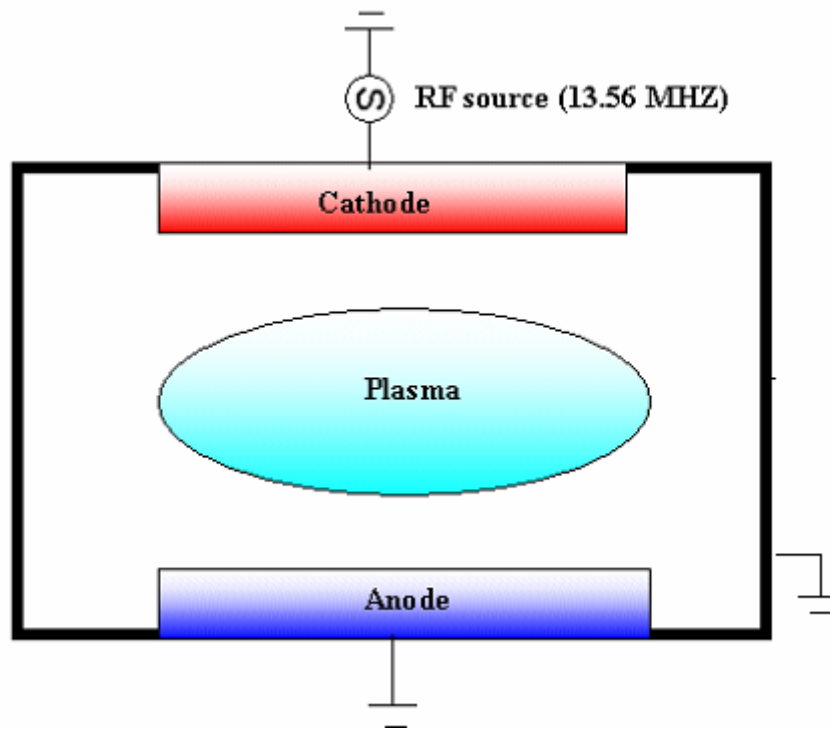


Figure 4.23 Sketch of the 3D RF gas discharge plasma.

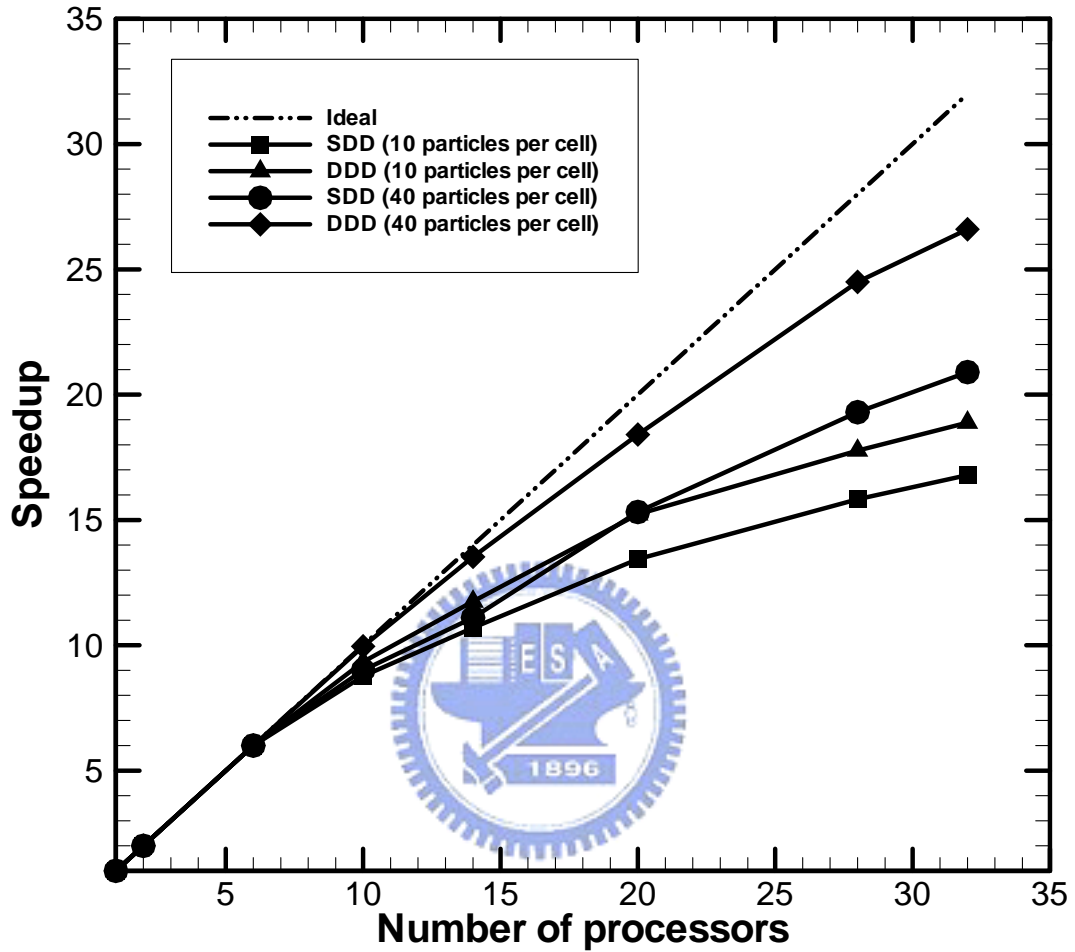
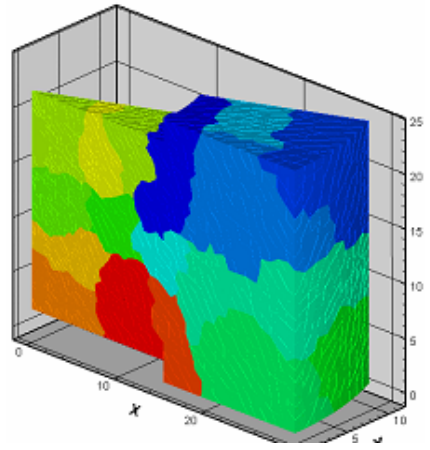
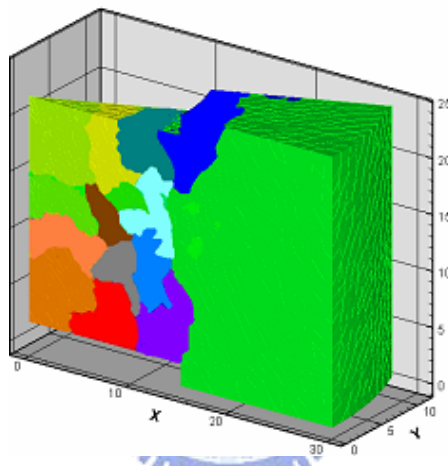


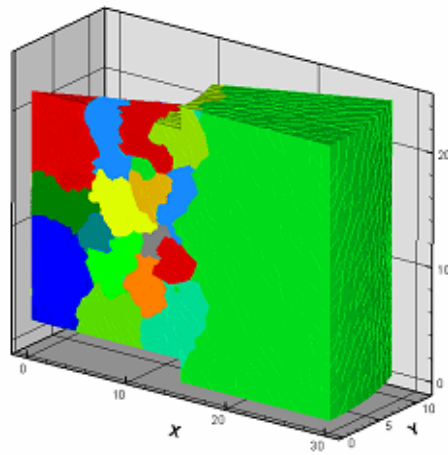
Figure 4.24 Parallel speedup as a function of number of processors for 3D RF plasma at different numbers of particle on HP IA-64 clusters machine (maximum 32 processors).



(a)

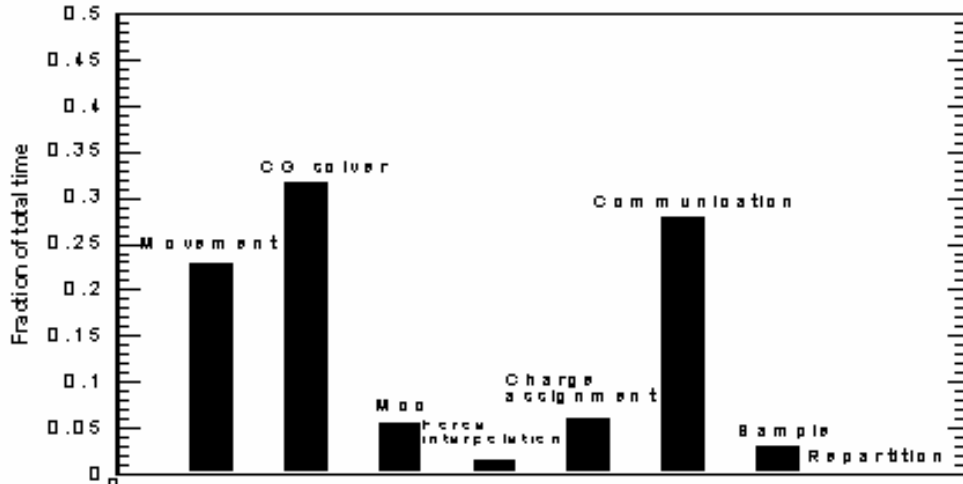


(b)

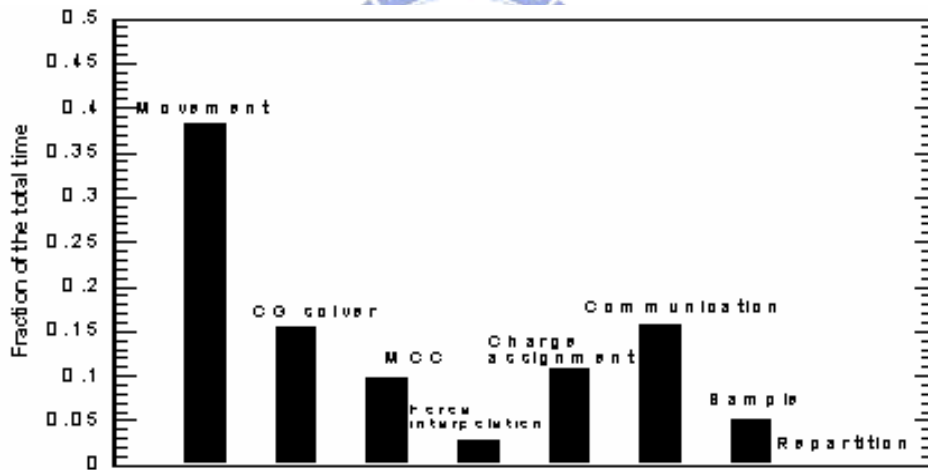


(c)

Figure 4.25 Evolution of domain decomposition using 20 processors, during the simulation for a RF gas discharge plasma (a) initial (b) intermediate (c) final.



(a)



(b)

Figure 4.26 Time breakdown of various steps in PIC-FEM on 32 processors with (a) 10 particles per cell (b) 40 particles per cell.

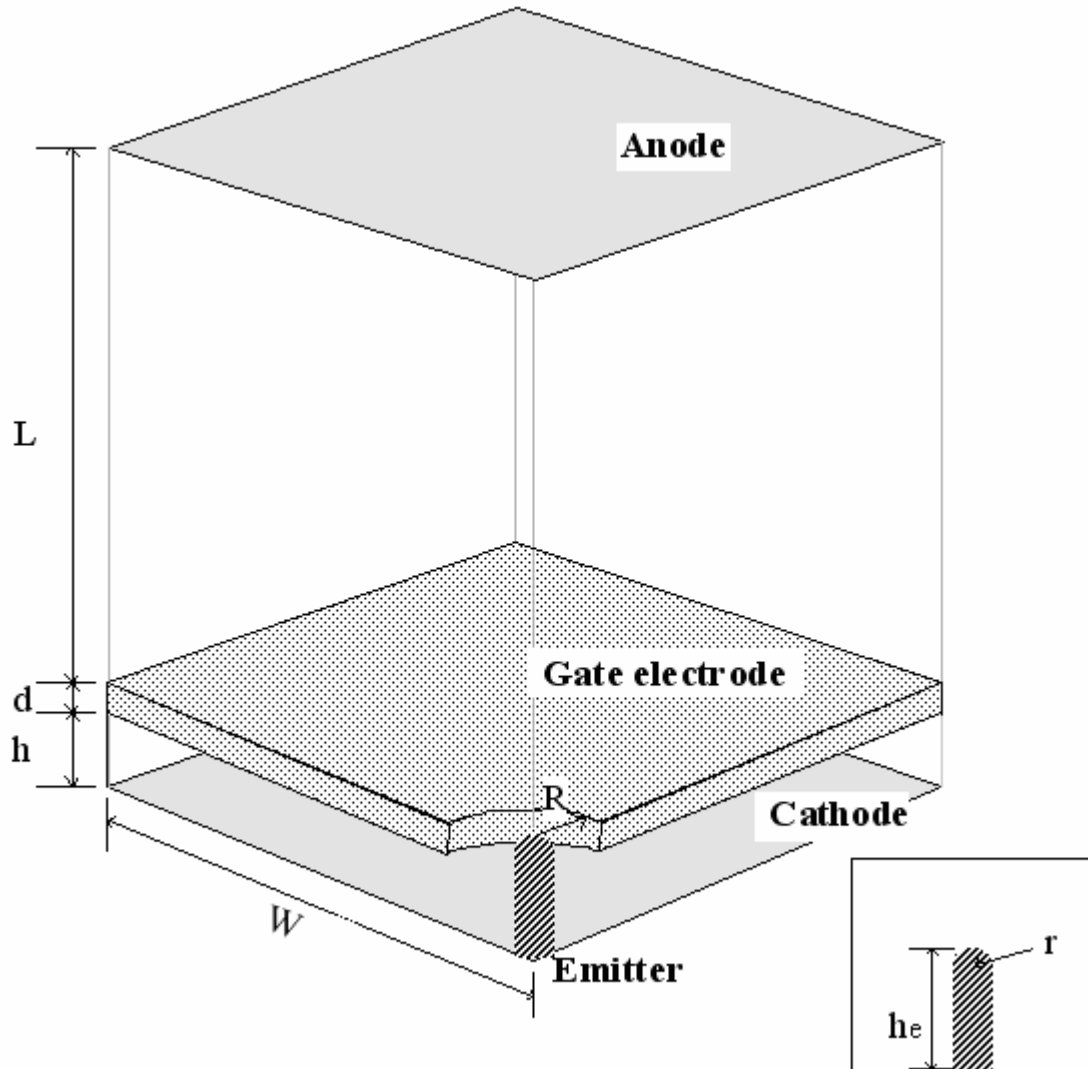
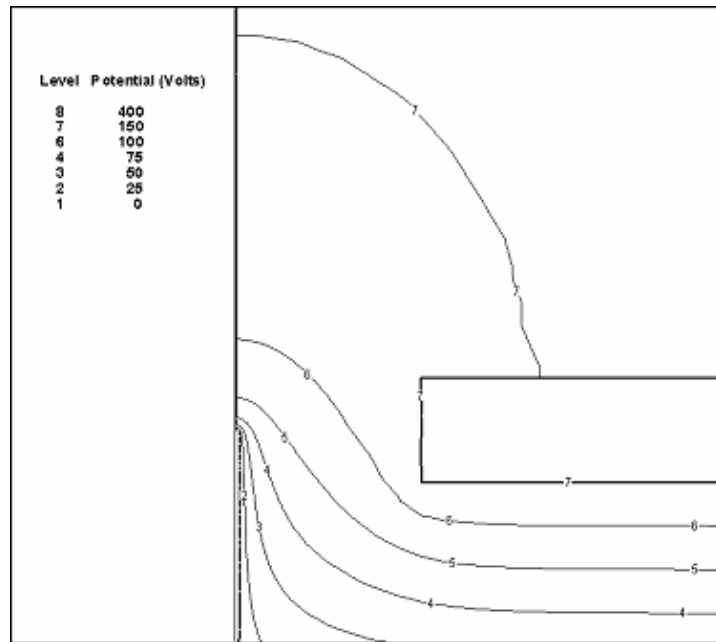
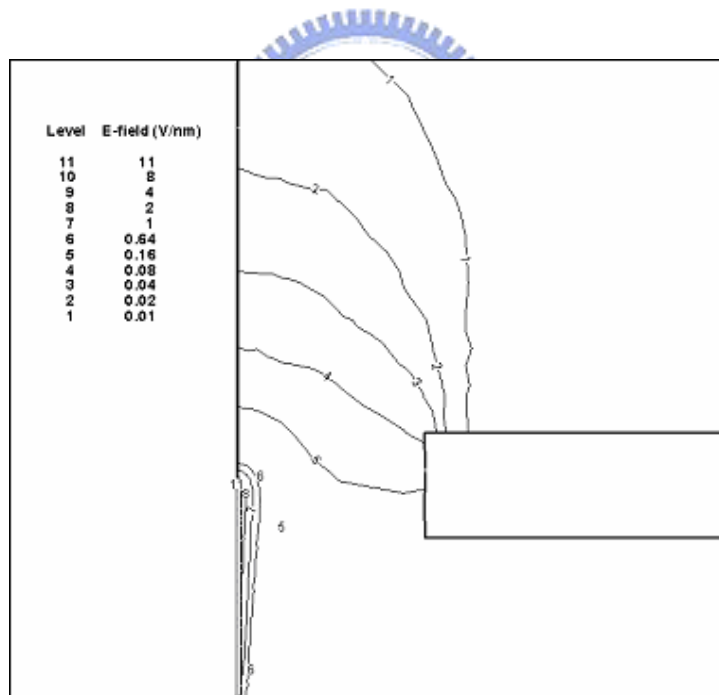


Figure 5.1 Schematic diagram of the simulation domain for a typical CNT triode-type field emitter within a periodic cell. The important geometrical parameters are: $R=500$ nm, $r=10$ nm, $he=600$ nm, $h=500$ nm, $L=49.3 \mu\text{m}$, $d=200$ nm and $W=25 \mu\text{m}$.



(a)



(b)

Figure 5.2 Contours of the (a) electric potential and the (b) electric field distribution near the tip of the CNT triode-type field emitter with gate voltage 150 volts, anode voltage 400 volts and the grounded cathode.

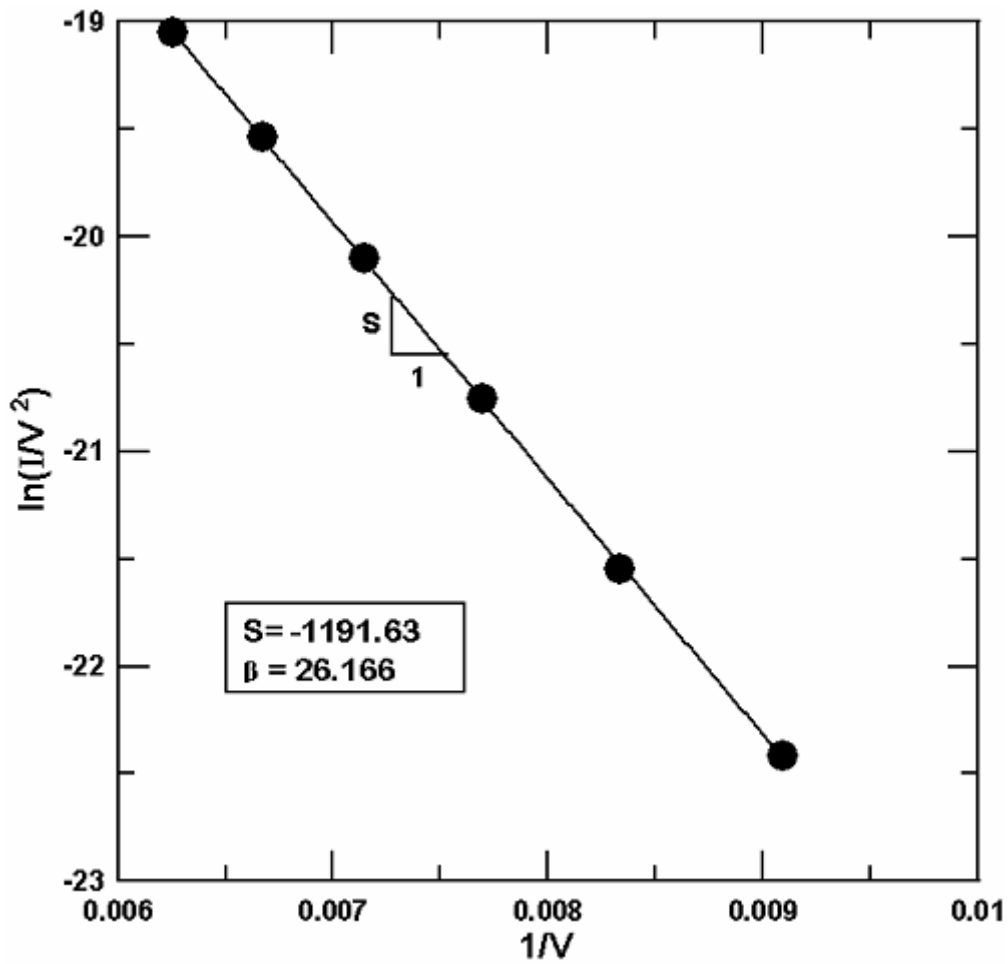


Figure 5.3 FN plot of the field emission characteristics of CNT triode-type field emitter (height is 600 nm) with gate voltage 110-160 volts, anode voltage 400 volts and the grounded cathode. ($S \equiv slope = -3244.25 \phi^{3/2} / \beta$, $\phi = 4.52$ eV).

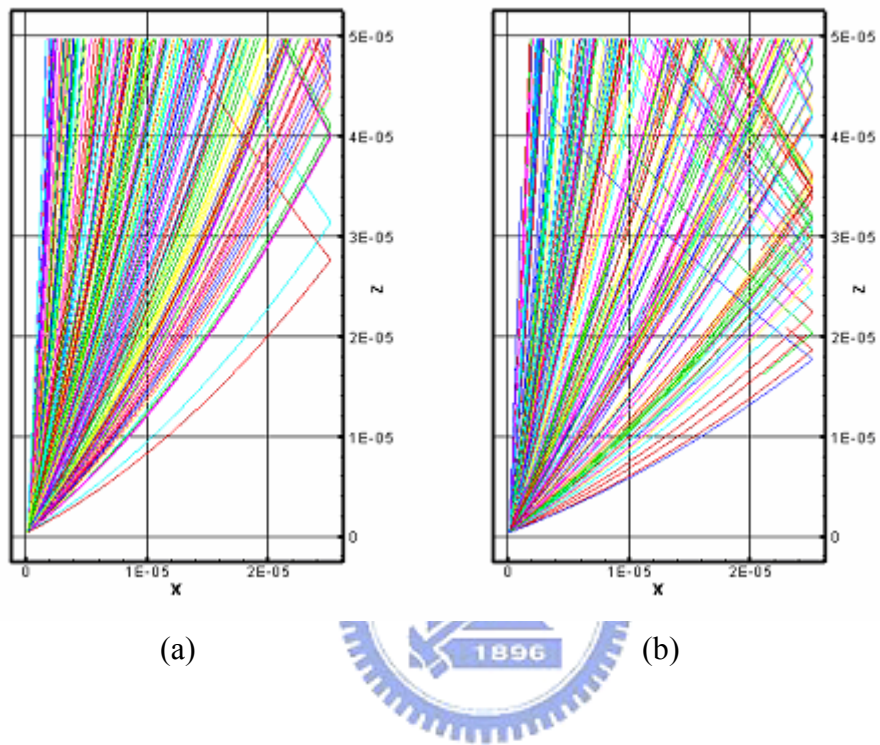


Figure 5.4 Trajectories of the emitted electrons inside the periodic cell of CNT triode-type field emitter with the grounded cathode, anode voltage 400 volts and two different gate voltages: (a) 110 volts (b) 160 volts.

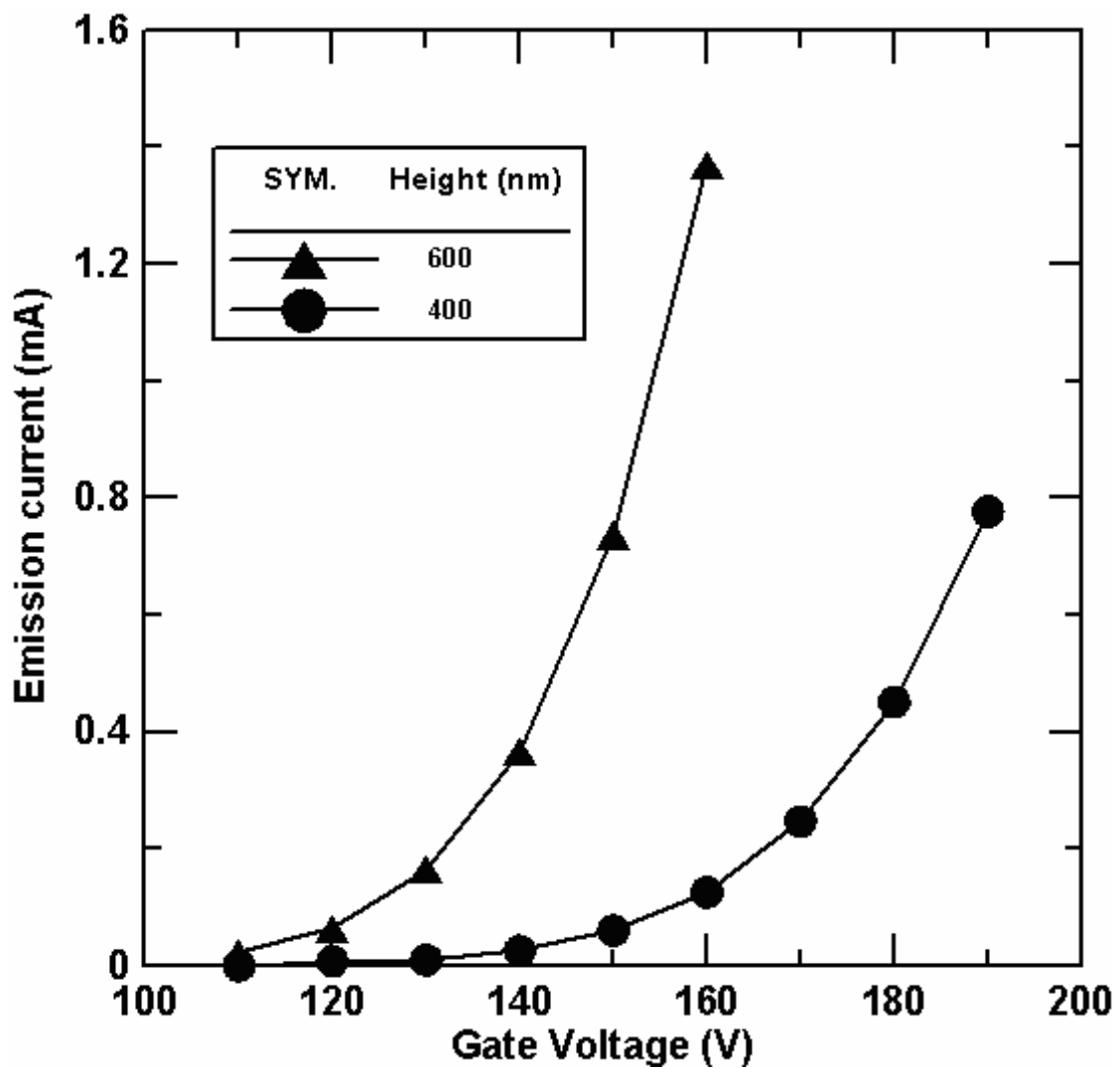


Figure 5.5 Effect of the gate voltage on the emission current for two different CNT triode-type field emitter heights with anode voltage 400 volts and the grounded cathode.

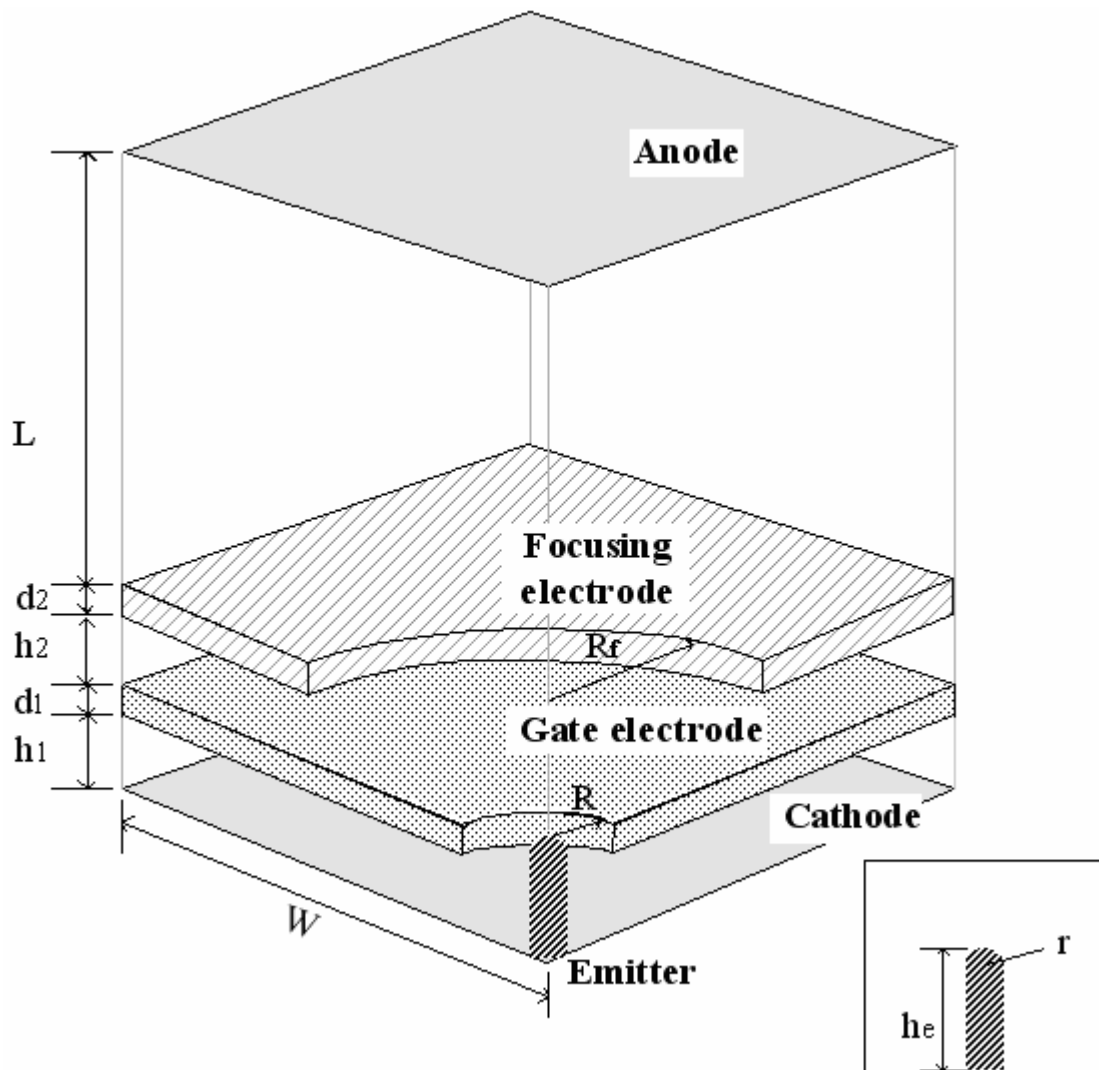


Figure 5.6 Schematic diagram of the simulation domain for a typical CNT tetrode-type field emitter within a periodic cell. The important parameters are: $R=500$ nm, $R_f=1500$ nm, $r=10$ nm, $h_e=600$ nm, $h_1=500$ nm, $h_2=500$ nm, $L=48.6 \mu\text{m}$, $d_1=200$ nm, $d_2=200$ nm and $W=25 \mu\text{m}$.

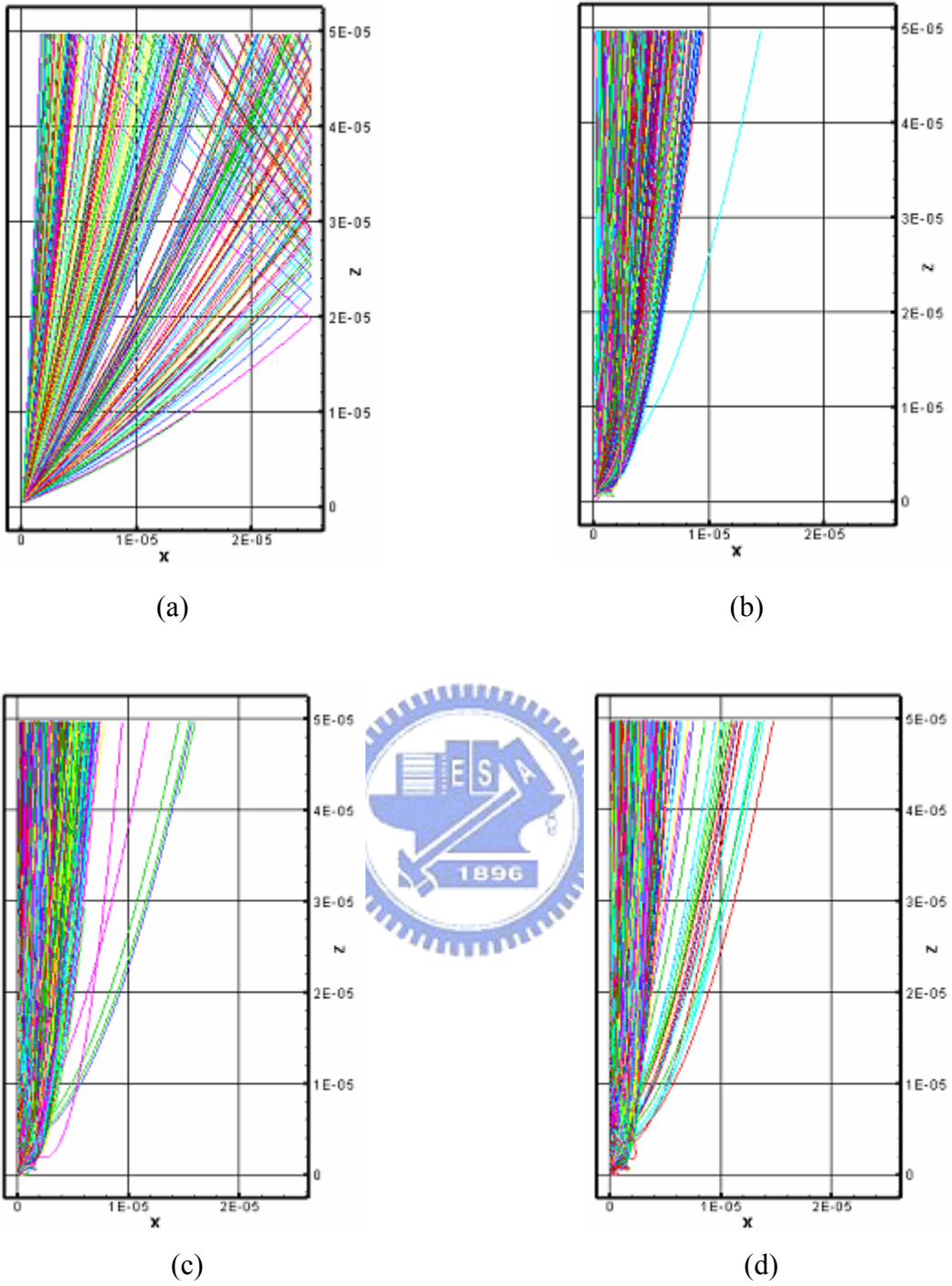


Figure 5.7 Comparisons of the trajectories of the emitted electrons between (a) CNT triode-type field emitter with the grounded cathode, anode voltage 400 volts and the gate voltage 150 volts and tetrode-type field emitter with the additional three different focusing voltages: (b) 5 volts (c) 0 volts (d) -5 volts.

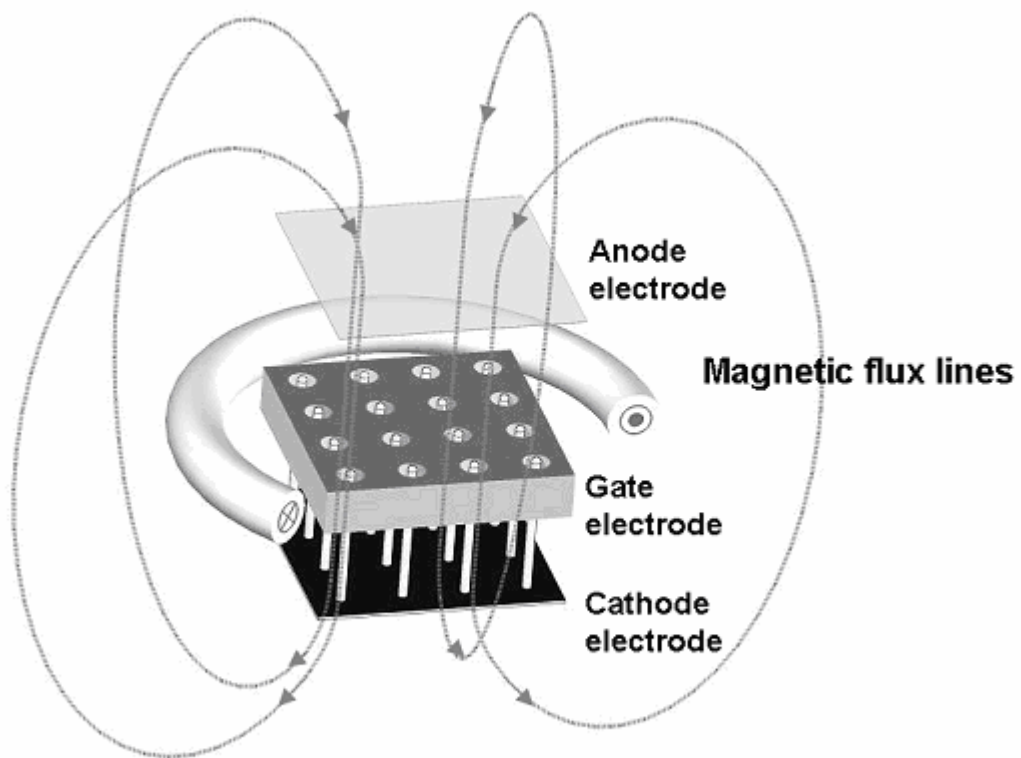


Figure 5.8 Perspective view of the structure of the magnetic focusing carbon nanotube field emission arrays

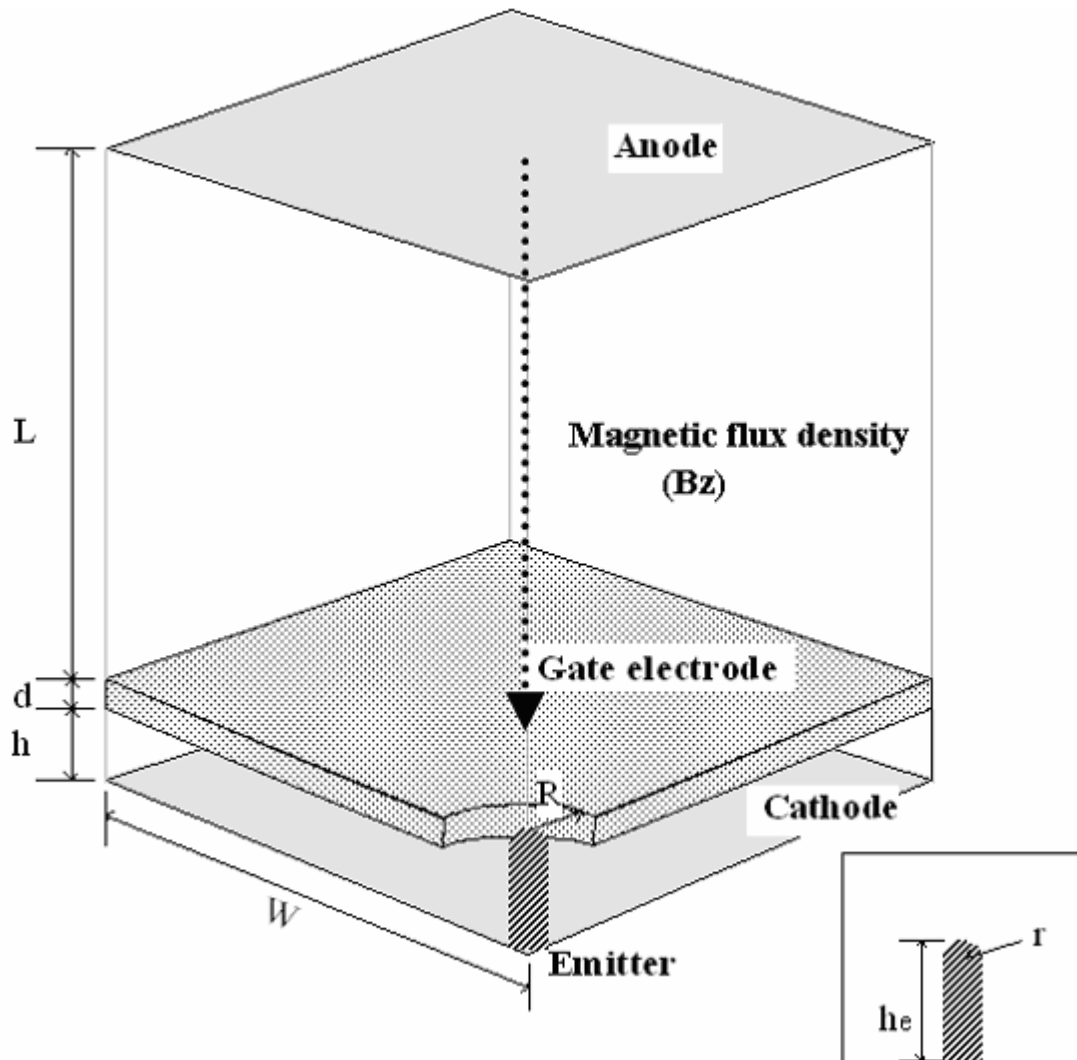


Figure 5.9 Schematic diagram of the 1/4 simulation domain for a typical CNT-based triode-type field emitter within a periodic cell. The important geometrical parameters are: $R=500\text{nm}$, $r=10\text{nm}$, $he=600\text{nm}$, $h=500\text{nm}$, $d=200\text{nm}$, $L=0.9\text{mm}$ and $W=0.3\text{mm}$

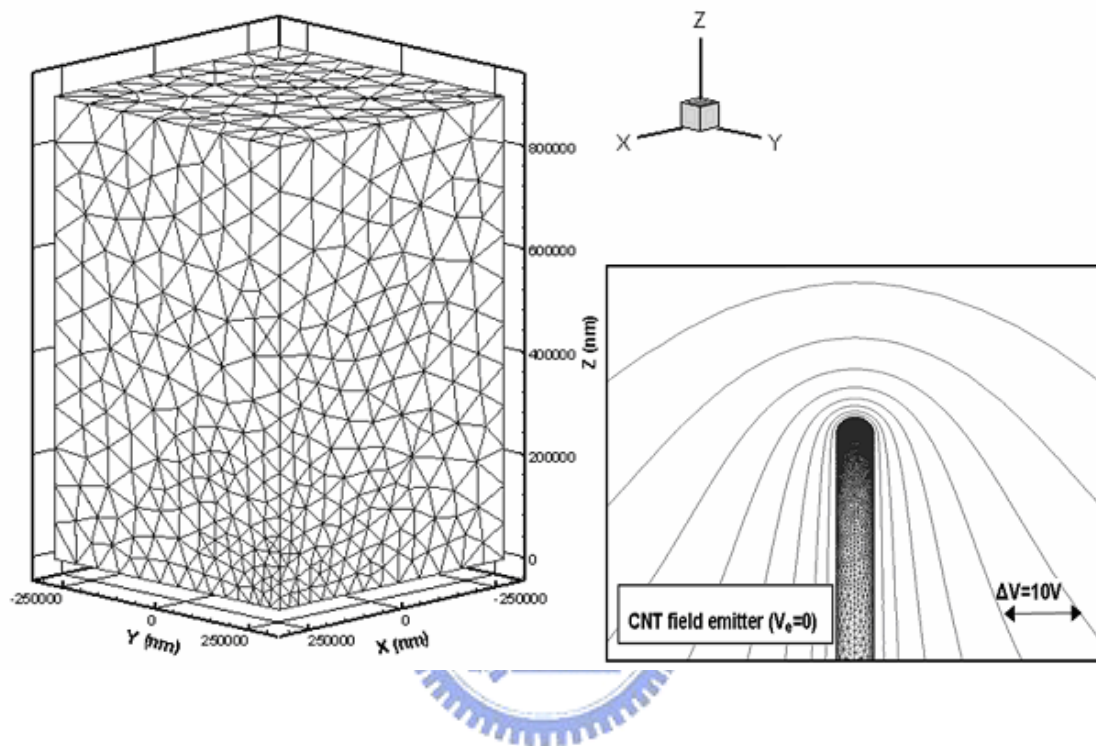


Figure 5.10 LHS shows surface mesh distribution of a single CNT triode-type field emitter within a periodic cell. RHS shows surface mesh distribution of the CNT field emitter and equipotential lines near the tip for $V_g=120V$. Unstructured tetrahedral adaptive mesh is ideal for the simulation structure, which consists of a smaller emitter within a larger periodic cell

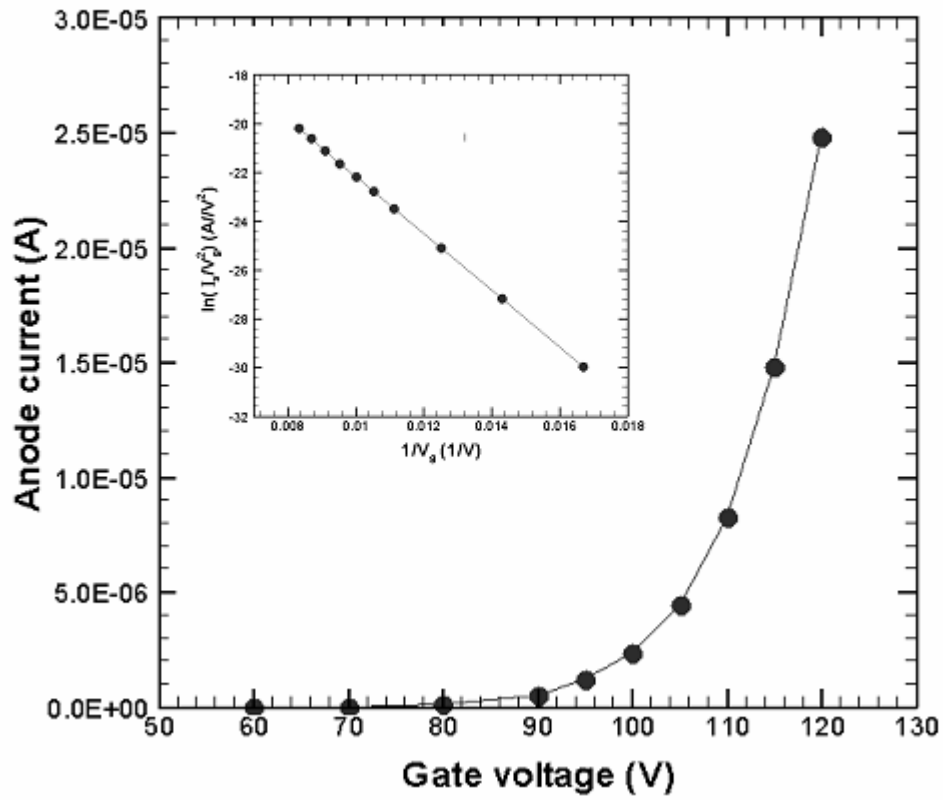


Figure 5.11. Field emission I-V characteristic of a single gated CNT field emitter without the externally applied downward magnetic field

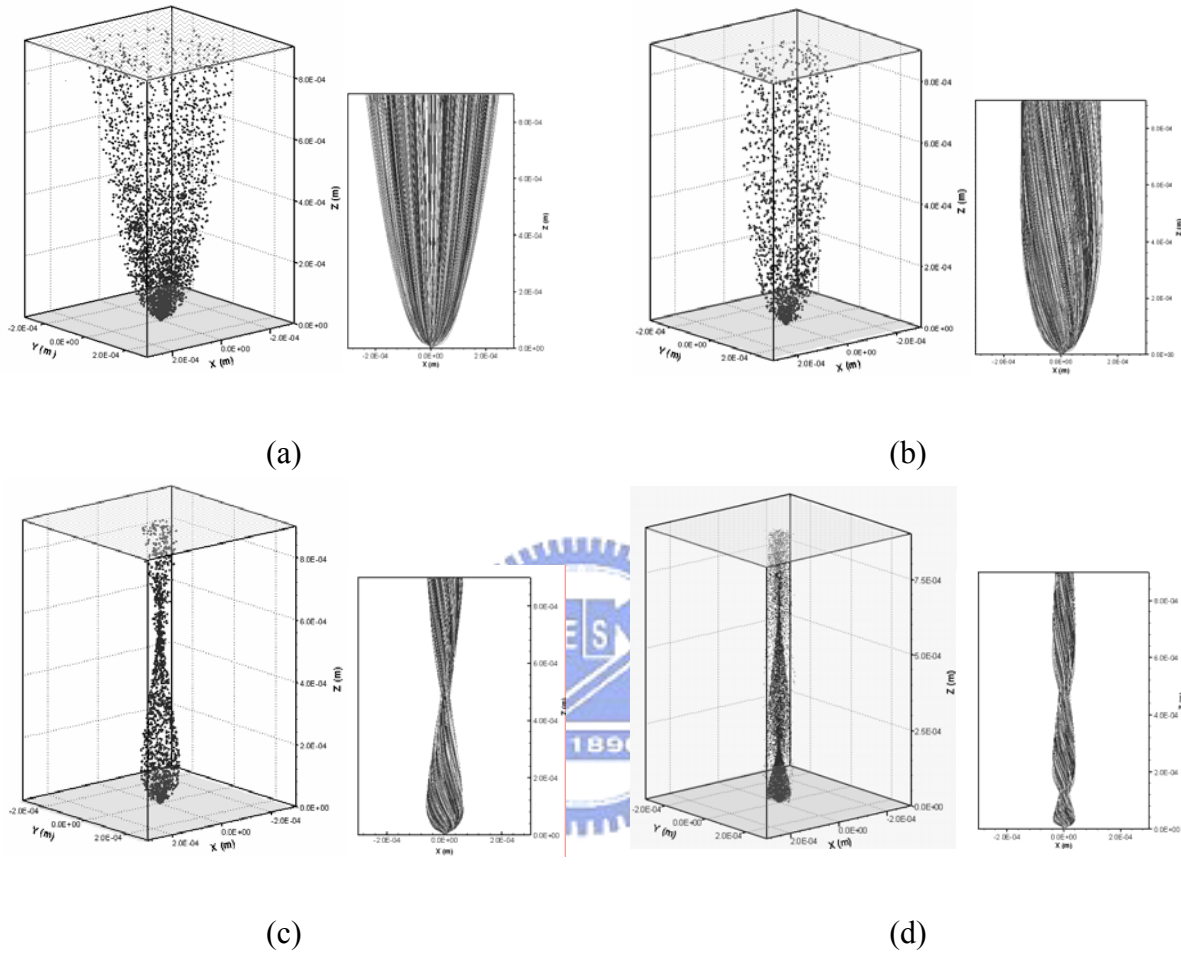


Figure 5.12 Snapshots and trajectories of electrons for (a) $B_z = 0$ T, (b) $B_z = -0.2$ T, (c) $B_z = -0.5$ T, and (d) $B_z = -1.0$ T. The gate voltage and the anode voltage are fixed to 120V and 1 kV, respectively.

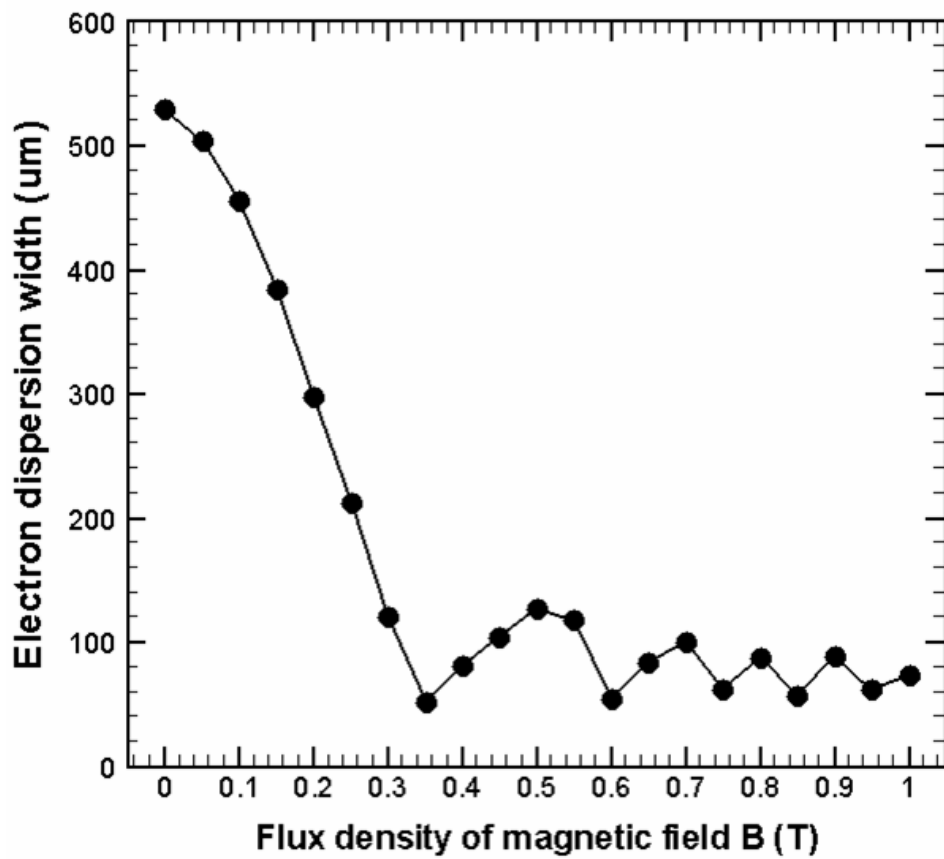


Figure 5.13 Dependence of electron beam diameter at the anode on the flux density of magnetic focusing field.

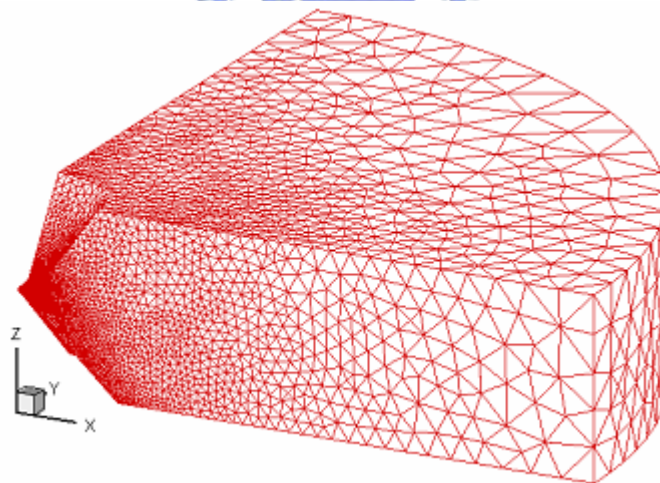
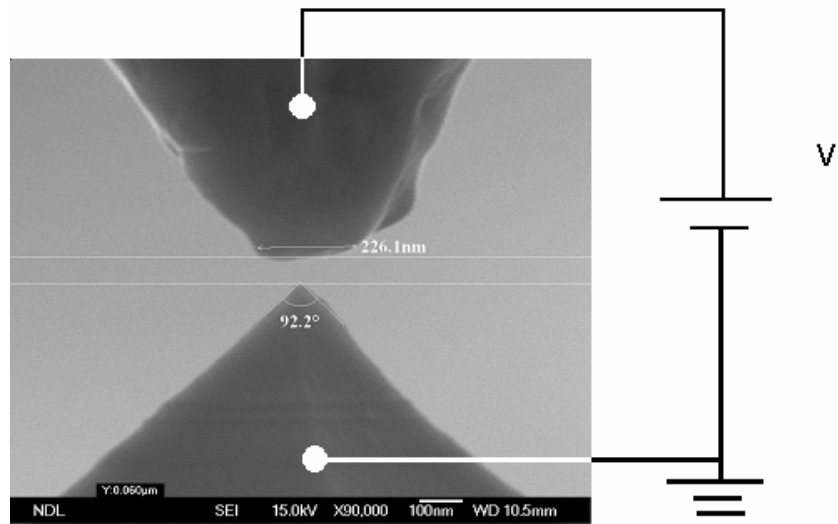
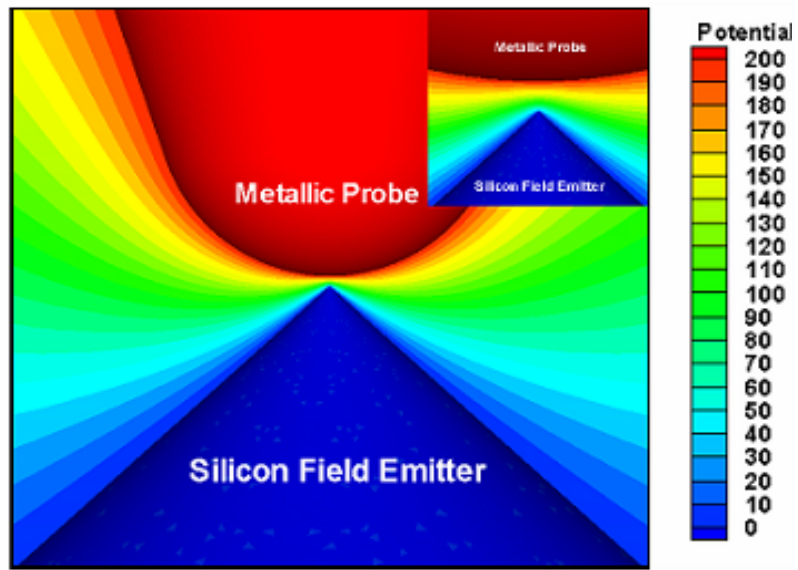
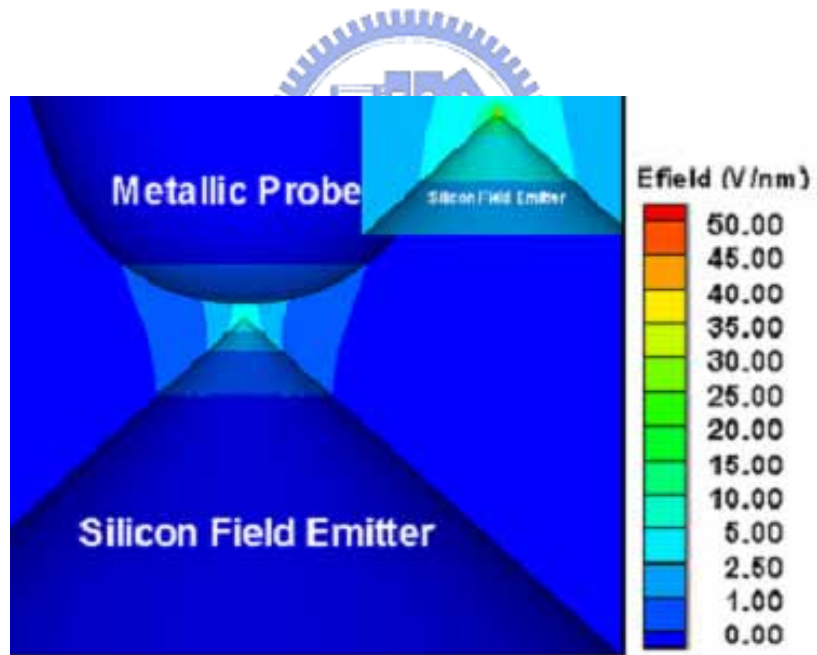


Figure 5.14 (a) SEM image and (b) surface mesh distribution of a single silicon based field emitter within a periodic cell.



(a)



(b)

Figure 5.15 Contours of the (a) electric potential and the (b) electric field distribution near the tip of the single silicon based field emitter with anode voltage 200 volts.

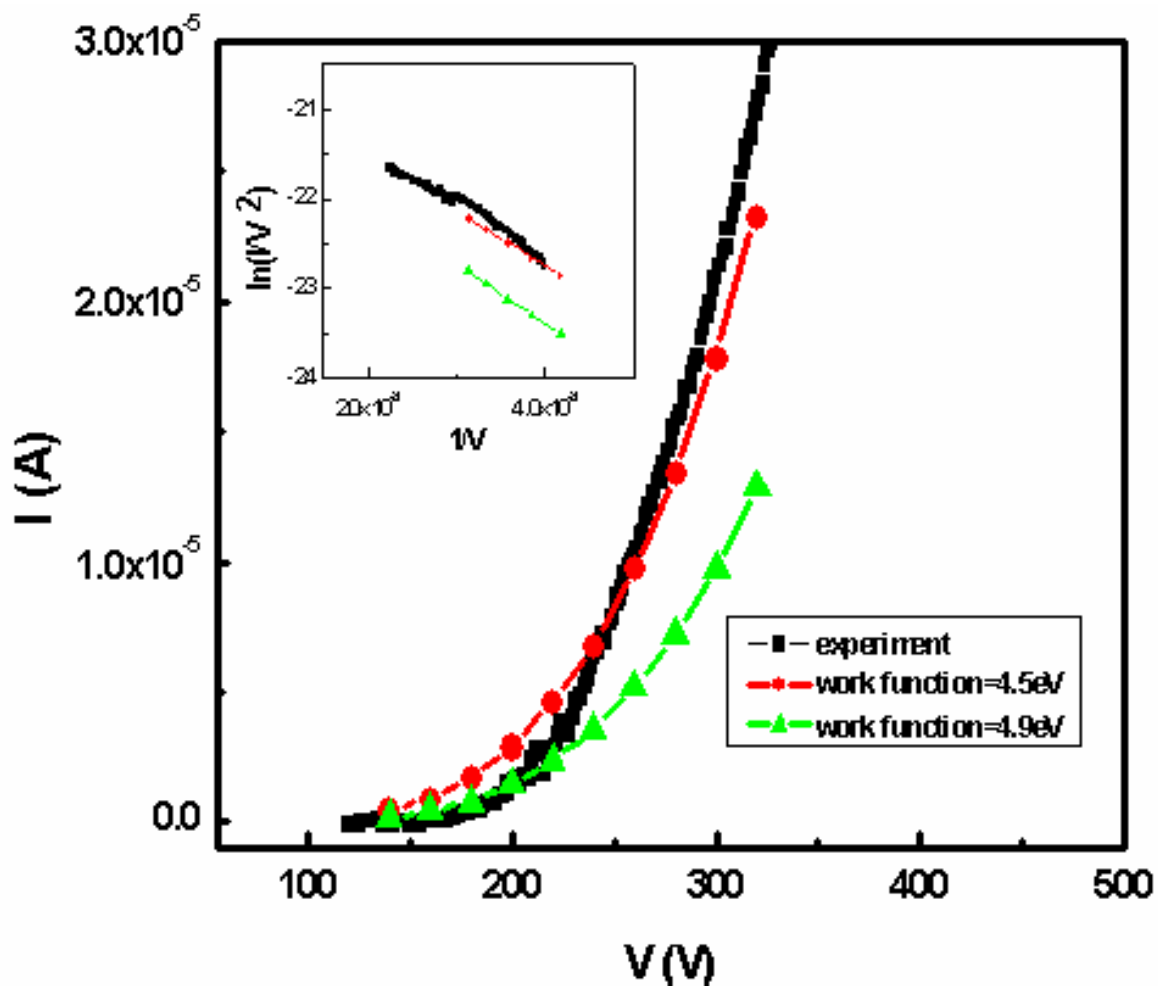
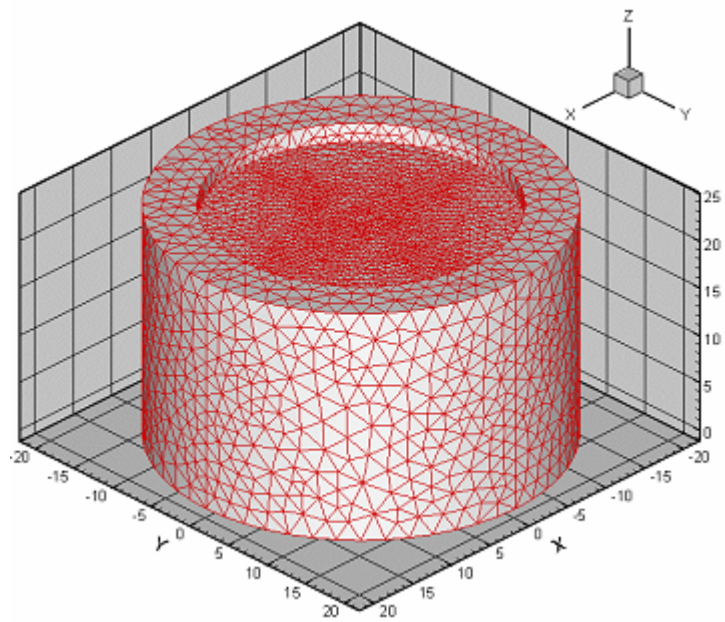
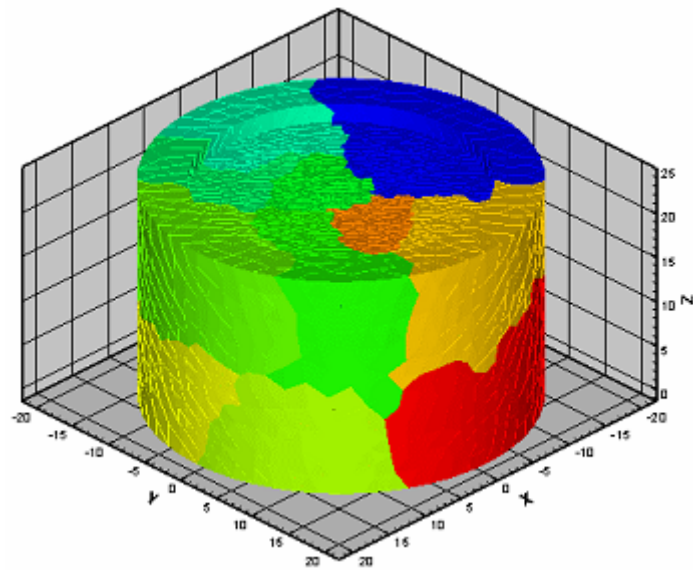


Figure 5.16 Field emission I-V characteristic and F-N plot of single silicon based field emitter with work function 4.5eV and 4.9eV.

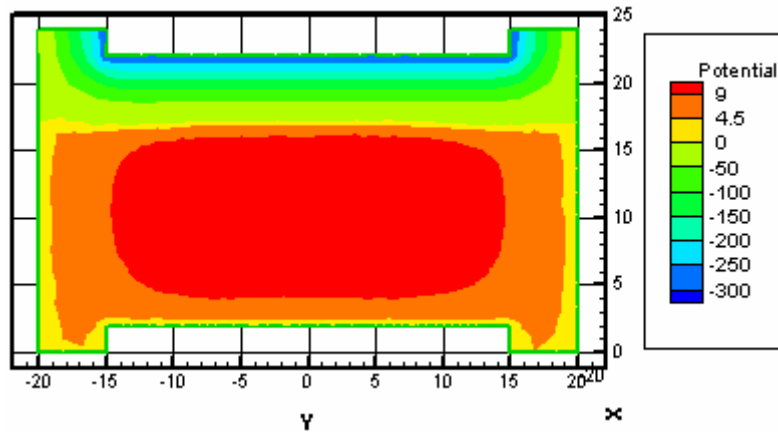


(a)

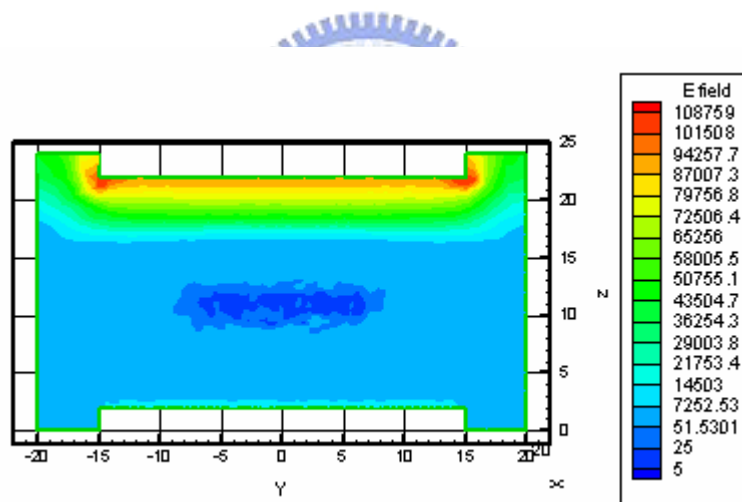


(b)

Figure 5.17 (a) The surface mesh plot and (b) domain decomposition profile of 3D DC gas discharge plasma.

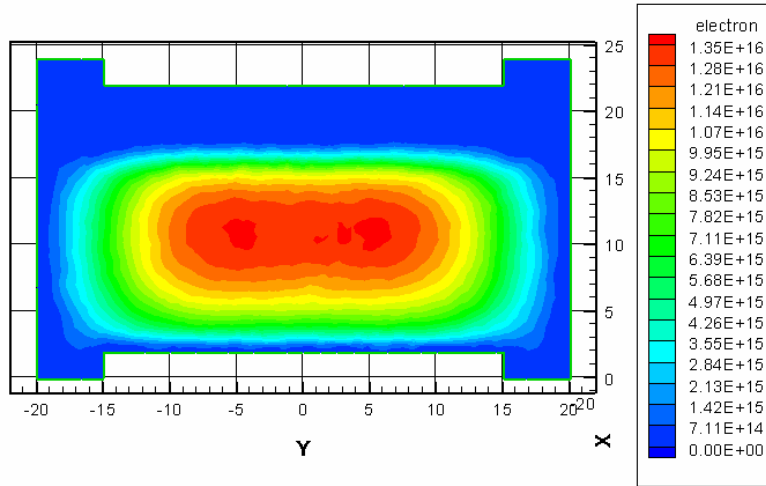


(a)

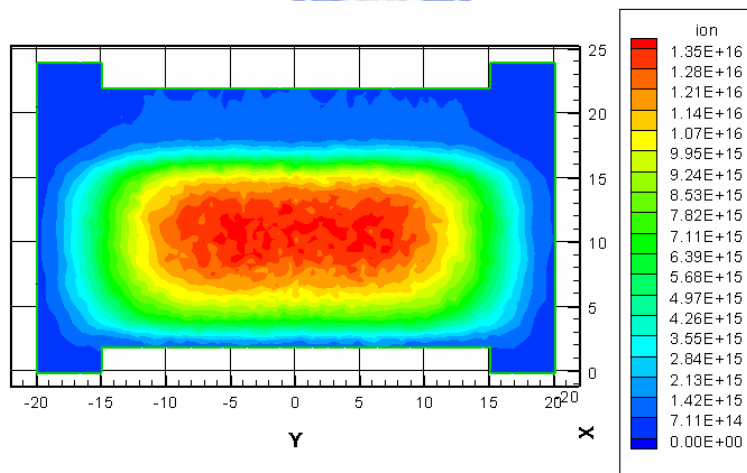


(b)

Figure 5.18 Contours of the (a) electric potential and the (b) electric field distribution of 3D DC glow discharge.

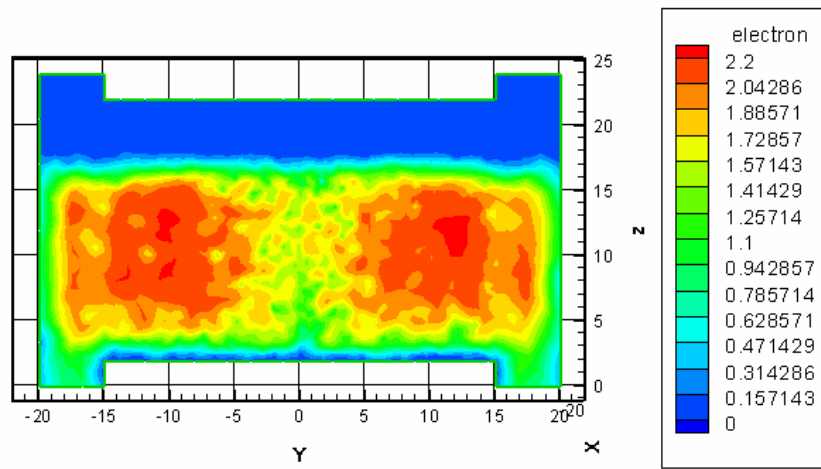


(a)

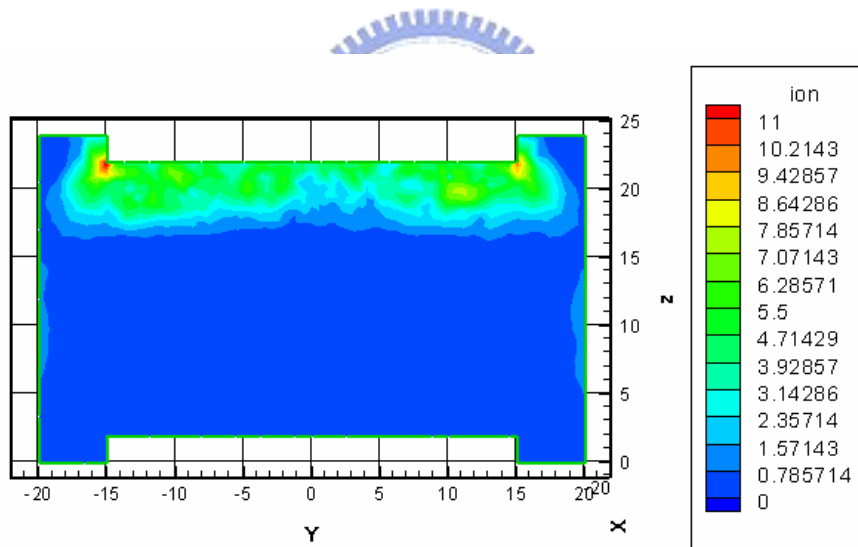


(b)

Figure 5.19 Contours of (a) electron and (b) ion number densities of 3D DC glow discharge.

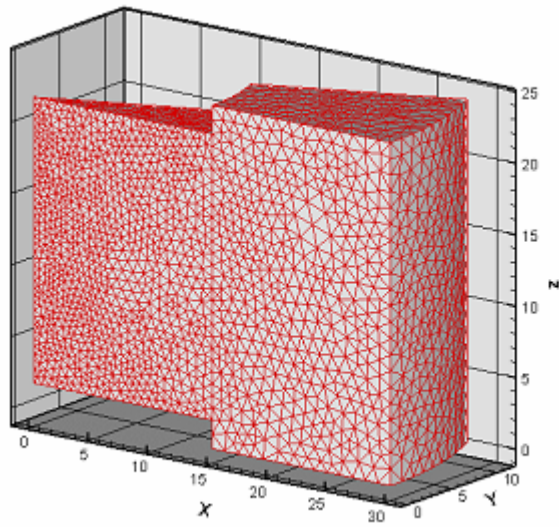


(a)

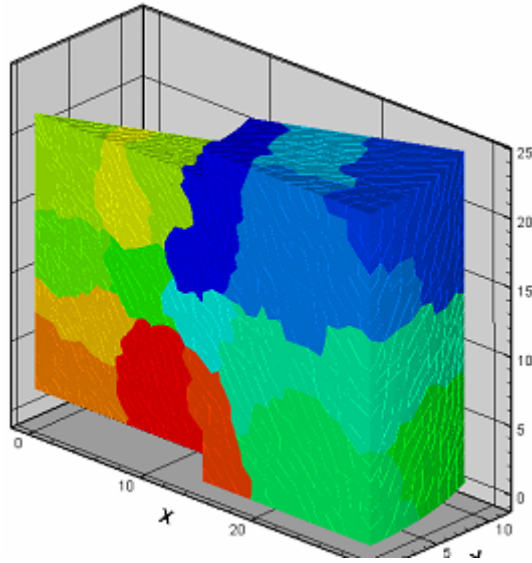


(b)

Figure 5.20 Contours of (a) electron and (b) ion kinetic energies of 3D DC glow discharge.



(a)



(b)

Figure 5.21 (a) The surface mesh plot and (b) domain decomposition profile of 3D RF gas discharge plasma.

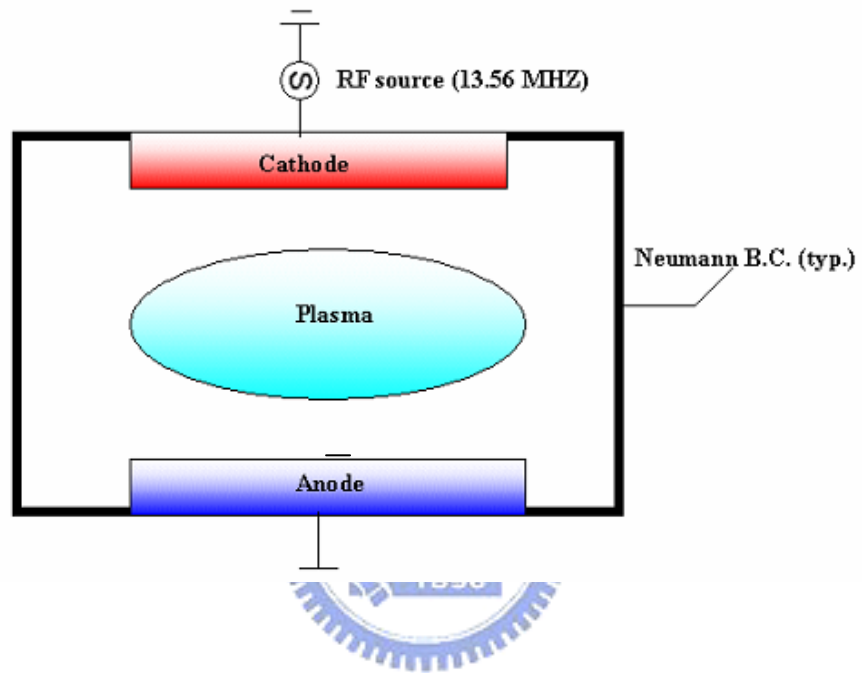


Figure 5.22 Sketch and boundary condition of the 3D RF discharge plasma enclosed by a dielectric chamber wall.

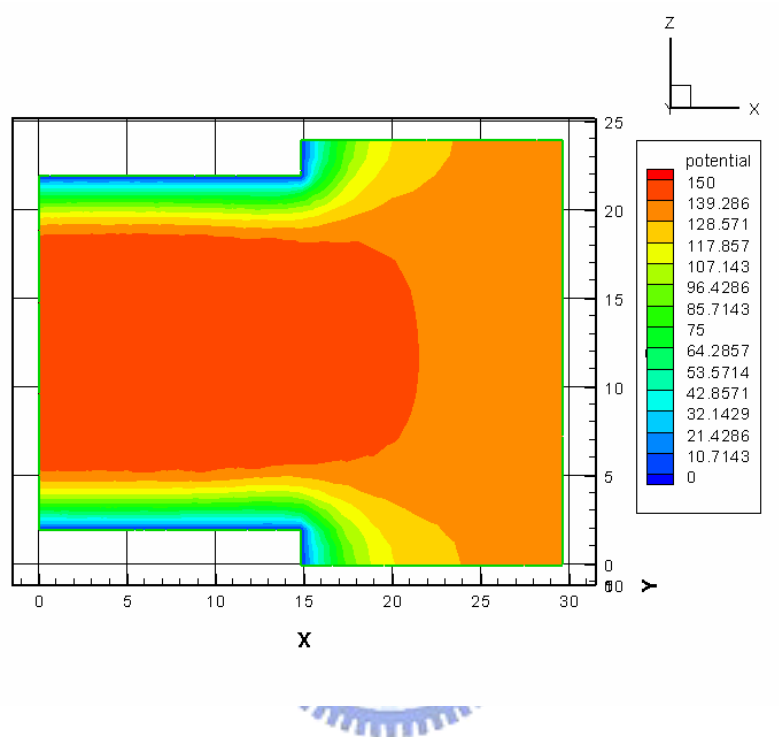
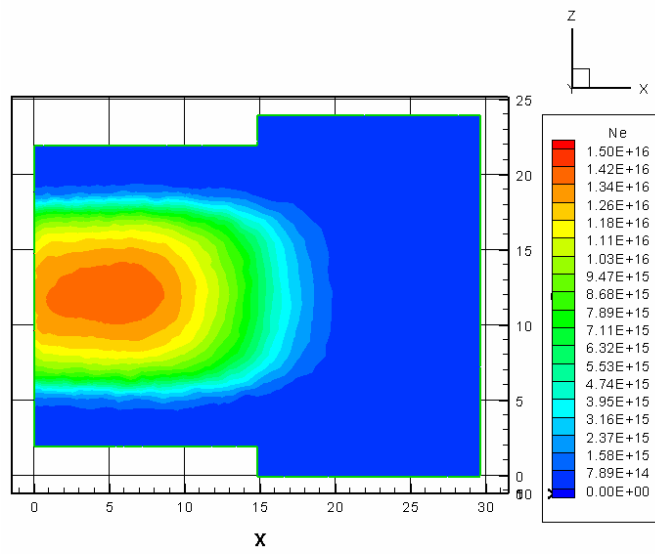
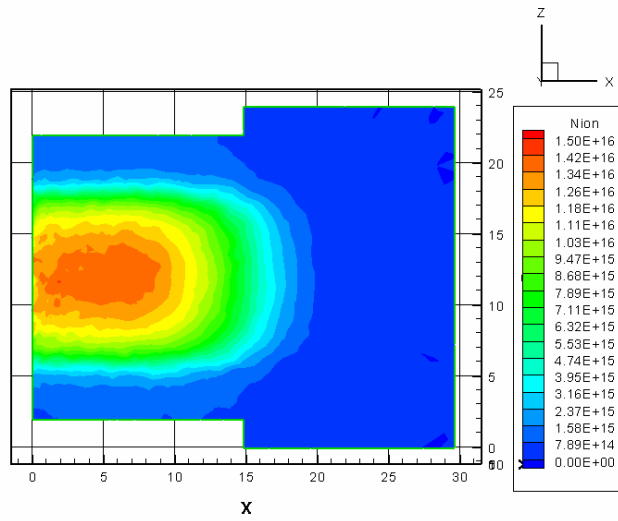


Figure 5.23 Potential contour of 3D RF discharge plasma enclosed by a dielectric chamber wall.

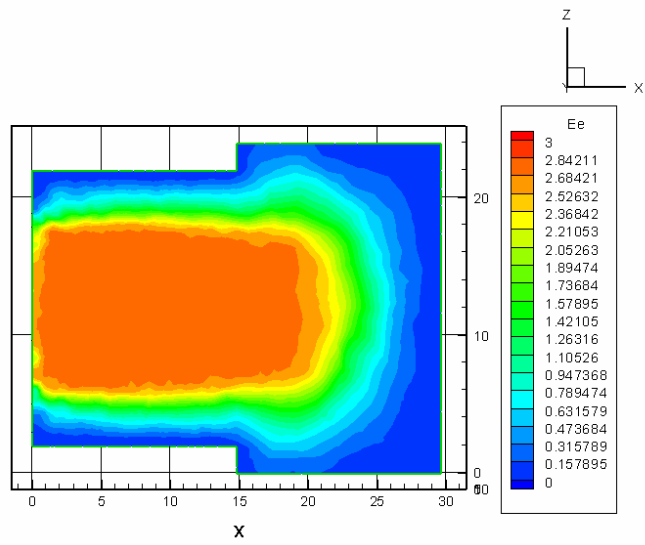


(a)

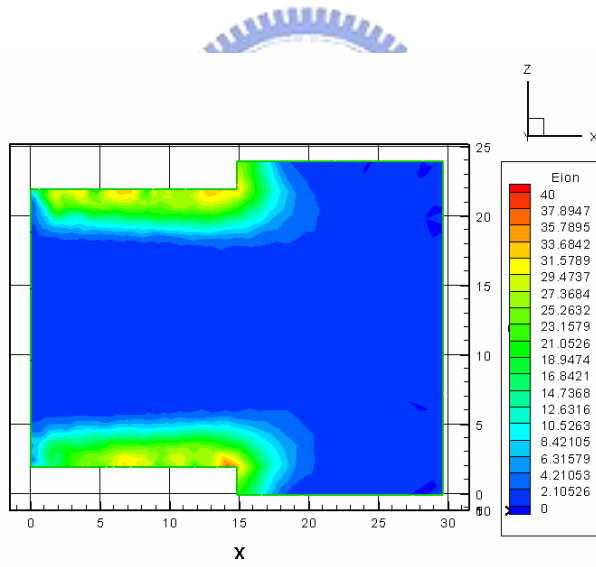


(b)

Figure 5.24 Contours of (a) electron and (b) ion number densities of 3D RF discharge plasma enclosed by a dielectric chamber wall.

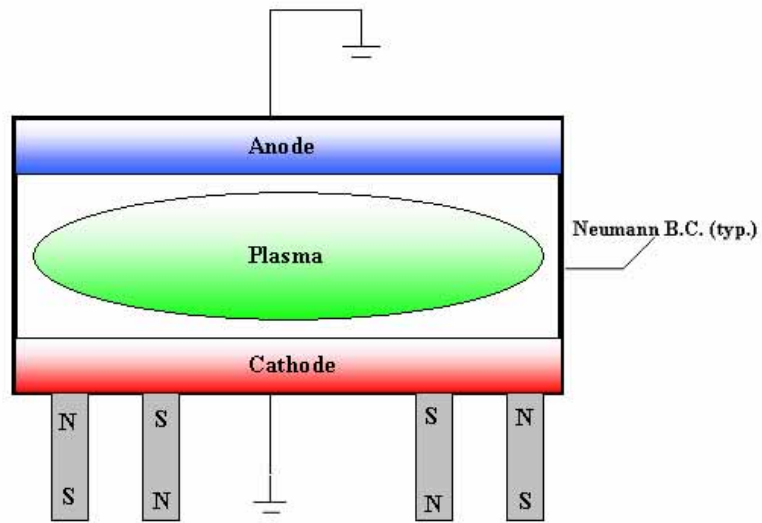


(a)

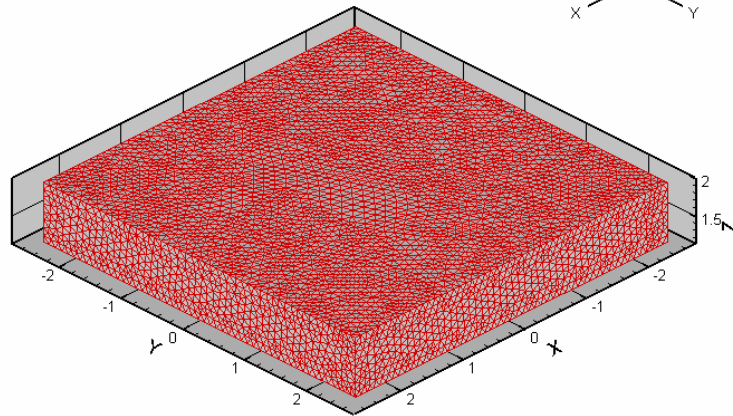
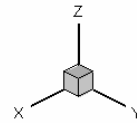


(b)

Figure 5.25 Contours of (a) electron and (b) ion kinetic energies of 3D RF discharge plasma enclosed by a dielectric chamber wall.



(a)



(b)

Figure 5.26 Sketch and surface mesh distribution of the 3D DC magnetron plasma.

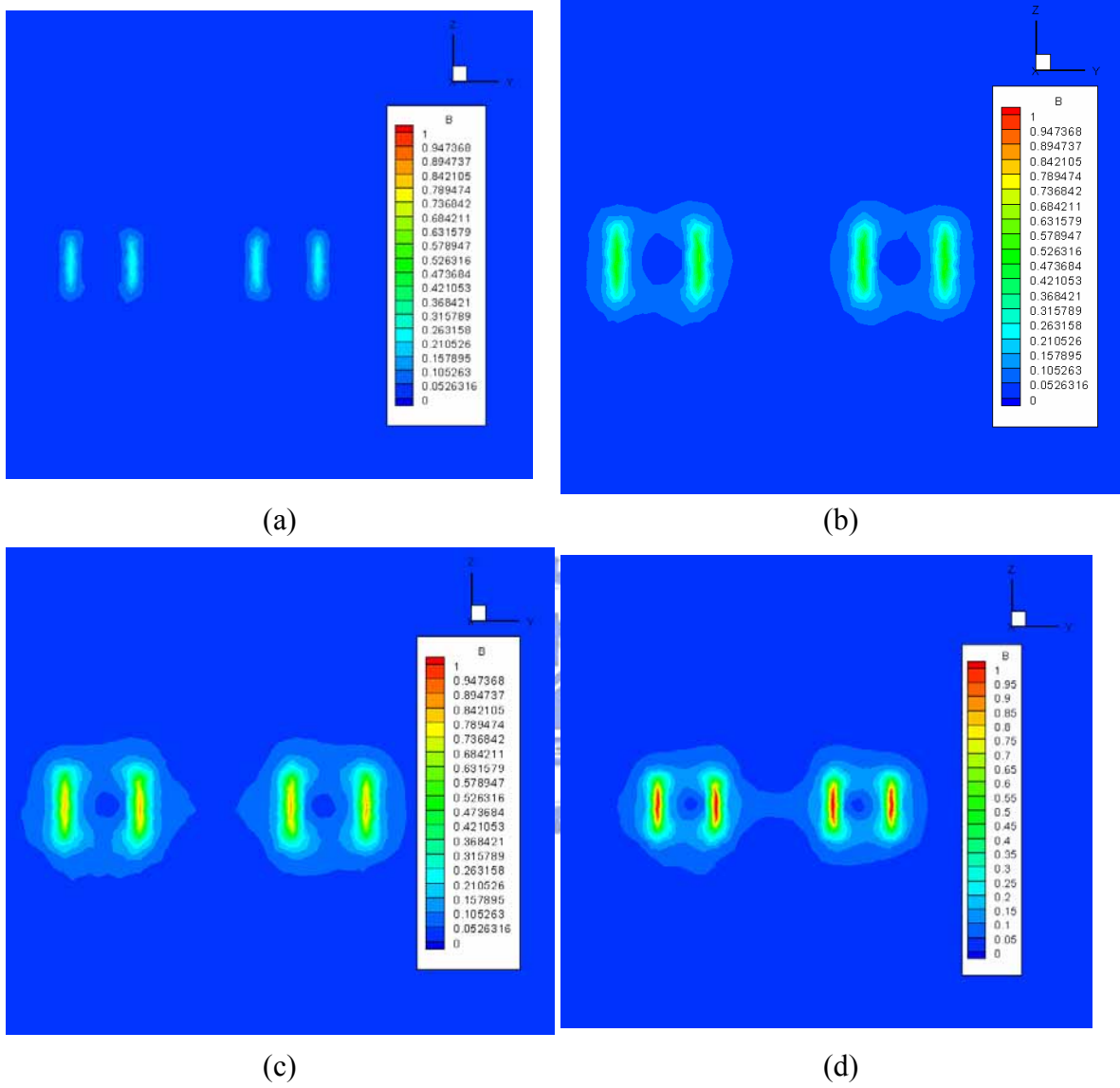
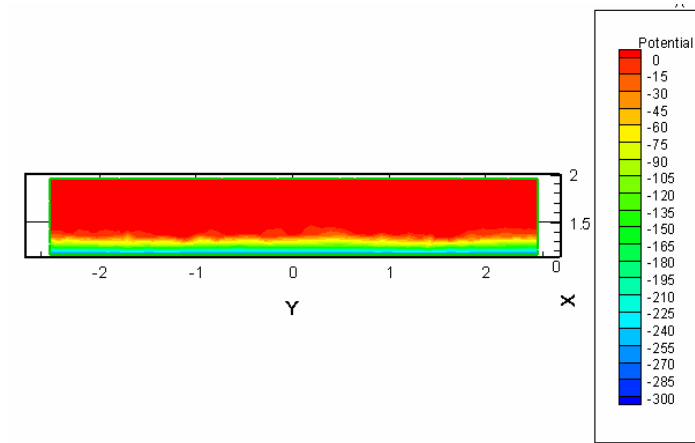
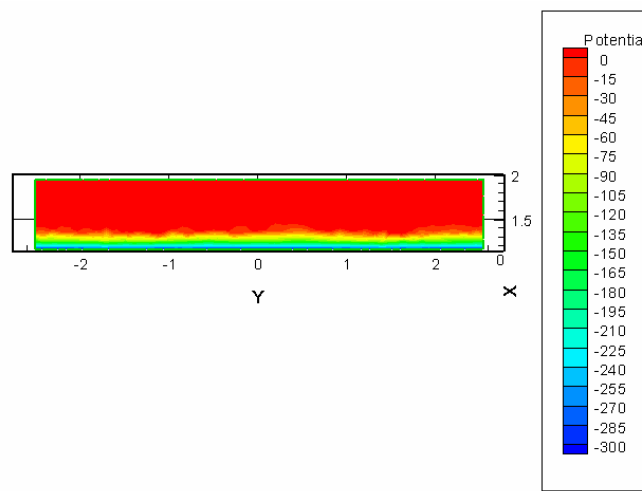


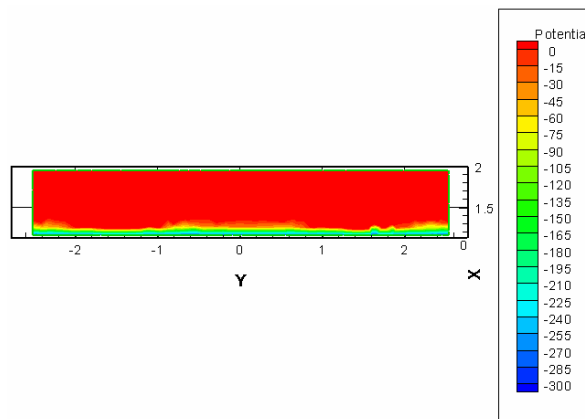
Figure 5.27 Contours of magnetic flux density with magnetization (a) 0.25 T (b) 0.5 T (c) 0.75 T (d) 1.0 T of permanent magnet systems.



(a)

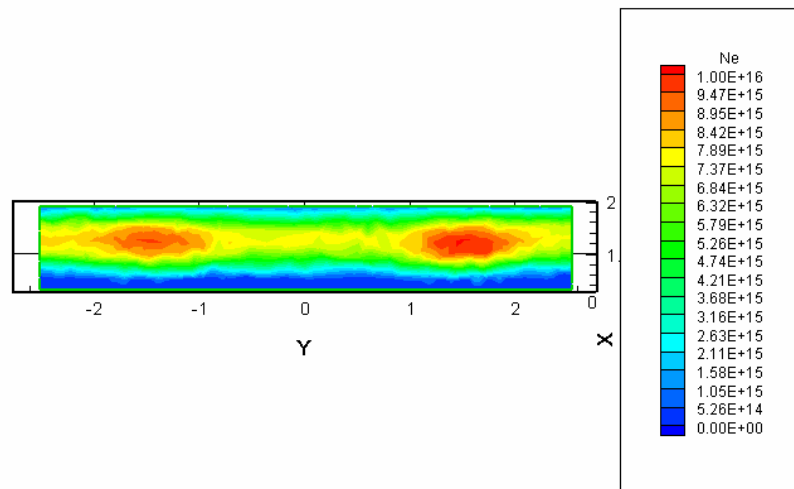


(b)

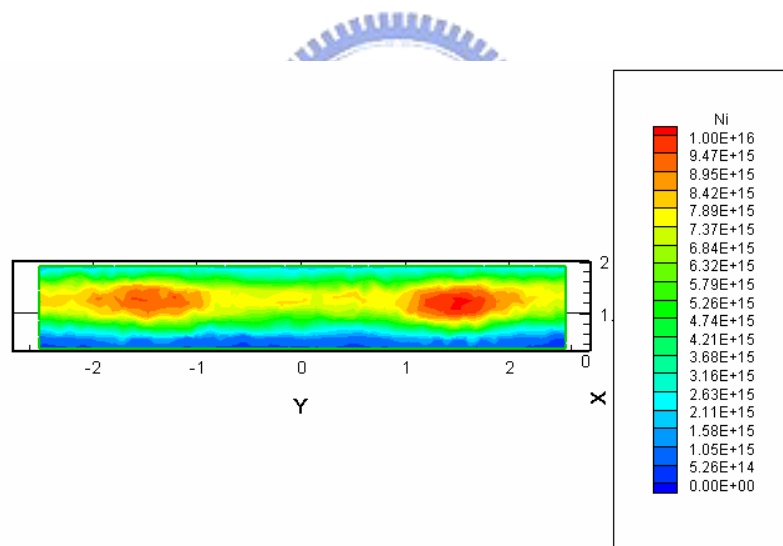


(c)

Figure 5.28 Potential contours of 3D DC magnetron plasma with (a) $M=0.125T$, $\gamma =0.06$, (b) $M=0.125T$, $\gamma =0.1$, and (c) $M=0.1875T$, $\gamma =0.06$.

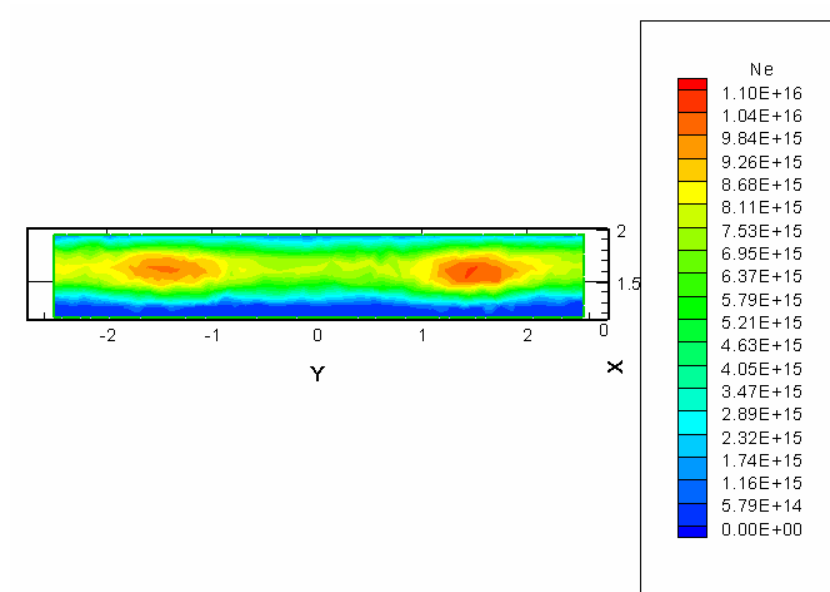


(a)

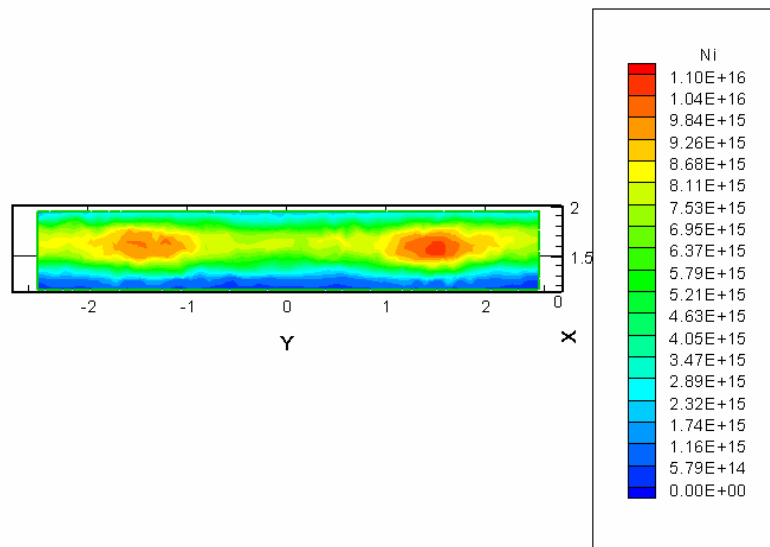


(b)

Figure 5.29 Contours of (a) electron and (b) ion number densities of 3D DC magnetron plasma with $M=0.125T$ and $\gamma=0.06$

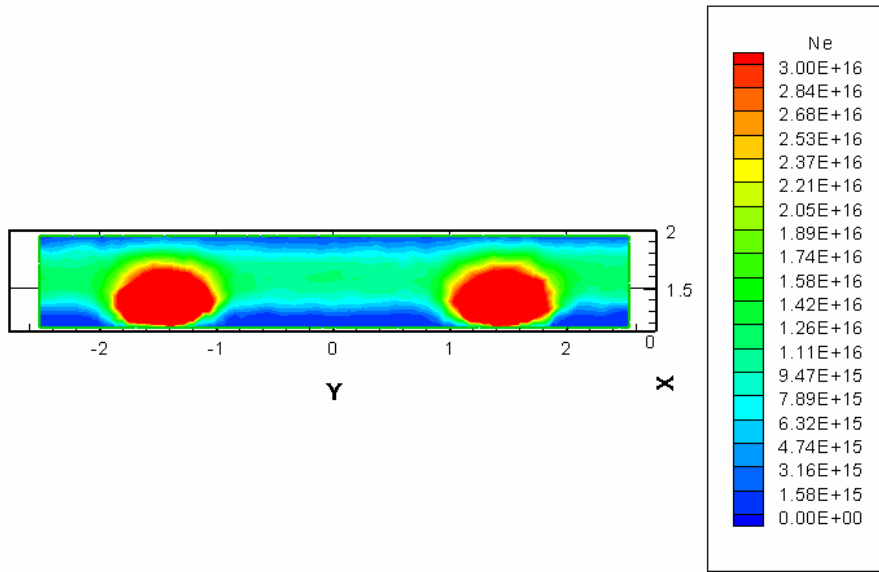


(a)

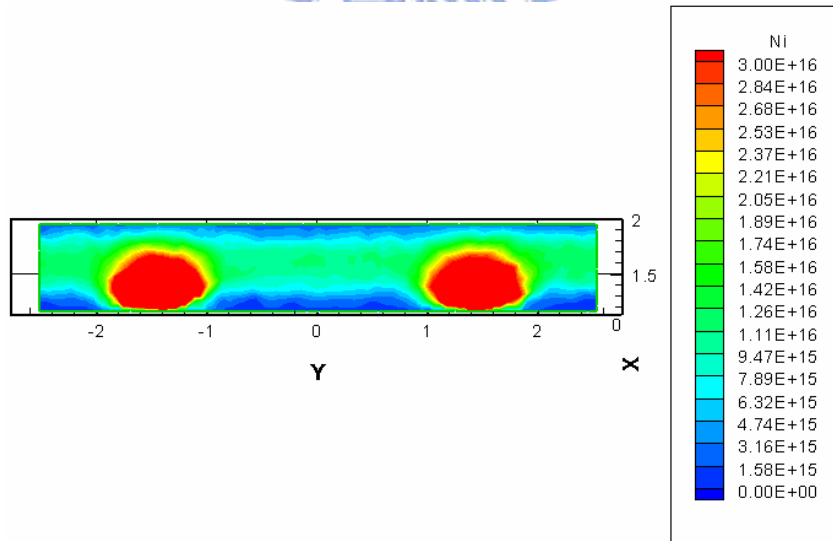


(b)

Figure 5.30 Contours of (a) electron and (b) ion number densities of 3D DC magnetron plasma with $M=0.125T$ and $\gamma =0.1$.

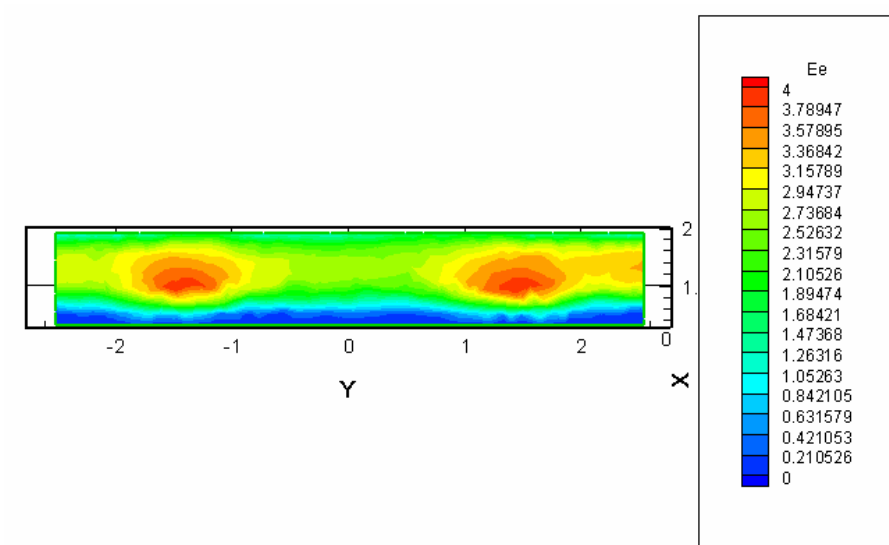


(a)

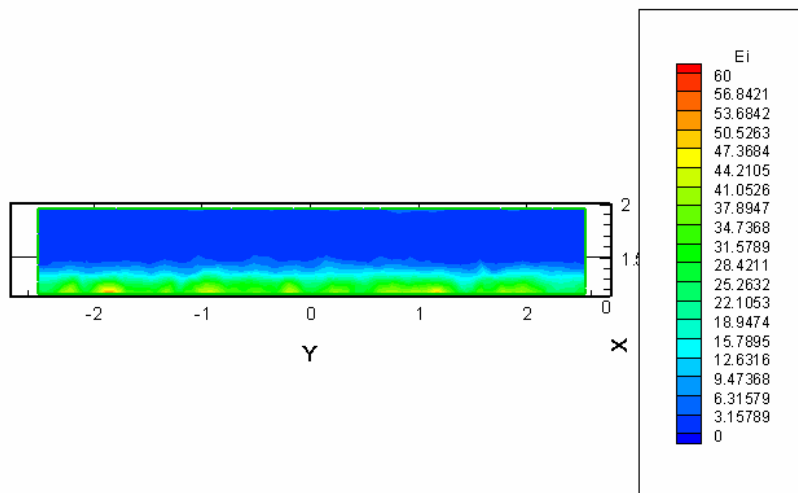


(b)

Figure 5.31 Contours of (a) electron and (b) ion number densities of 3D DC magnetron plasma with $\mathbf{M}=0.1875\text{T}$ and $\gamma=0.06$.

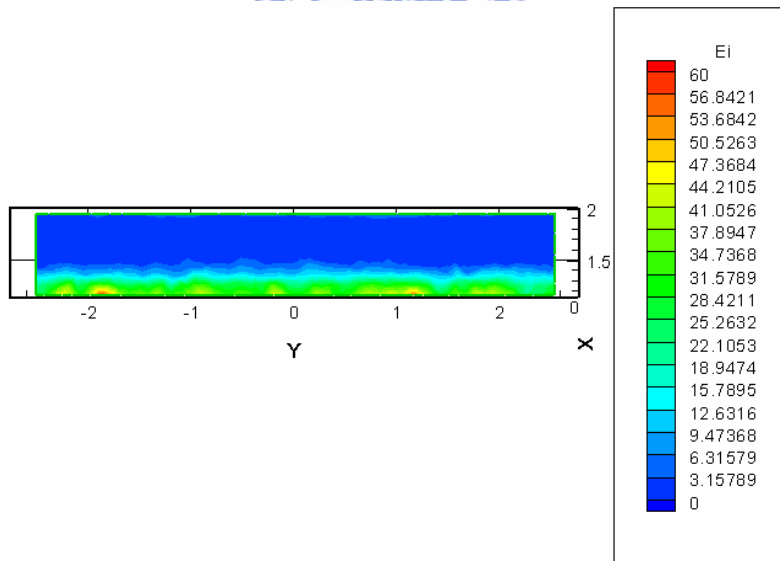
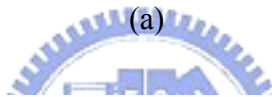
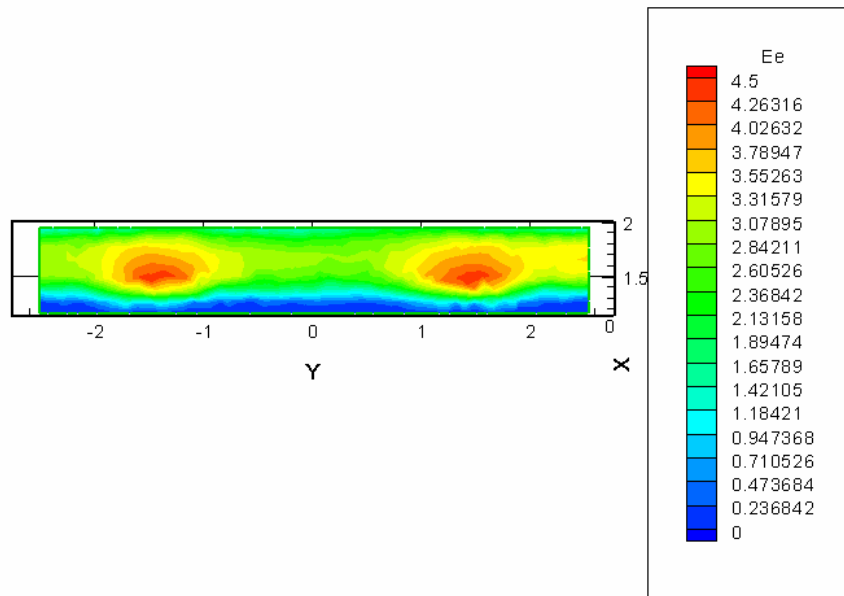


(a)



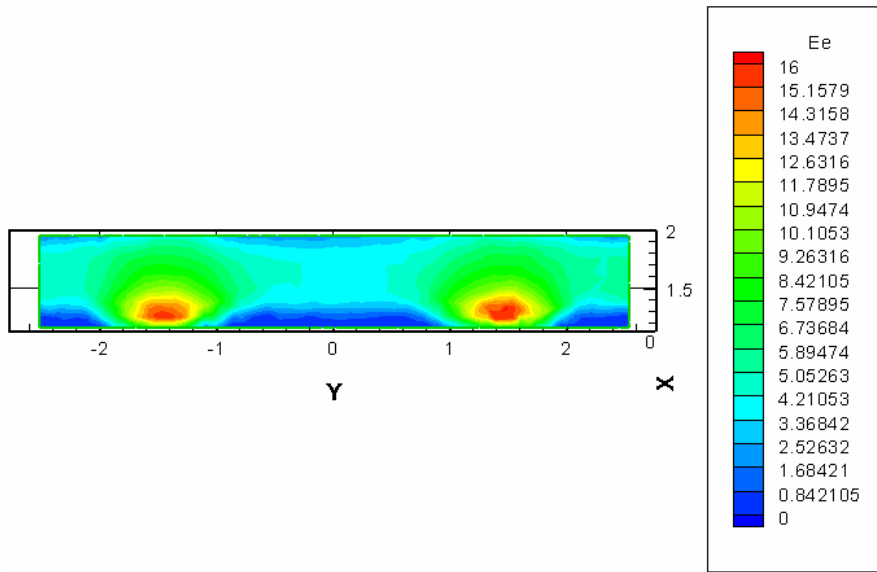
(b)

Figure 5.32 Contours of (a) electron and (b) ion kinetic energies of 3D DC magnetron plasma with $M=0.125T$ and $\gamma = 0.06$

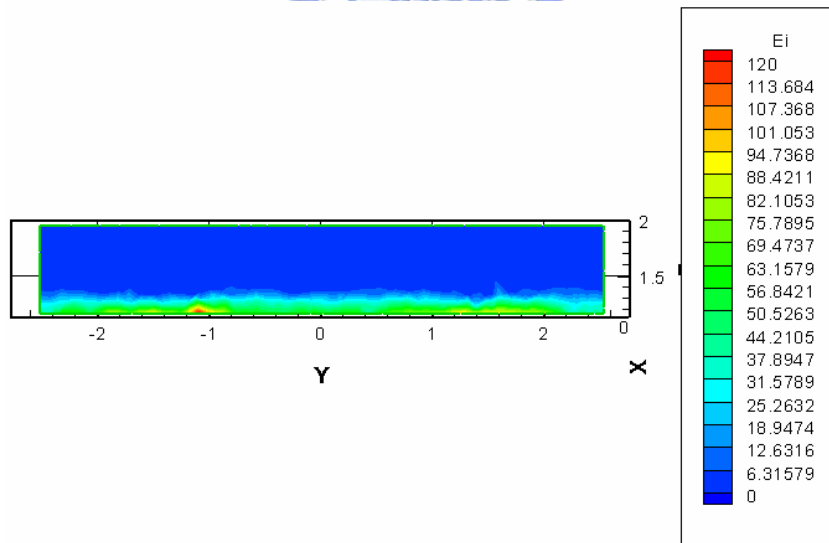


(b)

Figure 5.33 Contours of (a) electron and (b) ion kinetic energies of 3D DC magnetron plasma with $M=0.125T$ and $\gamma = 0.1$

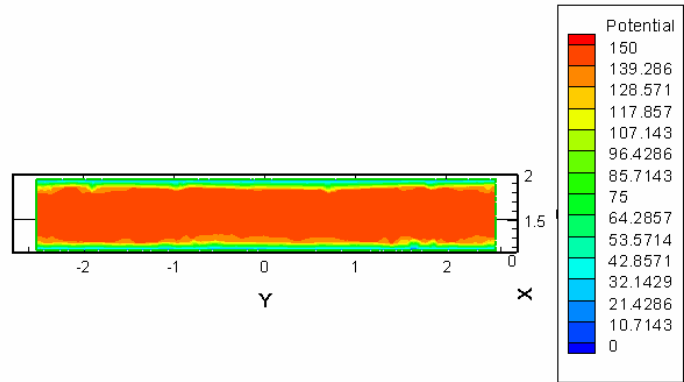


(a)

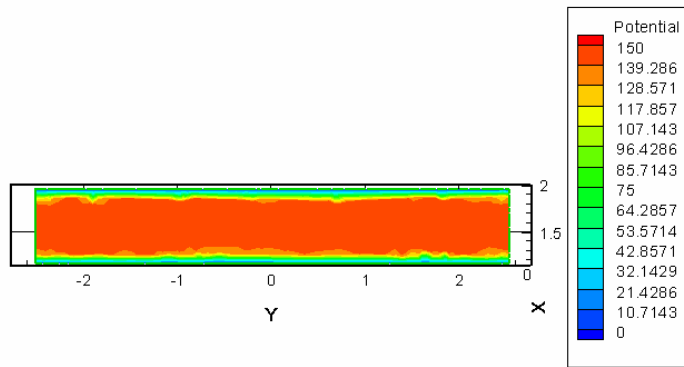


(b)

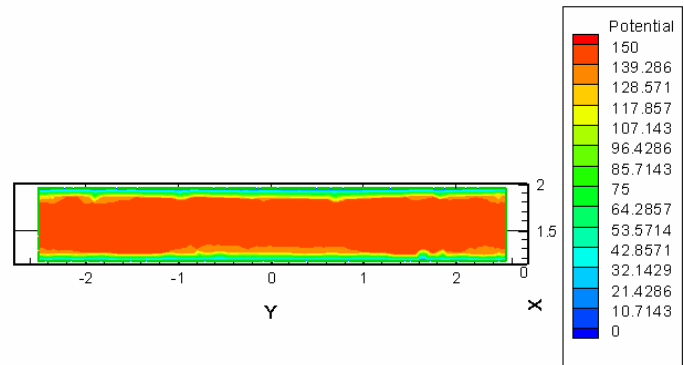
Figure 5.34 Contours of (a) electron and (b) ion kinetic energies of 3D DC magnetron plasma with $M=0.1875T$ and $\gamma = 0.06$.



(a)

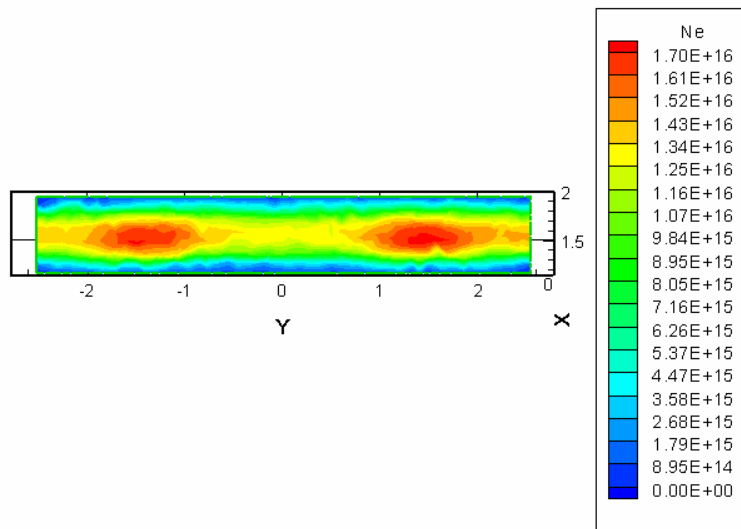


(b)

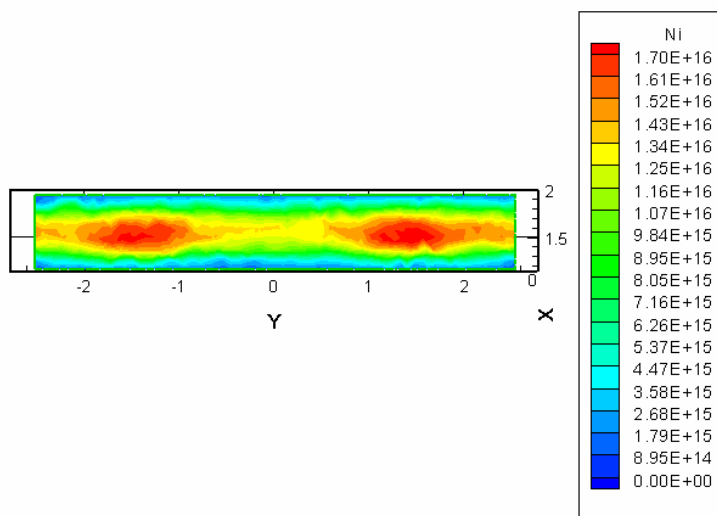


(c)

Figure 5.35 Potential contours of 3D RF magnetron plasma with (a) $M=0.125T$, $\gamma=0$ (b) $M=0.125T$, $\gamma=0.06$ (c) $M=0.25T$, $\gamma=0.06$.

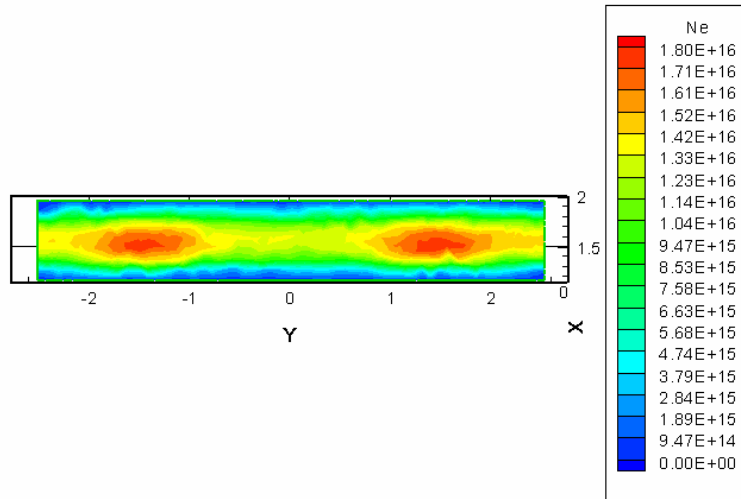


(a)

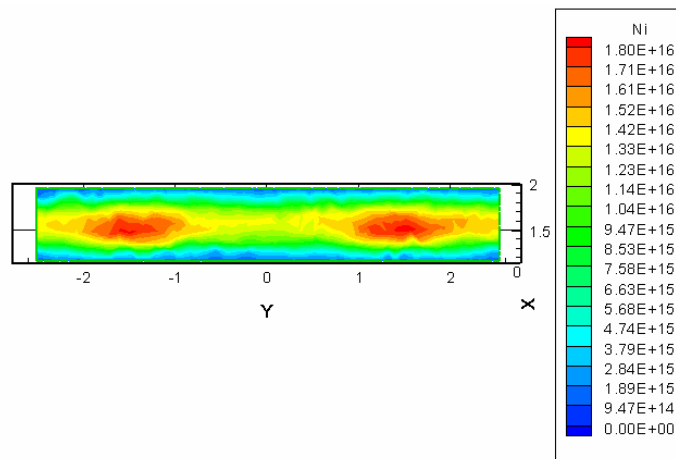


(b)

Figure 5.36 Contours of (a) electron and (b) ion number densities of 3D RF magnetron plasma with $\mathbf{M}=0.125\text{T}$ and $\gamma=0$



(a)



(b)

Figure 5.37 Contours of (a) electron and (b) ion number densities of 3D RF magnetron plasma with $M=0.125T$ and $\gamma=0.06$

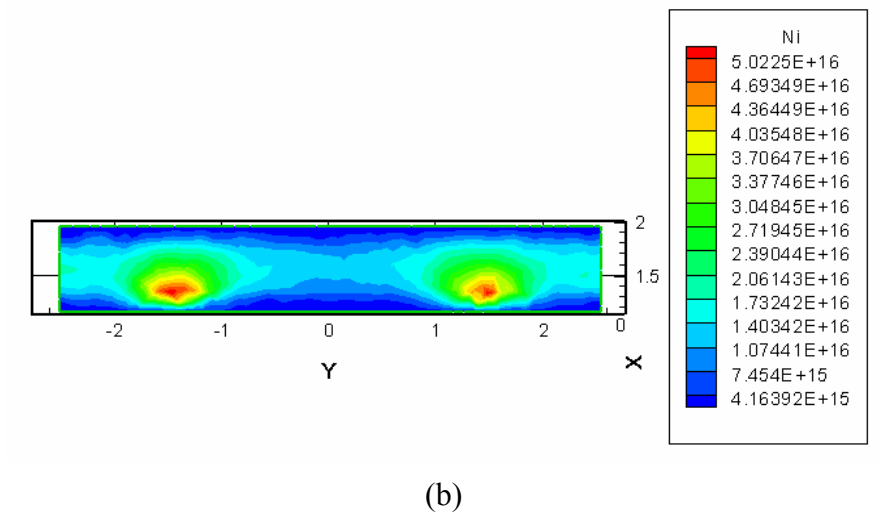
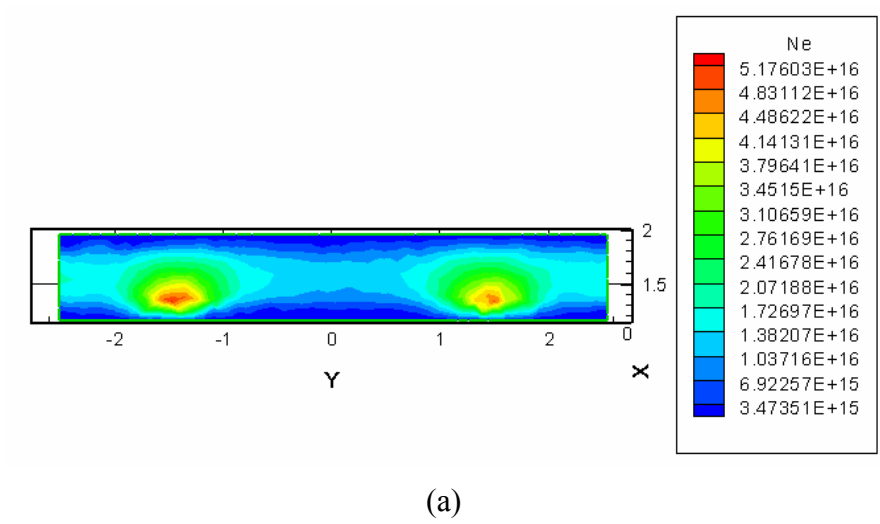
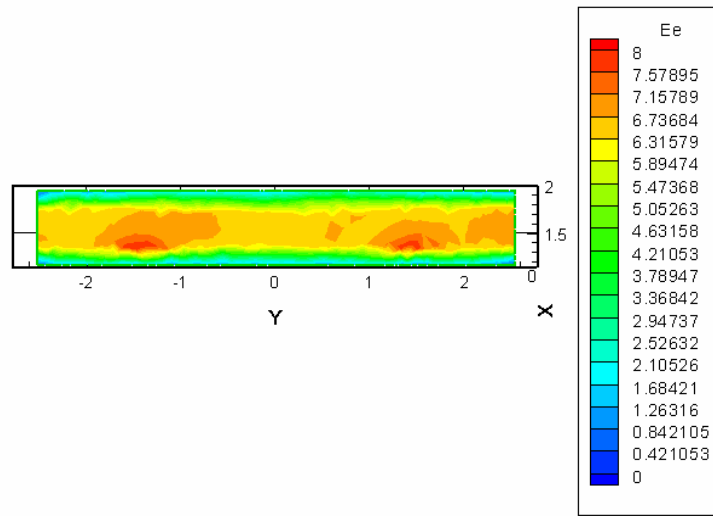
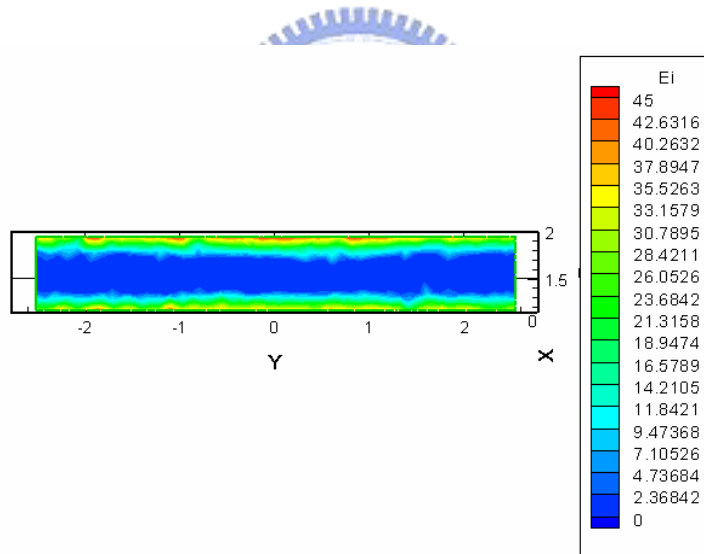


Figure 5.38 Contours of (a) electron and (b) ion number densities of 3D RF magnetron plasma with $\mathbf{M}=0.25\text{T}$ and $\gamma=0.06$

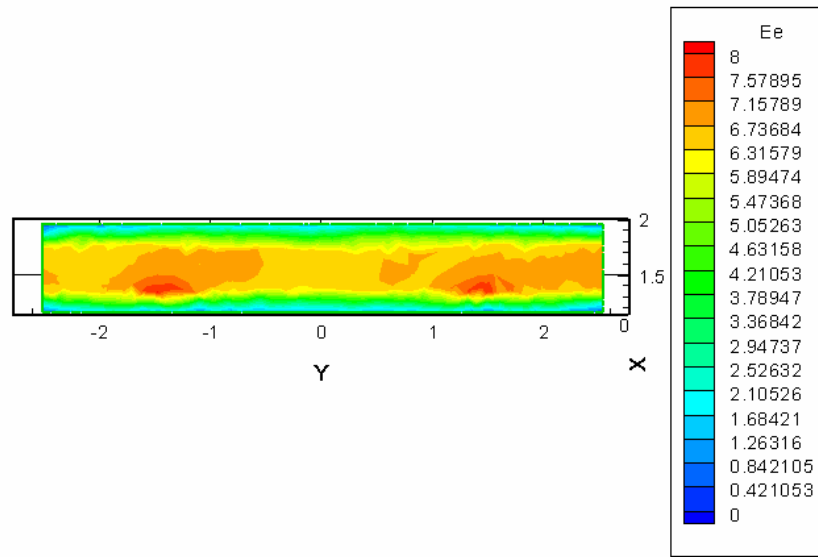


(a)

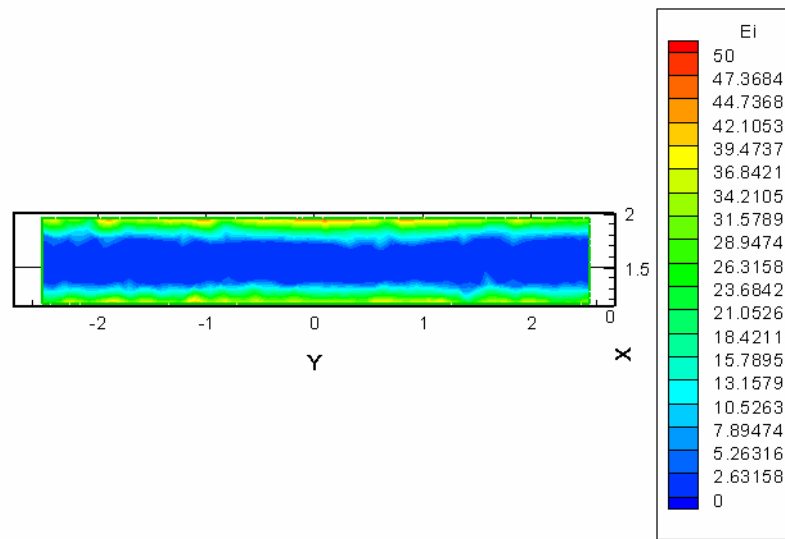


(b)

Figure 5.39 Contours of (a) electron and (b) ion kinetic energies of 3D RF magnetron plasma with $M=0.125T$ and $\gamma=0.0$

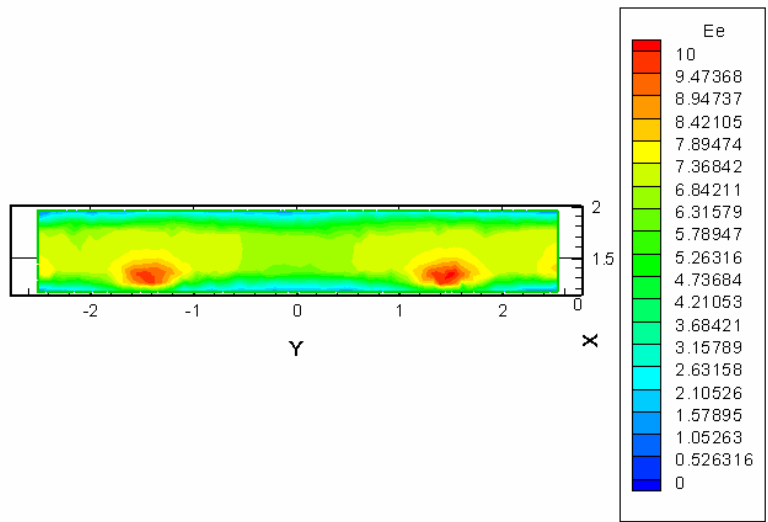


(a)

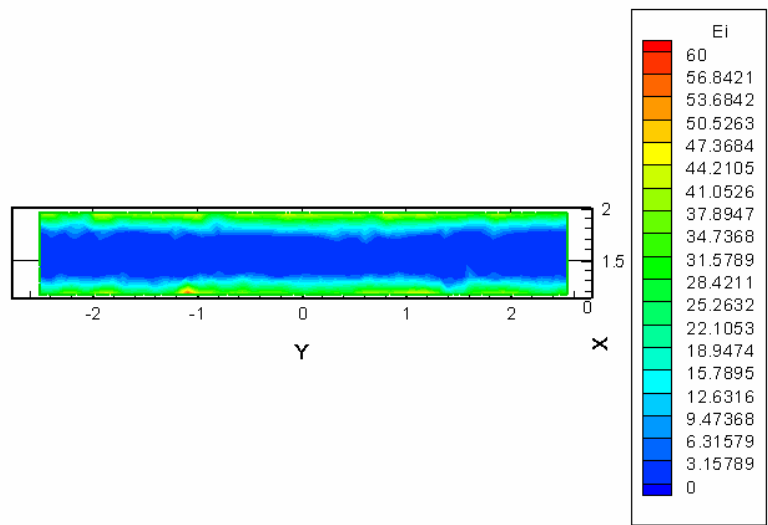


(b)

Figure 5.40 Contours of (a) electron and (b) ion kinetic energies of 3D RF magnetron plasma with $M=0.125T$ and $\gamma=0.06$.



(a)



(b)

Figure 5.41 Contours of (a) electron and (b) ion kinetic energies of 3D RF magnetron plasma with $M=0.25T$ and $\gamma=0.06$

Autobiography

Kuo-Hsien Hsu (許國賢)

Phone: 0910-713-967 (H) 03-5712121*55175 (o)	Mailing Address: ee309, Department of Mechanical Engineering, National Chiao-Tung University, Hsinchu 3005, Taiwan
Email: khhsu.me88g@nctu.edu.tw	
Status: Ph.D. candidate	Advisor: Professor Jong-Shinn Wu

Education

Ph.D. in Mechanical Engineering

National Chiao-Tung University, July 2006 (expected)

*Thesis: Development of a Parallelized PIC-FEM Code Using a
Three-Dimensional Unstructured Tetrahedral Mesh and Its applications*

Advisor: Prof. Jong-Shinn Wu

M.S. in Mechanical Engineering

National Chiao-Tung University, June 2001

*Thesis: Characterization of a Low-Speed Wind Tunnel with Variable Thermal
and Turbulent Properties*

Advisor: Prof. Jong-Shinn Wu

B.S. in Mechanical Engineering

I-Shou University, June 1999

List of Publications

Journal Publications (* represent those directly related to the PhD thesis)

1. J.-S. Wu, **K.-H. Hsu**, P.-M. Kuo and H.-J. Sheen, "Evaporation Model of a Single Hydrocarbon Fuel Droplet Due to Ambient Turbulence at Intermediate Reynolds Numbers," International Journal of Heat & Mass Transfer, Vol. 46, No. 24, pp. 4741-4745, 2003.
2. J.-S. Wu and **K.-H. Hsu**, "Parallel Implementation of a 3-D Electrostatic PIC-MCC Method Using Unstructured Tetrahedral Mesh," Journal of Plasma Physics, 2005 (accepted).*
3. **K.-H. Hsu**, P.-Y. Chen, C.-T. Hung, L.-H. Chen and J.-S. Wu, "Development of a Parallel Poisson's Equation Solver with Adaptive Mesh Refinement and Its Application in Field-Emission Prediction," Computer Physics Communications, 2006 (in press).*
4. P.-Y. Chen, **K.-H. Hsu**, Y.L. Hsu, T.-C. Cheng, K.-W. Cheng, C.-T. Hung and J.-S. Wu "Modeling of the Magnetic Focusing Spindt-type Field-Emission Device with Single Carbon Nanotube," Journal of Vacuum Science and Technology B, 2006 (accepted).*
5. Y.-L. Shao, **K.-H. Hsu**, Y.-Y. Lian and T.-L. Jung and J.-S. Wu, "Parallel Implementation of a 3-D Poisson-Boltzmann Equation Solver Using Finite-element Method with Adaptive Mesh Refinement," Journal of Computational Chemistry, 2006 (in revision).
6. **K.-H. Hsu**, K.-W. Cheng, P.-Y. Chen and J.-S. Wu, "Development of a Parallel Vector Poisson's Equation Solver with Adaptive Mesh Refinement and Its Application in Predicting magnetic field around permanent magnets," 2006 (preparing)*

International Conference Papers (* represent those directly related to the PhD thesis)

1. J.-S. Wu, **K.-H. Hsu**, and C.T. Hung, "On The Performance Improvement of a Parallel 3-D PIC-FEM Code," 33rd IEEE Plasma Conference, Traverse, Michigan, USA (June 4-8, 2006).*
2. **K.-H. Hsu** and J.-S. Wu, "Assessment of matrix solver for PIC-MCC method", Taiwan-Korea Plasma Conference, Hsinchu, TAIWAN, (January 16-18,2006).*
3. J.-S. Wu and **K.-H. Hsu**, "Parallel PIC Simulation of Low-Temperature Plasma Using Dynamic Domain Decomposition," TMS & AMS Joint International Conference, Taichung, TAIWAN, (December 14-18, 2005)*

4. J.-S. Wu and **K.-H. Hsu**, "Development of a 3-D PIC-MCC Method Using Unstructured Tetrahedral Mesh," 6th Asian CFD Conference, Taipei, TAIWAN, (October 23- 27, 2005).*
5. J.-S. Wu and **K.-H. Hsu**, "Parallel Implementation of a 3-D Electrostatic PIC/MCC Method Using Unstructured Tetrahedral Mesh," ICNSP-2005 (ATPPC-19), Nara, Japan (July 1-5, 2005).*
6. J.-S. Wu and **K.-H. Hsu**, "Dynamic Domain Decomposition for a Parallel 3-D Electrostatic PIC/MCC Code Using Unstructured Mesh," 32nd IEEE Plasma Conference, Monterey, California, USA (June 18-23, 2005).*
7. J.-S. Wu and **K.-H. Hsu**, "Parallel Implementation of a 3-D Electrostatic PIC Method Using Unstructured Mesh," 32nd IEEE Plasma Conference, Monterey, California, USA (June 18-23, 2005).*
8. J.-S. Wu, Y.-B. Chen, **K.-H. Hsu**, J.-Y. Hsu, J.-H. Chen and J.-L. Liu, "Finite-Element Solution for a New DFT Formulation in Quantum Mechanics," 24th International Symposium on Rarefied Gas Dynamics, Bari, Italy (July 10-16, 2004).

National Conference Papers (* represent those directly related to the PhD thesis)

1. J.-S. Wu and **K.-H., Hsu**, "Development of a Parallel 3D PIC-MCC method Using a Tetrahedral Mesh," 12th CFD Conference, Kaohsiung, Taiwan (August 19-21, 2005).*

